SORA

Stratospheric Observatory Research Aircraft

AE3200 - Group 19

Isabel Akkerman	5793882	Davide Mangini	5762731
Egeberk Baruh Karabulut	5906075	Sam Rotteveel	6006280
Diogo Canas	5919827	Gregory Wójcik	5302005
Walter Davidson	5783984	Yue Yue	5910617
Eve de Groot	5979188		

Delft University of Technology

TU Delft

This page is intentionally left blank.

SORA

Stratospheric Observatory Research Aircraft

AE3200 - Group 19

by

Isabel Akkerman	5793882	Davide Mangini	5762731
Egeberk Baruh Karabulut	5906075	Sam Rotteveel	6006280
Diogo Canas	5919827	Gregory Wójcik	5302005
Walter Davidson	5783984	Yue Yue	5910617
Eve de Groot	5979188		

Tutors:	Dr. F. Yin & Prof.dr. A. Gangoli Rao
Coaches	A.U. Garcidueñas Correa MSc & S. Binth Hamza MSc
Course:	Design Synthesis Exercise
Course Code:	AE3200
Teaching Assistant:	E. Sanches
Institution:	Delft University of Technology
Place:	Faculty of Aerospace Engineering, Delft
Date:	23-06-2026
Cover image:	3D render of SORA generated in CAD software over AI-enhanced background image

TU Delft

Preface

As DSE group 19, we would like to express our gratitude to all those who supported and guided us throughout this course.

We specially want to express our gratitude to our tutors Dr. Feijia Yin and Prof. Dr. Arvind Gangoli Rao for giving us the opportunity to work on this project and their guidance throughout the project.

We would also like to thank our coaches Alam Garcidueñas Correa MSc and Swaliha Binth Hamza MSc for their expertise and feedback during the design process.

A special thanks to Alfredo Serrano from Sceye for giving us information about their expertise with designing and operating high altitude platforms.

A word of acknowledgement to the teaching assistants that were available for any questions or concerns that we had.

Finally, a word of thanks to the OSCC for the organisation behind the scenes of DSE.

Group 19
Delft, June 2026

Executive Overview

Project Background and Objective

1. **Project Title**: Stratospheric Observatory Research Aircraft (SORA)
2. **Project Tutors**: Dr. F. Yin & Prof.dr. A. Gangoli Rao
3. **Coaches** A.U. Garcidueñas Correa MSc & S. Binth Hamza MSc
4. **Teaching Assistant**: E. Sanches

A large share of aircraft emissions occur at cruising altitude, where they significantly affect climate. While models are being developed to study these impacts, their validation is limited by scarce measurements at high altitudes. Existing efforts to use instrumented aircraft are constrained by fleet availability and limited endurance, resulting in poor temporal coverage, while measurements from satellites have poor spatial resolution. To address these limitations, this project focuses on designing a medium to high altitude, long-endurance observatory aircraft for continuous measurement of atmospheric composition, cruise emissions, and radiation for climate research. SORA (Stratospheric Observatory Research Aircraft) was developed to fulfil this mission.

Requirements

The stakeholder requirements and their current status are listed in Table 1. These are the overarching requirements which governed the design process. Stakeholder requirements were assigned a category: constraint (C), operational requirement (O), or functional requirement (F). From these requirements, system and subsystem level requirements were derived.

Table 1: *Stakeholder Requirements*

Identifier	Requirement	Stakeholder	Category	Status
REQ-STK01	The aircraft shall be controllable	Drone pilots / operators	F	Completed
REQ-STK02	The aircraft shall effectively handle data storage and transmission	Customer	F	Completed
REQ-STK04	The aircraft shall allow operator input	Drone pilots / operators	F	Completed
REQ-STK06	The aircraft shall be reliable	Customer	F	TBD
REQ-STK07	The aircraft shall manage energy distribution and storage	Customer	F	Completed
REQ-STK08	The aircraft shall be capable of performing atmospheric measurements during operations	Customer	O	Completed
REQ-STK09	The aircraft shall operate at a cruise altitude between 15 km and 25 km	Customer	O	Completed
REQ-STK10	The aircraft shall operate without onboard crew	Customer	O	Completed
REQ-STK11	The aircraft shall be capable of sustained cruise flight with an endurance of 60 days	Customer	O	Completed
REQ-STK12	The aircraft shall operate globally	Customer	O	Completed
REQ-STK17	The aircraft shall maintain within the budget of 1 million	Customer	C	Not met
REQ-STK20	The aircraft shall maintain safe ground operations	Regulators	C	TBD
REQ-STK21	The aircraft shall at all times follow the airspace regulations of the state's airspace it is flying within	National governments	C	TBD
REQ-STK23	The aircraft's operations shall not violate the privacy of any member of the public	General Public	C	TBD
REQ-STK24	The aircraft shall comply to all relevant safety regulations	Regulators	C	TBD
REQ-STK25	The aircraft shall comply with established noise limits	General Public	C	TBD

Identifier	Requirement	Stakeholder	Category	Status
REQ-STK26	The aircraft shall prioritise sustainability where possible	Customer	C	Completed
REQ-STK27	The aircraft shall be able to be manufactured	Part Suppliers/Manufacturers	C	TBD

REQ-STK17 (cost) is not met, as the estimated cost of 4.2 million euro exceeds the 1 million euro budget. For various requirements it cannot be said with reasonable certainty that they are met, these are indicated with a To Be Determined (TBD) status.

Market Gap

A market analysis was conducted to determine the current state of atmospheric measurement platforms and to position SORA within this market. The market was subdivided into the following segments: defence, civil operational monitoring (which includes meteorological agencies and intergovernmental organisations), civil scientific research, and civil commercial applications.

A gap in the market was identified: no existing platform enables persistent in-situ tropospheric and lower stratospheric measurements over monthly timescales and at altitudes up to 25 km. SORA therefore occupies a position across multiple segments, combining the high-altitude, long-endurance characteristics of defence reconnaissance platforms with a dedicated scientific payload, serving civil scientific research, operational monitoring, and commercial customers. The closest competitors were identified as low Earth orbit satellites and other UAVs.

A SWOT analysis was performed and confirmed that SORA's strengths come from its purpose-built design, autonomous operation, and flexible mission profile. The main threats are regulatory and certification complexity along with the unproven nature of the design, introducing a technical risk. Key stakeholders were identified and include meteorological agencies, research institutions, civil aviation regulators, and national governments, all of whom represent potential customers or mission-critical partners.

Trade-Off and Preliminary Design

From a design option tree, several different design options for SORA's configuration were considered feasible: a fixed wing, a flying wing, an airship and a hybrid option, that combines the fixed wing and airship solutions. A comprehensive trade-off was performed based on lift efficiency, controllability, payload, physical robustness, cost, and sustainability. In the end, the fixed wing option scored the highest and was selected as the baseline design. A similar trade-off method was used to determine the aircraft's launch method, wing positioning and tail configuration.

Operations and Mission Overview

The operational profile defines the latitude, month, and top cruise altitude which is feasible, taking into account weather conditions, atmospheric properties and airspace regulations. An ideal battery mass is then found to be 53 kg with 20.7 litres volume. With this information a potential flight profile can be developed as shown in Figure 1.

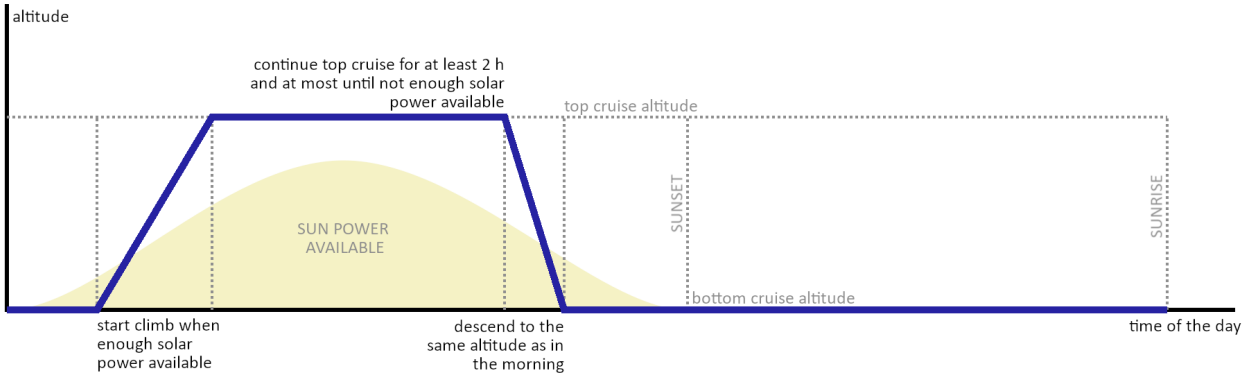

Figure 1: *Operational Profile Model Diagram*

Detailed Design

The detailed design followed from the preliminary design. Each subsystem was further developed and then integrated into a complete aircraft. The final configuration is shown in Figure 2. SORA has a 36 m wingspan, and a total fuselage

length of 12 m, and it weighs 218.5 kg. The wing will be fitted with solar panels across its upper surface, which generate electrical energy during the day, powering the aircraft's subsystems and charging batteries which support night operation. The propulsion subsystem consists of 4 electrically-powered propellers, attached to the underside of the wing structure. To ensure stability and controllability, the aircraft features a V-tail, attached at the rear end of the fuselage, as well as ailerons on the wings. The payload scientific instruments are placed at the nose of the aircraft.

Figure 2: *SORA's Final Design*

Payload

The most important mission objective is to gather scientific data to validate climate models, through means of a high-altitude, long-endurance platform. The payload plays a central role in the aircraft's design, as it sets non-negotiable constraints on mass and required power. To select the payload instruments, an extensive literature study was performed on the required measurements for climate models, and on the available measurement techniques. The instruments found were subjected to a feasibility study to eliminate instruments which showed clear drawbacks compared to other options. Finally, the remaining feasible instruments underwent a trade-off analysis to determine the final payload configuration, which is showcased in Table 2.

Table 2: *Payload Overview*

Target measurement	**Instrument**	**W [kg]**	**P [W]**	**Resolution**	**Measurement Range**	**Spatial Resolution[m]**	**Cost [€]**
Temperature	Radiosonde DFM-17	0.063	2	0.01 °C	−90–+60 °C	36	100
Pressure	Radiosonde DFM-17	0.063	2	0.01 hPa	1–1100 hPa	36	100
Humidity	Radiosonde DFM-17	0.063	2	0.1 %rH	0–100%rH [1]	36	100
Short wave radiation	SMP22x	0.6	10.06	±5 W/m²	250–3500 nm	72	7900
Long wave radiation	SGR4	0.6	10.1	1 W/m²	4400–50000 nm	650	7000
Trace gases SWIR spectrum	Pika SWIR imager	4	4	7.7 nm	1000-2500nm	9	190000
Trace gases UV/Vis spectrum	Pika UV imager	3	3.4	2.8 nm	330-800nm [2]	1.5	30000

[1] Humidity measurement range is valid across the instrument's specified temperature (–90 to +60 °C) and pressure (1–1100 hPa) ranges
[2] This measurment range includes the visible range (380-700 nm), functioning as a conventional camera

Target measurement	Instrument	W [kg]	P [W]	Resolution	Measurement Range	Spatial Resolution[m]	Cost [€]
Trace gases SWIR spectrum	NIRQuest+2.5 point	1.6	15	3.4 nm	900-2500nm	-	31500
Trace gases UV/Vis spectrum	QEPRO point	1.2	2.5	0.14 nm	185-1100nm	-	15500
Air sampling	VSI AS-110	1	5	—	—	-	—
Aerosols	Handix POPS	0.9	5	5%	130 nm–3 µm	36	10000
Contrail physical properties; aerosols	MiniMPL LiDAR	13	100	5 m	100m-15km	12	35000
TOTAL		**25.963**	**157.06**				**>327000**

Once the payload selection was finalised, a payload bay was sized to house the instruments requiring a controlled environment, such that each remained within its operating temperature and pressure limits. The remaining instruments are to be mounted externally on the aircraft. The layout of the payload bay is shown in Figure 3. In which the position of all payload components can be seen, including cabling and lenses.

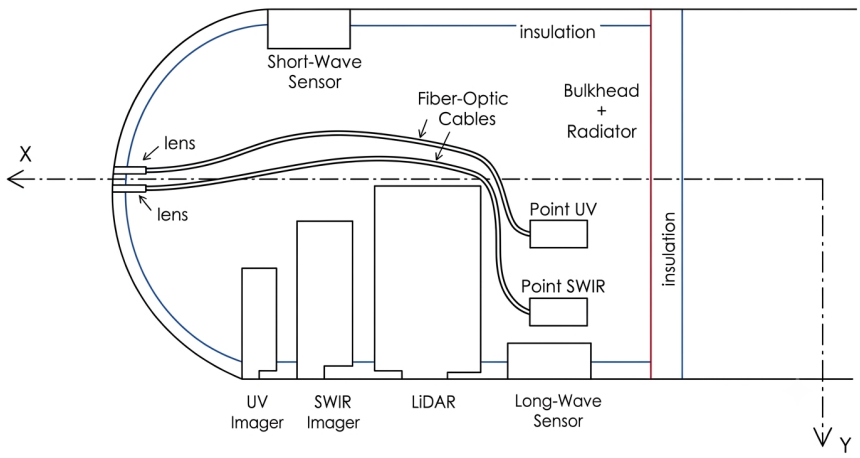

Figure 3: *Payload arrangement in compartment (AI-enhanced image based on sketch by group member)*

The compartment size was approximated as a cylinder of length 727 mm and diameter of 500 mm, with cutouts to allow optical instruments to measure undisturbed, with 15 mm of silica gel insulation and a coat of FSS-99 overcoated silver. It was determined that the total power requirement for instruments, including heating, is 202 W during the day and 193 W during the night. The total mass of the payload was determined at 26 kg.

Aerodynamics

Multiple airfoils were considered for the wing, specializing in high lift at low Reynold number conditions. Out of the compared airfoils, the MH114 was selected as it performed the best considering its endurance factor.

The NACA0012 airfoil was selected for the V-tail. The optimal wing lift coefficient for minimum power required is 1.38 at a cruise speed of 36 m/s. The 3D wing properties are summarised in Table 3. The distributed load along the span approaches an elliptical distribution due to tapering, resulting in a high Oswald efficiency factor (e). The total aerodynamic drag for the aircraft is calculated at 85.2 N, which requires a total power output of 3108 W. This total is comprised of the individual contributions from the wing (incorporating both parasitic and induced drag), the tail, the fuselage (combining skin friction and pressure drag), and the propulsion system.

A detailed breakdown of the drag forces and their corresponding power requirements for each element is presented in Table 4.

Table 3: *Final Wing Design and Performance*

Parameter	Value	Units
e	0.93	[-]
$C_{L,\text{opt}}$	1.38	[-]
C_D	0.049	[-]
$C_{L-\alpha}$	6.71	[1/rad]
$C_{M-\alpha_{ac}}$	-0.1645	[1/rad]
D	77.8	[N]
V_{cruise}	36.6	[m/s]
Re_{MAC}	1.569×10^5	[-]

Table 4: *Drag and Power Breakdown*

Element	Drag [N]	Power [W]
Wing	77.8	2844
Tail	2.9	102
Fuselage	2.7	97
Propulsion	1.8	65
Total	**85.2**	**3108**

Structures

The structures subsystem focuses on the structural design and material selection of the wing and the fuselage. The loads investigated were vertical and horizontal shear, in and out-of-plane bending, and torque. The selected material must have tensile, shear and compressive strengths which are able to withstand those loads. A cylindrical wing box was selected as the main load carrying device in the wings, with the skin and ribs primarily functioning to maintain the aerodynamic shape. The main spar is located at 33.5% of the chord, with an additional rectangular rear spar at 70% of the chord placed in the aileron region, in order to carry the loads caused by aileron deflection. A total of 84 ribs are placed at even intervals along the wing span. The fuselage is constrained by the size of the payload bay, with a maximum radius of 0.25 m, and by the loads from the V-tail. The final length of the fuselage is 11.8 m and the total mass of the aircraft's structures is 85 kg.

Propulsion

The propulsion system consists of 4 electric motors driving propellers, attached to the wing of the aircraft. This configuration ensures redundancy and reduces yaw moment in case one of the engines fails. Furthermore, the propellers will have 2 blades each, which is the most efficient blade configuration for the altitudes SORA will cruise at. The blades will use the FX 63-137 airfoil, a decision based on previous research into high-altitude UAV propellers. The sizing of the propulsion subsystem in terms of the number of engines, propeller radius and RPM each engine shall operate at took into account constraints like blade-tip velocity, power required and generated drag, while trying to minimise the mass of the subsystem. The power required profile and rate-of-climb profile were also analysed across the full operational altitude range of the aircraft. The final design features propellers with a 0.6 m blade radius, which will operate at 3200 RPM. The full subsystem will weigh 16 kg and require at most 5915 W of power.

Power

In order to operate continuously on missions of up to 60 days, the aircraft must generate its own power. The power subsystem therefore consists of two main components: solar panels and batteries. The solar panels were selected based on the highest available efficiency, which expands the selection to include lab-ready technologies that are not yet market-ready. As such, the aircraft will be equipped with triple-junction solar cells based on thick quantum-well superlattices, which have a preliminary estimated efficiency of 37% at SORA's operational altitudes. These solar cells will be placed along the upper surface of the wing. For the batteries, the Amprius SiCore 450 Wh/kg cell was selected due to its high energy density and proven suitability for high-altitude platforms. The battery is designed to be removable and is placed in the wing of the aircraft. This subsystem is integrated with the rest of the aircraft through additional components, including a DC–DC converter, electronic speed controllers, a battery management system, a maximum power point tracking device, and a power distribution unit. The final subsystem consists of 27.2 kg of solar panels and 53.1 kg of batteries.

Communication

The primary communication link consists of a Starlink Mini Terminal, housed in a radome on the aircraft's fuselage. This setup can achieve the necessary transmission data rate of 3 Mbps and operates in the Ku frequency band. An Iridium communication system was selected as a back-up link for controlling the aircraft and transmitting telemetry. For onboard data storage a solid state drive with 2 TB storage was selected. Both the uplink and the downlink budgets closed, ensuring that the communication system can function under nominal, degraded and failure conditions. The total system mass has a weight of 5.06 kg and requires 58 W of power.

Stability and Control

The aircraft was required to be stable and controllable. Moreover, special consideration was given to the V-tail and ruddervators, which introduce coupled yaw and pitch. As the tail controllability requirement, the aircraft has to

maintain lateral and longitudinal equilibrium under one-engine-inoperative condition. To achieve this, the tail arm was found to be 8.18 m, with an angle of 100° between the two V-tail surfaces. Each tail surface has a half-span of 3.1 m. The ailerons were sized according to an imposed controllability requirement (reaching a maximum roll rate of $25\,^{\circ}\,s^{-1}$ with a maximum aileron deflection of 20°), which led to an aileron positioning from 49% to 90% per wing half-span, and an aileron hinge at 79% of the local wing chord length. To control the aircraft, a fly-by-wire flight control system was selected. The Veronte Autopilot 1x was chosen as the flight control computer to provide a hybrid of autonomous and manual control, with Pegasus PA-RR-340-7-IH as the actuator for the ailerons and ruddervators. The flight control system has a mass of 10 kg and requires a power of 200 W.

Sustainability

Sustainability was considered throughout the manufacturing, operation and end of life phases. In the design process it was governed by material choice and power source selection. The selected material, Galvorn, is a light weight, durable and, most importantly for sustainability, recyclable composite fibre. Additionally, it has a carbon negative manufacturing process and needs only fractions of the energy needed by other aerospace materials to support the same weight. To ensure compliance with the zero emissions requirement an electric thrust generation mechanism was selected, powered by solar energy.

Budgets

To guide the design process, mass and power budgets were set as baseline goals and updated as the design matured. A final not-to-exceed mass cap of 250 kg was set, against which the converged design came in at 218.5 kg, leaving margin on the total. On power, the 7795 W budget was retained as the final target, with the converged design drawing approximately 6642 W. Differences between target and actual exist at subsystem level, but both totals fall well within their allocated budgets. The final mass and power budgets are given in Table 5.

Table 5: *Actual (A) Mass and Power Budgets against their Targets (T)*

Subsystem	**T [kg]**	**A [kg]**	Δ
Structure	103.8	80.6	−23.2
Power	94.4	80.9	−13.5
Propulsion	11.8	16.1	+4.3
Avionics & ctrl	10.0	10.0	0
Communication	5.0	5.1	+0.1
Payload	25.0	26.0	+1.0
Total	**250.0**	**218.5**	−31.5

(a) *Mass budget*

Subsystem	**T [W]**	**A [W]**	Δ
Propulsion	7260	5915	−1345
Payload	230	205	−25
Avionics & control	200	200	0
Communication	55	58	+3
Power (battery heating)	50	264	+214
Total	**7795**	**6642**	−1153

(b) *Power budget*

This aircraft is not being designed for profit but rather for furthering climate research models; as such, the return on investment is non monetary. However a detailed cost budget was created dividing the costs into each phase of life, with the development costs being driven by the selected material and the payload. The final estimated cost for production (excluding labour and machine costs) is approximately 4.2 million euros.

Technical Risk Assessment

Risks can threaten the progress, performance, and operational safety of the SORA mission. Therefore, it was necessary to identify technical risks at an early stage and define mitigation measures before they occurred. Risks were first assessed using a likelihood and severity ranking from 1 to 5 and, based on this criterion, risks were identified for the main life-cycle phases of the aircraft, including design, manufacturing, assembly, integration and testing, operations, maintenance, and end-of-life. In total, more than 50 technical risks were identified and placed in a pre-mitigation risk map to show their initial risk level. Several risks were identified as unacceptable, such as the aircraft encountering adverse weather, the design not converging within the project time frame, and malfunctioning of the scientific payload after launch.

After the initial assessment, mitigation strategies and contingency plans were proposed for each identified risk. The mitigation strategies aimed to reduce the probability or impact of the risks, while the contingency plans defined the actions to be taken if the risks still occurred. Finally, the remaining risks after mitigation are shown in a post-mitigation risk map. By comparing the pre- and post-mitigation risk maps, the effectiveness of the proposed risk control measures is visualised. After mitigation, all risks were deemed acceptable.

Verification and Validation

Verification was done on design tools throughout the design process for each subsystem. This consisted of unit testing any code used for input/output handling, logic and reason. This ensured that all the design tools used were performing as properly and providing the expected outputs. Additionally, a sensitivity analysis was done to determine which parameters drive the design and have a large influence on other subsystems. Finally, global verification of the final manufactured design will be composed of inspection, analysis and testing. Several requirements can be considered (partially) verified, although most require physical testing or more advanced analysis techniques to complete their verification.

Validation is needed to ensure the final aircraft is accomplishing its mission. This is done by checking that it is capable of fulfilling the four critical needs of the mission: adequate data for climate models, global mission profile, long endurance and high altitude operations. The product is partially validated for all these needs, but needs further testing to achieve full validation.

Quality Assurance

A RAMS analysis (reliability, availability, maintainability and safety) shows that the design has several fall back options in the case of a failure as well as a safe-life design philosophy to ensure that critical components are designed with sufficient margins. Additionally, the aircraft is designed with maintainability in mind through easily replaceable parts and continuous autonomous diagnostics.

A sensitivity analysis consisted of a one-at-a-time analysis which showed that the design is most sensitive to the aspect ratio. Payload weight drives the design linearly and taper ratio and wing position are not as sensitive. Secondly, a Monte Carlo Analysis indicates that the current design parameters are conservative and the design will not exceed 220.1 kg with a 95% confidence.

List of Figures

List of Tables

List of Symbols

Symbol	Description	Unit	Symbol	Description	Unit
A	Area	m^2	A_{encl}	Enclosed area of the spar cross-section	m^2
$A_{exposed}$	Surface area exposed to outside air	m^2	A_{prop}	Propeller disk area	m^2
A_{proj}	Projected area exposed to sunlight	m^2	$A_{surface}$	Payload-compartment or fuselage-skin surface area	m^2
AR	Aspect ratio	–	AR_{tail}	Tail aspect ratio	–
b	Wing span	m	b_{tail}	Tail span	m
B	Number of propeller blades	–	c	Local chord length	m
c_r	Root chord	m	c_t	Tip chord	m
$c_{r,tail}$	Tail root chord	m	C	Cost	EUR
C_D	Drag coefficient	–	$C_{D,0}$	Zero-lift drag coefficient	–
$C_{D,i}$	Induced drag coefficient	–	$C_{D,fus}$	Fuselage drag coefficient	–
$C_{D,pressure}$	Fuselage pressure drag coefficient	–	$C_{D,skin}$	Skin-friction drag coefficient	–
$C_{d,laminar}$	Laminar drag coefficient	–	$C_{d,turbulent}$	Turbulent drag coefficient	–
C_L	Lift coefficient	–	$C_{L,\alpha}$	Lift-curve slope	rad^{-1}
$C_{L,h}$	Tail lift coefficient	–	$C_{L,h,max}$	Maximum tail lift coefficient	–
$C_{L,h_{\delta e}}$	Tail lift derivative due to elevator/ruddervator deflection	rad^{-1}	C_M	Moment coefficient	–
C_{m_α}	Pitching-moment derivative with respect to angle of attack	rad^{-1}	C_{m_q}	Pitch damping derivative	–
$C_{m_{\delta e}}$	Pitching-moment derivative due to elevator deflection	rad^{-1}	C_{Y_β}	Side-force derivative with respect to sideslip angle	rad^{-1}
$C_{Y_{\delta r}}$	Side-force derivative due to rudder command	rad^{-1}	C_{n_β}	Yawing-moment derivative with respect to sideslip angle	rad^{-1}
C_{n_r}	Yaw damping derivative	–	C_{n_p}	Yawing-moment derivative due to roll rate	rad^{-1}
$C_{n_{\delta r}}$	Yawing-moment derivative due to rudder command	rad^{-1}	C_{l_β}	Rolling-moment derivative with respect to sideslip angle	rad^{-1}
C_{l_p}	Roll damping derivative	–	C_{l_r}	Rolling-moment derivative due to yaw rate	–
$C_{l_{\delta a}}$	Rolling-moment derivative due to aileron deflection	rad^{-1}	$C_{l_{\delta r}}$	Rolling-moment derivative due to rudder command	rad^{-1}
C_P	Propeller power coefficient	–	C_T	Propeller thrust coefficient	–
$C_{rate,ch}$	Battery charging C-rate	–	C_{cell}	Battery cell capacity	Ah
d	Distance or communication-link range	m / km	$d(z)$	Offset between distributed load and flexural axis	m
dR	Propeller blade element width	m	D	Drag force	N
D_f	Fuselage drag force	N	D_{prop}	Propeller drag force	N
D_{tail}	Tail drag force	N	D_w	Wing drag force	N
D_{sensor}	Sensor diameter	mm	D_{window}	Required window diameter	mm
DR	Data rate	bit/s	e	Oswald efficiency factor	–
E	Young's modulus	Pa	E_{bat}	Battery energy capacity	Wh
E_{cell}	Energy stored in one battery cell	Wh	E_b/N_0	Energy-per-bit to noise-density ratio	dB
$EIRP$	Equivalent isotropic radiated power	dBW	f	Frequency or Prandtl tip-loss exponent	Hz / –
f_1	Fraction of payload-compartment area covered by insulation	–	f_2	Fraction of payload-compartment area covered by windows	–
f_{maint}	Maintenance cost factor	–	$f_{op,margin}$	Operational cost margin factor	–
f_{test}	External testing and certification cost factor	–	F	Prandtl tip-loss factor	–
F_{skin}	Tension force in the wing skin	N	F_{tail}	Resultant tail force	N
$F_{tail,lat}$	Lateral component of tail force	N	$F_{tail,vert}$	Vertical component of tail force	N

Symbol	Description	Unit	Symbol	Description	Unit
$FSPL$	Free-space path loss	dB	G	Solar irradiance or antenna gain	W/m^2 / dB
G/T	Receiver gain-to-noise-temperature ratio	dB/K	G_{SC}	Solar constant	W/m^2
G_{rx}	Receiver antenna gain	dB	h	Altitude or convective heat-transfer coefficient	m / W/(m^{2}K)
$H(z)$	Horizontal shear-force distribution	N	I	Solar irradiance or second moment of area	W/m^2 / m^4
I_{avg}	Average actuator current	A	$I_{\text{cell,ch}}$	Battery cell charging current	A
$I_{\text{cell,dis}}$	Battery cell discharge current	A	$I_{\text{dis,max}}$	Maximum battery cell discharge current	A
$I_{\text{pack,ch}}$	Battery pack charging current	A	$I_{\text{pack,dis}}$	Battery pack discharge current	A
I_{xx}	Second moment of area about the x-axis	m^4	I_{yy}	Second moment of area about the y-axis	m^4
I_{xy}	Product of inertia of the cross-section	m^4	J	Advance ratio or polar moment of inertia	– / m^4
k	Thermal conductivity or Boltzmann constant	W/(mK) / J/K	k_s	Shear buckling coefficient	–
l	Length	m	l_h	Tail arm	m
$l_{\text{separation}}$	Separation distance between sensor and window	mm	L	Lift / characteristic length / latitude	N / m / °
L_{rib}	Rib spacing	m	M	Mach number or bending moment	– / Nm
$M_x(z)$	Out-of-plane bending moment distribution	Nm	$M_y(z)$	In-plane bending moment distribution	Nm
M_{cr}	Critical buckling moment	Nm	MAC	Mean aerodynamic chord	m
MAC_w	Wing mean aerodynamic chord	m	m	Mass	kg
m_{act}	Actuator mass	kg	m_{bat}	Battery mass	kg
m_{cell}	Battery cell mass	kg	m_{rec}	Recyclable or reprocessable structural mass	kg
m_{sp}	Solar-panel mass	kg	$m_{\text{sp,est}}$	Estimated specific solar-panel mass	kg/m^2
m_{struct}	Total structural mass	kg	$m_{\text{CO}_2\text{eq,cruise}}$	Carbon-dioxide-equivalent emissions during cruise	kg
$m_{\text{CO}_2\text{eq,LTO}}$	Carbon-dioxide-equivalent emissions during landing and take-off	kg	N_{avg}	Average number of personnel during development	–
N_{cells}	Total number of battery cells	–	$N_{\text{cells,raw}}$	Raw required number of battery cells before rounding	–
N_p	Number of parallel battery strings	–	N_s	Number of series-connected battery cells	–
N_{op}	Number of operation personnel	–	Nu	Nusselt number	–
n	Load factor or propeller rotational speed	– / s^{-1}	n_{max}	Maximum load factor	–
n_{roll}	Load factor used for roll manoeuvre sizing	–	$n_{\text{propellers}}$	Number of propellers	–
p	Roll rate	rad/s	p_{max}	Maximum roll rate	rad/s
P	Pressure or power	Pa / W	P_{act}	Actuator power consumption	W
$P_{\text{available}}$	Available power	W	P_{avg}	Average actuator voltage/power term used in actuator sizing	V / W
P_{bat}	Battery output power	W	$P_{\text{bat,heat}}$	Battery heating power required after internal heat generation	W
$P_{\text{cell,ch}}$	Resistive heat generated by one cell during charging	W	$P_{\text{cell,dis}}$	Resistive heat generated by one cell during discharge	W
P_{heat}	Heat generated or dissipated	W	$P_{\text{heat,required}}$	Thermal power required to maintain battery temperature	W

Symbol	Description	Unit	Symbol	Description	Unit
$P_{\text{pack,ch}}$	Battery pack heat generation during charging	W	$P_{\text{pack,dis}}$	Battery pack heat generation during discharge	W
$P_{\text{payload,heat}}$	Payload heating power	W	$P_{\text{prop,night}}$	Propulsion power required during night operation	W
P_{req}	Required power	W	P_{shaft}	Shaft power	W
$P_{\text{single-prop}}$	Useful power generated by one propeller	W	P_{system}	Total system power demand	W
P_{total}	Total required propulsion power	W	P_{motor}	Motor power	W
Pr	Prandtl number	–	q	Dynamic pressure or distributed load	Pa / N/m
q_{ail}	Distributed aileron load	N/m	q_{land}	Dynamic pressure during landing	Pa
Q	First moment of area or heat transfer rate	m^3 / W	Q_{required}	Heat required to maintain payload-compartment temperature	W
r	Radial coordinate or yaw rate	m / rad/s	R	Radius or thermal resistance	m / K/W
R_1	Thermal resistance of insulation	K/W	R_2	Thermal resistance of windows	K/W
R_{cell}	Battery cell internal resistance	Ω	R_{eq}	Equivalent thermal resistance of the payload compartment	K/W
R_{inner}	Inner radius of cylindrical spar	m	R_{outer}	Outer radius of cylindrical spar	m
Re	Reynolds number	–	ROC	Rate of climb	m/s
RPM	Rotational speed	rev/min	S	Wing reference area	m^2
S_h	Horizontal-tail equivalent area	m^2	S_{tail}	Total V-tail surface area	m^2
S_w	Wing area	m^2	S_{eff}	Effective annual salary used for development cost	EUR/year
S_{op}	Annual salary per operator	EUR/year	S_{wet}	Fuselage wetted area	m^2
SF	Safety factor	–	t	Thickness or time	m / s
$t_{\text{axial,pb}}$	Required skin thickness from pressure-bending axial stress	m	$t_{\text{cell,ch}}$	Battery cell charging time	h
t_{climb}	Climb time	s	t_{dev}	Development time	year
t_{sc}	Solar-powered cruise time	s	t_{scmax}	Maximum solar-powered cruise time	s
t_{skin}	Skin thickness	m	$t_{\text{skin,press}}$	Required skin thickness from pressurisation	m
$t_{\text{skin,shear}}$	Required skin thickness from shear	m	t_{wall}	Wall thickness	m
T	Thrust or torque	N / Nm	$T(z)$	Internal torque distribution	Nm
T_{env}	Environmental temperature	K	T_{interior}	Payload-compartment interior temperature	K
T_{skin}	Fuselage skin temperature	K	T_{support}	Torque at rear-spar support	Nm
T_{required}	Required window thickness	mm	T_{roll}	Time to reach maximum bank angle	s
T_{sys}	System noise temperature	K	$u_{z1}(z)$	Unit step function for point-load location	–
$u_{ze,i}(z)$	Unit step function for engine location	–	U_{de}	Design gust velocity	m/s
v	Velocity or deflection	m/s / m	v_{TAS}	True airspeed	m/s
v_{cruise}	Cruise speed	m/s	v_{relative}	Relative velocity at a propeller blade element	m/s
$v_{\text{tangential}}$	Tangential velocity at a propeller blade element	m/s	v_{tip}	Propeller blade-tip velocity	m/s
V	Flight speed or internal shear force	m/s / N	$V(z)$	Vertical shear-force distribution	N
V_{avg}	Average actuator voltage	V	V_{bat}	Battery volume	L
$V_{\text{cell,nom}}$	Nominal cell voltage	V	V_{cr}	Cruise speed used for control sizing	m/s

Symbol	Description	Unit	Symbol	Description	Unit
V_h/V	Tail-to-wing dynamic pressure or velocity ratio	–	V_{lost}	Lost air volume from pressurised compartment	L
$V_{\text{pack,dis}}$	Battery pack discharge voltage	V	V_{stall}	Stall speed	m/s
V_{support}	Shear force at rear-spar support	N	W	Aircraft weight	N
W_{engine}	Engine weight	N	W_{fus}	Fuselage weight	N
W_s	Wing loading	N/m^2	x	Chordwise coordinate	m
x_{ac}	Aerodynamic-centre location	m	x_{cg}	Centre-of-gravity location	m
$x_{\text{cp,aileron}}$	Aileron centre-of-pressure location	–	$x_{\text{rear spar}}$	Rear-spar chordwise location	–
y	Spanwise coordinate	m	$y_{T,i}$	Vertical offset of thrust line for engine i	m
z	Spanwise coordinate used in structural loading	m	α	Angle of attack or absorptivity	rad / –
α_0	Zero-lift angle of attack	rad	α_{local}	Local blade angle of attack	rad
β	Propeller blade pitch angle or Prandtl–Glauert correction factor	rad / –	δ	Allowable deflection / empirical Oswald-efficiency correction / solar declination	m / – / °
δ_a	Aileron deflection	rad	$\delta_{a,\max}$	Maximum aileron deflection	rad
δ_e	Elevator/ruddervator pitch deflection	rad	$\delta_{e,\max}$	Maximum elevator/ruddervator pitch deflection	rad
δ_r	Rudder/ruddervator yaw deflection	rad	$\delta_{r,\max}$	Maximum rudder/ruddervator yaw deflection	rad
Δn	Gust-induced load factor increment	–	ΔP	Pressure difference	Pa
$\Delta P_{\max}$	Maximum pressure difference	Pa	ϵ	Downwash angle or emissivity	rad / –
η	Efficiency	–	η_{avg}	Average solar-cell efficiency	–
η_{dis}	Battery discharge efficiency	–	η_p	Propeller efficiency	–
η_{rec}	Recycled or reprocessable structural mass percentage	%	η_{sp}	Solar-panel efficiency	–
Γ_{tail}	V-tail dihedral angle used for force decomposition	rad	γ	Structural knock-down factor	–
λ	Taper ratio	–	λ_{air}	Thermal conductivity of air	W/(mK)
λ_w	Wing taper ratio	–	μ	Dynamic viscosity	Pa s
ν	Poisson's ratio	–	ρ	Air density or material density	kg/m^3
σ	Stefan–Boltzmann constant or normal stress	W/(m^{2}K^4) / Pa	σ_{allow}	Allowable normal stress	Pa
σ_{cr}	Critical buckling stress	Pa	$\sigma_{\text{fail,lg}}$	Longitudinal failure stress	Pa
σ_{skin}	Wing-skin tensile stress	Pa	σ_z	Normal stress in spanwise direction	Pa
τ	Shear stress	Pa	τ_{allow}	Allowable shear stress	Pa
τ_{cr}	Critical shear buckling stress	Pa	$\tau_{\text{fail,tv}}$	Transverse shear failure stress	Pa
τ_{shear}	Shear stress due to vertical shear force	Pa	τ_{torque}	Shear stress due to torque	Pa
ϕ	Bank angle or blade inflow angle	rad	$\phi_{\max}$	Maximum bank angle	rad
Ω	Earth rotational speed or angular velocity	rad/s			

List of Abbreviations

Abbrev.	Definition	Abbrev.	Definition
ADS-B	Automatic Dependent Surveillance–Broadcast	ICAO	International Civil Aviation Organization
AI	Artificial Intelligence	IFR	Instrument Flight Rules
AIAA	American Institute of Aeronautics and Astronautics	INS	Inertial Navigation System
AIC	Aircraft-Induced Cloudiness	ITCZ	Intertropical Convergence Zone
AIT	Assembly, Integration, and Testing	KNMI	Royal Netherlands Meteorological Institute

Abbrev.	Definition	Abbrev.	Definition
AR	Aspect Ratio	LCA	Life Cycle Assessment
ATC	Air Traffic Control	LEO	Low Earth Orbit
BET	Blade Element Theory	LiDAR	Light Detection and Ranging
BMS	Battery Management System	LOPC	LASP Optical Particle Counter
BR	Baseline Review	LTO	Landing and Take-Off
CAGR	Compound Annual Growth Rate	MALEO4CRE	Medium-Altitude Long-Endurance Observatory Aircraft for Climate Research
CAD	Computer-Aided Design	MiniMPL	Mini Micro Pulse LiDAR
CFRP	Carbon Fibre Reinforced Polymer	MNS	Mission Need Statement
CFRTP	Carbon Fibre Reinforced Thermoplastic	MPPT	Maximum Power Point Tracking
CFD	Computational Fluid Dynamics	MTR	Mid-Term Review
CG	Centre of Gravity	NASA	National Aeronautics and Space Administration
CNF	Carbon Nanotube Fibre	NO	Nitric Oxide
CNT	Carbon Nanotube	NOAA	National Oceanic and Atmospheric Administration
DAA	Detect and Avoid	O_3	Ozone
DC	Direct Current	OSCC	Design Synthesis Exercise Coordination Committee
DID	Deliverable Item Description	PBN	Performance-Based Navigation
DLR	German Aerospace Center	PFC	Perfluorocarbon
DSE	Design Synthesis Exercise	POPS	Portable Optical Particle Spectrometer
EAR	Easy Access Rules	RAMS	Reliability, Availability, Maintainability, and Safety
EASA	European Union Aviation Safety Agency	RCP	Required Communication Performance
EOL	End of Life	REQ	Requirement
ERA5	ECMWF Reanalysis v5	ROI	Return on Investment
ESA	European Space Agency	RPM	Revolutions Per Minute
ESC	Electronic Speed Controller	RPAS	Remotely Piloted Aircraft System
EUMETSAT	European Organisation for the Exploitation of Meteorological Satellites	SMP	Smart Pyranometer
FAA	Federal Aviation Administration	SNR	Signal-to-Noise Ratio
FBD	Functional Breakdown Diagram	SO_2	Sulphur Dioxide
FBS	Functional Breakdown Structure	SORA	Stratospheric Observatory Research Aircraft
FDR	Flight Data Recorder	SOP	Standard Operating Procedure
FEM	Finite Element Method	SWIR	Short-Wave Infrared
FFD	Functional Flow Diagram	SWOT	Strengths, Weaknesses, Opportunities, and Threats
FL	Flight Level	TBD	To Be Determined
FOV	Field of View	TPED	Tasking, Processing, Exploitation, and Dissemination
GHG	Greenhouse Gas	TTL	Tropical Tropopause Layer
GNSS	Global Navigation Satellite System	TU Delft	Delft University of Technology
GPS	Global Positioning System	UARS	Upper Atmosphere Research Satellite
GWP	Global Warming Potential	UAS	Unmanned Aircraft System
HALE	High-Altitude Long-Endurance	UAV	Unmanned Aerial Vehicle
HAPS	High-Altitude Platform System	UV	Ultraviolet
HFC	Hydrofluorocarbon	UV/Vis	Ultraviolet/Visible
		V&V	Verification and Validation
		VLM	Vortex Lattice Method
		VSI	Vienna Scientific Instruments
		WBS	Work Breakdown Structure
		WMO	World Meteorological Organization
		WWF	World Wide Fund for Nature

Contents

1

Introduction

Climate change represents one of the most pressing challenges facing the world today. In 2024, the global annual mean air temperature exceeded the 1.5 degrees threshold set by the Paris Agreement for the first time [1], marking a critical milestone that underscores the urgency of understanding and mitigating its effects. Among its wide-ranging consequences, climate change drives increasingly severe weather events, rising sea levels, and loss of biodiversity[1]. In this context, air travel and transport are responsible for about 3.5% of human-induced global warming [2]. Most of aviation's global warming impact is caused by aircraft emissions (such as CO_2, NO_x, SO_2 and H_2O) and aircraft induced clouds (contrails) occurring at cruise altitudes.

To understand and map these effects, climate models are used to simulate the Earth's climate system and project future conditions. However, accurate models require validation with real-world observational data. A key limitation in this regard is the scarcity of in-situ atmospheric measurements at high altitudes, as well as difficulties with current efforts to adapt existing aircraft for the collection of this data, which are limited by fleet availability and limited endurance, resulting in poor spatial and temporal coverage. The growing scientific interest in this altitude regime has consequently created demand for high-altitude, long-endurance platforms capable of operating autonomously in the lower stratosphere.

The aim of this report is to develop and evaluate a conceptual unmanned aerial vehicle (UAV) design that satisfies the mission requirements of the MALEO4CRE project. Firstly, the report defines the precise mission needs by addressing the current observational gap. Secondly, the report aims to explain the design process of the final product: SORA (Stratospheric Observatory Research Aircraft), a high-altitude, long-endurance observatory aircraft capable of continuously measuring atmospheric composition, aircraft cruise emissions and radiation for climate research. Finally, the report aims to give a full analysis of the key subsystems on a detailed level, including aerodynamics, structures, propulsion, power, communications, and flight controls. Additionally, throughout the design process sustainability is considered a driving parameter.

This report starts by defining the market gap, project objective and subsequent requirements in Chapter 2. The design process to achieve this objective is then described in Chapter 3. From here, the final design concept is shown in Chapter 4, and the process to achieve this design is explained in the following chapters. First, the operational profile must be established in Chapter 5, then the payload and measurement systems are fixed in Chapter 6. With the global parameters defined, detailed design of the subsystems begin with aerodynamics in Chapter 7, structures and materials in Chapter 8, propulsion in Chapter 9, power systems in Chapter 10, communications in Chapter 11, and finally, stability and control in Chapter 12.

All the subsystems are then integrated into a complete system and their performance is analysed in Chapter 13, then a preliminary production plan is set up for the aircraft in Chapter 14. A mass, power, and cost budget is then found taking future life phases into account in Chapter 15, and the technical risk assessment is updated in Chapter 16. Global verification and validation, along with future validation plans are explained in Chapter 17. In Chapter 18 , sensitivity, RAMS, and iterative loop analyses are conducted to assure the quality of the outputs of this paper. Lastly, several recommendations for future design stages are elaborated on in Chapter 20.

[1] URL: https://www.un.org/en/global-issues/climate-change [cited on 11/06/2026]

2

Project Objectives and Requirements

In this chapter the mission definition is explained. In Section 2.1 the project objective of the mission is stated. Section 2.2 illustrates the market and explains the market gap SORA should fill. After which, in Section 2.3 the stakeholder requirements can be found. Finally, the sustainability philosophy during the design process can be found in Section 2.4.

2.1. Project Objective

Climate change is one of the most pressing global challenges. The aviation sector contributes to climate change through both carbon dioxide (CO_2) and non carbon dioxide effects, including emissions of nitrogen oxides (NO_x), soot, and the formation of contrails [3].

The consequences of climate change include increased risks of heatwaves, droughts, floods, wildfires, rising sea levels, food insecurity, and loss of biodiversity[1]. Understanding and mitigating these impacts requires reliable predictions of future climate conditions.

Climate models are tools used to simulate the Earth's climate system and to assess future climate scenarios. The predictive capability of climate models depends strongly on their validation against real-world observations. Continuous and accurate observational datasets are therefore essential for assessing model performance. A challenge in climate model validation is the limited availability of atmospheric measurements in high-altitudes [4].

Addressing this observational gap requires a platform capable of performing long-duration measurements in regions of the atmosphere that are currently undersampled. The resulting Mission Need Statement (MNS) can therefore be stated as follows:

> *The aircraft shall perform long-duration measurements of atmospheric parameters at medium and high altitudes in order to increase the availability of in-situ data for the validation and improvement of climate models.*

In order to fulfil this mission, the Project Objective Statement is formulated as follows:

> *This DSE project aims to design a medium/high-altitude long-endurance observatory aircraft that reliably and continuously measures atmospheric composition, aircraft cruise emissions including contrails and contrail cirrus, and radiation for climate research.*

Although climate model validation forms the primary motivation for the mission, the scientific value of the collected data extends considerably beyond this application. For example, the platform could provide valuable observations for contrail research. Recent research suggests that the short-term warming effects of contrails may exceed that of all aviation CO_2. However, these warming effects are poorly quantified in high-altitude regions [5, 6]. Measurements acquired directly within the relevant altitude regime could help reduce these uncertainties.

Furthermore, SORA could support research into air quality and atmospheric pollution transport. Wildfire plumes can reach high altitudes, where they remain suspended for extended periods, amplifying their climatic impact [7]. Detailed vertical observations of aerosol concentration are currently limited [8], making a vertically flexible observatory platform useful.

Finally, the platform may provide more insight for weather forecasting and early-warning systems. Currently, the main in-situ database for forecasting relies on radiosondes and airliner observations, introducing horizontal and vertical data gaps [9]. Additional in-situ observations from SORA could provide valuable data.

In conclusion, while the primary objective of SORA is to provide atmospheric measurements for climate model validation, its scientific use extends to a wide range of climate, atmospheric, and meteorological applications, further emphasising the value of developing such a platform.

[1] URL: https://www.un.org/en/global-issues/climate-change [cited 11/06/2026]

2.2. Market Analysis

This section examines SORA from a market perspective. First, Subsection 2.2.1 defines the market in which the concept operates and outlines the growing need for atmospheric measurement platforms. Next, Subsection 2.2.2 identifies the main stakeholders involved in or affected by the mission. Subsequently, Subsection 2.2.3 analyses the most relevant market segments and their specific needs. Based on this, Subsection 2.2.4 presents a SWOT analysis to assess the internal strengths and weaknesses of the concept, as well as the external opportunities and threats. Following, Subsection 2.2.5 discusses the main competitor categories in the market. Finally, the position of SORA can be found within the market derived from the information obtained in Subsection 2.2.6.

2.2.1. Market Definition

As mentioned in Section 2.1, there is a growing need for accurate atmospheric measurements to improve understanding of climate processes. This market demand is reflected in the environmental monitoring market, which was valued at "$14.4 billion in 2024 and is projected to reach $20.1 billion by 2030, growing at a CAGR (Compound Annual Growth Rate) of 5.7%".[2] Atmospheric monitoring therefore represents an important segment within this broader environmental monitoring market, as reliable in situ and remote observations are essential for climate research, emissions assessment, and the development of effective mitigation strategies. This need is further reinforced by governments, research institutions, and commercial operators, all of whom require increasingly accurate atmospheric data to improve climate models, monitor environmental change, and assess the environmental impact of aviation.[3]

2.2.2. Stakeholder Identification

Stakeholders are the individuals or groups who influence or are influenced by the project, and were therefore identified at an early stage. All the stakeholders that warrant mentioning are summarized in Table 2.1, ranked by their importance to the mission.

Table 2.1: *Overview of Identified Stakeholders.*

Stakeholder name	**Identifier**	**Relation to project**	**Explanation**
(Primary) Customer(s)	ST-01	Both affects and is affected by the operational mission	They purchase and use the UAV, and therefore both affect the project through their needs and requirements, and are directly affected by its performance, cost, and operational value.
(Civil Aviator) Regulators	ST-02	Affects the operational mission	Regulators affect the mission through certification requirements, safety regulations, and airworthiness standards that must be satisfied.
National governments	ST-03	Affect the operational mission	National governments will have regulations concerning flying the UAV in their airspace.
Part suppliers / manufacturers	ST-04	Affects the operational mission	They supply essential components, such as structural parts, whose quality directly influences mission success. If these components do not meet the required standards, the UAV may experience structural damage, system malfunction, or even self-ignition.
Air traffic controllers (ATC)	ST-05	Affected by and affect the operational mission	The ATC are affected by the mission because the controllers have to separate other traffic from the UAV during take-off and landing. The ATC affect the mission since the UAV will have to comply with ATC instructions during take-off and landing.
Aircraft crews from other aircraft	ST-06	Affected by and affect the operational mission	Aircraft crews are affected by the mission since the unmanned aircraft will fly in the same airspace. Therefore, aircraft crews also affect the mission since the unmanned aircraft shall strive not to affect the regular course of other air traffic.

Continued on next page

[2] URL: https://www.grandviewresearch.com/industry-analysis/environmental-monitoring-market [cited 01/05/2026].
[3] URL: https://wmo.int/media/news/state-of-global-climate-observing-system-2021 [cited 23/04/2026].

Stakeholder name	Identifier	Relation to project	Explanation
Meteorological agencies	ST-07	Affects the operational mission and is affected by the mission.	The UAV will operate with the information given by the meteorological agencies regarding the weather conditions in the atmosphere. The passive and active measurement data coming from the UAV can be used to improve predictions.
Drone pilots/-monitors	ST-08	Affect and are affected by the operational mission	They can provide valuable feedback to improve the user-friendliness of the UAVs, whereas a more complex control system would make their work more difficult.
Maintenance workers	ST-09	Affect and are affected by the operational mission	They can provide valuable feedback to improve the maintainability of the UAVs, whereas a more complex system would make their work more difficult.
Environmental groups (E.g. Greenpeace, WWF)	ST-10	Affected by and affect the operational mission	The environmental groups may use the measurements taken by the aircraft. Additionally, environmental groups may be critical about the aircraft operating in certain environmentally critical areas.
General public	ST-11	Affected by the operational mission	The general public may encounter the UAV in their sight or hear the aircraft's noise. The findings of the mission may affect general public opinion on aviation's impact on climate change.
Airports	ST-12	Affected by and affects the operational mission	The UAV will take-off at any airport and shall be able to land at any airport at the end of the mission.

Using the information provided in Table 2.1, a stakeholder map was created to illustrate the identified stakeholders and their connection to the project, and can be seen in Figure 2.1. The stakeholders in the yellow section should be managed closely, those in green should be kept satisfied, blue stakeholders should be kept informed and those in the red section only need to be monitored.

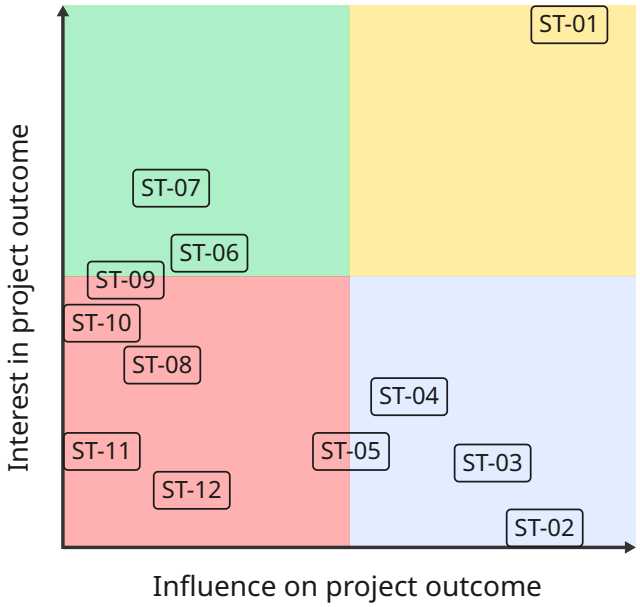

Figure 2.1: *Stakeholder Map*

2.2.3. Market Segment Analysis

This section describes the identification of market segments within the market definition stated in Subsection 2.2.1. This leads to a better understanding of customer needs within the market.

Defence
The defence segment consists of militaries and defence companies around the world. The main need of this sector within the defined market consists of surveillance and reconnaissance. To this end, platforms have been developed such as the Airbus Zephyr UAV[4] and Dzyne ULTRA[5] that can provide high resolution imaging. Moreover, long endurance is also needed for these systems. The Zephyr platform was developed for high altitude and ultra long endurance, whereas the Dzyne ULTRA was developed to carry a more elaborate payload, including a hardened-GPS unit, and has lower endurance than Zephyr.

Civil - Operational Monitoring
The civil operational monitoring segment consists of institutes, government agencies and intergovernmental bodies that continuously require atmospheric data for public products. Some key customers in this segment are EUMETSAT, the WMO and national weather services, such as the Dutch KNMI. Unlike research campaigns, the data need in this segment is recurring and stems from an operational need. It feeds directly into activities such as weather forecasting, air quality reporting and climate trend monitoring. Examples are WMO's Global Atmosphere Watch program[6], weather balloons[7] and EUMETSAT's Meteosats[8]. Customers in this segment value cost-effectiveness, long-term operational sustainability and reliable, standardised measurement capability that integrates with existing observing infrastructure.

Civil - Scientific Research
This market section consists of atmospheric science programs that require high-quality in situ measurements and continuous atmospheric data collection. An example is STRATEOLE-2, a balloon-based system used to measure wind circulation, humidity, temperature, and trace atmospheric properties in the Tropical Tropopause Layer (TTL) and the lower stratosphere (altitude from 18km to 20km)[10]. For this market segment, long endurance is one of the primary requirements, as it enables extended observation periods and the collection of scientifically valuable data. Payload capacity (around 20 kg for STRATEOLE-2) is of secondary importance but still relevant for carrying the necessary scientific instruments. Another example is ESA's Sentinel-5[9], which measures atmospheric composition and air quality.

Civil - Commercial
The civil commercial sector consists of private companies and service providers around the world. One type of company is aircraft engine manufacturers. In the last couple decades, these manufacturers developed more efficient engines. In order to make these engines even more efficient, it is important to evaluate the overall atmospheric impact of an aircraft mission [11]. Therefore, there is a commercial market for obtaining these measurements. Other than the engine manufacturers, there is also a commercial market for oil and gas companies, maritime surveillance, agriculture, and telecom support. This market is served by the Dzyne ULTRA [5].

2.2.4. Market SWOT Analysis
To better position the product within the market, a SWOT analysis was conducted to identify the internal strengths and weaknesses of the concept, as well as the external opportunities and threats that could influence its market potential. The results are summarised in Table 2.2.

Table 2.2: *SWOT Analysis*

Category	Identifier	Description
Strengths	MKT-ST-01	The design is not strongly constrained by cost, allowing greater flexibility in selecting high-performance technologies and subsystems.
	MKT-ST-02	The aircraft is purpose-built for atmospheric and climate observations, enabling it to better satisfy mission-specific requirements than general-purpose platforms.
	MKT-ST-03	Autonomous operation reduces the need for continuous human intervention and improves operational efficiency.

Continued on next page

[4]URL: https://www.aaltohaps.com/about-us/ [cited 23/04/2026]
[5]URL: https://dzyne.com/airborne-systems/ [cited 23/04/2026]
[6]URL:https://community.wmo.int/site/knowledge-hub/programmes-and-initiatives/global-atmosphere-watch-programme-gaw[cited 23/04/2026]
[7]URL:https://www.knmi.nl/kennis-en-datacentrum/uitleg/weerballon-of-radiosonde [cited 23/04/2026]
[8]URL:https://www.eumetsat.int/about-us/who-we-are [cited 23/04/2026]
[9]URL:https://sentinels.copernicus.eu/missions/sentinel-5 [cited 23/04/2026]

Category	Identifier	Description
	MKT-ST-04	Real-time data transmission enables direct access to measurements during operation, improving responsiveness and mission value.
	MKT-ST-05	Onboard data storage provides redundancy and ensures measurement data can still be retained in case of communication failure.
	MKT-ST-06	Low maintenance requirements can reduce lifecycle costs and improve operational availability.
Weaknesses	MKT-WE-01	The design is unproven and can only be validated to a limited extent within the project scope, which increases technical uncertainty.
	MKT-WE-02	The conceptual nature of the design may result in suboptimal design choices compared with a fully matured product.
	MKT-WE-03	Development costs are high due to the advanced technologies and long-endurance performance requirements.
	MKT-WE-04	The aircraft is highly sensitive to the operating environment, particularly atmospheric and weather conditions.
	MKT-WE-05	Propulsion system options are limited because few existing solutions are suitable for very long-endurance, high-altitude operations.
	MKT-WE-06	Material selection is constrained by the demanding environmental and structural requirements of the mission.
	MKT-WE-07	The long mission duration creates a strong dependence on system reliability, making failures more critical.
Opportunities	MKT-OP-01	The growing demand for climate research data increases the need for dedicated atmospheric measurement platforms.
	MKT-OP-02	There is limited availability of long-endurance atmospheric measurement platforms, leaving room for a specialised solution to enter the market.
	MKT-OP-03	Few aircraft are capable of operating effectively at the required altitudes, which strengthens the competitive position of the proposed design.
	MKT-OP-04	The project offers partnership potential with research institutions, government agencies, and environmental organisations.
	MKT-OP-05	The platform could support the validation of satellite-based climate measurements by providing complementary in-situ data.
	MKT-OP-06	The climate and environmental monitoring market is large and growing, creating favourable conditions for future deployment.
	MKT-OP-07	A multi-parameter payload capability increases the range of possible applications and broadens the customer base.
	MKT-OP-08	A longer endurance than competing platforms could provide a strong market advantage and unique operational value.
Threats	MKT-TH-01	Public and institutional concerns regarding autonomous flying systems may reduce acceptance and slow adoption.
	MKT-TH-02	Cybersecurity risks, including UAV hacking, may threaten safe and reliable operation.
	MKT-TH-03	A strict certification process may increase development time, cost, and regulatory complexity.
	MKT-TH-04	Competition from existing UAVs, satellites, and crewed measurement aircraft may reduce market share.
	MKT-TH-05	Supply chain constraints, such as limited availability of specialized electronic components, may delay development and production.
	MKT-TH-06	Operational restrictions caused by weather, geopolitical conditions, or limited airspace access may reduce deployment flexibility.
	MKT-TH-07	In some regions, the platform may face political sensitivity or misinterpretation of its purpose, which could restrict operations.

2.2.5. Market Competitors Analysis

Although the market for climate measurement is still emerging and expected to grow, several competing solutions already exist. Based on the market segment analysis in Subsection 2.2.3, the main competitor categories are low Earth orbit (LEO) satellites, modified aircraft, balloons, and UAVs.

Table 2.3: *Main Competitor Categories Identified*

Competitor category	Advantages	Disadvantages	Level of competition
Low-Earth-Orbit Satellites	Global coverage, long operational lifetime, and the ability to monitor remote or inaccessible regions. They are highly suitable for large-scale and repetitive observations.	Limited spatial and temporal flexibility, very high development and launch costs, and less suitability for in situ measurements or rapid mission adaptation.	High
Modified aircraft	High payload capacity, operational flexibility, and the ability to carry advanced scientific instrumentation with human supervision on board.	High acquisition and operating costs, limited endurance compared with balloons or satellites, and significant fuel consumption.	Low
Balloons	Very long endurance, relatively low cost, and strong suitability for persistent atmospheric observations at high altitude.	Limited manoeuvrability, dependence on wind conditions, low operational control, and restricted payload capability compared with aircraft.	Medium
UAVs	High operational flexibility, relatively low operating cost, easier deployment, and good suitability for targeted regional measurements.	Limited payload capacity, regulatory constraints, and generally lower endurance and altitude capability than satellites or balloons.	High

2.2.6. Market Position

Based on the market segments identified in Subsection 2.2.3, SORA occupies a position that no existing product fills. It combines the high-altitude, long-endurance flight capabilities associated with defence segment and its reconnaissance and surveillance platforms, with a dedicated scientific payload for measuring atmospheric composition. Moreover, to effectively contribute to advances in climate research, SORA needs long-term operational sustainability and reliable measurement capability as in the operational monitoring segment. This cross-segment position presents an opportunity for a gap in the market: offering persistent in-situ tropospheric and stratospheric measurements on a seasonal timescale that satellites and balloons cannot replicate and short-duration aircraft campaigns cannot sustain.

2.3. Requirements

Based on the identified market gap, presented in Subsection 2.2.6, stakeholder requirements were set up, which can be seen in Table 2.4. This table consists of the requirement identifier, requirement description, respective stakeholder corresponding to the requirement, and category: constraint (C), operational requirement (O), or functional requirement (F). Based on the stakeholder requirements, system requirements were set up; the compliance of the final design with these can be seen in Section 17.3.

Table 2.4: *Stakeholder Requirements*

Identifier	Requirement	Stakeholder	Category
REQ-STK01	The aircraft shall be controllable	Drone pilots / operators	F
REQ-STK02	The aircraft shall effectively handle data storage and transmission	Customer	F
REQ-STK04	The aircraft shall allow operator input	Drone pilots / operators	F
REQ-STK06	The aircraft shall be reliable	Customer	F
REQ-STK07	The aircraft shall manage energy distribution and storage	Customer	F

Identifier	Requirement	Stakeholder	Category
REQ-STK08	The aircraft shall be capable of performing atmospheric measurements during operations	Customer	O
REQ-STK09	The aircraft shall operate at a cruise altitude between 15 km and 25 km	Customer	O
REQ-STK10	The aircraft shall operate without onboard crew	Customer	O
REQ-STK11	The aircraft shall be capable of sustained cruise flight with an endurance of 60 days	Customer	O
REQ-STK12	The aircraft shall operate globally	Customer	O
REQ-STK17	The aircraft shall maintain within the budget of TBD	Customer	C
REQ-STK20	The aircraft shall maintain safe ground operations	Regulators	C
REQ-STK21	The aircraft shall at all times follow the airspace regulations of the state's airspace it is flying within	National governments	C
REQ-STK23	The aircraft's operations shall not violate the privacy of any member of the public	General Public	C
REQ-STK24	The aircraft shall comply to all relevant safety regulations	Regulators	C
REQ-STK25	The aircraft shall comply with established noise limits	General Public	C
REQ-STK26	The aircraft shall prioritise sustainability where possible	Customer	C
REQ-STK27	The aircraft shall be able to be manufactured	Part Suppliers/Manufacturers	C

2.4. Sustainable Development Strategy

Sustainability was considered throughout the design process of SORA with the goal of minimising the environmental impact of the aircraft, without compromising its performance. A detailed overview of sustainable design configurations can be found in this chapter. Subsection 2.4.1 lists the main sustainability requirements. After which, in Subsection 2.4.3 and Subsection 2.4.4, the sustainability considerations for the propulsion and structural subsystems were explored respectively.

2.4.1. Sustainability Requirements

In order to ensure sustainable design choices, several sustainable mission requirements have been listed:

- REQ-STK26-MIS03: The aircraft should be zero-emissions during cruise missions by using sustainable power sources and prioritising efficiency.
- REQ-STK26-MIS02: If applicable, during the landing and take-off cycle, emissions should comply with the latest ICAO (International Civil Aviation Organization) certification standards.
- REQ-STK26-MIS01: The whole aircraft lifecycle should be at least 50% recyclable/re-processable. This can be confirmed through a comprehensive LCA and the prioritisation of sustainable materials.
- REQ-STK08, POS: The aircraft systems should be able to provide valuable insights for future climate research, which can be used to validate climate models.

The main areas in which sustainability was addressed within the design were the selection of the propulsion system and the material choice for the aircraft structure.

2.4.2. Measuring Sustainability

To evaluate the effectiveness of the sustainability strategy, quantitative indicators are required. These indicators allow the environmental performance of the aircraft to be assessed in a measurable way, rather than only through qualitative discussion. In this project, sustainability is mainly evaluated using two parameters: the recycled mass percentage and the direct operational emissions. The recycled mass percentage is used to assess material recovery at the end of the aircraft life cycle, while the operational emission assessment is used to quantify the direct environmental impact of the aircraft during flight.

The recycled mass percentage is defined as the ratio between the mass of recyclable or reprocessable structural

materials and the total structural mass of the aircraft. This is expressed as:

$$\eta_{\text{rec}} = \frac{m_{\text{rec}}}{m_{\text{struct}}} \times 100\% \tag{2.1}$$

where m_{rec} is the mass of recyclable or reprocessable structural material and m_{struct} is the total structural mass. Based on the selected structural materials and the mass breakdown of the aircraft, it was found that approximately 88% of the structural mass is recyclable or reprocessable. This indicates that the aircraft has a high potential for material recovery at the end of its life cycle.

The operational emission performance is assessed by estimating the direct greenhouse gas emissions produced during operation and converting them into carbon dioxide-equivalent emissions using Global Warming Potential (GWP) [12]. The greenhouse gases considered in this assessment include carbon dioxide (CO_2), methane (CH_4), nitrous oxide (N_2O), hydrofluorocarbons (HFCs), perfluorocarbons (PFCs), sulphur hexafluoride (SF_6), and nitrogen trifluoride (NF_3)[10]. Since the aircraft uses electric propulsion powered by solar energy and battery storage, no fuel is combusted during cruise. Therefore, the cruise emission requirement is defined as:

$$m_{\text{CO}_2\text{eq,cruise}} = 0 \tag{2.2}$$

2.4.3. Propulsion and Power System Design

The propulsion and power system directly supports the sustainability targets defined in Subsection 2.4.2. In particular, the system was designed to eliminate direct greenhouse gas emissions during cruise while still providing sufficient energy for long-endurance operation. For this reason, an electric propeller-based propulsion system was selected instead of a jet engine configuration.

The use of propellers is suitable for this mission because they can be driven by electric motors. In contrast, conventional jet engines require fuel combustion and therefore produce operational emissions such as CO_2[11]. Since the aircraft is designed for climate research and has a zero-emission operational objective, an electric propeller-based propulsion system is more appropriate than a combustion-based propulsion system.

To supply the propulsion system and the other onboard electrical loads, a solar-powered system with battery storage was selected. During daylight, the solar panels generate electrical energy for aircraft operation and battery charging. During the night, the batteries provide the required power to maintain continuous flight. This architecture avoids onboard fuel combustion during operation and therefore supports the cruise emission requirement defined in Equation 2.2. It also avoids the high technical complexity and mass penalties associated with alternative zero-emission technologies, such as hydrogen-based power systems.

However, the use of battery storage introduces an important design consideration related to battery lifetime and maintenance. Since the aircraft is required to perform long-endurance missions, the battery pack will undergo repeated charge and discharge cycles. Over time, these cycles cause battery degradation, reducing the available energy storage capacity and potentially limiting the endurance and performance of the aircraft. For this reason, a removable battery concept was selected. This allows degraded battery packs to be replaced during maintenance without retiring the complete aircraft. As a result, the aircraft lifetime can be extended, maintainability is improved, and material waste is reduced.

The removed batteries must be handled through a controlled end-of-life process. Improper processing or disposal of spent lithium-ion batteries can lead to contamination of soil, water, and air, and can also have negative effects on human health [13]. Therefore, used batteries shall be returned to authorised battery collection or recycling facilities. This process shall be monitored in accordance with local regulations to ensure proper end-of-life battery management and to support the overall sustainability strategy of the aircraft.

2.4.4. Material Selection

For a high-altitude, long-endurance aircraft, a strong and lightweight material is ideal. For this reason, multi-layer composite materials were chosen for most of the structural components. Typically, these materials include CFRP (Carbon Fibre Reinforced Polymer), mylar, etc. These materials are not commercially recyclable. Therefore to satisfy REQ-STK26-MIS01 a novel material with near equivalent material properties to CFRP was selected as the primary material for the aircraft, this was Galvorn, produced by Dexmat.

Galvorn is fully recyclable and retains its properties throughout and after the process [14]. Since its production process is simpler and more efficient than carbon fibre it results in carbon negative process emission (-5kg CO_2 per kg of fibre)[12]. Additionally, Galvorn's specific strength is higher than other materials so less material is needed to

[10] URL: https://naei.energysecurity.gov.uk/greenhouse-gases [cited 01/05/2026]
[11] URL: https://ourworldindata.org/global-aviation-emissions [cited 5/06/2026]
[12] URL: https://dexmat.com/blog/carbon-fiber-alternative/ [cited 05/06/2026]

carry the same loads. Displacing other more GHG-intense materials in structural applications has a large impact on the environmental impact of the project. The emissions of Galvorn to support the same weight as other typical aerospace materials are shown in Figure 2.2 [13]. Additionally, Galvorn has a long lifetime due to its non-corrosive properties[14] and high wear resistance. This results in fewer necessary repairs, reducing material waste during the products' operational lifetime.

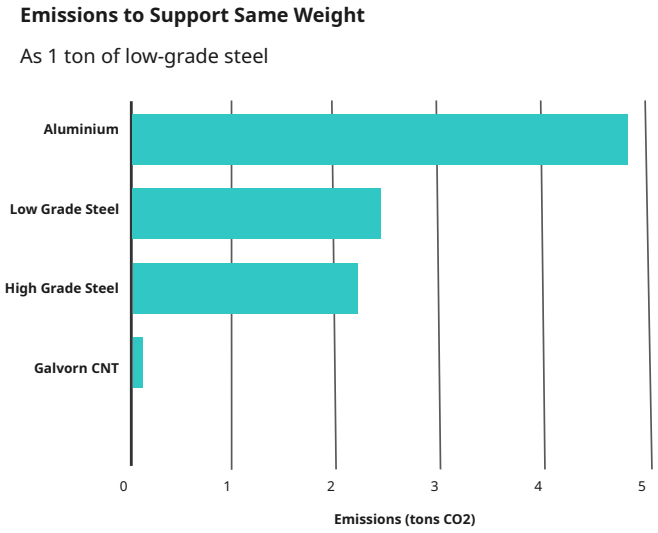

Figure 2.2: *Galvorn Carbon Footprint*

[13] URL: https://dexmat.com/wp-content/uploads/DexMat_Galvorn-Spec-Sheet-1.pdf [cited 05/06/2026]
[14] URL: https://dexmat.com/wp-content/uploads/Galvorn-Guide_21MAY2026.pdf [cited 05/06/2026]

3

Design Process

This chapter describes the overall design process of the SORA aircraft. Section 3.1 provides a top-level overview of the project development logic using a Functional Flow Diagram (FFD) and Functional Breakdown Structure (FBS). Section 3.2 summarises the trade-off procedure used to select the baseline configuration. Section 3.3 presents the system-level design methodology, and finally Section 3.4 outlines future project development logic after preliminary design, up to end-of-life.

3.1. Functional Diagrams

The revised Functional Breakdown Diagram (FBD) and Functional Flow diagram (FFD) can be seen on Figure 3.1 on page 12 and Figure 3.2 on page 13 respectively. The FBS represents the hierarchical decomposition of system functions down to sub-subsystem level. The FFD complements this by representing the temporal and operational flow of system functions. Both follow the same structure: starting with the design phase, after which the manufacturing, AIT (assembly, integration and testing), maintenance, and operational phases follow. Finally, it describes end-of-life practises.

3.2. Trade-Off

In this section the trade-off procedure is summarised. The full trade-off procedure can be found in the Midterm Report [15]. Subsection 3.2.1 explains selected design options, after which Subsection 3.2.2 discusses the criteria and results of the trade-off.

3.2.1. Design Options

To perform the system-level trade-off, a large set of aircraft configurations was generated using a Design Option Tree. Thereafter the clearly non-feasible options were eliminated. Four candidate configurations were selected for further evaluation: a fixed-wing aircraft, a flying wing, an airship, and a hybrid configuration. The fixed-wing concept consists of a conventional fuselage-wing-tail arrangement, while the flying wing integrates all systems within a single lifting surface. The airship generates lift through buoyancy provided by a gas-filled envelope, whereas the hybrid configuration combines buoyant and aerodynamic lift mechanisms. These concepts were evaluated against a set of weighted criteria to determine the most suitable configuration for the mission.

3.2.2. Criteria and Results

To perform the trade-off, evaluation criteria were defined based on system requirements. The criteria were weighted according to the relative importance with a total weight sum of 100%.

Lift Efficiency - 25% Lift efficiency, defined as the lift-to-power ratio (L/P), provides a quantitative measure of aerodynamic performance. Efficient lift generation is critical for achieving long-endurance flight, particularly at high altitudes. This criterion is supported by REQ-STK09, REQ-STK11 and REQ-STK12.

Controllability - 20% Controllability reflects the aircraft's ability to maintain stability, recover from disturbances, and perform the required pitch, roll, and yaw manoeuvres. It also includes resilience to gusts, crosswinds, and conflicts with other aircraft. This is a mission-critical requirement (REQ-STK01).

Payload - 20% Evaluates payload accommodation and capacity. As the payload is essential for collecting the required scientific data, this criterion is critical to mission success (REQ-STK08).

Physical Robustness - 15% Assesses the ability of the aircraft to withstand environmental conditions such as temperature, radiation, pressure, vibrations, icing, and gusts. It supports global operability (REQ-STK12).

Cost - 10% Considers development, certification, maintenance, and operational costs, including the impact of technology maturity and regulatory compliance. While relevant (REQ-STK17), it is not mission critical.

Sustainability - 10% Evaluates how easily the design can meet recyclability and reprocessability requirements (REQ-STK26), but has limited impact on mission performance.

The results of the trade-off can be seen in Table 3.1. The fixed-wing configuration achieved the highest overall score (3.6) and was therefore selected. A sensitivity analysis was performed to ensure the robustness of this decision, confirming that the fixed-wing configuration is the best design choice from the 4 concepts.

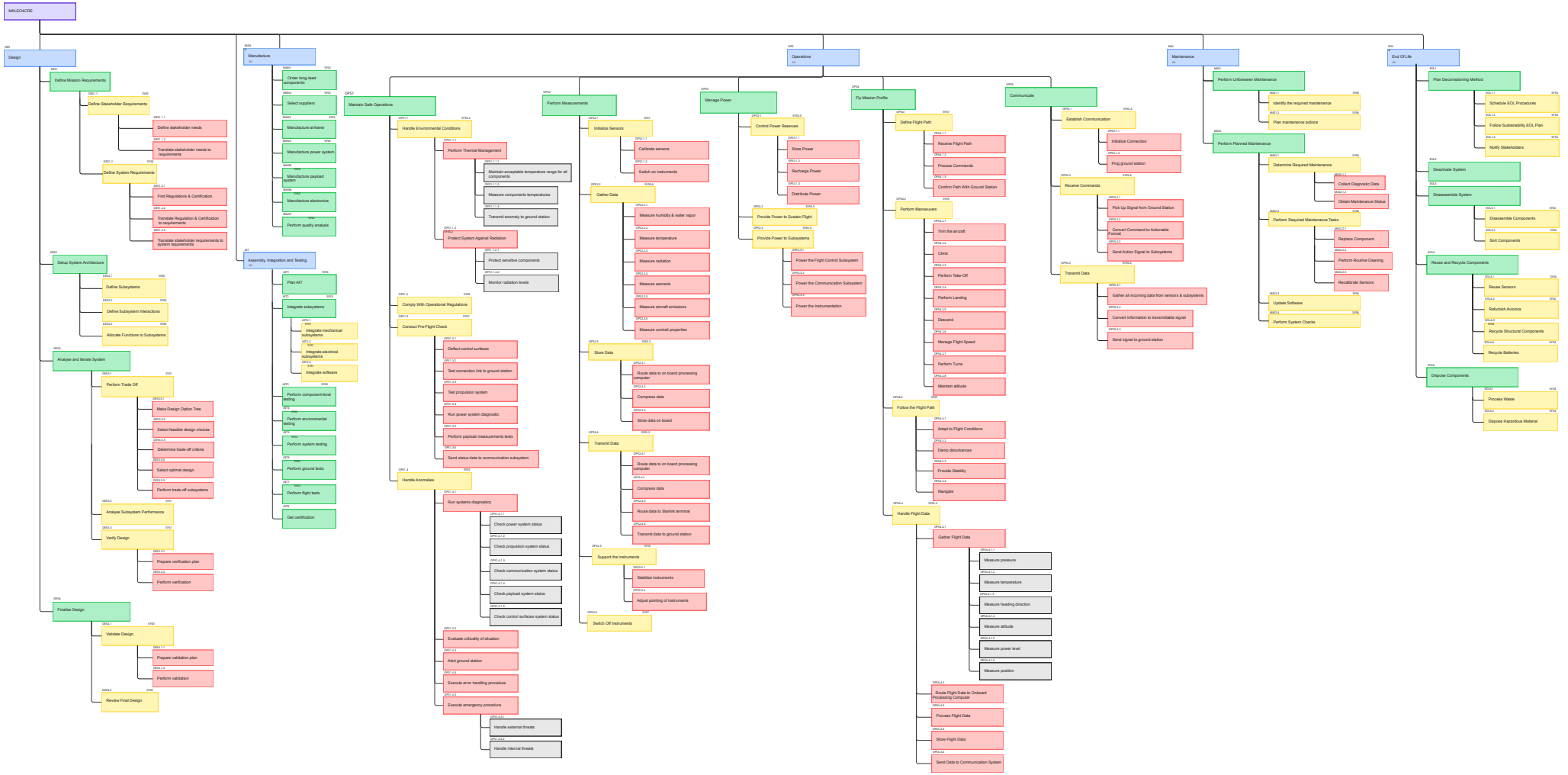

WBS Structure Key

4.
4.
Phase
All

4.1
Category
THREE

4.1.1
Section

4.1.1.1
Sub Section

4.1.1.1.1.
Sub Sub Section

System ID

SYS0 - Management Team	SYS5.1 - Propulsion Unit
SYS1 - Design Team	SYS5.2 - Structural Frame
SYS2 - Quality Control Team	SYS5.3 - Data Handling Module
SYS3 - Production Team	SYS5.4 - Communications Module
SYS4 - Decommissioning Team	SYS5.5 - Power Module
SYS5 - Aircraft	SYS5.6 - Payload Module
SYS6 - Maintenance Team	SYS5.7 - Flight Control Module
SYS7 - Operations Team	

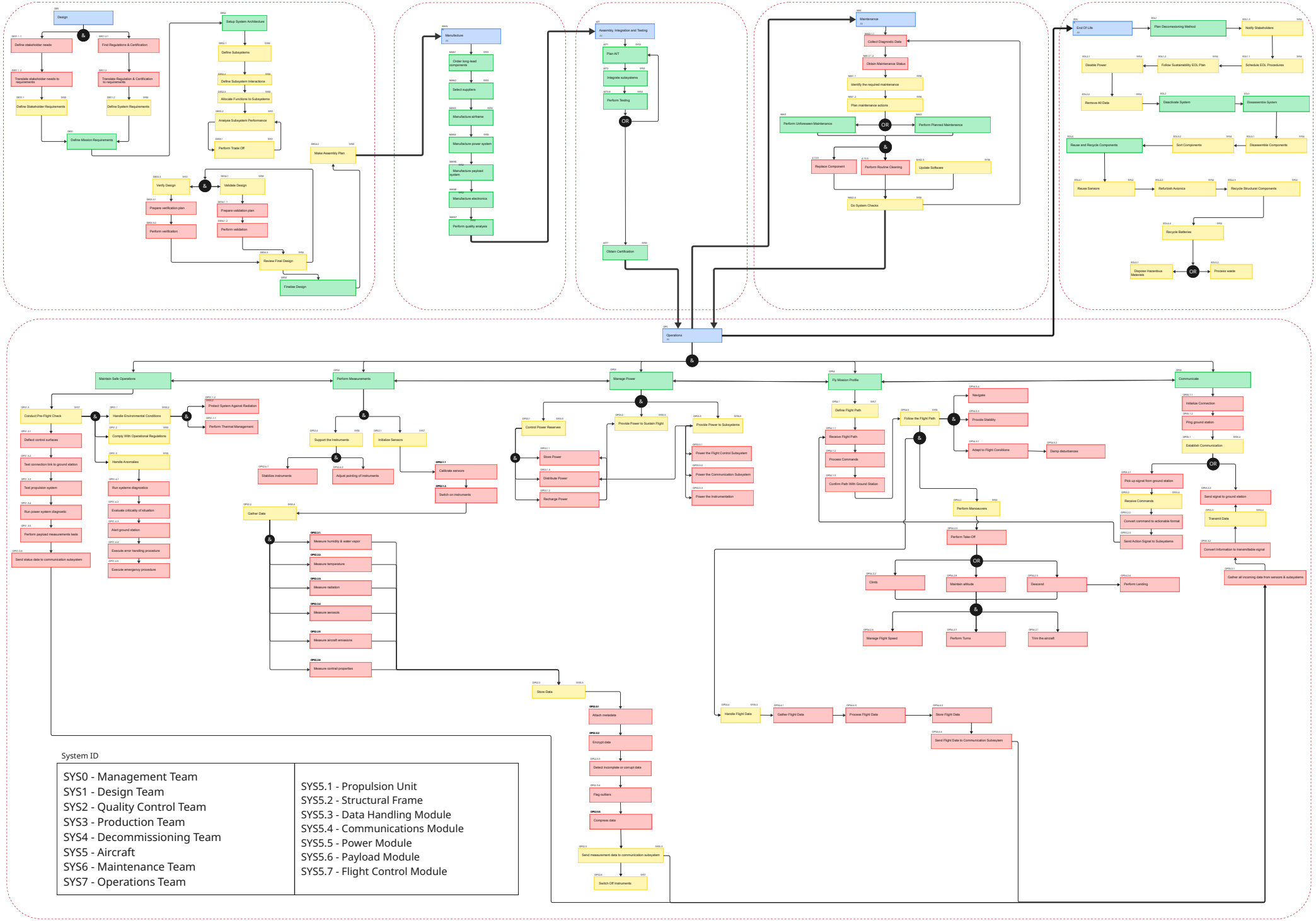

System ID

SYS0 - Management Team	SYS5.1 - Propulsion Unit
SYS1 - Design Team	SYS5.2 - Structural Frame
SYS2 - Quality Control Team	SYS5.3 - Data Handling Module
SYS3 - Production Team	SYS5.4 - Communications Module
SYS4 - Decommissioning Team	SYS5.5 - Power Module
SYS5 - Aircraft	SYS5.6 - Payload Module
SYS6 - Maintenance Team	SYS5.7 - Flight Control Module
SYS7 - Operations Team	

Table 3.1: *Design Configuration Trade-off Matrix*

Criteria \ Design	Airship	Fixed Wing	Flying Wing	Hybrid
Lift Efficiency (25%)	Infinite L/P due to buoyancy	Requires forward motion, fuselage effects	Requires forward motion, no fuselage drag	Lifting body, high drag
Control (20%)	Slow response, difficult to manoeuvre accurately	Fast response and has tail authority	Hard to control at low speeds but fast response	Slow response but controllable
Payload (20%)	Lots of space & mass budget	Can be integrated in fuselage or wing, lower mass budget	Must be integrated in wing, less storage volume	Many sub systems so less space but not as mass constrained
Robustness (15%)	No easily breakable parts	Proven conventional structure	Strong integrated body	Complex integration
Cost (10%)	Less developed technology	Well established proven concept	Somewhat established concept	Undeveloped technology, high certification effort
Sustainability (10%)	Unique materials	Well established, common materials	Well established, common materials	Unique materials
Total	3.4	3.6	3.35	3.05

Additionally, trade-offs were performed for several subsystem-level design choices. These design choices had multiple possible options with several contributing factors, thus warranting a separate trade-off. The launch mechanism trade-off identified hand launch as the highest scoring option; however, due to the expected aircraft mass, a temporary landing gear system was selected as the most feasible solution. For the longitudinal stability configuration, a V-tail achieved the highest score, offering the best balance between weight, drag, stability, and controllability. Finally, a high-wing configuration was selected based on its superior performance in payload integration, aerodynamic efficiency, landing support, and lateral stability.

3.3. System Analysis in Python

Following the selection of the fixed-wing configuration, the system was decomposed into the following subsystems: payload, aerodynamics, structures, propulsion, power, communication, and flight control and stability. Each subsystem was further analysed and optimised based on performance, integration constraints, and mission requirements. Detailed design decisions, including analysis methods and justification, are provided in Chapter 6 through Chapter 12.

Each subsystem developed tools to adequately analyse and size the subsystem. This collection of tools was made in a collaborative coding workspace, where a "main" script was written in order to integrate all sizing tools into an iterable loop that produces a converged design solution. Sizing tools are detailed per subsystem in chapters 6-13. The code is visualised in Figure 3.3.

The main script works by first populating the state.json file. This file was used by the sizing tools to read and write results to, such that interdependent subsystems could exchange information. Thereafter the modules were run in the following order: aerodynamics→power→structures→stability and control→cg. At the end of each iteration the change in mass and cg were checked against a convergence criterion. If the $\Delta W_{tot} \leq 0.5$ kg and $\Delta cg \leq 0.05$ m were both satisfied, then the iteration stopped and the state.json could be read to extract converged dimensions, masses and loads.

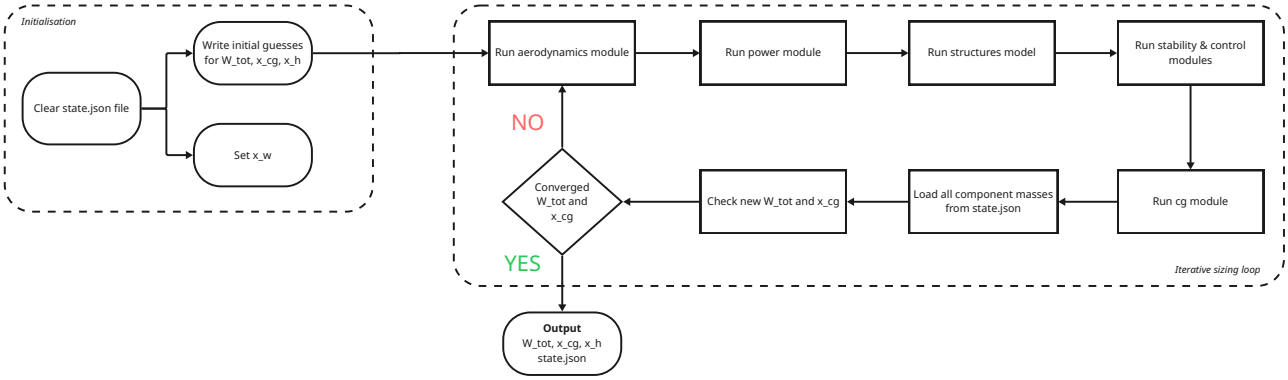

Figure 3.3: *Flow Chart Code Main File*

3.4. Project Design and Development Logic

After the preliminary design phase is finished, several phases need to be completed before the project reaches its end. Firstly, in Phase 1, the detailed design of all subsystems is finalised, after which a Critical Design Review is held to approve the manufacturing release. In Phase 2, all components are procured and manufactured, followed by Phase 3 in which the subsystems are assembled and integrated into the full aircraft. Subsequently, Phase 4 covers all testing activities, ranging from component-level and environmental testing to ground and flight testing. Once the aircraft has been validated, Phase 5 addresses certification and Phase 6 the operational phase, during which it performs its measurement missions over a projected service life of ten years. Finally, the aircraft reaches Phase 7: end-of-life, where the aircraft is decommissioned, disassembled, and recycled where possible.

A detailed overview of the post-DSE development logic and task dependencies is provided in Figure 3.4, while the corresponding project timeline is shown in Figure 3.5.

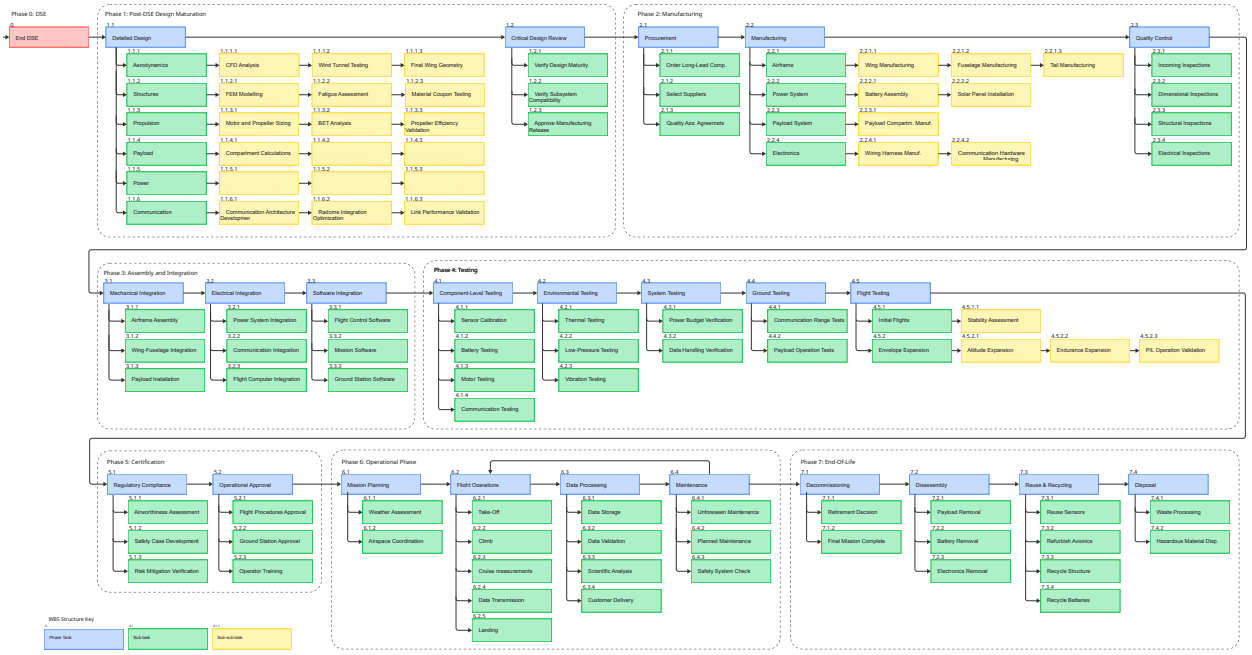

Figure 3.4: *Post-DSE Development Logic*

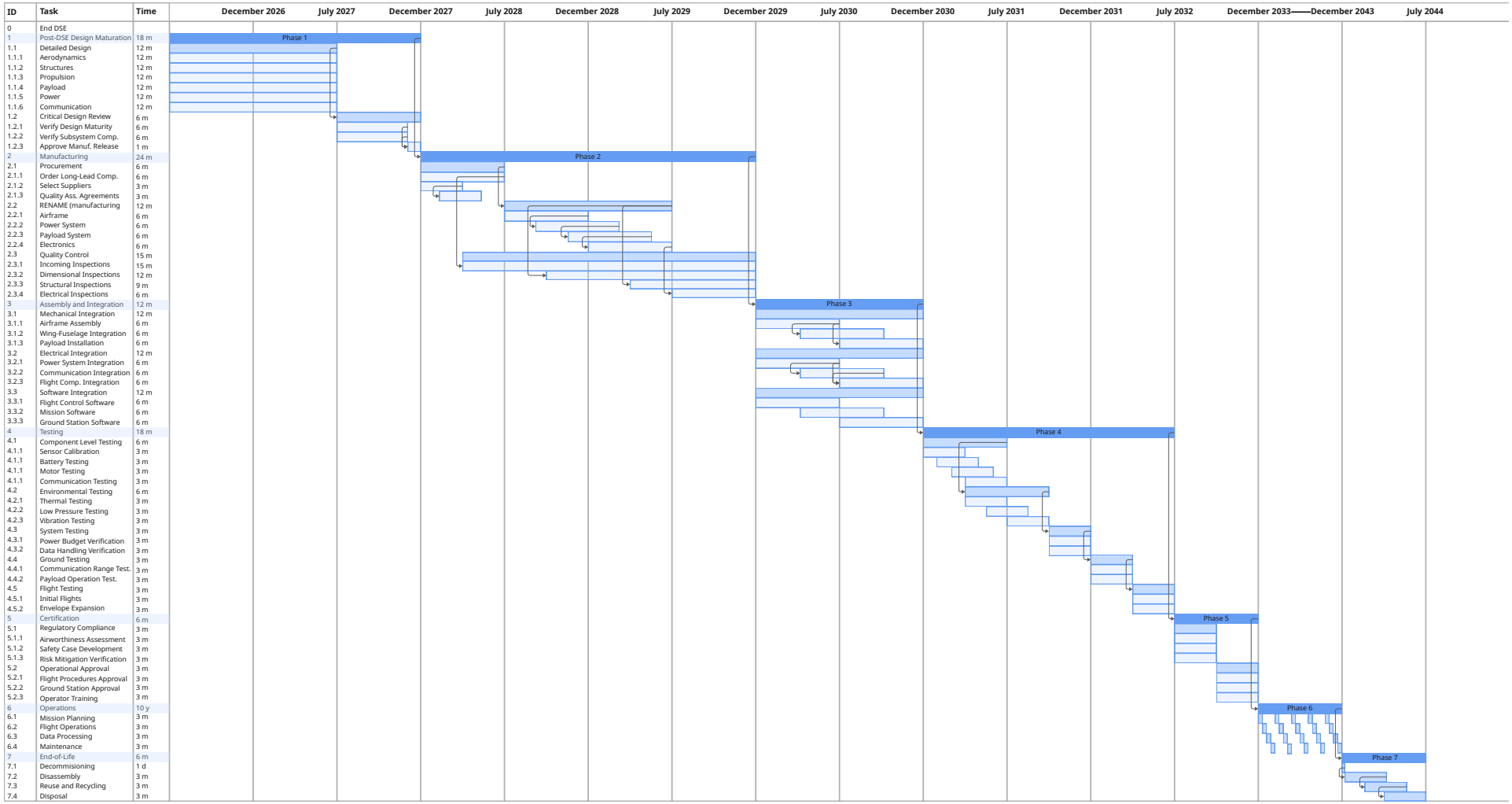

Figure 3.5: *Post-DSE Gantt Chart*

4

Concept and Configuration

This chapter showcases the final achieved configuration for the design of SORA. Section 4.1 briefly describes the top-level characteristics of the aircraft and presents the resulting 3-view drawings. Section 4.2 shows the hardware block diagram of the aircraft.

4.1. Selected Concept Description

The final design of SORA consists of a fixed wing aircraft, with a 36-meter wingspan, a fuselage of 12m length and a total weight of 218.5kg. The wing will be fitted with solar panels across its upper surface, which generate electrical energy during the day, powering the aircraft's subsystems and charging batteries which support night operation. The propulsion subsystem consists of 4 electrically-powered propellers, attached to the underside of the wing structure. To ensure stability and controllability, the aircraft features a V-tail, attached at the rear end of the fuselage, as well as ailerons on the wings. The scientific instruments will be placed at the nose of the aircraft. The ones which would not survive the external environment of the stratosphere are placed inside a heated and pressurized compartment.

A CAD generated render of the final design achieved for SORA can be seen in Figure 4.1

Figure 4.1: *SORA's Final Design*

The 3-view drawings of the design can be seen in Figure 4.2 on page 18

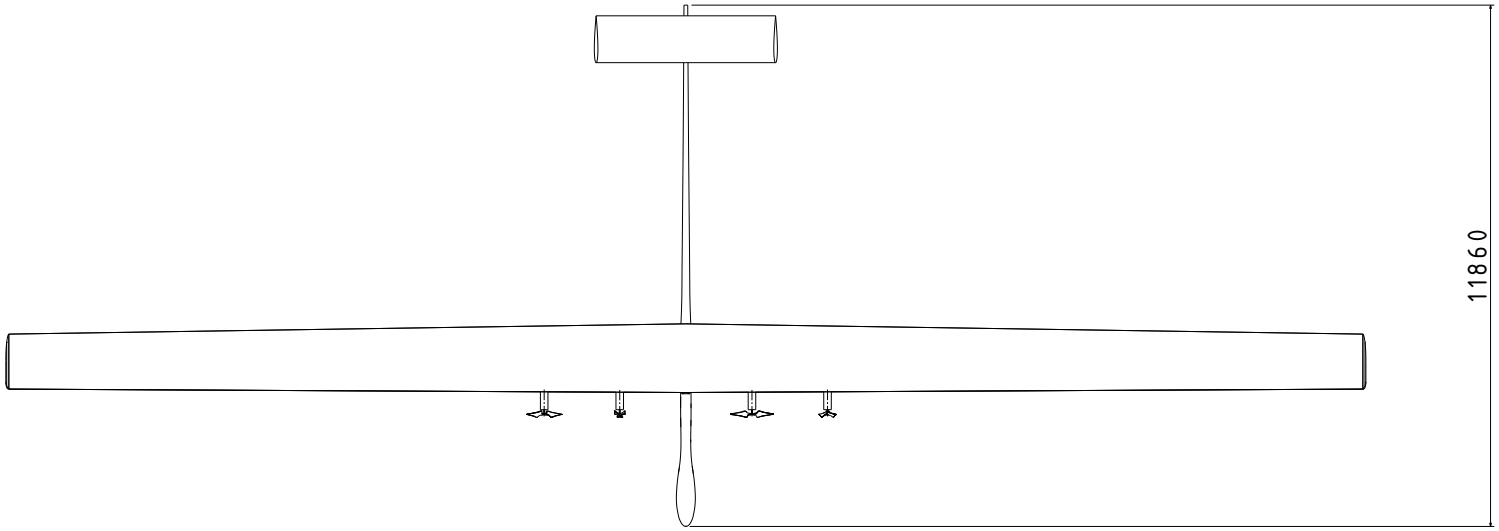

ALL DIMENSIONS IN MILIMETERS

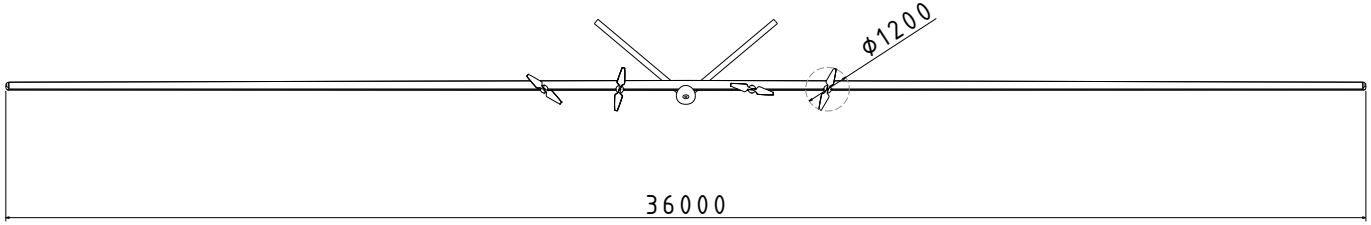

4.2. Hardware Block Diagram

Every different component in the aircraft has to work together to be able to perform its tasks. To visualize this, a hardware block diagram was created, shown in Figure 4.3. It accounts for the power distribution to the different systems, as well as data flow and feedback. If multiple components are commonly shared by one subsystem, a dashed box has been included to group them. This allows to show the power as being distributed to the general subsystem. A software diagram was considered but deemed out of the scope of this project.

Examining the diagram in detail, it is possible to see how almost every system is connected to the flight computer, processing flight instruments data (pitot tube, angle of attack sensor, GPS, ADSB), control actuators position, power and propulsion status. The flight computer then is connected with the communication system to transmit telemetry as well as receiving commands from the ground. The communication system is also linked to the payload system, directly transmitting the scientific data.

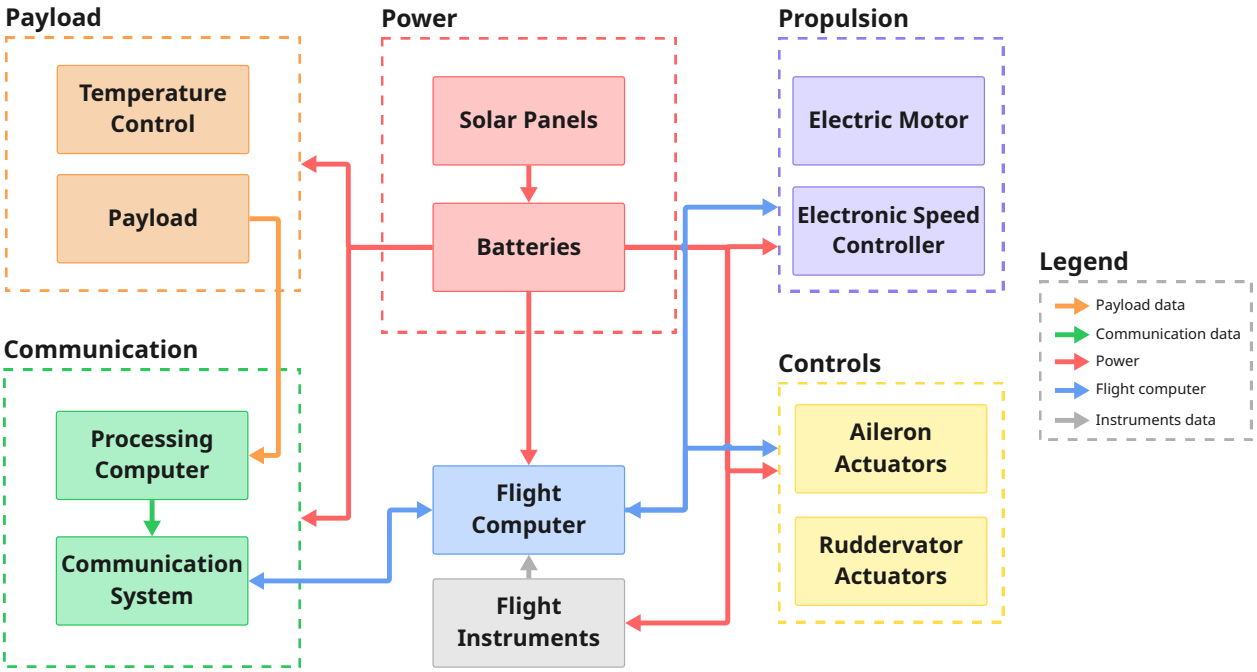

Figure 4.3: *Hardware Block Diagram*

5

Operations and Logistics

This chapter discusses the operational environment and mission constraints. Firstly, the atmospheric conditions are explained in Subsection 5.1.1 divided into wind and turbulence, temperature, moisture, icing, radiation and ozone- each of which has a significant impact on the aircraft and its performance. Next, the solar power availability is found in Subsection 5.1.2, these conditions are combined with a flight plan in Subsection 5.1.3 to get the operational profiles as in Section 5.2. From the selected feasible profiles from Subsection 5.2.1 the battery weight in Subsection 5.2.2 is determined and an example mission is explained in Section 5.4. Lastly, all results are verified and validated in Section 5.5.

5.1. Operational Constraints

The operational constraints are important to determine where this aircraft will be able to fly. This involves analysing atmospheric conditions and weather properties, solar availability and airspace guidelines. Firstly, the atmospheric conditions were analysed. After that, research was done in the solar availability at different latitudes on Earth. Eventually, the flight plan was set up with the results regarding the atmospheric conditions, weather properties, and solar availability.

5.1.1. Atmospheric Conditions

Wind and Turbulence

Maximum wind speed allowed at cruise altitude is an important parameter for the design. It has been determined to be equal to 50 m/s based on analysis of the ERA5 average monthly dataset from 2023, shown in Figure 5.1, which reflects most of the high winds during a year that occur between ±30-60° latitude, mainly due to jet streams (in the tropopause). With the highest seasonal wind determined around 60° S at around 25 km altitude due to the South Polar Vortex, reaching 80 m/s [16]. However, this is a localised and extreme seasonal phenomenon, and therefore it has been decided that it should not be driving the design. Therefore, access to latitudes around 60° S will be limited.

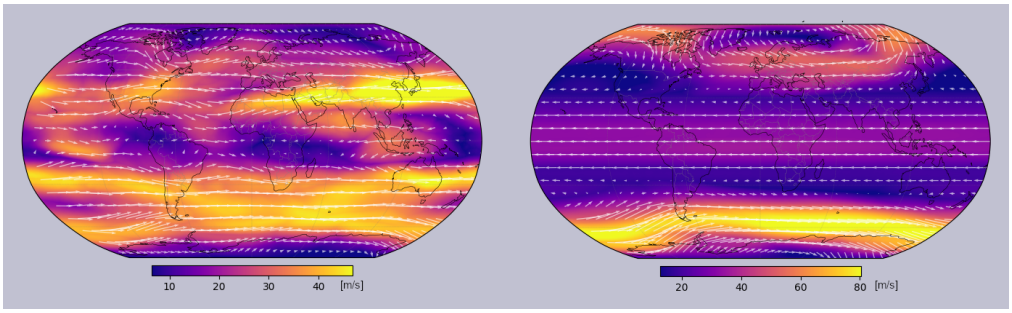

Figure 5.1: *Maximum yearly winds from 2023 at altitudes of around 15 km (125 hPa, on the left) and 25 km (20 hPa, on the right) derived from monthly ERA5 dataset [16]*

Moderate, severe and extreme turbulence shall be avoided. This is especially relevant for the climb and descent phases, as the turbulence is highest in the troposphere [1], especially in the summer [17]. Particular attention shall be paid to atmospheric fronts, high winds such as jet streams (especially on the cold air side), mountain-wave presence, wind shear and thermal activity in the troposphere. Launch, climb, descent and landing shall take place in the morning, evening or at night, when the thermal activity is the lowest [1]. Strong turbulence regions exist in the stratosphere over East Asia and South Africa [17] and shall be avoided.

Careful planning has to be done for each mission regarding current frontal situation, jet stream location and activity, wind speeds, terrain roughness and its potential effect (turbulence, wind shear), thermal activity and timing of the mission. Planning the launch and landing day has to include a particularly detailed assessment of the lower part of the troposphere, and these phases of the mission shall be planned during the morning or evening hours or at night.

[1] URL:https://www.weather.gov/media/zhu/ZHU_Training_Page/turbulence_stuff/turbulence2/turbulence.pdf [cited 16/06/2026]

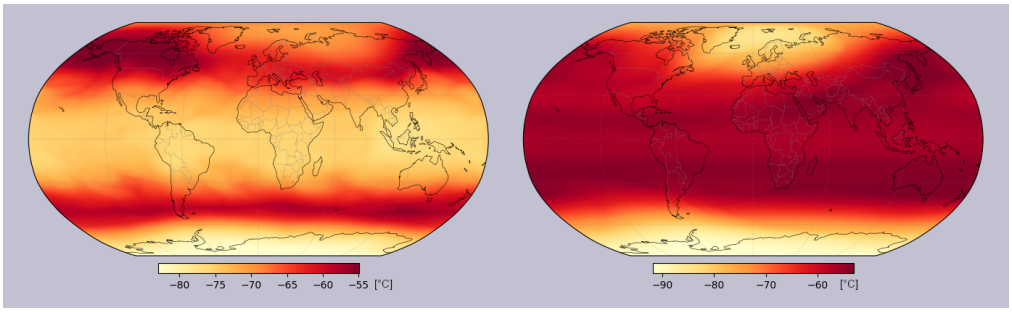

Figure 5.2: *Minimum yearly air temperatures from 2023 at altitudes of around 15 km (125 hPa, on the left) and 25 km (20 hPa, on the right) derived from monthly ERA5 dataset [16]*

Temperature
The temperature of the stratosphere shall also be considered for designing the aircraft. The minimum temperature in the lower stratosphere ranges from -40° to -80°C [18], except the area over the South Pole where it can fall below -90°C at the altitude of 25 km [16]. Therefore, the aircraft shall be designed to operate in a temperature of -80°C and the South Pole accessed only if the air temperature is within this limit.

While the diurnal temperature range of the air at altitudes between 15 and 25 km is very small (less than 3K, highest in tropical regions) [19], the aircraft is likely to experience high variations of skin temperature and thermal stresses due to very high solar radiative heating. As a reference, Zephyr's skin can heat up by as much as 64°C due to radiative heating [20]. This also necessitates well-designed heat management to ensure satisfactory temperature range for the scientific payload, avionics and batteries.

Air temperature varies significantly with latitude, as visualised from the ERA5 dataset in the minimum yearly temperature maps in Figure 5.2, which is reflected in the design. It also varies with season, but this effect is most significant beyond ±60° of latitude (up to around 40°C over polar regions at 20 km altitude).

Moisture and Icing
Icing shall be avoided due to aerodynamic reasons and material degradation. Moisture absorbed during operation may freeze during ascent and gradually damage the structure. Therefore, launch and recovery operations should be conducted in dry, cloud-free conditions [2]. Since icing from supercooled droplets in the air generally can occur in moist air at temperatures above 40°C, clouds, precipitation, frontal systems and humid regions shall be avoided for launch, climb, descent and landing [3].

Tropical regions shall be avoided when flying in the troposphere due to inter-tropical convergence zones (ITCZ) with frequent heavy rainfalls and thunderstorms, especially in the summer months [4].

Radiation and Ozone
At 25 km altitude the radiation dose rate reaches approximately 30 µSv/h [12], causing increased rate of material degradation [21]. This radiation dose rate is reflected in the material choice for the aircraft, but skin degradation will be inevitable. Therefore, the aircraft shall be designed to withstand at least this level throughout the mission duration. Significantly higher ozone concentrations in the stratosphere compared to the troposphere (partial pressure of ozone at the altitude of 25 km can be even around 40 times as high as at 10 km [5]) create a highly oxidative environment that is considered in material selection.

5.1.2. Solar Power Availability
The availability of daily solar power is a significant driver for the design in terms of aircraft mass and region of applicability. As presented by a Sceye representative, with current technology the latitude range of an all-year mission is generally limited to around ±40°, assuming the aircraft is intended to stay at a specific location throughout the mission [2]. Missions with shorter duration or those in which the aircraft location is strategically adapted during the year can reach further latitudes, but only during the right season.

A geometric model for available solar power analysis was developed based on the assumption that the solar panel is at an orientation parallel to the surface of the Earth. The solar declination at a specific day of the year and the latitude of the aircraft were the main parameters taken into account. Earth's varying distance from the Sun was accounted

[2] Sceye representative, unpublished interview, May 2026
[3] URL: https://www.weather.gov/source/zhu/ZHU_Training_Page/icing_stuff/icing/icing.htm [cited 16/06/2026].
[4] URL: https://www.noaa.gov/jetstream/tropical/convergence-zone [cited 16/06/2026]
[5] URL: https://gml.noaa.gov/obop/mlo/programs/esrl/ozonesondes/ozonesondes.html [cited 19/05/2026]

for in the expression for the maximum solar flux taken from the typical model [22]. The resulting governing equation is shown in Equation 5.1.

$$G = 0.9\,G_{SC}\left(1 + 0.033\cos\left(\frac{360^\circ d}{365}\right)\right)[\sin(L)\sin(\delta) - \cos(L)\cos(\delta)\cos(\Omega t)] \tag{5.1}$$

In this equation, G_{SC} is the solar constant of 1366.1 W/m^2, d is the day of the year, L is the latitude, δ is the solar declination, Ω stands for the Earth's speed of rotation over its axis and t is the local solar time. The effect of the altitude was not directly considered, but conservatively approximated by assuming 90% transmittance. This was based on the measurements of solar spectral transmittance at the altitude of 11.6 km [23], which showed that, at this altitude, solar spectral transmittance has a value bigger than 90% for wavelengths higher than 400 nm. The UAV will be operating at an altitude even higher than this, hence why assuming 90% transmittance is indeed a conservative assumption.

Both daily and yearly plots have been generated using the model. The daily plots show how solar irradiance changes during a specific day at all latitudes. The yearly plots show the total daily energy available for all days and latitudes. The yearly plot is shown below in Figure 5.3.

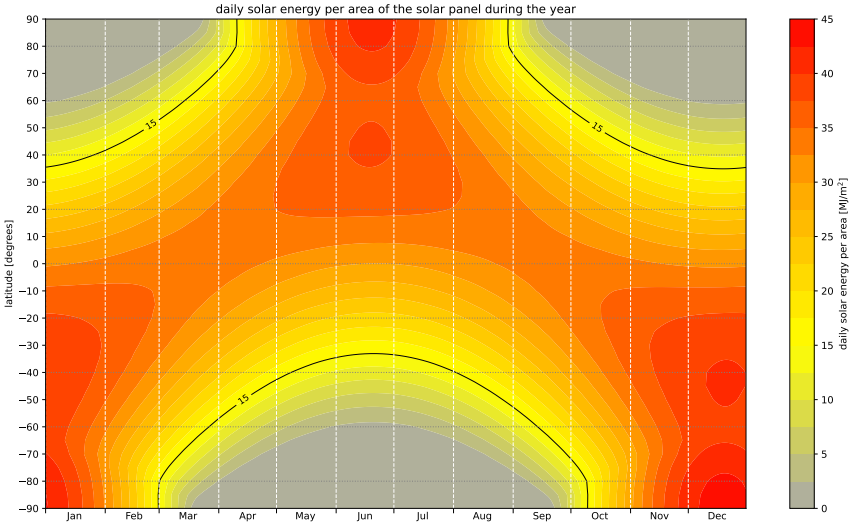

Figure 5.3: *Contour map of the total daily solar energy available for each latitude-month combination*

Based on the results of early iterations and the aforementioned ±40° latitude constraint mentioned by Sceye representative [6], a preliminary region corresponding to a minimum availability of 15 MJ/m^2 daily available solar energy (for the solar panels parallel to Earth's surface) was determined, as shown in Figure 5.3. The combinations of time of the year and latitude corresponding to this region were used for generating feasible flight profiles, as is explained in Section 5.2.

5.1.3. Flight Planning

There are no strict rules for planning HAPS missions yet, due to no existing regulations for the high altitude operations (above FL550) [24]. Therefore, currently the best reference for such missions is to follow the non-binding Eurocontrol guidelines for high-altitude long-endurance remotely-piloted aircraft systems (HALE RPAS) [25]. Moreover, the approach to integrating RPAS with other air traffic varies per region and detection and avoidance (DAA) systems for such aircraft are still in development stage. Current European guidance therefore relies on IFR operations and segregated airspace usage [25]. While the concept of Dynamic Cooperative Zones is currently being proposed by the HAPS Alliance to ensure self-deconfliction of high-altitude unmanned vehicles, currently aircraft have to rely on an ADS-B transponder for deconfliction [26].

According to Eurocontrol HALE RPAS guidelines, due to lack of existing detect-and-avoid capability of high-altitude remotely-piloted aircraft, the current recommended strategy for traffic separation is to use a segregated airspace for the climb and descent and fly above the general air traffic or also in a segregated airspace during cruise [25]. While the upper limit of controlled airspace varies per country, as of September 2025, FL470 was the highest recorded flight level used by general air traffic [25]. Therefore, it is considered satisfactory as the minimum cruise altitude for the

[6] Sceye representative, unpublished interview, May 2026

aircraft being designed. Since airspace below the Karman line is governed by respective countries, they have to grant permission for flying the aircraft over their territory, which might limit applicability of the aircraft (above countries not willing to cooperate) [8].

Mission planning shall be coordinated with air traffic management in ensuring safe separation during take-off and landing, setting the segregated airspaces for climb and descent and the deconfliction flight level above which no other traffic will be permitted by ATC. Moreover, the pilot shall be in contact with ATC, especially in case of control link loss or emergency [25].

HALE guidelines concern remotely-piloted aircraft that are automatic rather than autonomous: they are either flying automatically under the pilot's supervision, manually by the pilot, or - in case of loss of command link - automatically executing a pre-programmed procedure. However, such an aircraft is not making its own (possibly unanticipated) decisions. This means that in case of control link loss (usually defined as persisting for more than 30 seconds), the aircraft shall automatically perform a pre-programmed sequence [25].

Lastly, as mentioned in the Midterm Report, balloon launch remains a potential alternative to a conventional take-off and climb, because it may simplify regulatory approval by classifying the vehicle as an unmanned free balloon under FAA Part 101 regulations [8] [15].

5.2. Operational Profiles - Approach

Since flight conditions and available solar power depend on many parameters and vary across the latitude, time of the year, time of the day and chosen profile of the flight during the day, there is no clear critical or optimal case to design for. Earlier in the design process it has been identified that battery mass shall be minimised for the best performance. This is because the battery is the largest component of the power subsystem and the required propulsive power (being the most significant fraction of the total power of the aircraft) is proportional to the 3/2 power of the total weight, assuming that other design parameters are unchanged (including $C_{L_{opt}}$ and $C_{D_{opt}}$ optimised for minimum power), as derived in Equation 5.2. As the battery mass is fully determined by intended flight envelope, the power and operational design have been partially performed together.

$$P_{req} = D \cdot V = L \left(\frac{C_D}{C_L}\right)_{opt} \cdot \sqrt{\frac{2L}{\rho\, S\, C_{L_{opt}}}} = W \left(\frac{C_D}{C_L}\right)_{opt} \cdot \sqrt{\frac{2W}{\rho\, S\, C_{L_{opt}}}} \propto W^{3/2} \tag{5.2}$$

In view of no direct optimisation for a critical case being possible, a different approach has been used, based on first determining all the possible flight profiles and then determining which are the most optimal. First, all possible flight profiles (with a certain resolution) for all the different cases were generated and the required battery mass and other relevant parameters were determined for each of them. Then, the most optimal profiles were selected for each case and lastly the final battery mass and the resulting operational envelope of the aircraft were determined based on those optimal profiles. This process is explained in Figure 5.4 and is elaborated on in the rest of this section. The process described is repeated in the same way during each of the main design iterations.

The power system is optimised for cruise profiles, with the assumption that the mission climb phase energy requirement is less than that for cruise at top altitude. Additionally, the climb vertical speed is higher at low altitudes due to higher air density and more efficient lift generation for the same power used. The descent phase of the mission is unpropelled, therefore the power and energy requirement for the battery for that phase has also been deemed as not driving the design. However, both the climb and descent phases shall be analysed in detail in further power system design.

5.2.1. Feasible Profiles Generation

First, all the feasible daily flight profiles were calculated by the code `power_profile.py`, the flowchart of which is shown on the right in Figure 5.4. This was done in four main nested loops, iterating between the different cases of latitude and month and different durations and altitudes of the lower and upper cruise and climb and descent within each profile. The latitude-month cases considered are those corresponding to at least 15 MJ/m^2 of daily solar energy available, as shown in Figure 5.3. The assumed shape of the flight profiles is shown in Figure 5.5. In the innermost loop in `power_profile.py`, the total energy required and available balance was verified. If a profile passed this check, its required battery energy capacity and resulting battery mass and volume were calculated and saved as a feasible profile and passed on to further analysis.

In the profile generation, top and bottom altitudes are chosen between 15 km and 25 km in steps of 2.5 km. The climb duration is chosen between 0.5 hour (which is the time resolution of the flight profile analysis) and the daylight time with the minimum time for measurements subtracted. The measurements were assumed to take place during the top cruise phase - therefore the minimal duration of this phase was set at 2 hours. With the climb time as input,

the climb power was calculated using code written for the propulsion subsystem. Conversely, the descent time was calculated using zero thrust as input. If there was not enough time to descend to initial altitude before the dawn next day, such a profile was discarded, as same morning and night altitude is required ensuring the flight profile is repeatable over consecutive days.

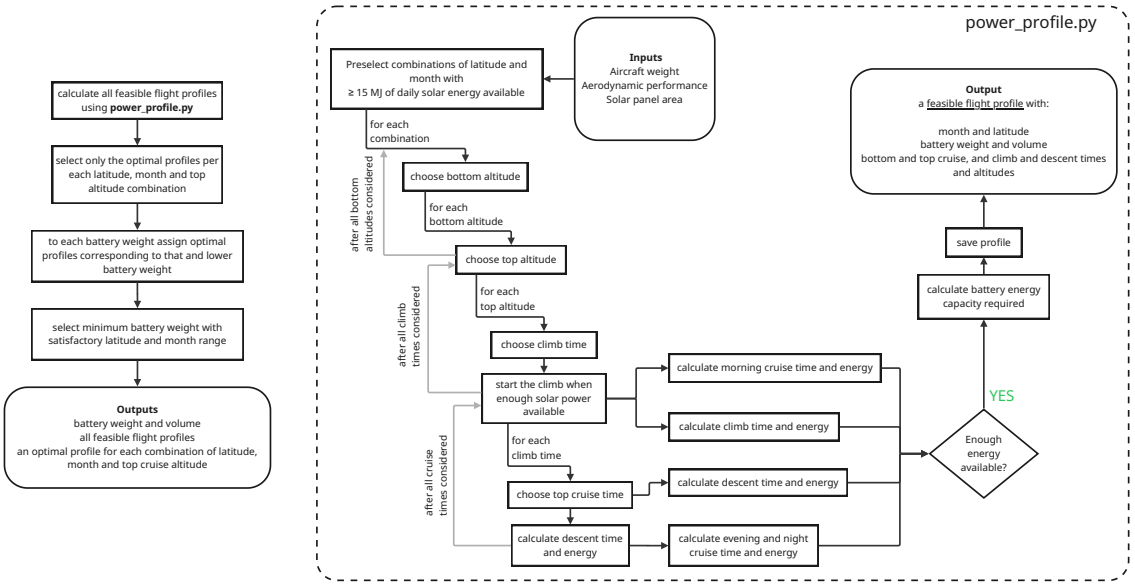

Figure 5.4: *Flowchart of the Combined Operation and Power Analysis*

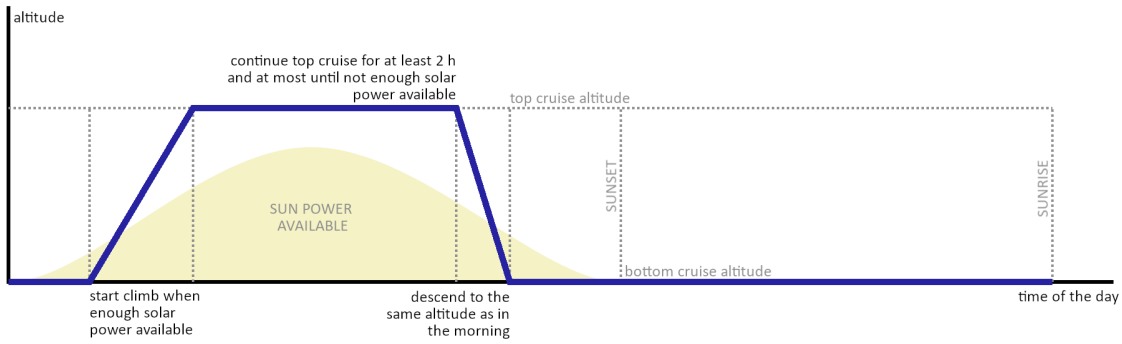

Figure 5.5: *Operational Profile Model Diagram*

As already mentioned in the Midterm Report a higher cruise altitude leads to higher required propulsive power [15]. This has no effect on performance if enough solar power is available. However, when this is not the case, the average power required directly drives the required battery weight. Therefore, the following constraints were made to minimise such impact:

- The climb happens as early as possible, but only when there is enough solar power to fully sustain it.
- The maximum duration of the top cruise phase is limited by the availability of solar power required to fully sustain it.
- The descent is performed at L/D optimised for minimum power required using no thrust.
- If top cruise cannot be sustained with available solar power, such profile is discarded.
- If bottom cruise or descent cannot be sustained with available solar power, the remaining amount of required power is assigned to be provided by the battery. This also applies to the morning cruise before the climb.

An unexpected observation has been made during the analysis: in cases with significant night duration and enough solar power, high difference between top and bottom altitude is preferred to achieve low battery mass. In such a case, since the climb starts as early as possible after sunrise, the available power increases during the climb and allows for the extra climb duration. Moreover, the extended descent time (due to high altitude difference) can save a significant part of the energy capacity required for the battery. Since the bottom cruise is always the most efficient at the lowest possible altitude, the preferred profile for such case is one starting at 15 km, with top cruise at 25 km, and descent to 15 km as late as possible.

Two types of special cases were considered separately: no-climb and 24-hour-day cases. The first occurs when the bottom and top cruise altitudes are the same resulting in a flat profile. The latter type happens when there is no night, but does not necessarily mean no need for a battery or a no-climb profile, as the available solar power might still be temporarily insufficient.

5.2.2. Battery Weight Determination

With a broad range of possible flight profiles for different cases of latitude and time of the year (almost 168,000 in total), the optimal profiles have been selected first (reducing their number to 560). First, all profiles were grouped into cases of a specific month-latitude-top altitude combination. This is because these three quantities have been identified as the most fundamental parameters for planning the mission. Cruise time is not one of them, as during the verification of the code for generating the profiles, it has been found that long cruise times are feasible in most cases. The selection logic of the optimal profiles per case was based on choosing the profile with the highest score, as shown in Equation 5.3, that favours long solar-powered top cruise time and low battery mass.

$$\frac{t_{sc}}{t_{sc_{max}}} - 4 \times \frac{W_{bat}}{W_{bat_{max}}} \tag{5.3}$$

In this equation, t_{sc} is the solar-powered cruise time at top altitude, $t_{sc_{max}}$ is the maximum solar-powered cruise time at top altitude per case, W_{bat} means the battery weight and $W_{bat_{max}}$ the maximum battery weight per case.

With the optimal profiles determined, the grouping has been flipped again. First, all optimal battery weights were found per case. Then, all optimal profiles corresponding to that or lower battery weight were grouped per each of the weights. The choice of the final battery weight was based on the combined result of the highest possible top cruise altitude at each latitude and month, such that flexibility in mission planning, global application, high-altitude capability and low battery weight were all prioritised. During the first iterations, this has been done manually based on contour plots visualising the resulting capability for various battery mass ranges. In the final design iteration code, the choice was automated and reduced to the choice of the lowest battery weight that allowed the top cruise altitude of 25 km at at least 4 different discrete latitudes in the grid of 15° steps for every month (ensuring at least 45° latitude range during each month). The contour plots generated for the final design iteration are shown in the following subsection.

5.3. Operational Profiles - Results

5.3.1. Feasible Profiles

In total 167,925 feasible profiles were generated. Out of those, for each combination of latitude, month and top cruise altitude four different types of profiles were found: that correspond to lowest possible battery mass, highest battery mass, the optimal profile (one with simultaneously the highest top cruise times and lowest battery mass) and the median profile (the profile corresponding to the median battery mass for the specific case, used to visualise a non-optimised profile). If multiple profiles corresponded to the minimum or maximum battery mass, then the one with highest top cruise time was chosen. Different profiles for an example case of 0° latitude in May are shown in Figure 5.6. It is worth noting that the minimum battery mass and optimal profiles coincide in all cases (the blue line is therefore not visible). This is because the high top cruise time generally does not adversely affect the battery mass and low battery mass was preferred more strongly than long top cruise duration.

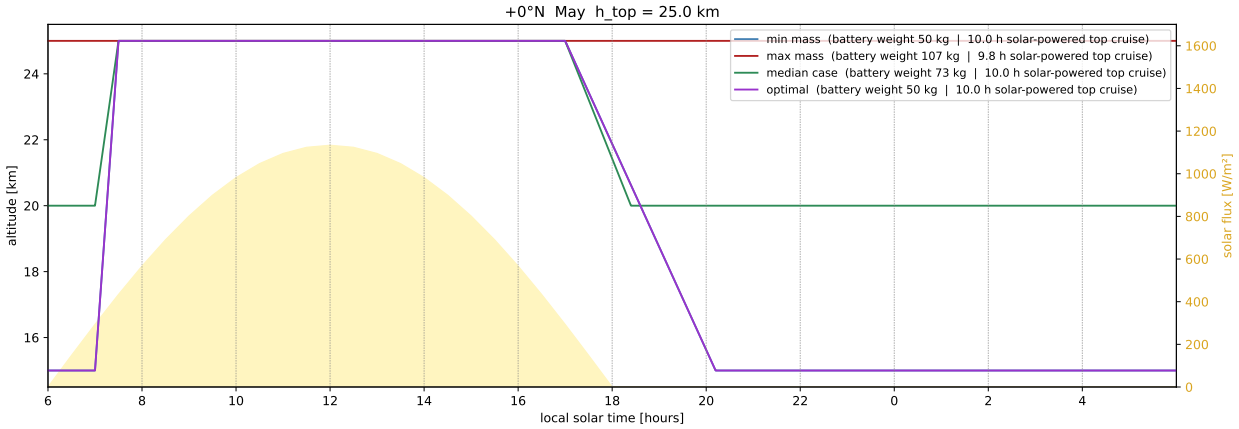

Figure 5.6: *Examples of Feasible Profiles for 0° latitude in May*

5.3.2. Optimal Profiles

The choice of the battery size was done based on the optimal profiles . In total 560 such profiles were found for each combination of latitude, month and top cruise altitude. The battery weight chosen in the final design iteration is 53.1 kg with a battery volume is 20.7 L. The range of optimal flight profiles possible with such battery size is shown in Figure 5.7. This is the same type of plot as was used for the battery size selection in each iteration.

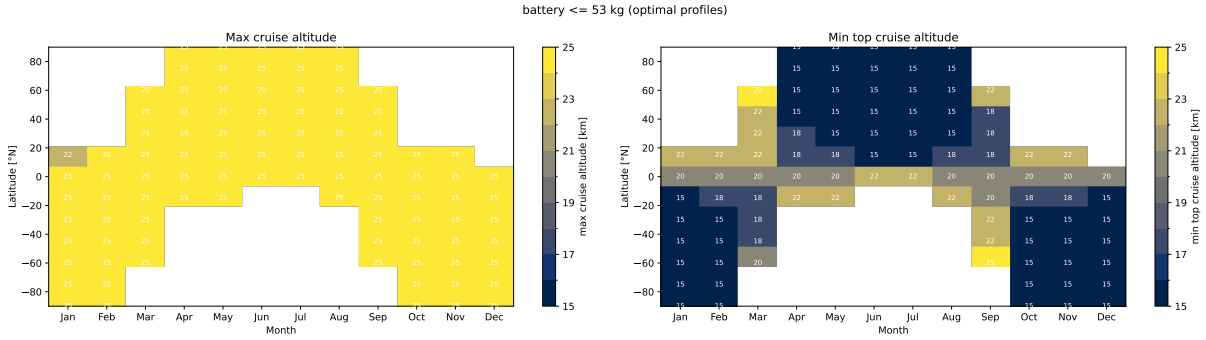

Figure 5.7: *Maximum and Minimum Top Cruise Altitude per Latitude and Month with the Design Battery Mass (53 kg)*

As visible on the right part of Figure 5.7, the minimum top cruise altitude is limited to higher values for low latitudes. This is due to the fact that these profiles require long unpowered descent for minimal battery weight, as already explained in the previous section. Additionally, in Figures 5.8 and 5.9, cases of battery weight smaller and larger by 5 kg are shown to illustrate the effect of battery sizing on the operational envelope.

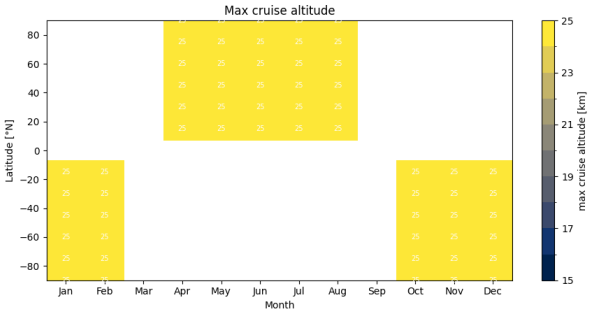

Figure 5.8: *Maximum Cruise Altitude per Latitude and Month with Battery Mass of 48 kg (5 kg Below the Design Mass)*

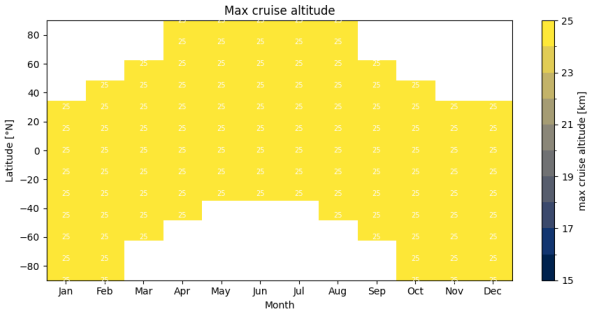

Figure 5.9: *Maximum Cruise Altitude per Latitude and Month with Battery Mass of 58 kg (5 kg Above the Design Mass)*

5.4. Mission Logistics

Based on the constraints mentioned in this chapter, two locations are proposed for launch and recovery with frequent clear weather. First one, in the south of Spain is at the latitude of around 38°N, allows for the start and end of the mission from March to September, as can be inferred from the Figure 5.7. From May to August, the climb can be shorter, as with the chosen battery mass there is sufficient energy to sustain a flat daily cruise profile at the altitude of 15 km. In the rest of the year (from October to February), the launch and recovery can be done in inland Kenya instead, as its latitude of around 0° ensures enough solar energy all year long. However, operations from this location shall be limited to the aforementioned months, as only then the air is dry (Kenya is in the region of ITCZ) [7].

In both cases, take-off and landing shall take place from an aerodrome and be supported by a ground crew. First, a general launch window is found aided by meteorological forecasts, ideally in spring or summer to ensure long daylight hours. Next, radiosondes and weather balloons are launched to get a better idea of what the weather conditions are at higher altitudes. One day in advance the final decision for the launch date is made and the airspace-managing agency is informed. The use of the launch site must be coordinated with air traffic control. Temporary landing gear is used for take-off, therefore SORA will be easy to move around the aerodrome with 4 people or more. Special attention has to be paid to ensuring wing tips clearance during ground operations.

As the launch and climb are expected to be the most power-intensive phases of the flight, they have to be planned to maximally harvest the solar power available. Therefore, the launch should happen around dawn with fully charged

[7] URL: https://www.britannica.com/place/Kenya/Climate [cited 23/06/2026]

batteries, such that solar energy from the full day can be used if needed. This also reflects the low turbulence related to thermal activity in the air during the morning hours. Following the launch, the aircraft crosses the boundary of aerodrome operations and enters the segregated airspace climbing up to at least FL510, this climb will be done via large-radius turns (increasingly larger due to increasing true air speed during the climb) and the airspace's activation can be timed/ pre-planned to minimise impact on other aircraft. This also means that the climb through the troposphere (the most vulnerable phase of the flight) is limited to a relatively small ground trajectory, therefore it can be planned with higher certainty.

The cruise of the aircraft happens at altitudes over the civilian traffic, in high troposphere or low stratosphere (between 15 and 25 km). This is the part of the mission optimised for long endurance and the requirements of the measurements done by the payload, and due to high power requirements to sustain flight at such high altitudes it is a very energy-intensive phase of the flight. To minimise the energy usage and the required weight of the batteries, the aircraft might need to descend during the night when there is no solar power available.

After the initial cruise to reach the target altitude band, the aircraft can climb and descend to whichever altitude is required for the measurements given that there is enough power. Due to the long mission duration the aircraft could potentially fly around the Earth up to 4.5 times, this means that measurement locations are not limited by take off and launch location. An example measurement period could look like: climbing or descending to required altitude above location of interest (such as an airport or dense transport location)- entering a loiter phase which can consist of tight circular or tangential patterns over the prescribed area.

The descent is analogous to the climb in airspace use, weather planning and timely coordination with the air traffic management. However, it is vastly different in terms of energy management. With high wing aspect ratio and being at the top of the troposphere, the aircraft is well suited for a glided descent. This means that adverse weather conditions (clouds, turbulence) can be avoided by descending at night. Regardless, it is recommended that the aircraft starts the descent with the batteries fully charged: this is to ensure that enough energy is available for waiting for landing in case of unforeseen circumstances (such as bad weather) and to perform necessary manoeuvres. To ensure good visibility for the ground crew, the ideal time for landing is at dawn, when the air over ground is still.

Landing requires very still air, as low speed might make the V-tail less responsive to wind gusts. With the indicated airspeed of less than 10 m/s, the aircraft can safely perform a belly landing and is expected to decelerate very quickly once on the ground. After landing, the landing gear can be attached for towing SORA off the runway.

5.5. Verification and Validation

The code used to determine the operational profile was tested using three levels/philosophies of pytests. Firstly, software verification using mock data sets test that plots run, inputs and dimensions are correctly handled to confirm that the code is properly executed without any crashes. Next, physical consistency is checked, which makes sure that no outputs are unphysical and that there are no faults in the logic. This includes simple checks to verify that there are no missed logical fallacies. For example, the battery mass should never be negative as this would be impossible, day and night hours sum up to 24 and summer energy should be greater than winter energy. Additionally, sanity checks are performed on the outputs to ensure that while physically possible, the results are also reasonable. Lastly, regression tests check that if something should be changed in one part of the code, later functions still work and perform as expected. After having passed all these verification tests, it can be assumed that the code performs as expected and is able to properly handle inputs and outputs.

At this stage validation can primarily be done through comparison with published data and papers. The solar values and derived equations were compared with published models [22]. The results were found to be consistent and produce similar values for solar models. Additionally, alignment of the calculated maximum operational latitude with those set by Sceye [8] gives confidence that these limits are consistent. The assumptions made surrounding the atmosphere were confirmed by separate sources. Wind and temperature limits derived form the ERA5 dataset were checked against climatological studies of the stratosphere [9]. The flight profiles were qualitatively compared with existing HAPS. In particular, Airbus Zephyr [20], that independently demonstrates that the night descent and daylight climb strategy is preferred which validates this approach. Lastly, future validation using flight test data would further enhance confidence in the conclusions of this chapter.

[8] Sceye representative, unpublished interview, May 2026

[9] URL: https://weather.uwyo.edu/upperair/sounding.shtml [cited 17/06/2026]

6

Payload and Measurement Systems

One of the most essential components of the aircraft is the payload. From the early planning of the project, it was determined to select the payload early in the development, as it will dictate the rest of the design. This chapter firstly focuses on the literature study performed and the selection process, which is followed by analysing the preliminary payload configuration and the design of the payload compartment.

6.1. Literature Study

Before selecting the payload instruments, the required measurements and suitable sensing techniques must be defined.

6.1.1. Atmospheric Conditions

The atmospheric conditions relevant to this study are primarily temperature, pressure, humidity and radiation, as these parameters strongly govern the physical and radiative environment in the upper troposphere and lower stratosphere [27]. Temperature and humidity are especially critical near the tropopause, the transition region between the troposphere and stratosphere, where small changes in altitude can lead to large variations in atmospheric state. These atmospheric conditions and their variations influence processes such as contrail formation [28].

Since the aircraft will have a cruising altitude range of 15 to 25 km, extreme atmospheric conditions will be experienced, a more elaborate discussion can be seen in Chapter 5. Furthermore, atmospheric temperatures can reach, at their lowest, values below -80 °C at the tropopause over the equator [18]. Ambient pressure decreases to the order of 2 kPa at 25 km according to the International Standard Atmosphere. Humidity measurements are challenging at high altitudes due to the very low absolute water vapour content and the increased relative influence of instrumental and environmental biases under low-pressure conditions [29]. These conditions place strong requirements on atmospheric measurement instrumentation.

Radiation is commonly separated into shortwave and longwave components. Shortwave radiation is partially reflected and absorbed, while longwave radiaton is emitted by the Earth and the atmosphere towards space [1]. Contrails influence the radiative budget by reflecting incoming shortwave radiation and trapping outgoing longwave radiation, thereby contributing to aviation-induced radiative forcing [30]. Accurate characterization of the background radiation field is therefore essential for quantifying the additional radiative impact of contrails.

6.1.2. Trace Gases

Trace gases are atmospheric gases present in very low concentrations (i.e., all gases other than nitrogen, oxygen and argon) [2]. Several contribute significantly to global warming as quantified by their Global Warming Potential, primarily CO_2, CH_4 and N_2O and, to a lesser extent, fluorinated greenhouse gases ($HFCs$, $PFCs$, SF_6 and NF_3) [31]. The UAV must therefore be capable of measuring the concentrations of these gases throughout its mission.

One other important gas to measure is ozone O_3, since this gas forms the ozone layer (located at an altitude range between 15km and 35km), which is responsible for filtering UV radiation that would be harmful to life on Earth [32].

Furthermore, one of the high-level requirements for the UAV is to be able to measure aircraft emissions. The main emissions generated by aircraft are: CO_2, H_2O, NO_x (NO and NO_2), hydrocarbons, CO, soot and SO_2 [33]. This means that the UAV will need to be able to, apart from the trace gases already mentioned before, also measure NO, NO_2, CO and SO_2.

Measurement Techniques

When looking at possible measurement techniques that can be used to measure atmospheric trace gases, the first major decision is on whether to use in-situ sensors (i.e. sensors that need to come into close contact with the sample being measured), or remote sensing inurements (i.e. sensors that make use of technologies that enable measurements of the relevant sample from a distance). Given that the UAV will be operating at an altitude range between 15 and 25 km, and considering most commercial aircraft operate at an altitude range up to 13 km [3], the use of in-situ sensors to measure emissions from other aircraft would require the UAV to descend from its operational

[1] URL: https://science.nasa.gov/ems/13_radiationbudget/ [cited 11/05/2025]
[2] URL: https://gml.noaa.gov/education/carbon_toolkit/ [cited 12/05/2026]
[3] URL: https://wayman.edu/how-high-do-planes-fly/ [cited 12/05/2026]

range to go through the emission plume of a certain aircraft shortly after said aircraft passes through the region. This would raise a number of operational and power management complexities, and, as such, it is decided that remote sensing is the best approach.

Remote sensing of trace gases is a well-explored research area. Gerald Wetzel et al. [34] demonstrated the suitability of satellite-borne Fourier-Transform spectrometers operating in the mid-infrared range for detecting trace gases such as H_2O, CO_2, N_2O and CO. It is mentioned that nadir-directed measurements offer high horizontal resolution, while limb-sounding (where the spectrometer is pointed tangentially to Earth's curvature, as shown in Figure 6.1) provides good vertical resolution of atmospheric composition [34].

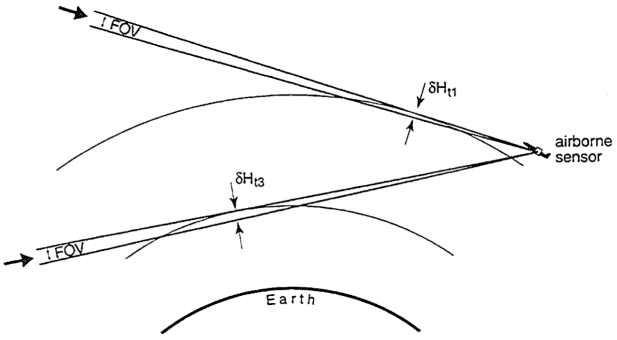

Figure 6.1: *Limb-Measurement Illustration [35]*

Though predominantly used on satellites such as UARS and Envisat [36], Roscoe and Hill [35] showed limb-sounding is also viable from high-altitude aircraft, even achieving smaller errors than satellite platforms. Vertical resolution degrades with distance below the aircraft altitude, and is directly improved by a smaller sensor field of view (FOV), which is an important consideration for sensor selection.

As such, for the UAV being designed, research into sensors for trace gas detection will focus on the use of spectrometers. However, before individual sensors can be researched, it is necessary to identify the spectral range that these sensors will need to address. This stems directly from the spectral signatures of the gases whose concentrations will need to be measured. Table 6.1 summarizes the spectral signature of each trace gas that will be targeted for measurement.

Table 6.1: *Spectral Signature Trace Gases*

Gas	Spectral signature (nm)	Source
CO_2	≈ 2000	[37]
CH_4	$\approx 2305 - 2385$	[38]
N_2O	≈ 2300	[39]
O_3	≈ 255	[40]
NO	≈ 227	[41]
NO_2	≈ 438	[41]
CO	≈ 2300	[42]
SO_2	$\approx 310 - 330$	[43]
H_2O	≈ 1380	[44]

Note that there is overlap in the frequency bands of some gases, namely CH_4, CO and N_2O. As such, the instruments chosen will require as large of a spectral resolution as possible, as well as a high Signal to Noise Ratio, in order to be able to distinguish between different gases with overlapping spectrums. [4]

[4] URL: https://sunex.com/2021/02/17/swir/ [cited 14/05/2026]

6.1.3. Aerosols

Aerosols are shown to have a serious effect on Earth's climate[5]. It is thus important to know the properties of aerosols in the stratosphere, where an aerosol layer (Junge layer) influences Earth's radiative budget [45]. Various campaigns with the objective of measuring aerosols in the atmosphere have been run. To highlight the types of measurements done on these campaigns, a 2014 DLR campaign is investigated: ML-CIRRUS [6]. The scope of this campaign included the formation, lifetime, properties and radiative/chemical impact of cirrus clouds, including contrails. Instruments used for measuring aerosol size distributions include wing-mounted optical spectrometers. These instruments are designed for aircraft integration and require cabin infrastructure, making them unsuitable for a HAPS platform. However, in-situ measurement is essential for developing stratospheric aerosol models [45]. A class of lightweight optical particle sensors has been developed specifically to be used on balloon and UAVs such as the Handix POPS instrument [7].

6.1.4. Contrails

Aircraft emissions in the atmosphere consist of water vapours, metallic powders, sulphuric particles and other non-volatile particles [46]. When exposed to the low temperature at the cruise altitudes, and if the conditions meet the Schmidt-Appleman Criterion [47], those particles can act as nucleation points for ice crystals [48]. The effect of contrails on the climate has been studied since 1919, and it has been estimated that contrails impact on the global annual mean radiative forcing (the heat flux as a result of aircraft induced clouds (AIC)) is three time as much as the contribution from the CO_2 emissions [47]. Most AIC measurements are done either from the ground or from satellites and lack temporal tracking [49].

The UAV will be flying at a minimum cruise altitude of 15 km, with most contrail formation happening at lower altitudes, between 8 and 12 km [47]. Flying above the contrails allows the UAV to have a high field of view of the AIC while being closer than satellites, allowing for higher resolution from its instruments, although it eliminates the possibility of in-situ measurements. This limits the instruments to remote sensing options, like Light Detection and Ranging (LiDAR) and multispectral cameras to collect high resolution data on the contrail. Focusing on contrail physical properties such as length, width and thickness, altitude, ice particles distribution and temporal movement. More detailed information on reflectivity and radiative forcing can be collected together with radiation sensors described in Subsection 6.1.1.

6.2. Trade-off Methodology

For every sensor category, an extensive market research study was completed, producing multiple sensor options for every category. To select the best sensor for the mission, a feasibility study was performed, in certain cases followed by a trade-off analysis when multiple options were identified as feasible. The criteria for feasibility were not set a priori but analysed case by case, ensuring a realistic analysis was performed. This allowed the team to maintain a concrete understanding of the market options and elaborate alternative solutions for unfeasible sensors; for example, temperatures outside operating ranges can be solved with a heated compartment.

To complete the trade-off, every sensor having passed the feasibility study was evaluated and given a score, and for all the sensors the following criteria were set:

Measurement Range - 30% For any kind of sensor, one of the main selection points is the range over which it can perform measurements. This takes into account for what the sensor can be used for, what are its limitations and allows the team to understand what can be the workarounds. Into this criterion, the limitations in operation were also taken into account, for example temperature limitations or pressure constraints. Due to the importance of this criterion it was given a weight of 30%.

Accuracy - 25% Accuracy or resolution was selected as the second criterion with a score of 25%, slightly lower than the measurement range. This criterion encompasses the resolution of the sensor, allowing the team to discard low resolution solution and focus on the necessary accuracy needed in the measurements to allow correct validation for climate models.

Power Consumption - 20% The main challenge in designing a high altitude long endurance aircraft (HALE) are the power limitations, especially considering a solar powered plane that can not generate power during the night. The power consumption of every sensor will play an important role in sizing the power subsystem, resulting in a weight of 20%.

Mass - 15% Another concern is the mass of individual sensors. As when flying at high altitudes, every kilogram has

[5]URL: https://science.nasa.gov/science-research/earth-science/climate-science/aerosols-small-particles-with-big-climate-effects/ [cited 12/05/2026]
[6]URL: https://halo-research.de/science/previous-missions/mlcirrus/ [cited 12/05/2026]
[7]URL:https://handixscientific.com/pops/ [cited 12/05/2026]

an extended impact on the performance and total power required. Due to this relation, mass was identified as less important than raw power consumption, being assigned a weight of 15%.

Cost - 10% Cost was chosen as a criterion as the overall aircraft has a budget of 1 million Euros. But it was given a score of 10% as it was determined that the success of the mission, and the gathering of accurate data were more important than the final cost. Furthermore, price of certain sensors was not publicly available and would result from negotiation with the manufacture, decreasing the total weight for this criterion. If the mission would not provide new insightful data, there would be no point in developing such aircraft.

6.3. Sensors for Trace Gases Detection

Following the outcome of the literature study in Subsection 6.1.2, it is now possible to research the specific sensors that will be part of the trade-off. In Subsection 6.1.2 it has already been identified that there will be a need for spectrometers targeting the UV/Visual range, and the short wave infrared (SWIR) range. Furthermore, in terms of the main working principle of the spectrometer, having an imager in each of the spectral ranges will be useful, since it allows for snapshots of a larger area [8], making it possible to observe full emission plumes of other aircraft, for example. Imaging spectrometers, however, have a relatively large field of view, which makes it impossible to do the limb-sounding measurements as explained in Subsection 6.1.2. As such, the UAV will also need to carry point spectrometers, which measure the light spectrum from a single point, thus having a much narrower field of view [9]. The aircraft will thus have to carry four instruments for trace gas sensing: a UV/Visual imager, a SWIR imager, a UV/Visual point spectrometer and a SWIR point spectrometer. The trade-off will then be performed for each of these categories.

For the trade-off of the trace gases sensors, the criteria set in Section 6.2 shall be followed. The *Accuracy* criterion will in this case be evaluated considering the sensor's spectral resolution and Signal to Noise Ratio (SNR), since these are the most important characteristics in distinguishing between gases which, apart from the relevant fact of being in very low concentration in the atmosphere, have in some cases the added complexity of close spectral signatures, as explained in Subsection 6.1.2.

6.3.1. UV/Visual Imager

For the UV/Visual imager, three commercially available candidate instruments were identified: the Resonon Pika UV [10], the Corning microHSI 410 SHARK [11] [50] and the HySpex Mjolnir V-1240 [12]. The trade-off is shown in Table 6.2.

Table 6.2: *Trade-Off Analysis for UV/Visual Imager*

Criteria \ Sensor	Resonon Pika UV	Corning microHSI 410 SHARK	HySpex Mjolnir V-1240
Measurement Range (32.5%)	330-800nm	400-1000nm	400-1000nm
Accuracy (27.5%)	Spectral resolution = 2.8nm; SNR = 361	Spectral resolution = 2nm; SNR = 250	Spectral resolution = 3nm; SNR = 180
Power Consumption (22.5%)	3.4W	19.1W	25W
Mass (17.5%)	3kg	0.7kg	3kg
Final Score	4.5	3.4	2.9

In terms of cost, no publicly available data could be found on the price of these sensors, and only the company responsible for the Corning microHSI 410 SHARK answered a request for a quote, listing the sensor's price at ≈ 30000€, so the cost was not considered for the trade-off (its weight of 10% was equally distributed among the remaining criteria). The winning option is considered to have a cost of ≈ 30000€.

As can be seen, the Resonon Pika UV sensor scores the highest. Note that, even though it scored highest on the *Measurement Range* criterion, it is still not enough to cover all the UV spectral signatures shown in Table 6.1: it only

[8] URL: https://www.specim.com/technology/how-does-spectral-sensing-work/ [cited 14/05/2026]
[9] URL: https://www.specim.com/technology/how-does-spectral-sensing-work/ [cited 14/05/2026]
[10] URL: https://resonon.com/content/files/Resonon---Camera-Data-Sheets-Pika-UV.pdf [cited 22/05/2026]
[11] URL: https://www.corning.com/media/worldwide/csm/documents/microHSI_410%20Sensor_and_microHSI_410_SHARK.pdf [cited 22/05/2026]
[12] URL: https://is.earsel.org/workshop/11-IS-Brno2019/wp-content/uploads/2018/08/HySpex_Mjolnir_VS-620v2.pdf [cited 22/05/2026]

covers the spectrums of NO_2 and SO_2, and fails to cover NO and O_3. Unfortunately, no imagers were found that are able to cover lower spectral ranges than the ones considered for the trade-off.

6.3.2. SWIR Imager

For the SWIR imager, two commercially available candidate systems were identified: the Resonon Pika SWIR [13] and the HySpex Mjolnir S-620 [12]. Both of these options have very close specifications for the criteria to be considered for the trade-off, except the Resonon Pika SWIR has lower power consumption (4 W vs. 25 W) and better SNR (1825 vs. 900). As such, it is clear that the Resonon Pika SWIR is the best option, and there is no need to develop a trade-off table. Once again, no publicly available data was found on the cost of these specific sensors, and the respective companies did not answer requests for a quote, and as such, the cost was not considered for the trade-off. However, based on publicly available information on the cost of SWIR imagers, the cost of this type of sensor is estimated to be ≈ 190000€ [14].

6.3.3. UV/Visual Point Spectrometer

For the UV/Visual Point Spectrometer, two candidate sensors were identified: the Ocean Insight QEPRO [15] and the Ocean Insight Maya2000 Pro [16]. Both of these models have very similar specifications, with respect to the criteria that would be used for the trade-off, but the OceanInsight QEPRO has much better SNR (1000 vs. 450), despite its slightly higher cost (15500€ [17] vs. 10000€ [18]). Having as high of an SNR as possible is crucial to detect with accuracy gases that have faint spectral signatures due to their low concentration in the atmosphere. This made it clear that the Ocean Insight QEPRO is the better option. So, no trade-off table was developed.

The point spectrometer will also need to be paired with a lens suitable to collect the light that will be fed to the instrument Ocean Insight, the same company that manufactures the QEPRO also sells these type of lenses. The 74-UV lens [19] is chosen for this purpose. This lens is connected to the spectrometer by means of a fibre optic cable.

6.3.4. SWIR Point Spectrometer

For the SWIR point spectrometer, two candidate sensors were identified: the Avantes AvaSpec-NIR256/512-2.5-HSC-EVO [20] and the Ocean Insight NIRQuest+2.5 [21]. The trade-off is shown in Table 6.3:

Table 6.3: *Trade-Off Analysis for SWIR Point Spectrometer*

Criteria \ Sensor	**Avantes AvaSpec-NIR512-2.5-HSC-EVO**	**Ocean Insight NIRQuest+2.5**
Measurement Range (32.5%)	1000-2500nm	900-2500nm
Accuracy (27.5%)	Spectral resolution = 3.1nm; SNR = 4000	Spectral resolution = 3.4nm; SNR = 10000
Power consumption (22.5%)	40W	15W
Mass (17.5%)	3.5kg	1.6kg
Final Score	3.4	4.6

The Ocean Insight NIRQuest+2.5 comes out as the better option due to its better SNR and lower power consumption. Information regarding the cost of these sensors was only found for the Ocean Insight NIRQuest+2.5, priced at ≈ 31500€ [22]. The company responsible for the Avantes AvaSpec-NIR512-2.5-HSC-EVO did not answer a request for a

[13] URL: https://resonon.com/content/files/Resonon---Camera-Data-Sheets-Pika-SWIR.pdf [cited 22/05/2026]
[14] URL: https://surfaceoptics.com/hyperspectral-camera-price/ [cited 17/05/2026]
[15] URL: https://www.ill.eu/documents/1328/Spectro00.pdf [cited 17/05/2026]
[16] https://intins.co.kr/mayapro.pdf [cited 17/05/2026]
[17] URL: https://www.edmundoptics.com/p/ocean-optics-qe-pro-nir-spectrometer/57211/ [cited 17/05/2026]
[18] URL: https://www.ebay.com/itm/406155011231 [cited 17/05/2026]
[19] URL: https://www.oceanoptics.com/accessories/sampling-accessories/collimating-lenses/ [cited 17/05/2026]
[20] URL: https://www.avantes.com/content/uploads/2020/11/DS-Spec-AvaSpec-NIR256512-2.5-HSC-EVO-200702.pdf [cited 22/05/2026]
[21] URL: https://spegroup.ru/upload/wikifiles/1589842.pdf [cited 22/05/2026]
[22] URL: https://www.edmundoptics.com/p/ocean-optics-nr-near-infrared-nir-25-spectrometer/57402/[cited 17/05/2026]

quote, as such, the cost was removed from the trade-off and its weight of 10% was equally distributed among the remaining criteria.

The NIRQuest+2.5 will need to be paired with a lens. While Ocean Insight sells lenses for its spectrometers, none of them are able to capture up to the wavelength required ($\approx 2300nm$). As such, the COL-UV/VIS lens by Avantes [23] is chosen. This lens captures light up to a wavelength of 2500nm, and it has the same connector type as the lenses by Ocean Insight, so it is expected it will be fully compatible with the NIRQuest+2.5.

6.3.5. Air sampler

There are some trace gases which are outside the targets of the sensors mentioned previously, since during the literature study of Subsection 6.1.2, they have been identified as less relevant within the project scope. Nonetheless, there could be an interest by the future users of the UAV on capturing at least some data regarding these gases. As such, it has been decided to include an air sampler as part of the payload of the UAV, that will extract and store samples of the atmosphere, which can later be analysed in a laboratory.

After thorough literature analysis, it has been decided to equip the UAV with the Vienna Scientific Instruments VSI AS-110 Whole Air Sampler [24]. This instrument samples air up to 12 vacuumed-out glass vials, and it was specifically developed for UAVs, having already been tested up to the stratosphere. Other technologies like NOAA's AirCore [25] system were also considered. But the AS-110 was chosen in the end without a formal trade-off, due to the fact of it being commercially available, and having already been validated in missions very close to the type of mission MALEO4CRE will perform. No information could be found on the cost of this equipment, and the company did not answer a request for a quote.

6.4. Sensors for Contrail Properties

To select the correct sensors for the measurements regarding contrail properties, an in depth research was completed and a trade-off table was developed for LiDAR only. As other important properties are measured by the radiation sensors found in the atmospheric conditions sensors in Section 6.6 and by the spectral cameras used for the trace gases in Section 6.3. The LiDAR itself can then focus on contrail properties like thickness, altitude and ice crystals size distribution.

Multiple LiDAR solutions were initially found, ranging from cheap handheld systems to complex units and ceilometers. An initial feasibility study was performed and it eliminated most of the found option, as the majority of market LiDARs focuses on just distance measurements and does not take into account single photon return due to backscatter. This resulted in three main options for the trade-off : Mini Micro Pulse LiDAR [26], Ceilometer CL51, CS135 LIDAR Ceilometer [51].

From the trade-off, the Mini Micro Pulse LiDAR won due to its lower weight and high accuracy. It is important to notice that no price was publicly available and a quotation from the manufacturer needs to be obtained.

6.5. Sensors for Aerosols Detection

The aerosol sensor is selected to be an optical particle sensor. This follows from an extensive literature and market study, shown in Subsection 6.1.3. A number of on-the-market commercial solutions and off-market scientific solutions were reviewed. These sensors must conduct in-situ measurements, so most options were discarded due to their operating pressure ranges not covering the stratosphere. It was found that most sensors rely on air pumps and are not designed for the low ambient pressure of the stratosphere. In the end, two feasible options remained, both designed for HALE applications: the scientific instrument, LASP Optical Particle Counter (LOPC), from the Laboratory for Atmospheric and Space Physics (LASP) and the commercial Handix Scientific Portable Optical Particle Spectrometer (POPS) [27]. Handix POPS was selected over LOPC due to the lower weight (1 kg vs 2 kg) and the readily available power and size figures, which facilitates the integration of the payload onboard. LOPC has no publicly available information on power requirements or size.

Note that the Mini MPL LiDAR discussed in Section 6.4 can also obtain information about aerosol concentration in the atmosphere, and as such it will be used to complement the in-situ measurements from the Handix POPS.

[23] URL: https://www.avantes.com/products/fiber-optics/fiber-optic-accessories/collimating-lenses/ [cited: 18/05/2026]
[24] URL: https://www.vienna-scientific.com/research/iso-drone/ [cited 14/05/2026]
[25] URL: https://gml.noaa.gov/ccgg/aircore/ [cited 14/05/2026]
[26] URL: https://www.dropletmeasurement.com/product/mini-mpl/ [cited 22/05/2026]
[27] URL: https://handixscientific.com/pops/ [cited 13/05/2026]

6.6. Sensors for Atmospheric Conditions

For the atmospheric condition instruments, a screening study was performed, after which the only compliant candidate was selected directly without a full trade-off. The process is described here: It was observed that most candidate sensors achieved similar scores for criteria such as mass, cost, and power consumption. However, the measurement range proved to be the restricting factor, as the atmospheric conditions within the operational altitude range of 15-25 km are extreme. Consequently, sensors that could not satisfy the required operational ranges were excluded from further consideration.

Temperature, pressure, and humidity measurements are essential for characterising the upper troposphere and lower stratosphere. Literature indicates that temperatures at target cruise altitudes can decrease to approximately -80 degrees Celsius, while ambient pressure can reduce to nearly 2 kPa as can be read in Subsection 6.1.1. Furthermore, humidity measurements at high altitude are particularly challenging. Since these conditions exceed the operational range of many conventional atmospheric sensors, only high-altitude-capable systems were considered feasible.

Based on these requirements, the Radiosonde DFM-17 was selected for atmospheric measurements. The system satisfies the required temperature, pressure, and humidity measurement ranges while combining all three sensing capabilities within a single unit. This integrated configuration reduces the overall system mass, power consumption, and wiring complexity compared to separate sensor installations. [28] [29] [30]

Radiation measurements were divided into short wave and long wave radiation components. For short wave radiation measurements, the SMP22x [31] was selected, while the SGR4 [32] [33] was selected for long-wave radiation measurements. Both sensors provide suitable measurement performance for high altitude atmospheric research applications while maintaining relatively low mass and power requirements.

6.7. Preliminary Payload Configuration

Following the extensive literature study and market research performed, a preliminary payload was selected and the most important information is summarised in Table 6.4.

More information, like physical size, accuracy drift over time, signal-to-noise ratio and instrument specific values were researched and used for the selection process of the sensors. An important note has to be made on cost, as most of the instruments do not have a publicly available price, and an inquiry with the company is required. If a similar sensor was found online, its price was used to estimate the actual instrument cost, but this strategy was not possible for every sensor. As the project progresses, inquiry and quotes can be sent and used to gather more specific cost information.

Furthermore, it is important to notice that the LiDAR sensor is responsible for 50% of the total payload mass and 63% of the total power required. This sensor was selected as it has low mass and low power consumption compared to similar instrumentation, and its ability to measure the distance, thickness and average particle distribution of contrails are valued as essential to proper contrail measurement.

Note that the values in the *spatial resolution* column were calculated in different ways depending on the respective instrument. For the sensors which take measurements in situ (i.e. the Radiosonde DFM-17, the SMP22x, the SGR4 and the Handix POPS), their spatial resolution was calculated considering the sampling time and the speed the UAV will fly at during cruise. For the imagers (i.e. the Pika SWIR and the Pika UV), it was calculated considering the Field Of View of their lenses, the number of spatial pixels in the resulting image, and their distance to the target (assumed to be equal to 15km, in case the UAV is flying at 25 km altitude and measuring a target at 10km altitude). For the LiDAR, it was calculated considering the angular divergence of the LiDAR beam and the distance to the target (once again assumed to be 15km). For the point spectrometers, no value was calculated, since the spatial resolution greatly depends on distance to the target. For limb-measurements, which is the main type of measurement the point spectrometers will be doing for vertical profiling of the atmosphere (see Subsection 6.1.2), since the instruments are pointed tangentially to the Earth, this "distance to the target" varies greatly (as a reference, Roscoe and Hill [35] managed to obtain a vertical resolution of 1.5 km when using a similar sensor).

Finally, the values in Table 6.4 are from direct sources, but usually they refer to a complete instrument, with a complete case and individual power supply. While integrating the instrument together in the aircraft, any unwanted

[28] URL: https://www.weather.gov/media/upperair/Documents/DB-DFM-17-EN_V01.06.pdf [cited 22/05/2026]
[29] URL: https://wiki.recessim.com/view/DFM-17_Radiosonde#Specs_.5B2.5D [cited 22/05/2026]
[30] URL: https://govtribe.com/award/federal-contract-award/delivery-order-1305m222dnwwg0001-1305m225f0330 [cited 22/05/2026]
[31] URL: https://cdn.hach.com/1XMCM0ZF/at/rhvp966mh48jtqtc5c8s37q/KippZonen_Data_sheet_SMPx_2025_online.pdf [cited 22/05/2026]
[32] URL: https://www.kippzonen.com/products/sgr4-pyrgeometer [cited 22/05/2026]
[33] URL: https://manuals.plus/m/ffce9e900a60bf52fdaa59136b249ebfe439f37f339704e6cb892c36ef7762ed.pdf [cited 22/05/2026]

support systems can be discarded, reducing overall weight. This technique is called "skeletonizing", and it can be assumed to bring a weight reduction of 20% based on engineering judgement. This also has an impact on the operating range, as removing insulation will result in narrower temperature ranges. Overall, there will be the need for a heated and pressurized compartment to house payload instruments that require it to ensure they remain within their operating ranges.

Table 6.4: *Payload Overview*

Target measurement	**Instrument**	**W [kg]**	**P [W]**	**Resolution**	**Measurement Range**	**Spatial Resolution[m]**	**Cost [€]**
Temperature	Radiosonde DFM-17	0.063	2	0.01 °C	−90–+60 °C	36	100
Pressure	Radiosonde DFM-17	0.063	2	0.01 hPa	1–1100 hPa	36	100
Humidity	Radiosonde DFM-17	0.063	2	0.1 %rH	0–100%rH [34]	36	100
Short wave radiation	SMP22x	0.6	10.06	±5 W/m²	250–3500 nm	72	7900
Long wave radiation	SGR4	0.6	10.1	1 W/m²	4400–50000 nm	650	7000
Trace gases SWIR spectrum	Pika SWIR imager	4	4	7.7 nm	1000-2500nm	9	190000
Trace gases UV/Vis spectrum	Pika UV imager	3	3.4	2.8 nm	330-800nm [35]	1.5	30000
Trace gases SWIR spectrum	NIRQuest+2.5 point	1.6	15	3.4 nm	900-2500nm	-	31500
Trace gases UV/Vis spectrum	QEPRO point	1.2	2.5	0.14 nm	185-1100nm	-	15500
Air sampling	VSI AS-110	1	5	—	—	-	—
Aerosols	Handix POPS	0.9	5	5%	130 nm–3 µm	36	10000
Contrail physical properties; aerosols	MiniMPL LiDAR	13	100	5 m	100m-15km	12	35000
TOTAL		**26**	**157**				**>327000**

6.8. Payload housing compartment

Since several of the payload instruments listed in Table 6.4 are not made to sustain operation up to the stratosphere, there will be the need for a specialized heated and pressurized compartment that will house said instruments.

6.8.1. Payload Compartment Dimension

The instruments that will need to be housed inside this compartment will be: the SMP22x short-wave radiation sensor, the SGR4 long-wave radiation sensor, the Resonon Pika SWIR imager, the Resonon Pika UV imager, the Ocean Insight NIRQuest+2.5 SWIR point spectrometer and respective lens, the Ocean Insight QEPRO UV point spectrometer and respective lens, and the MiniMPL (DMT) LiDAR. The remaining payload instruments are graded to work at least up to the stratosphere.

[34] Humidity measurement range is valid across the instrument's specified temperature (–90 to +60 °C) and pressure (1–1100 hPa) ranges

[35] This measurment range includes the visible range (380-700nm), functioning as a conventional camera

The dimensions of the instruments that will be inside the specialized compartment are listed in Table 6.5.

Table 6.5: *Instruments Dimensions*

Instrument	Dimension (mm)
SMP22x	167x167x68
SGR4	150x150x76.5
MiniMPL LiDAR	240x305x480

Instrument	Dimension (mm)
Resonon Pika SWIR	339x117x114
Resonon Pika UV	230x107x85

Instrument	Dimension (mm)
NIRQuest+2.5	182x110x47
+ Lens	50x6x6
QEPRO	182x110x47
+ Lens	50x5x5

However, since the MiniMPL (DMT) LiDAR comes in a package which includes its own casing and power source, it is assumed that its dimensions can be reduced by ≈ 20% to 190x244x380 mm.

The instruments disposition is then as follows: the point spectrometers' lenses will need to be pointed towards the front of the aircraft in order to carry-out limb measurements; the SWIR and UV imagers will need to be pointed nadir in order to measure emission plumes from other aircraft; the LiDAR will need to be pointed nadir in order to measure contrails from other aircraft; the long-wave radiation sensor will need to be pointed nadir in order to measure infrared radiation blocked by contrails; the short-wave radiation sensor will need to be pointed up to measure short-wave radiation from the Sun.

The payload will then be arranged in a heated and pressurized compartment at the nose of the aircraft, as seen in Figure 6.2, where the X axis points towards the nose of the aircraft, and the Y axis towards the Earth.

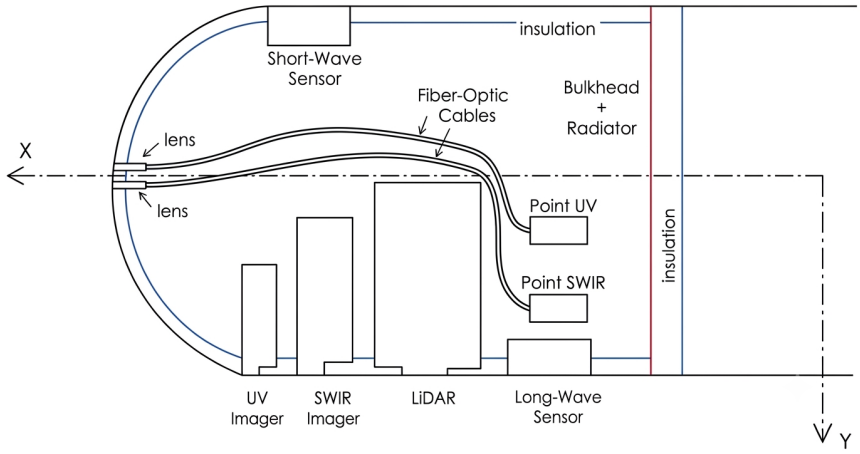

Figure 6.2: *Payload Arrangement in Compartment (AI-enhanced image based on sketch by group member)*

Note that Figure 6.2 serves purely as an illustration. Considering the dimensions stated in Table 6.5, and following the arrangement shown in Figure 6.2, this results in a required compartment height of 416 mm and length of 606 mm. The width is limited by the width of the LiDAR instrument, giving then a required width of 244 mm. Assuming the fuselage will have a circular cross-section, this results in a required diameter of 416 mm.

Furthermore, applying a margin factor of 1.2, to account for the fact that the instruments can not be placed perfectly close together, this results in a length of 727 mm and a diameter of 500 mm.

6.8.2. Heating and Pressure Analysis

In order to finish designing the payload compartment, it is necessary to consider its heat balance, to understand what insulation, and possibly even supplemental heating power, might be needed.

The surface area of the compartment will be covered by two materials: most of it will be covered by insulation, and a smaller part will need to be windows for the payload instruments to look through. For the insulation material, it has been chosen to use silica aerogel, since it has the lowest thermal conductivity among commonly available materials [36], with a thermal conductivity of $0.023 W/mK$ [37].

[36] URL: https://www.engineersedge.com/heat_transfer/insulation_material_thermal_conductivity_chart__13170.htm [cited 19/05/2026]

[37] URL: https://www.buyaerogel.com/product/thermal-wrap-2-5-mm-blanket/ [cited 19/05/2026]

As for the windows, the material chosen needs to be able to let through radiation with wavelengths from 220 nm to 2300 nm, so that the instruments can carry out the required measurements. As such, it has been chosen to use Suprasil300 [38], which has a transmission coefficient of more than 90% from ≈ 210 nm to ≈ 2500 nm.

To size the windows, it is first necessary to consider the diameter of the lenses and sensors that will need to be able to "look out" of the aircraft. Table 6.6 shows the diameter of these components, along with the diameter for the respective windows and the required window thickness. The diameter of the windows is obtained according to Equation 6.1, and a margin factor of 50% is applied to account for vibrations or the possibility that some sensors might need to be placed further away from the camera than assumed:

$$D_{window} = D_{sensor} + 2 \cdot l_{separation} \cdot \tan\left(\frac{FOV}{2}\right) \tag{6.1}$$

where D_{window} is the required window diameter, D_{sensor} is the diameter of the sensor, $l_{separation}$ is the separation between the sensor and the window (assumed to be equal to 5 mm) and FOV is the field of view of the sensor.

Table 6.6 also includes the required thickness for each window according to Equation 6.2 for the design of pressure windows [39]:

$$T_{required} = D \cdot \sqrt{SF \cdot \frac{K}{4}} \cdot \sqrt{\frac{P}{F_a}} \tag{6.2}$$

where $T_{required}$ is the required window thickness in mm, D is the window diameter in mm, SF is the safety factor (suggested in the same document to be equal to 6), K an empirical constant (defined to be equal to 1.1 for unclamped windows), P is the pressure load in N/mm^2 (defined to be equal to 0.1 since the compartment will be kept at sea-level atmospheric pressure, to make sure all payload instruments work correctly) and F_a is the elastic limit of the material in N/mm^2 (taken to be equal to 67 since this is Suprasil's bending strength).

Table 6.6: *Instrument Window Specifications*

Instrument	D_{lens} **(mm)**	D_{window} **(mm)**	$T_{required}$ **(mm)**
UV point spectrometer lens	5	30	1.5
SWIR point spectrometer lens	6	shared with above instrument	
Imager UV	40	63	3.1
Imager SWIR	50	78	3.9
Lidar	80	120	6.0
Long wave radiation sensor	50	-	-
Short wave radiation sensor	40	-	-

Note that the two lenses used for the point spectrometers will share the same window for the sake of simplicity, since they will be placed very close together. Furthermore, the long wave and short wave radiation sensors will not use windows, and will instead have their sensor "poking out" of a hole with the same size. This is considered possible given that their operating temperature goes down to -40°C, and as such it is expected that the temperature of the sensor will not drop below this value given that the main sensor body will remain inside the payload compartment; this then has the advantage that there are no windows to cause any type of interference on the readings from these two instruments.

The "required thickness" column in Table 6.6 ensures the windows will survive the pressure load. Since the maximum window thickness required is 6 mm, all windows will be sized with a 6 mm thickness, for the sake of simplicity. Furthermore, due to thermal conductivity concerns, the windows will be double paned, with two panels of 6 mm thickness each, separated by a 4 mm air gap.

Now that the dimensions of the payload housing compartment have been obtained, it is necessary to calculate the required heat power that will need to be provided by the radiator in order to keep the payload compartment at a temperature of 20°C (which satisfies the operational range of all of the instruments that will need to be kept inside the compartment).

For this, the payload compartment will be modelled as a cylinder, which will then have the following surface area:

$$A_{surface} = 2\pi \cdot R \cdot l + 2\pi \cdot R^2 = 2\pi \cdot 250 \cdot 727 + 2\pi \cdot 250^2 = 1.53 \times 10^6 mm^2 = 1.53 m^2 \tag{6.3}$$

[38] URL: https://www.uqgoptics.com/wp-content/uploads/2019/03/Suprasil.pdf [cited 19/05/2026]

[39] URL: https://www.crystran.com/wp-content/uploads/2025/09/design-of-pressure-windows_1-1.pdf [cited 19/05/2026]

The heat balance of the payload compartment is driven by thermal conduction with the outer skin of the fuselage. As such, it is necessary to determine what the temperature of the fuselage skin will be depending on the altitude and on the time of day (during the day, solar radiation will cause the outer fuselage to heat up more, while during the night this effect is not present). The heat balance must be analysed in two main constraining scenarios: the scenario where outside conditions are as warm as expected during the aircraft's operation, and the aircraft is exposed to sunlight (this will drive overheating concerns and set a maximum allowed thickness for the insulation), and the scenario where the aircraft is in the coldest expected environment, during the night (this will allow to understand the maximum heating power that the heater needs to be sized for).

The heat balance for the fuselage skin is driven by Equation 6.4.

$$\alpha \cdot I \cdot A_{proj} - \epsilon \cdot \sigma \cdot A_{surface} \cdot (T_{skin}^4 - T_{env}^4) - h \cdot A_{exposed} \cdot (T_{skin} - T_{env}) - A_{surface} \cdot \frac{T_{skin} - T_{interior}}{R_{eq}} = 0 \tag{6.4}$$

The first term represents heat power from solar radiation absorption (α is the absorptivity of the skin material, I is the solar irradiance and A_{proj} is the projected area exposed to sunlight); the second term represents heat power lost due to the infrared radiation emitted by the skin (ϵ is the emissivity of the skin material, σ is the Stefan-Boltzmann constant, $A_{surface}$ is the surface area of the fuselage skin, assumed to be equal to the surface area of the payload compartment, T_{skin} is the temperature of the fuselage skin and T_{env} is the temperature of the surrounding environment); the third term represents heat power lost due to convection with the outside air (h is the convective heat transfer coefficient and $A_{exposed}$ is the surface area exposed to the outside air); the last term represents heat absorbed/lost due to conduction with the interior of the compartment ($T_{interior}$ is the temperature inside the compartment and R_{eq} is the thermal resistance of the interior compartment).

Going back to Equation 6.4, there are two parameters that need to be calculated separately: R_{eq} and h. R_{eq} is influenced by the thermal conductivity and thickness of both the windows and the insulation as seen in Equation 6.5.

$$R_{eq} = \frac{1}{\frac{f_1}{R_1} + \frac{f_2}{R_2}} \tag{6.5}$$

Where f_1 is the fraction of surface area of the compartment covered by insulation, R_1 is the thermal resistance of the insulation (taking into account its thickness and thermal conductivity), f_2 is the fraction of surface area of the compartment covered by windows and R_2 is the thermal resistance of the windows (taking into account the fact that they are double-paned).

As for h, it is calculated using the following procedure [40] considering laminar flow over flat plates. Firstly, the Reynolds number is calculated using Equation 6.6.

$$Re = \frac{\rho \cdot V \cdot L}{\mu} \tag{6.6}$$

Where ρ is the outside air density, V is the airspeed, L is the characteristic length of the compartment and μ is the dynamic viscosity of the outside air. This allows to calculate the Nusselt number, for which the formula is visualised in Equation 6.7 (assuming that, for effects of convective cooling, the outer skin behaves as a flat panel).

$$N_u = 0.664 \cdot \sqrt{Re} \cdot P_r^{1/3} \tag{6.7}$$

Where P_r is the Prandtl number of the outside air. The convective heat transfer coefficient h can then be obtained using Equation 6.8.

$$h = \frac{N_u \cdot \lambda_{air}}{L} \tag{6.8}$$

Where λ_{air} is the thermal conductivity of the outside air.

Then, with the value obtained for the skin temperature, it is possible to calculate the heat required to maintain the interior of the compartment at the intended temperature with Equation 6.9.

$$Q_{required} = A_{surface} \cdot \frac{T_{interior} - T_{skin}}{R_{eq}} \tag{6.9}$$

As such, at this stage there are three variables that can be controlled in the design: the thickness of the insulation t, and the absorptivity α and the emissivity ϵ of the outer skin, which can be controlled by the chosen coating for the outer skin.

[40] URL: https://www.mikrocontroller.net/attachment/2415/convection_coeff.pdf [cited 21/05/2026]

A Python script was developed considering all of the above equations. This script takes the three user inputs defined above, numerically calculates the value of T_{skin}, for both day and night conditions, and then returns the heat required to be supplied/taken away from the payload compartment during both day and night conditions.

It was found that having an outer skin coating with the minimum possible values of absorptivity α and emissivity ϵ is beneficial for both preventing the payload compartment from overheating during the day and losing heat during the night. Following a chapter of the book "Spacecraft Thermal Control Handbook" by Gilmore et al. [52], which showcases emissivity and absorptivity of different commonly used coatings in aerospace applications, it has been decided to choose a coating of **FSS-99 overcoated silver**, since it has the lowest values for these two coefficients, with $\alpha = 0.03$ and $\epsilon = 0.02$.

Then, the insulation was sized such that the compartment does not overheat during the day, when flying at the highest expected external environmental temperature. This returned a maximum insulation thickness of 15 mm. The fact that the payload instruments stored inside the compartment need a total of 145 W of power, which eventually gets converted into heat, was also taken into account (considering the aircraft's payload instruments only operate during the day for the sake of saving power).

Considering this, when flying at the lowest environmental temperature (which as previously discussed will be -80°C), the UAV will require 45 W of heating during the day and 193 W during the night (during the day there is much less additional heating required since the payload instruments inside the compartment also produce heat, as mentioned earlier).

This results in the following most constraining values for total required power by the payload during operations (considering both the payload instruments power and the additional heating power): 202 W of total power during the day and 193 W during the night. The total power required during the night actually ends up lower than during the day, since during the night all payload instruments are turned off, including the ones not inside the heated compartment, which means the required power during the night is purely the one associated with heating the payload compartment.

If during operations the environmental conditions change from these most extreme conditions, such that the outside temperature, air density or solar radiation change, the radiator output will need to be adjusted considering these changes.

As for the pressurization of the compartment, a document by Glenair [53] suggests that typical aerospace hermetic connectors should have a leak rate of no more than $1 \times 10^{-7} atm \cdot cc/s = 1 \times 10^{-7} mbar \cdot L/s$. Assuming the pressurized payload compartment will be built according to these specifications, this results in a total air volume lost described in Equation 6.10.

$$V_{lost} = \frac{\text{leak rate} \cdot t}{P} \tag{6.10}$$

Where t is the time in seconds and P is the pressure in mbar. Over a mission of 60 days, $t = 5.184 \times 10^6$ s. Considering the payload compartment will be kept at sea-level pressure, this results in $V_{lost} = 0.512$ mL

This value is negligible, as such we can assume the payload compartment can be pressurized before the mission and it should hold the pressure throughout, so there is no need to design a system capable of re-pressurizing the compartment during the mission.

6.9. Final Overview

To summarize the main outcome of this chapter, a table with final mass, power requirement (considering both heat power and payload instruments power) and cost overview for the payload subsystem can be seen in Table 6.7.

Table 6.7: *Final Payload Parameters*

Parameter	Value
Total Mass	26 [kg]
Max Power Required (day)	202 [W]
Max Power Required (night)	193 [W]
Total Cost	327,000 [€]

Additional payload instruments that have not yet been addressed in this chapter include a simple temperature sensor to monitor the temperature inside the payload housing compartment, and a pitot tube which will be attached outside the aircraft, providing pressure readings to allow the aircraft to measure its airspeed.

7

Aerodynamics

Aircraft design is centred on aerodynamics, aiming at providing the necessary lift to overcome weight with the minimum drag penalty. In this chapter, the aerodynamic design of the wing is discussed, including 2D analysis and 3D performance estimation. Furthermore, additional drag estimations are performed on the tail, fuselage and propulsion system. The total drag and propulsive power required are calculated and used for sizing of both the propulsion and power systems. Finally, a verification and validation section is included.

7.1. Aerodynamics Requirements

The aerodynamic design and analysis are essential steps needed to proceed with the design, following the payload mass and power requirements. Top level requirements from stakeholders set the first constraints on the design, EQ-STK12-MIS02-SYS01 specifies the wing span to ensure global operation capabilities, while REQ-STK04-MIS01-SYS01 sets the maximum cruise altitude. From the international standard atmosphere, the air density at the maximum altitude can be found to be 0.03947 [Kg/m^3], around 3% of the sea-level value.

The wing design inputs are summarized in Table 7.1, while Table 7.2 contains further necessary inputs to estimate total drag and power required.

Table 7.1: *Wing Design Inputs*

Symbol	Value	Unit	Rationale
b	36	[m]	REQ-STK12-MIS02-SYS01
AR	22	[-]	High performance aspect ratio
h_{max}	25000	[m]	REQ-STK04-MIS01-SYS01
λ	0.8	[-]	Efficient lift distribution
C_L	1.4	[-]	Design lift coefficient

Table 7.2: *Analysis Input*

Symbol	Value	Unit	Rationale
C_{D_f}	0.1	[-]	Streamlined shape [54]
d_f	0.5	[m]	From Chapter 6
k_f	0.8	[-]	High turbulence ratio due to wing-fuselage interactions
S_{wet}	9.87	[m^2]	From Chapter 8
C_{D_p}	0.015	[-]	From literature [55]
S_h/S	0.3	[-]	From literature [56]
V_h/V	0.95	[-]	From literature [56]
$d\epsilon/d\alpha$	0.2	[-]	From literature [56]
N_p	4	[-]	From Chapter 9
R_p	0.6	[m]	From Chapter 9

7.1.1. Airfoil Selection

A 2D airfoil needs to be selected before designing the entirety of the wing. Multiple airfoils were considered, found from literature [57] [58] and using a design tool [1], with focus on low Reynolds number and high lift coefficients. The analysed airfoils were: E423, MH114, S1223, SD7080 and MH 38 9.68%, compared at a Reynolds number of 2.25E+05 and a cruise Cl = 1.4, as shown in Figure 7.1. XFLR5 was utilized to compare the selected airfoil. This computational tool utilizes `XFOIL` for 2D aerodynamic analysis and includes a 3D solver for more detailed analysis.

The airfoil that performs the best on the endurance factor (${C_l}^3/{C_d}^2$) is selected, based on the analysis [59]. At the selected required lift coefficient and Reynolds number, the MH114 airfoil performed the best. Furthermore, this airfoil outperforms the others at a range of lift coefficients, allowing for design iterations with variation of the required lift coefficient and Reynolds number.

[1] URL: http://airfoiltools.com/ [cited 20/05/2026]

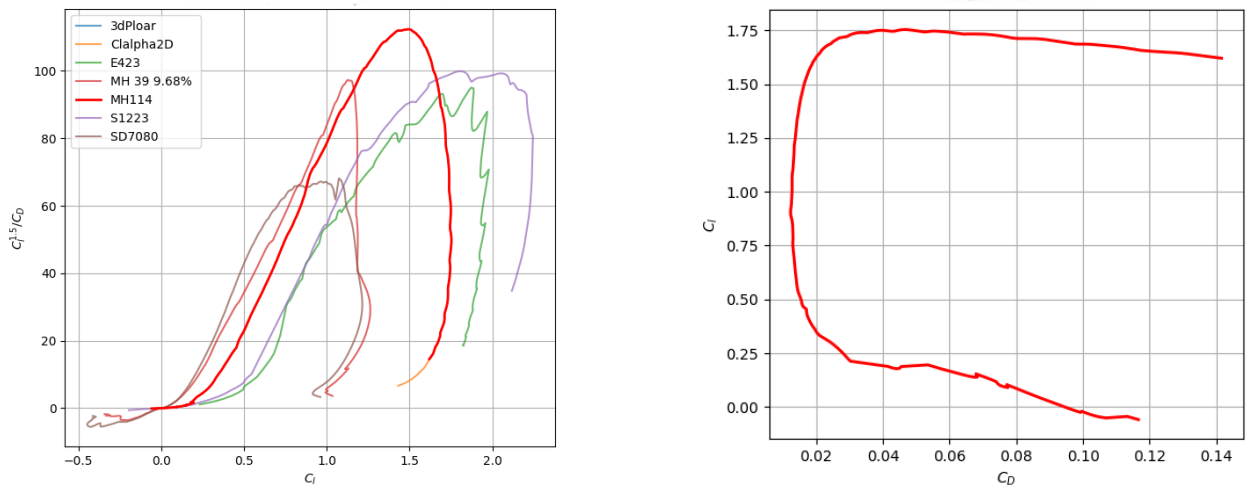

(a) $C_l^{1.5}/C_d$

(b) $C_l - C_d$

Figure 7.1: *Aerodynamic Analysis*

7.2. Wing Design

The design of the wing is broken down into 2D analysis and 3D analysis. To perform the calculations and analysis, a Python tool was created, relying on `XFOIL` to determine the performance of the selected airfoil at different flight operations. A concise flowchart, shown in Figure 7.2, goes over the main logic performed by the tool.

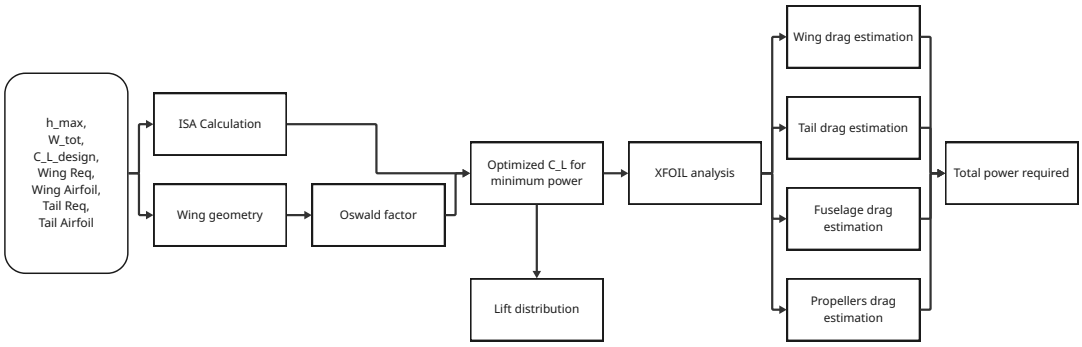

Figure 7.2: *Aerodynamics Flowchart*

Firstly, additional parameters must be calculated. These are presented in Table 7.3 using the relations shown in Equation 7.1.

$$
\begin{aligned}
S &= \frac{AR^2}{b}, \\
c_r &= \frac{2S}{b(1+\lambda)}, \\
c_t &= \lambda c_r, \\
\text{MAC} &= \frac{2}{3} c_r \frac{1+\lambda+\lambda^2}{1+\lambda}, \\
V_{cruise} &= \sqrt{\frac{2W}{\rho S C_L}}, \\
Re_{MAC} &= \frac{\rho \cdot V_{cruise} \cdot \text{MAC}}{\mu}
\end{aligned}
\tag{7.1}
$$

Table 7.3: *Calculated Parameters*

Parameter	Value	Units
S	58.9	[m^2]
c_r	1.81	[m]
c_t	1.45	[m]
MAC	1.64	[m]
V_{cruise}	36.55	[m/s]
Re_{MAC}	1.569e+05	[-]

7.2.1. Oswald Efficiency Factor

Once the airfoil is selected and the main geometry of the 3D wing is determined, the wing Oswald factor, e, can be estimated. The Oswald factor is a measure on how closely the lift distribution of a 3D wing matches with an elliptical lift distribution, the most efficient distribution to reduce induced drag. A formula to approximate the Oswald efficiency factor, shown in Equation 7.2, was found from literature [60], being specifically used for wings with taper ratios between 0.3 and 1, and valid with $AR \cdot \beta$ between 6 and 30, where β is the compressibility correction factor.

$$e = \frac{1}{1+\delta}, \quad \delta = \left(0.0015 + 0.016\,(\lambda - 0.4)^2\right)(AR \cdot \beta - 4.5), \quad \beta = \sqrt{1 - M^2} \tag{7.2}$$

7.2.2. Airfoil to Wing

The transitions from a 2D airfoil to a 3D wing are essential to properly compute and analyse, as they differ based on the geometry and efficiency of the wing design. To account for this, multiple steps and corrections are implemented. Firstly, the optimum lift coefficient for minimum power is calculated. This is done by calculating the profile and induced drag for every lift coefficient from 0 to 1.7 using `XFOIL`, and then recalculating the required cruise speed to provide the necessary lift. Using the newly calculated cruise velocity and drag, from Subsection 7.2.4, the required power can be calculated, and the C_L that requires the lowest power can be found. Secondly, the required 2D lift coefficient C_l is calculated, assumed to be 10% higher than the required wing C_L due to losses [57]. This required airfoil C_l is then used to calculate both the profile and the induced drag with the found Oswald factor and aspect ratio. Finally, the $C_{l-\alpha}$ and $C_{m-\alpha_{ac}}$ slopes found from `XFOIL` are corrected for a 3D wing utilizing the correction shown in Equation 7.3

$$C_{M-\alpha_{ac}} = C_{m-\alpha_{ac}} \frac{AR}{AR+2}, \quad C_{L-\alpha} = \frac{C_{l-\alpha}}{1 + \frac{C_{l-\alpha}}{\pi AR e}} \tag{7.3}$$

7.2.3. Wing Lift Distribution

Calculating the lift distribution over the wing span is essential to design the wing structure. Due to a non elliptical lift distribution, it needs to be approximated utilizing other methods. One option considered was to use computational fluid dynamics (CFD), but due to it being computationally intensive and time consuming it was chosen to utilize Schrenk's method [61]. This method has shown a 3% lift force error from CFD simulations, proving its use in preliminary UAV design. Schrenk's method approximates the lift distribution by averaging the chord distribution. The difference between the elliptical lift distribution and the chord distribution, the Schrenk's lift distribution, can be seen in Figure 7.3. As extra verification, Schrenk's lift distribution was integrated over the span to find the total half wing lift. This resulted in the calculated lift being off by 0.019% from the actual half span lift, showcasing the accuracy of this method.

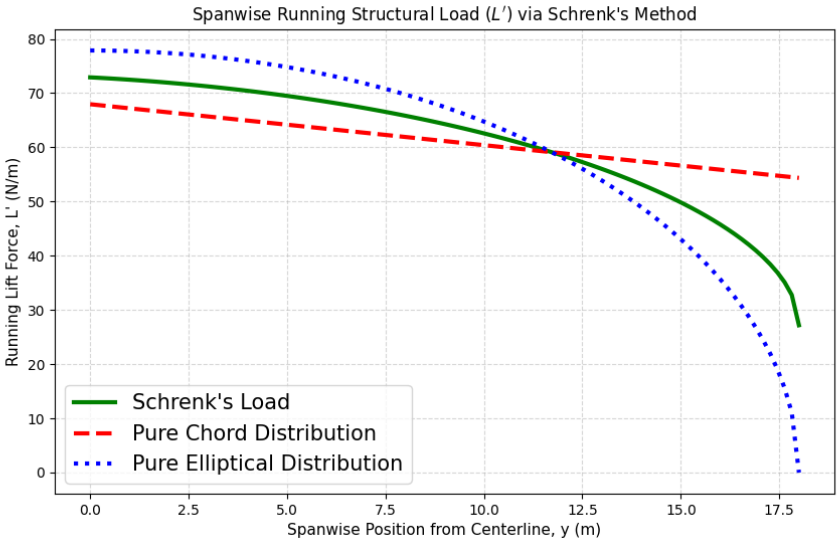

Figure 7.3: *Schrenk's Lift Distribution*

7.2.4. Wing Drag Estimation

To calculate the drag of the wing, both the profile drag and the induced drag have to be calculated. The profile drag is calculated utilizing XFOIL at the required C_l of the airfoil, from the $C_l - C_d$ graph shown in Figure 7.1b. To calculate the induced drag, it was decided to utilize a parabolic drag approximation, shown in Equation 7.4, using the total wing C_L. The total wing drag can then be computed as the sum of the profile and induced drag, multiplied by the dynamic pressure, as in Equation 7.5.

$$C_{d,i} = \frac{C_L^2}{\pi ARe} \tag{7.4}$$

$$D = \left(C_{d,0} + C_{d,i}\right) \frac{1}{2} \rho V_{cruise}^2 S_w \tag{7.5}$$

The final wing design can then be summarized into Table 7.4

Table 7.4: *Final Wing Design & Performance*

Parameter	Value	Units
b	36	[m]
AR	22	[-]
λ	0.8	[-]
S	58.9	[m^2]
MAC	1.64	[m]
Airfoil	MH114	[-]

Parameter	Value	Units
e	0.93	[-]
$C_{L,opt}$	1.38	[-]
C_D	0.049	[-]
$C_{L-\alpha}$	6.71	[1/rad]
$C_{M-\alpha_{ac}}$	-0.1645	[1/rad]
D	77.8	[N]
V_{cruise}	36.6	[m/s]
Re_{MAC}	1.569e+05	[-]

7.2.5. Additional Drag Estimation

To calculate the total power required for cruise, the drag of other elements needs to be accounted for. In the following section the estimation on tail, fuselage and propeller drag is explained.

Tail

From Chapter 12 the tail airfoil, size and geometry are known, respectively NACA0012, $S_h = 7.69$ [m^2] and $\text{MAC}_{\text{tail}} = 1.24$ [m], as well as the wing-tail interactions, $V_h/V = 0.95$. From these inputs, the velocity reaching the tail and the tail Reynolds number can be calculated from Equation 7.6.

$$V_h = \frac{V_h}{V} V, \quad Re_{\text{tail}} = \frac{\rho \cdot V_h \cdot \text{MAC}_{\text{tail}}}{\mu} \tag{7.6}$$

XFOIL is then used once again to perform an analysis on the tail airfoil at the required cruise lift coefficient. By analysing the drag polar, the profile drag of the tail can be estimated. Assuming for cruise conditions the tail will be providing a small amount of lift, either positive or negative, the induced drag can be considered negligible.

Fuselage

Another large contributor to the total drag of the aircraft is the fuselage, which has a maximum cross sectional area of 0.79 m^2, due to the payload bay as described in Section 6.8. The total drag of the fuselage is a factor of the shape or pressure drag and the skin friction drag. The first can be estimated from literature [54], where a drag coefficient of a streamlined object in reference to the cross sectional area is estimated to be $C_D = 0.04$ for $Re > 10^5$. Due to imperfect streamlined shape of the real fuselage, caused by wing-fuselage interaction, communication system radome and tail-fuselage interaction, the assumed drag coefficient was set as $C_{D,\text{pressure}} = 0.1$. To calculate the skin friction drag, laminar flow was assumed on 20% of the fuselage, with the remaining 80% being turbulent. This turbulent to laminar flow division is due to the wing-fuselage interaction disturbing the flow, and thus inducing turbulence. The skin drag was then evaluated with coefficients found in Equation 7.7, and scaling them accordingly to the flow division. The total drag was then evaluated from $D = C_{D,\text{skin}} \frac{1}{2} \rho V^2 S_{wet}$, where S_{wet} equals the wetted area of the fuselage, derived in Chapter 8.

$$C_{d,\text{laminar}} = \frac{1.328}{\sqrt{Re}}, \quad C_{d,\text{turbulent}} = \frac{0.074}{Re^{0.2}}, \quad C_{D,\text{skin}} = 0.8 C_{d,\text{turbulent}} + 0.2 C_{d,\text{laminar}} \tag{7.7}$$

The total fuselage drag is then:

$$D_f = C_{D,\text{fus}} \frac{1}{2} \rho V^2 S_{\text{wet}}, \qquad C_{D,\text{fus}} = C_{D,\text{pressure}} + C_{D,\text{skin}} \tag{7.8}$$

Propellers

The last contributors to drag are the propellers, because the blades are perpendicular to the airflow, drag is produced even when forward thrust is generated. The $C_{d,\text{prop}}$ was estimated from literature to be $C_{d,\text{prop}} = 0.015$ [55]. This value, combined with the radius for each propeller and the number of propellers from Chapter 9, can be used to determine the total drag of the propellers. The disk area is derived from the radius, $A_{\text{prop}} = \pi \cdot r_{\text{prop}}^2$

$$D_{\text{prop}} = C_{d,\text{prop}} \frac{1}{2} \rho V^2 A_{\text{prop}} n_{\text{prop}} \tag{7.9}$$

Total Aerodynamic Power Required

The required aerodynamic power is used to design the propulsion and power systems. This can be obtained by multiply each drag value by its corresponding velocity, as seen in Equation 7.10, resulting in a total final power of 3.1 kW. The breakdown of each component contirbution to the total drag and power is found in Table 7.8

$$P_{\text{req}} = D_w \cdot V_{\text{cruise}} + D_f \cdot V_{\text{cruise}} + D_{\text{prop}} \cdot V + D_{\text{tail}} \cdot V_h \tag{7.10}$$

7.3. Verification and Validation

As a coding tool was used to perform the aerodynamics analysis, proper code verification and validation was needed to ensure the tool behaved as expected. Verification consisted of comparing tool output to hand calculated values in mock scenarios to ensure correct implementation of the formulas. Validation focuses on checking if the tool is performed using the right logic, by comparing the final aerodynamic design with a solar powered plane.

7.3.1. Verification

Two types of verification were performed, one was code verification, focusing on the correct implementation of the formulas in the tool. The second was a comparison of the analysis with `XFLR5`, under the same flight conditions.

Code Verification

The python package `pytest` was used, by means of mock inputs and hand calculations performed in `Excel`. The resulting tests are summarized in Table 7.5. Because all the performed test passed, it can be said that the Aerodynamics code is verified at function level.

Table 7.5: *Aerodynamics Module Verification and Unit Test Summary*

Test Suite / Component	Tests Executed	Passed	Status
TestGeometry	5	5	PASSED
TestFlightMechanics	7	7	PASSED
TestAerodynamicCoefficients	4	4	PASSED
TestXfoilPolarAnalysis	4	4	PASSED
TestInterpolateAtCl	4	4	PASSED
TestHighLevelPipeline	1	1	PASSED
Total	**25**	**25**	**100%**

To verify `XFOIL` import functions no test were run, as the tool actually running `XFOIL` was a test by itself.

XFLR5 Verification

The tool's analysis output was compared against `XFLR5` Vortex Lattice Method (VLM), a validated tool for initial aircraft design [62]. This comparison was made to ensure key parameters were in the same order of magnitude and following the correct trend. To ensure fair comparison, only wing parameters are compared in Figure 7.6, and the results show an accurate tool, with a maximum error being 0.57%. This proves the correctness of the tool while reducing computational time and allowing easy integration in the python environment.

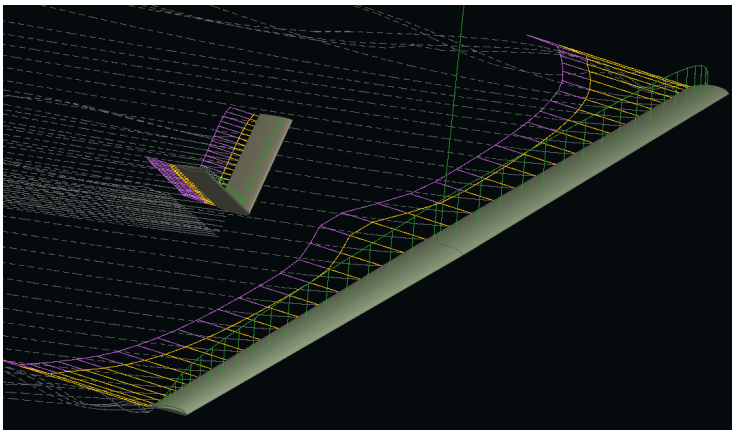

Figure 7.4: *XFLR5 Plane Analysis*

Table 7.6: *Compared Parameters*

Parameter	Tool	XFLR5
C_L	1.37	1.37
$C_{D,wing}$	0.049	0.05
e	0.93	0.94
L/D_{wing}	27.96	27.8

7.3.2. Validation

Validation consists of comparing the results to real test data, so it is usually performed at a later stage in the design process. Some preliminary validation can still be performed, by comparing results to similar, real world values. The PhD thesis of Philipp Oettershagen was used as a comparison, as it recaps the design stages and testing of a hand launched solar powered UAV [63]. The results are compared and summarized in Table 7.7, by first listing the inputs to highlight the main differences of the aircraft such as, surface area and weight. It can be determined that the values for SORA are comparable to the Atlaktick Solar plane, increasing the validity of the tool. Furthermore, `XFOIL` has been externaly validated and compared to CFD analysis, in the high lift low Reynolds number regime [64].

Table 7.7: *Validation Comparison*

INPUTS		
Parameter	**SORA**	**Atlantik Solar**
b [m]	36	5.69
MAC [m]	1.64	0.305
S [m^2]	58.91	1.73
M_tot [Kg]	218.5	6.93
V_cruise [m/s]	36.55	8.6
V_stall [m/s]	32.47	7.4
P_out [W]	3108	28.98
rho [Kg/m^3]	0.0395	1.225

COMPARISON		
Parameter	**SORA**	**Atlantik Solar**
AR	22	18.7
W/S	36.4	39.2
W/P	0.69	2.35
L/D	25.2	20.2
C_D	0.055	0.043
C_L	1.38	0.86
C_L_max	1.75	1.17
e	0.93	0.92

7.4. Aerodynamics Conclusion

The goal of the aerodynamic analysis was to produce a power required for cruise to size the power and propulsion systems. A breakdown of the power required for the aircraft, accounting for the wings, tail, fuselage and propellers is found in Table 7.8.

Table 7.8: *Drag and Power Breakdown*

Elements	Drag [N]	Power [W]
Wing	77.8	2844
Tail	2.9	102
Fuselage	2.7	97
Propulsion	1.8	65
Total	**85.2**	**3108**

8

Structures and Materials

This chapter encompasses many essential aspects of the aircraft design and gives a more complete picture of what the UAV will look like. First, it involves defining the loads the wing and fuselage are expected to experience during the mission in Section 8.1 and Section 8.2. Next, these loads must be integrated into the design, the wing spar in Section 8.4 and fuselage in Section 8.5 must both balance weight considerations with structural integrity. The methods used to attain the designs are verified and validated in Section 8.7 and the final mass estimates for each component - wing, tail and fuselage - are listed in Section 8.8.

8.1. Flight Envelope

The flight manoeuvre diagram defines the aircraft's operational constraints and limits. A conservative initial cap is set for the load factor at +2.5 g and -1 g which leads to an upper and lower boundary. The stall speed calculated from the $C_{L_{max}}$ creates a left boundary and the dive speed-which is calculated empirically is the right boundary with an additional never-exceed speed is also placed to ensure a margin of safety. The velocity (V) and load factor (n) are related as follows:

$$V = V_{stall}\sqrt{n} \tag{8.1}$$

All velocities are then translated into indicated airspeed values by multiplying by the factor $\sqrt{\frac{\rho}{\rho_0}}$. Each of these lines then creates an envelope within which it is safe to fly.

The gust loading diagram is also necessary to account for gust and wind loading encountered during cruise. In [65] the most extreme gusts (U_{de}) the aircraft might encounter in its flight profile are around 6 m/s. The change in loading factor (Δn) can then be calculated with the following formula where W_s is the wing loading, ρ is air density and V is velocity and a is the slope of the wing lift curve.

$$\Delta n = \frac{\rho V a U_{de}}{2W_s} \tag{8.2}$$

Lastly, these two graphs are combined and the most conservative flight envelope (outer boundary) is taken which is shown in Figure 8.1.

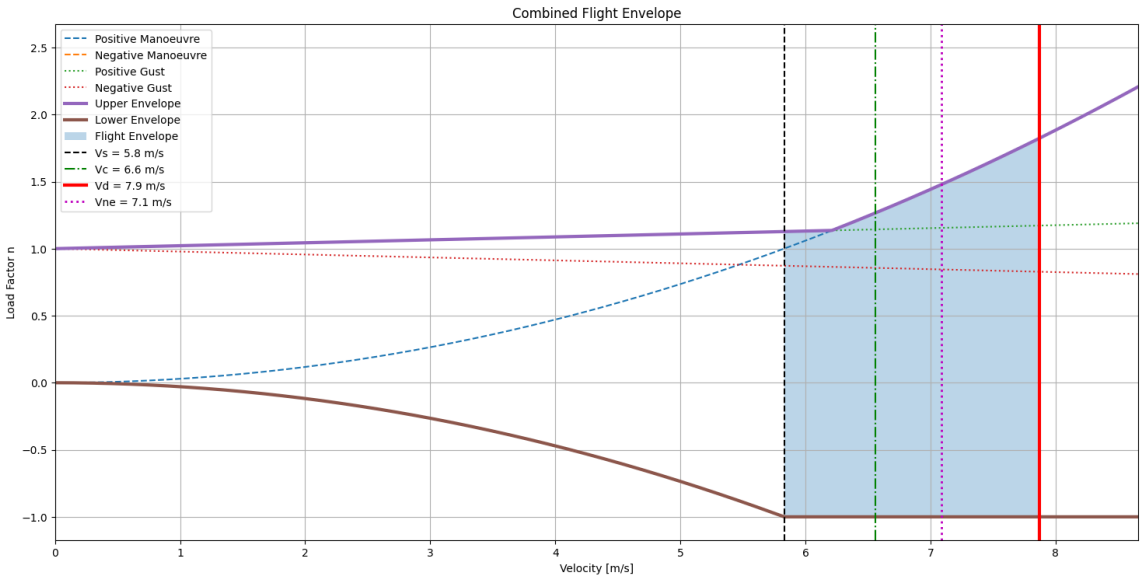

Figure 8.1: *Combined Flight Envelope*

8.2. Internal Loading

In order to allow sizing of the aircraft's wing structure, it is necessary to understand what is the internal loading that it will be subjected to, and, for this, the internal loading diagrams need to be created. For reference on interpreting

these diagrams, the coordinate system used is: positive x-axis pointing towards the tail of the aircraft, positive y-axis pointing down and positive z-axis pointing towards the right wing tip.

8.2.1. Internal Loading Equations

There are five different loading scenarios that should be considered: vertical shear force V, moment around the x-axis M_x, torque T, horizontal shear force H, and moment around the y-axis M_y.

Internal Vertical Shear Force V

Starting with the vertical shear force, its distribution $V(z)$ along the half wing span will follow Equation 8.3:

$$V(z) = -\int_z^{b/2} w(z)\,dz - P\left(1 - u_{z_1}(z)\right) \tag{8.3}$$

where $w(z)$ is the distributed vertical load along the span (accounting for the distributed lift and weight of the wing structure, solar panels and batteries, which will be stored inside the wing), and P are the point vertical loads acting along the span (which will be due to weight of the engines), with $u(z_1)$ being the heaviside function that allows the contribution of these point loads to be calculated at the right location.

Internal Out-Of-Plane Bending Moment M_x

The out-of-plane bending moment distribution $M_x(z)$ along the half wing span is governed by Equation 8.4:

$$M_x(z) = \int_z^{b/2} V(z)\,dz \tag{8.4}$$

where $V(z)$ is the vertical shear force distribution.

Internal Horizontal Shear Force H

The horizontal shear force distribution $H(z)$ along the half wing span will follow Equation 8.5:

$$H(z) = -\int_z^{b/2} D(z)\,dz - T\left(1 - u_{z_1}(z)\right) \tag{8.5}$$

where $D(z)$ is the distributed drag along the span, and T are the point horizontal loads acting along the span, due to the thrust of the engines.

Internal In-Plane Bending Moment M_y

The in-plane bending moment distribution $M_y(z)$ follows Equation 8.6:

$$M_y(z) = \int_z^{b/2} H(z)\,dz \tag{8.6}$$

where $H(z)$ is the horizontal shear force distribution.

Internal Torque T

Finally, the internal torque distribution is calculated according to Equation 8.7:

$$T(z) = -\int_z^{b/2} \left[w(z') \cdot d(z') + t(z')\right] dz' - \sum_{i=1}^{n} \left(T_i \cdot y_{T,i} + W_{\text{engine},i} \cdot d_{2,i}\right) \cdot u_{z_{e,i}}(z) \tag{8.7}$$

where $w(z)$ is the distributed vertical load due to lift and weight, $d(z)$ is the distance from the point where this load acts (assumed to be at the quarter chord of the wing) and the flexural axis of the wing (for which the spanwise location of the shear centre of the wing cross-section needs to be determined), $t(z)$ is the distributed torque caused by the aerodynamic pitching moment of the wing, T_i is the thrust of each engine, which contributes to the torque due to the vertical offset $y_{T,i}$ from the wing and $W_{engine,i}$ is the weight of each engine, which contributes to the torque due to horizontal offset from the wing.

Load Factor Considerations

Some terms in the equations above will require taking into account the load factors the UAV will be subjected to depending on manoeuvres and gust loads, taken from the flight envelope explained in Section 8.1. Considering this flight envelope, the critical operational scenarios that should be incorporated in the loading diagrams are the ones with the biggest positive and negative load factors, in combination with the biggest velocity (which results in the biggest dynamic pressure). As such, the scenarios that shall be tested are: cruise with a load factor $n = -1$, cruise with a load factor $n = 2.5$ and dive with a load factor $n = 2.5$. The flight envelope may not reach such high values of

load factor, depending on the global iteration procedure of the whole aircraft design, so these load factor values were taken conservatively, since in any case it is not expected the aircraft will ever reach higher load factors than these.

Furthermore, unlike more conventional aircraft, this UAV will not use High-Lift-Devices, which if used would modify the span-wise lift and moment distributions during take-off and landing, and, as such, there is no need to separately consider take-off or landing configurations.

8.2.2. Loading Diagrams

The internal loading equations were all integrated into the wing box sizing Python script, which will be further explained in Section 8.4. Considering the final converged design, this resulted in the loading diagram for cruise at $n = 2.5$ shown in Figure 8.2 (the other loading diagrams, for cruise with $n = -1$ and dive with $n = 2.5$, were also analysed, but not included).

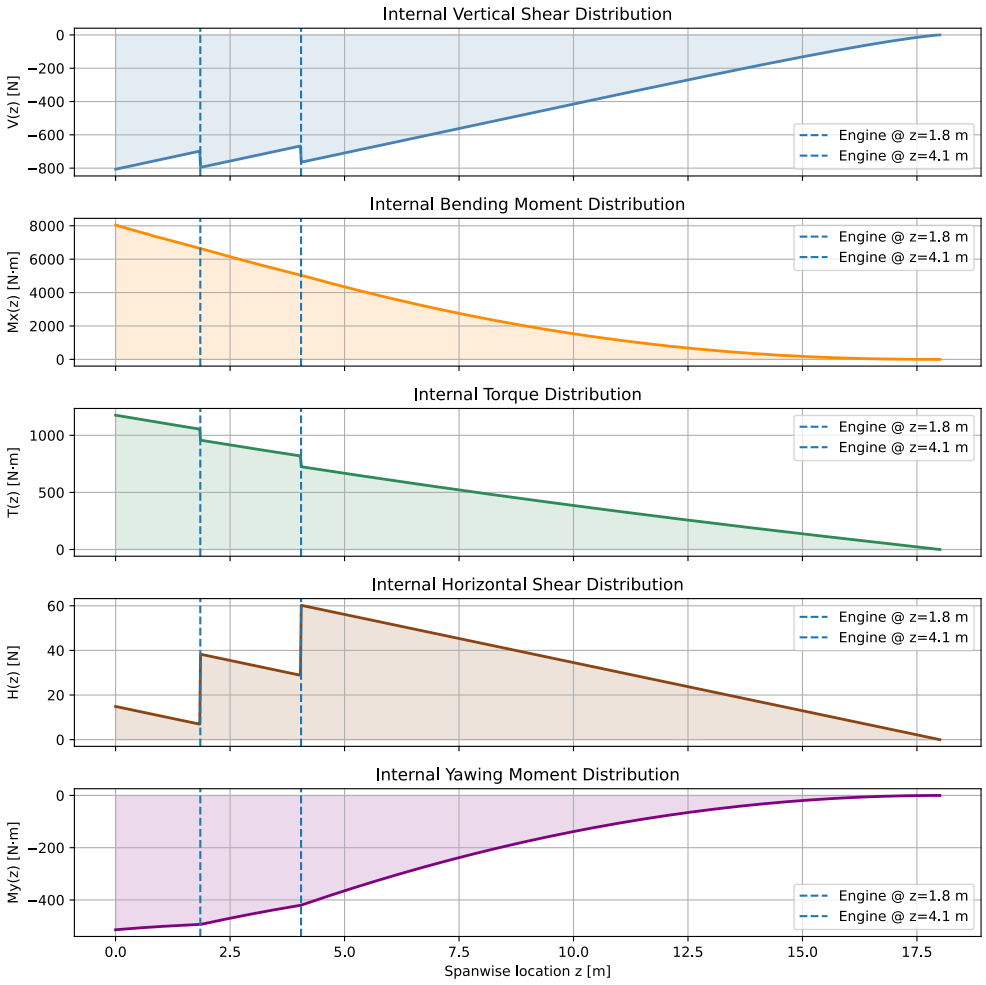

Figure 8.2: *Internal Loads at Cruise with $n = 2.5$*

8.3. Material Selection

There are several material options which are both lightweight and very strong. Initial calculations were performed using CFRP as the primary material for the fuselage, wing spar, and tail. However, following **REQ-STK26-MIS01** the aircraft must be 50% recyclable, therefore, several more sustainable alternatives were taken into account, focusing on minimizing performance loss. The explored materials are shown in Table 8.1, they include thermoplastic CFRP and Galvorn, a novel material. While both recyclable options show slightly lower mechanical performance it is not enough to impact the design significantly.

Table 8.1: *Material Options*

Material	Density (kg/cm^3)	Young's Modulus (GPa)	Tensile Strength (MPa)	Result
CFRP	1720	230	3400	1 [66]
CFRTP	1500	140	2500	3 [67]
Galvorn	1300	200	2400	2[1]

Table 8.2: *Properties of Galvorn*

Property	Value
Tensile Strength	2400 [MPa][1]
Compressive Strength	400 [MPa] [68]
Shear Strength	69 [MPa] [69]
Young's Modulus	200 [GPa] [1]
Density	1300 [kg/cm^3] [1]

The final selected material is the second ranked Galvorn. It is a newly developed composite made up of packed and aligned CNF (Carbon Nanotube Fibres), it does not corrode and has a long lifetime under repeated loading and as such is perfect for a HALE mission. It is a very efficient load carrying material which reduces material need and as a result is more sustainable[2] .Lastly, it is easily recyclable with no material quality degradation.

Since values for the compressive and shear strength were not available on the datasheet[1] they were inferred from research on CNF's [68],[69].

Other materials to be used in the aircraft include Mylar for the wing skin, CFRP honeycomb for the wing ribs, suprasil300 for the windows, and silica aerogel for insulation where required. Apart from their mechanical properties, these materials are fire-resistant, so they also ensure compliance with **REQ-STK24-MIS06-SYS02**.

8.4. Wing-Box Design

Now that the internal loading that the wing will be subjected to is known, the structural elements of the cross-section of the wing box shall be designed and optimised to ensure they can support these internal loads.

There were two main wing box geometries considered for the design. The first one was a geometry as commonly used by conventional aircraft, with front and rear I-beam spars, connected by load carrying skin on the top and the bottom to complete the wing-box shape, and fitted with stringers and ribs to increase the load carrying capabilities of the wing box. The second wing box geometry was inspired by the one showcased in a paper by Frulla et al. [70], regarding a research project aimed at designing a HALE solar-powered UAV, using a wing box fitted with a single cylindrical spar to carry all internal loads, with the wing skin and ribs purely serving to maintain the aerodynamic shape of the wing.

Early on in the design process for the wing box it was found that the loads that the UAV will be subjected to are small enough such that a single load-carrying cylindrical spar manages to fulfil the structural performance requirements while having mass values similar to the ones of the conventional wing box with stringers. Considering that the design and later manufacturing of a single cylindrical spar is much simplified when compared to the conventional wing box with stringers, it was decided to proceed with this design option, and all of the calculations explained below will then be regarding a wing box using a main cylindrical spar and non-load carrying ribs and skin.

Furthermore, the wing box will also have a rear spar responsible only for carrying the loads caused by the ailerons which will be attached to this spar. Lastly, while the Mylar wing skin will not be carrying any structural loads, it must be sized considering the continuous tension that it will have to be subjected to in order to avoid sagging due to the pressure differences its surface will be exposed to.

8.4.1. Applied Stresses

Main Spar

The main spar will be subjected to two types of stresses: tensile/compressive stress due to bending loads, and shear stress due to the shear force and internal torque loads. The equation that determines the tensile/compressive stress at a certain spanwise position of the wing is Equation 8.8:

$$\sigma_z = \frac{\left(M_x I_{yy} - M_y I_{xy}\right) y + \left(M_y I_{xx} - M_x I_{xy}\right) x}{I_{xx} I_{yy} - I_{xy}^2} \tag{8.8}$$

since the spar is symmetrical, its product moment of inertia is zero, which means that the equation simplifies to

$$\sigma_z = \frac{M_x}{I_{xx}} y + \frac{M_y}{I_{yy}} x$$

[1] URL: https://dexmat.com/wp-content/uploads/DexMat_solution-overview-digital.pdf [cited 04/06/2026]
[2] URL: https://dexmat.com/wp-content/uploads/DexMat_Galvorn-Spec-Sheet-1.pdf [cited 04/06/2026]

with M_x and M_y being obtained from the internal load diagrams, x and y being the distances of a certain point of the cross-section in relation to its centroid, and I_{xx} and I_{yy} having the same value, considering the spar is cylindrical, and being calculated according to Equation 8.9.

$$I = \frac{\pi}{4}(R_{outer}^4 - R_{inner}^4) \tag{8.9}$$

As for the shear stress that the spar will experience, it is divided into two types: shear stress due to the vertical internal shear force, and shear stress due to torque. The shear stress due to the internal shear force is calculated with Equation 8.10:

$$\tau_{shear} = \frac{S \cdot Q}{I_{xx} \cdot t_{eff}} \tag{8.10}$$

where S is the internal vertical shear force, t_{eff} is the effective shear carrying thickness of the spar ($t_{eff} = 2t_{wall}$ since the shear will be divided between the two walls of the cylinder) and Q is the first moment of inertia of the cylindrical spar, calculated according to Equation 8.11.

$$Q = \frac{2}{3}(R_{outer}^3 - R_{inner}^3) \tag{8.11}$$

Considering the shear stress due to the internal torque, it will follow Equation 8.12:

$$\tau_{torque} = \frac{T}{2 \cdot t \cdot A_{encl}} \tag{8.12}$$

with T being the internal torque, t being the wall thickness of the spar and $A_{encl} = \pi R_{inner}^2$ being the enclosed area. These two shear stress contributions shall be added up, to obtain the overall maximum shear stress the spar cross-section will be subjected to at a certain span-wise position.

Rear Spar

Apart from the main spar, which carries all main loads, the wing will need to include a rear spar to support the ailerons. This spar is assumed to then only carry loads induced by the operation of the ailerons, and its cross-section will have a rectangular thin-walled geometry.

In calculations, it is then assumed that the aerodynamic force F_{ail} generated by each aileron is uniformly distributed across the aileron's surface, as a distributed load q_{ail}. This force then causes three types of load on the rear spar: vertical shear, bending and torsion.

Since the rear spar is supported by the wing ribs, the maximum shear force that will be experienced anywhere on the spar happens at the junctions with the ribs, and is calculated using Equation 8.13:

$$V_{support} = \frac{q_{ail} \cdot L_{rib}}{2} \tag{8.13}$$

furthermore, the maximum bending moment is also felt at the supports, and is calculated with Equation 8.14 [1]:

$$M_{support} = \frac{q_{ail} \cdot L^2}{12} \tag{8.14}$$

as for the torque generated by the aileron load, its maximum value is calculated with Equation 8.15:

$$T_{support} = V_{support} \cdot \text{moment arm} \tag{8.15}$$

where moment arm = $(x_{cp_{aileron}} - x_{\text{rear spar}}) \cdot c_{local}$, where $x_{cp_{aileron}}$ is the aileron's centre of pressure location and $x_{\text{rear spar}}$ is the location of the rear spar, both expressed as a fraction of the local wing chord c_{local}.

Then, it is possible to calculate the shear stress τ and the normal stress σ that the rear spar is subjected to, in a similar way as was done for the main spar, but with slight changes to the equations to account for the fact that the rear spar has a thin-walled rectangular cross section.

[1] URL: https://structx.com/Beam_Formulas_015.html [cited 11/06/2026]

Wing Skin

The wing skin, made of Mylar film, will have to be tightly wrapped around the wing, such that it experiences continuous tension that counteracts sagging induced by the outside dynamic pressure. The expression that governs this is Equation 8.16, which is the equation for the "tension per unit width in the fabric of a wing plane", taken from a NASA technical report [71]:

$$F_{skin} = \frac{\Delta P_{max} \cdot L_{rib}^2}{8 \cdot \delta} \tag{8.16}$$

where $\Delta P_{max} = \frac{1}{2}\rho V^2 C_{p_{min}}$, with $C_{p_{min}}$ being the most negative pressure coefficient that the wing experiences. δ is the allowable sag of the wing skin, arbitrarily set to be equal to 1% of the mean aerodynamic chord.

8.4.2. Critical Constraints

Main Spar

Considering the stresses that the wing-box spar will be subjected to, the spar has to be sized such that these stresses do not exceed certain critical values.

Firstly, there are the properties of the Galvorn material of the wing spar (see Table 8.2), with a tensile strength of 2400MPa, a compressive strength of 400MPa and a shear strength of 69MPa.

Apart from these, it is also necessary to account for buckling constraints of the main spar. For this, there is a technical report published by NASA [72] on the different modes of buckling experienced by cylindrical shells.

There is first the buckling constraint for cylindrical shells under compression, governed by Equation 8.17:

$$\sigma_{cr} = 0.605 \cdot \gamma \cdot E \cdot \frac{t}{R} \tag{8.17}$$

where γ is a knock-down factor to account for imperfections in real cylinders compared to the technical model (suggested in the same technical report to be equal to 0.6), $E = 200 \times 10^9$Pa is the Young's modulus of Galvorn, t is the thickness of the spar, and R is its radius.

Then, there is the critical bending moment to avoid catastrophic buckling and collapse of a cylindrical shell under bending, due to cross-section ovalization, this being Equation 8.18:

$$M_{cr} = 0.987 \frac{E \cdot R \cdot t^2}{\sqrt{1-\nu^2}} \tag{8.18}$$

There is then also the shear buckling constraint for cylindrical shells, calculated using Equation 8.19:

$$\tau_{cr} = \frac{0.747 \gamma^{0.75} E}{\left(\frac{r}{t}\right)^{1.25} \left(\frac{L}{r}\right)^{0.5}} \tag{8.19}$$

where $\gamma^{0.75} = 0.67$, as per the report's recommendation, and L is the distance between consecutive wing ribs.

Furthermore, the wing will also need to comply with wing tip deflection and twist limits, and the main spar must be sized taking this into account. A study into structural performance of HALE UAVs [73] identifies typical wing tip deflection values of conventional configuration HALE UAVs (which will be the case for the SORA) up to ≈ 30% of the half-wing span, and wing tip twist up to ≈ 13°. The limits for SORA are then conservatively set to a wing tip deflection of 15% of the half-wing span, and a twist of 5°.

The wing deflection follows Equation 8.20:

$$\frac{d^2 v}{dz^2} = -\frac{M_x(z)}{EI_{xx}(z)} \tag{8.20}$$

where $v(y)$ is the spanwise wing deflection. The wing twist follows Equation 8.21:

$$\frac{d\theta}{dz} = \frac{T(z)}{GJ(z)} \tag{8.21}$$

where $\theta(z)$ is the spanwise wing twist distribution, G is the shear modulus of the spar material and $J(z)$ is the polar moment of inertia of the spar, calculated at each spanwise location according to Equation 8.22:

$$J = \frac{\pi}{2}(R_{outer}^4 - R_{inner}^4) \tag{8.22}$$

Rear Spar
When it comes to the rear spar, its applied loads should also not exceed Galvorn's mechanical properties. Apart from this, the spar will also be sized such that its two webs do not buckle under the shear stress exerted by the ailerons. This behaviour is governed by Equation 8.23:

$$\tau_{cr} = \frac{\pi^2 k_s E}{12(1-\nu^2)} \left(\frac{t}{b}\right)^2 \tag{8.23}$$

where $k_s \approx 9.5$ for clamped web edges and b is the web height.

Wing Skin
Considering the tension load applied on the wing skin, it is necessary to ensure that the resulting stress will not exceed Mylar's tensile strength ($\approx$ 200MPa [2]). The applied stress follows Equation 8.24:

$$\sigma_{skin} = \frac{F_{skin}}{t_{skin}} \tag{8.24}$$

8.4.3. Wing-Box Design Script Logic

A Python script was developed for the wing-box design, which takes into account all of the equations above mentioned. The script starts by taking the internal loads that the wing is subjected to, as explained in Section 8.2. Then, it considers a series of different design variables which fully define the wing box: the chordwise position of the main spar, the root radius of the main spar, the taper ratio of the main spar (which allows to optimize its weight as a function of the wing spanwise loads), the thickness-over-radius ratio of the main spar, the thickness of the wing skin, the number of wing ribs, and the thickness of the walls of the rear spar. The script also takes other inputs from other subsystems, for example the aileron spanwise location, the chordwise location of the aileron hinges, the wing airfoil profile, etc.

The script starts by choosing a random guess considering the above explained design variables, and iteratively changes parameters until the lowest wing box mass which still supports all applied loads and deflection/twist limits is achieved. An illustration of this process is shown in Figure 8.3.

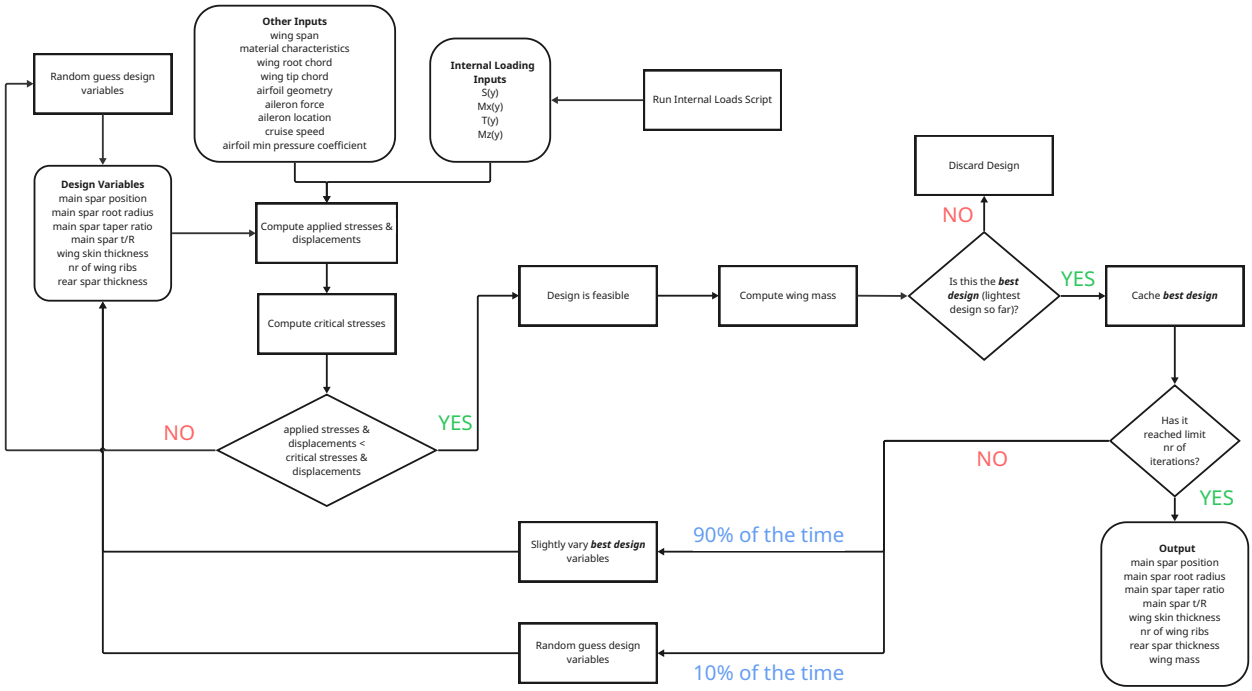

Figure 8.3: *Wing Sizing Flowchart*

8.4.4. Final Wing-Box Parameters

With the wing design process as showcased above, which was then inserted as part of the full aircraft design iteration loop (see Section 3.3) the final wing structural parameters are shown in Table 8.3:

[2] URL: https://matweb.com/search/datasheet.aspx?MatGUID=b8c2966eaa1d4f34a826258ada8ebf5f [cited 11/06/2026]

Table 8.3: *Final Wing-Box Parameters*

Parameter	Value
Total wing mass (excl. batteries and solar panels)	55.5 [kg]
Main spar chordwise location	33.5 [%]
Main spar root outer radius	110 [m]
Main spar tip outer radius	66 [mm]
Main spar $\frac{t}{R}$	0.005 [-]
Rear spar chordwise location	70 [%]
Rear spar wall thickness	1 [mm]
Rear spar mass	3.8 [kg]
Wing skin thickness	0.03 [mm]
Total number of wing ribs	84 [-]

The final wing root and tip cross sections are shown in Figure 8.4 (note how the root geometry does not include the rear spar since this rear spar only starts at the spanwise position where the aileron starts).

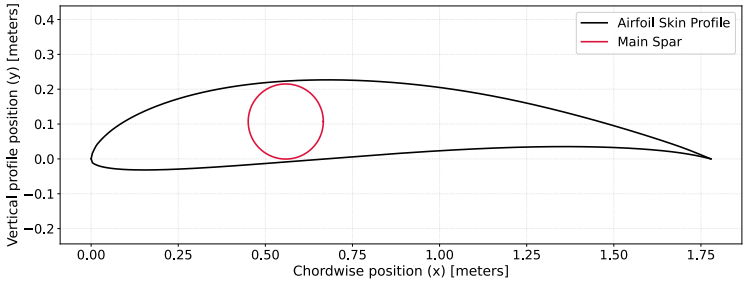

(a) *Root Cross-Section*

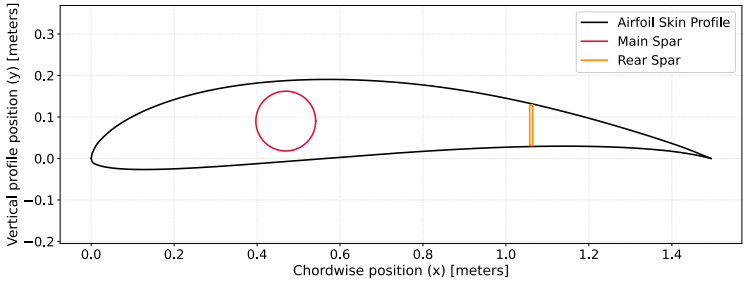

(b) *Tip Cross-Section*

Figure 8.4: *Wingbox Geometry*

This geometry resulted in the worst-case wing deflection and twist diagrams (between the three scenarios explained in Subsection 8.2.1) seen in Figure 8.5 (note that the negative wing deflection shown corresponds to an upwards deflection, due to the coordinate system established in Section 8.2).

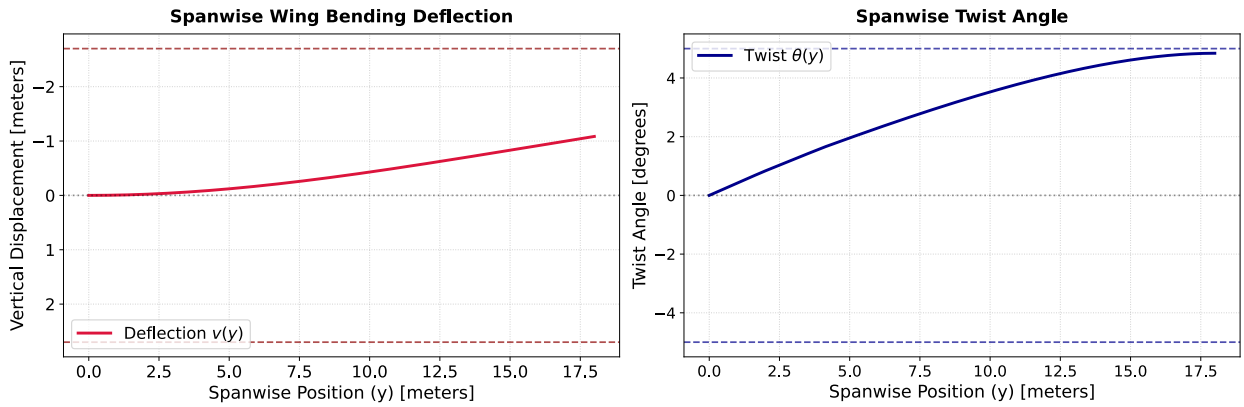

Figure 8.5: *Wing Deflection and Twist Profiles*

8.5. Fuselage Design

The design of the fuselage was mainly constrained by the size of the payload bay and the forces from the tail. The fuselage consists of a nose cone, a cylindrical payload bay and an exponentially tapering tail segment which can be seen in Figure 8.7. The radius at the end of the fuselage is 20% that of the payload bay. The design processes involved an iterative loop as shown in Figure 8.6 where an initial mass was guessed and the thickness was then calculated such that the relevant loads could be withstood, this resulted in a new mass and new loads. the loop continued until subsequent mass values differed by less than 0.5 kg.

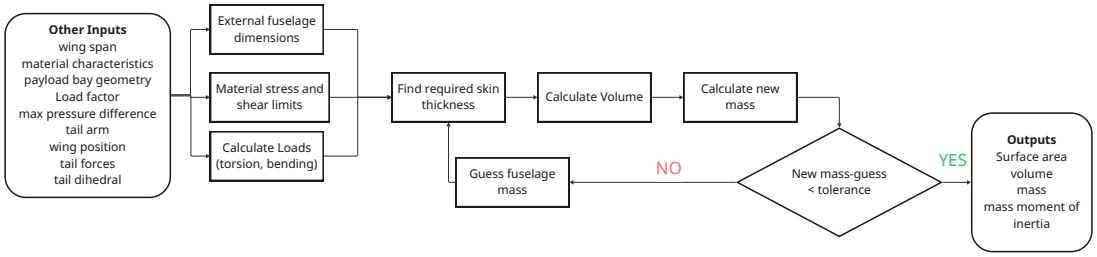

Figure 8.6: *Fuselage Design Process*

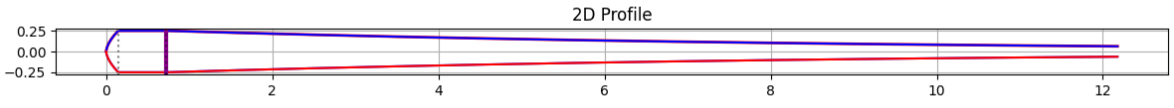

Figure 8.7: *Fuselage Design*

Most of the sizing is predetermined by other subsystems so the only factors which need to be calculated are the skin thickness and reinforcements to account for the forces the fuselage will experience from the tail and the wing. The main forces acting on the wing, described in Equation 8.25, are bending forces from the wing and tail ($M_{\text{bend, wing}} M_{\text{bend, tail}}$ which depend on fuselage weight W_{fus} and wing position x_{wing} and tail force F_{tail} (vertical and lateral) calculated in Equation 12.20, Equation 12.19 and position l_{tl} found in Equation 12.7 respectively. The torsional forces ($T_{torsion}$) from the V tail depend purely on the lateral tail force and the tail dihedral Ψ angle.

$$M_{\text{bend, wing}} = \frac{W_{\text{fus}}}{2} \cdot \frac{x_{\text{wing}}}{2} \tag{8.25}$$

$$M_{\text{bend, tail}} = \sqrt{F^2_{\text{tail, vert}} + F^2_{\text{tail, lat}}} \cdot l_{\text{tl}} \tag{8.26}$$

$$T_{\text{torsion}} = \frac{F_{\text{tail, lat}} \cdot 0.25}{\sin(\Psi)} \tag{8.27}$$

Next, the allowable stresses and material constraints are defined in Equation 8.28 as allowable shear stress τ_{allow} and tensile stress σ_{allow} determined by the transverse $\sigma_{\text{fail, tv}}$and longitudinal $\sigma_{\text{fail, lg}}$ material strengths respectively defined in Section 8.3 and a factor of safety (FOS) of 1.5. Lastly the pressurization of the payload bay to sea level pressure must also be taken into account the maximum ΔP is found at the ceiling altitude 25 km.

$$\sigma_{\text{allow}} = \frac{\sigma_{\text{fail, lg}}}{FOS_{\text{fus}}} \tag{8.28}$$

$$\tau_{\text{allow}} = \frac{\tau_{\text{fail, tv}}}{FOS_{\text{fus}}} \tag{8.29}$$

$$\Delta P = P_{\text{internal}}(h = 0) - P_{\text{external}}(h = H_{\text{max}}) \tag{8.30}$$

Using these constraints the various skin thickness requirements can be found in Equation 8.31 of which the largest, most constraining one is used. the maximum thickness to withstand the shear loads is $t_{\text{skin, shear}}$, similarly for tensile stress the thickness must be at least $t_{\text{str, pb}}$ and to with stand the pressurization the payload bay thickness must be at least $t_{\text{skin, press}}$. After running through all the iterations the final thickness was calculated as **1 mm**.

$$t_{\text{skin, shear}} = \frac{T_{\text{torsion}}}{2\pi r^2 \tau_{\text{allow}}} \tag{8.31}$$

$$t_{\text{axial, pb}} = \frac{M_{\text{max, pb}}}{\pi r^2_{\text{pl}} \sigma_{\text{allow}}} \tag{8.32}$$

$$t_{\text{skin, press}} = \frac{\Delta P \cdot r_{\text{pl}}}{\sigma_{\text{allow}}} \tag{8.33}$$

To ensure that the fuselage is properly reinforced at high load locations several internal frames were introduced at these points to ensure structural integrity. With the skin thickness defined the mass, the volume and mass moments of inertia can be calculated through integration techniques. A margin of 1.5 was included in the mass calculations to account for any assumptions and neglected aspects such as; the effect of cutouts for the payload and communication system, aeroelastic effects, as well as the insulation required for the payload bay. Additionally, it was assumed that an external structure would be used to attach the wing to the upper surface of the fuselage. The global parameters of the fuselage design are summarized in Table 8.4.

Table 8.4: *Final Fuselage Parameters*

Parameter	Value
Total Fuselage Mass (excl.payload)	18.6 [kg]
Surface Area	9.87 [m^2]
Total Length	11.86 [m]
x_{cg}	2.72 [m]
I_{xx}	0.25 [$kg \cdot m^2$]
I_{yy}, I_{zz}	96 [$kg \cdot m^2$]
Maximum wall thickness	1 [mm]

Lastly, back of the envelope calculations were done to estimate twist and deflection of the fuselage to ensure that while structurally sound any deflection would not lead to undesired drag or reduction of controllability. The results showed a maximum deflection of 80 mm and maximum twist of 0.22 degrees. On the scale of the fuselage length this is not significant.

8.6. Tail

For the tail an empirical formula [74] was used which is based on a long endurance high altitude UAV with a V-tail. In this formula, W_{to} is the take-off mass, n_y the load factor, S_{ht} the V tail area, b_{ht} the V tail span, T_{rht} the V-tail root chord thickness,C_{cwing} the wing mean aerodynamic chord length, and L_t the arm of force of the V-tail. These values can all be found in Chapter 12.

$$W_{ht} = 0.022\left(W_{to}^{0.813} \cdot n_y^{0.813} \cdot S_{ht}^{0.584} \cdot \left(\frac{b_{ht}}{T_{rht}}\right)^{0.033} \cdot \left(\frac{C_{cwing}}{L_t}\right)^{0.28}\right)^{0.91} \tag{8.34}$$

8.7. Structures Verification and Validation

To verify the code used in the structures section several different `pytests` were conducted to ensure that the code is running properly. Firstly, a mock input data set is generated to ensure constant conditions and an isolated testing environment. The formatting of the outputs is then checked against what is required by the JSON file and it is checked that all requirements are actually being calculated and correctly submitted into JSON. Additionally, the dimensionality of arrays and dictionaries is also verified to ensure there is no mismatch. Next, a sanity check is done for integrations and geometric operations to ensure no impossible or unphysical outcomes are outputted. For any convergence loops a test is conducted with extreme initial guesses to ensure the loop is robust. Lastly, any edge cases are tested to confirm that the code will transition to a fallback calculation or send out an error message. The Python files `Flight_envelope.py`, `InternalLoading.py`, `WingBox_Iterator.py`, and `fuselage_total.py` where each tested following the previous philosophies and all tests were passed. As such, it can be assumed that the content of the code is correct and the outputs are verified. Moreover, the reasonableness of the outputs was validated through comparison with the preliminary outputs from the excel sheet in the [15], this successfully showed no major differences in magnitude.

While it is difficult to validate the results of this section without full scale testing and simulation of the completed aircraft. Comparison and consistency with published data was possible. The wing, tail and fuselage masses were compared with the empirical formula values and the final mass fraction was analysed against those of reference aircraft and was found to be within a reasonable range providing confidence in the outputs of this section.

8.8. Conclusion

The final mass budget of the structures subsystem is summarized in Table 8.5.

Table 8.5: *Mass Division of Structures*

Part	**Value [kg]**
Wing	55.5
Tail	6.4
Fuselage	18.7
Total	**80.6**
Mass Fraction	0.37

Additional components which will be integrated into the structure of the aircraft and have not yet been mentioned include anti-collision and navigation lights, positioned at the wing's and fuselage's extremities, to comply with REQ-STK24- MIS07-SYS01, REQ-STK24-MIS07-SYS02 and REQ-STK24- MIS07-SYS03. One possible candidate for this are the AveoEngineering DroneV NXT lights [3], which are especially designed for this purpose.

[3] URL: https://aveoengineering.com/lightaveo/drone-uav-lights/dronev-nxt/ [cited 17/06/2026]

9

Propulsion

This chapter describes the design and sizing of the propulsion system. Firstly, the requirements for the propulsion system are generally discussed. Afterwards, based on these requirements, preliminary design decisions for the propulsion system are made. With the preliminary design of the propulsion system, the sizing model for the propulsion system is discussed. This sizing model runs two calculations: a power analysis and the blade element theory for sizing the propeller. After the setup of the model, the model is verified using unit testing and validated by analysing the performance of the designed system with efficiency coefficients in the real world. Finally, the final configuration of the propulsion system is presented.

9.1. Propulsion Requirements

For this mission, driver requirements, as described in Section 2.3, had a considerable influence on the design of this system. The primary driving requirements for the propulsion system are described in this section. To begin with, the aircraft shall produce zero emissions, according to **REQ-STK26-MIS03**, eliminating all propulsion systems that run on fuels. Additionally, **REQ-SRK11** requires that the aircraft shall fly for 60 days non-stop.

9.2. Preliminary Design Decisions

The trade-off performed in Section 3.2 showed that a fixed wing configuration was selected. Now that the lighter-than-air solution was eliminated, electric motors were selected for the propulsion system. This section describes the general structure of the system architecture, the configuration of the propellers, and the characteristics of the blade.

9.2.1. System Architecture

Based on the requirements, the selected fixed-wing design, and the choice of electric motors, propellers were chosen, since these are most efficient for high altitude platforms [75] and can operate on electricity when using electric motors, fulfilling the zero cruise emissions requirement. To generate the required power, solar panels and batteries were included in the power system design, supplying energy during the day and storing it for the night. The design of the power system is discussed in Chapter 10.

9.2.2. Propeller Configuration

Now that the propellers were selected for the propulsion system, their configuration had to be determined. An even number of propellers was chosen, as an odd configuration would require placement of a propeller on the fuselage or tail, increasing structural complexity, loads, and mass. Additionally, it was chosen to locate the propellers on the wings, as this positioning has the beneficial effect of increasing the local lift over the wing [76]. Due to redundancy concerns, two propellers were not considered feasible, as a single failure would generate a large yaw moment requiring a large and more complex control system to counteract it. With four or more propellers, thrust can be redistributed symmetrically by reducing power on the opposite propellers, ensuring that minimal yaw moment is created. If required, the aircraft may descend to reduce power demand and maintain controlled flight. Consequently, a minimum of four wing-mounted propellers were selected for the final configuration.

9.2.3. Blade Characteristics

After the configuration of the propellers was selected, the design of the propeller's blades also had to be explored. Considering that the aircraft shall be capable of flying at altitudes up to 25 km, it was important to design the blades to optimize performance at the required cruise altitude. Two blades per propeller are most efficient at these high altitudes due to the extremely low air density [77], and can also be seen on reference aircraft such as the Airbus Zephyr [77]. Additionally, the trade-off performed in Section 3.2 concluded that the design will not have landing gear to save on weight. Due to this, the aircraft will perform a belly landing, and therefore, it was essential that the blades avoid contact with the ground during landing, as this could cause damage. In order to prevent the blades from being damaged during landing, two-bladed propellers can be stopped in a position parallel to the wing just before landing.

It is important to select a blade airfoil that is capable of operating in low densities at high altitudes for long endurance. The FX 63-137 airfoil was selected, as this airfoil has the best results for high-altitude long endurance UAV propellers [78]. This airfoil has a zero lift angle α_0 of -5.5 °, a lift slope of 0.11, and a thickness-to-chord ratio $\frac{t}{c}$ of 0.137 [79]. For this airfoil, the highest $\frac{C_L}{C_D}$ ratio is at an angle of attack α of 7 °[79]. However, due to different local velocities of the blade, due to the radius, this angle of attack changes when no twist to the blade is applied. In order to have the

optimum α along the blade, twist was applied. The chord length also varies over the radius, as the optimum chord length changes over the blade span. A design optimization of a HALE propeller was conducted [80]. A more in-depth description of the design process for the blade twist and chord is explained in Section 9.3.

9.3. Sizing Model

With the preliminary design selected, the propulsion system could be developed further with the use of a custom made model, focusing on the number of propellers, blade dimension and motor RPM. Firstly, the inputs needed for the model had to be determined. A power analysis followed, to clarify the power requirements from the propulsion system in the entire flight envelope. Finally, the most efficient number of propeller and its dimensions for the required power were selected following a blade element theory analysis.

9.3.1. Inputs

Before calculations on sizing the propulsion could have been made, it was important to clarify what the inputs were needed for these calculations. Some general inputs were set, shown in Table 9.1. These include limitations for the radius and RPM. The minimal and maximal value for possible radii for the propeller ranged between 0.2 and 6.0 m, with a size step of 0.1 m. For the RPM, the range was limited to between 100 and 5000 with a step size of 100. To account the attachment of the blade onto the motor, the first 0.05 m of the blade was used for this. The propeller clearance is defined as the distance between the fuselage and the propeller tip as well as the distance between two propellers, and it was set to 1.0 m. For mass calculations, the shape factor of the blade was taken into account and was assumed to be 0.65.

Additional to the general inputs for the sizing model, variable inputs from other departments are visualised in Table 9.1. The total drag, wing area and wing lift coefficient were taken from the aerodynamics module, whereas the total aircraft weight was taken from the aircraft design module.

Table 9.1: *General Propulsion Sizing Inputs*

Input	Value	Rationale
γ	1.4 [-]	Heat capacity ratio
R	287.05 [J/kgK]	Universal gas constant
α	7.0 °	Blade AoA [79]
α_0	-5.5 °	Zero lift AoA [79]
LIFT_SLOPE	0.11 [-]	Blade lift slope [79]
t/c	0.137 [-]	Thickness-to-chord [79]
MAX_V_TIP	0.75 Mach [-]	Max tip velocity [81]
R_BLADE_START	0.05 [m]	Blade attachment start
N_BLADES	2 (-)	Number of blades [-]
MIN_BLADE_R	0.2 [m]	Min blade radius
MAX_BLADE_R	6.0 [m]	Max blade radius
ΔR	0.1 [m]	Step size (radius)
MIN_RPM	100 [-]	Min motor RPM
MAX_RPM	5000 [-]	Max motor RPM
ΔRPM	100 [-]	Step size (RPM)
PROP_CLEARANCE	1.0 [m]	Propeller clearance
ρ_{CFRP}	1550 [kg/m^3]	Density [82]
k	0.65 [-]	Blade shape factor

9.3.2. Power Analysis

To start the power analysis of the propulsion system, it is necessary to find the altitude at which the power required is the highest. The drag at every altitude is found with Equation 9.2, where D is the drag in N, and C_D the drag coefficient. The velocity of the aircraft at each altitude was calculated using Equation 9.1. Where v_{TAS} is the TAS in $\frac{m}{s}$, W is the weight of the aircraft in N, ρ is the air density at the corresponding altitude in $\frac{kg}{m^3}$, following the ISA, C_L is the lift coefficient of the wing, and S the wing area in m^2.

$$v_{TAS} = \sqrt{\frac{2 \cdot W}{\rho \cdot C_L \cdot S}} \tag{9.1}$$

$$D = \frac{1}{2} \cdot \rho \cdot v_{TAS}^2 \cdot C_D \cdot S \tag{9.2}$$

However, Equation 9.1 was substituted into Equation 9.2, resulting in Equation 9.3. So, the drag is constant for every altitude since v_{TAS} and ρ are eliminated from that formula. As both the drag and velocity are known for every altitude, the power required at every altitude was calculated using Equation 9.4, where P_{req} is the required power. The results of the power required for every altitude are shown in Figure 9.1. It can be seen that the power required is the highest for the maximum operational altitude. Therefore, for the altitudes below 25 km, there is power left that was used for climbing. With the power that was left, the rate of climb (ROC) in $\frac{m}{s}$ was calculated for every altitude using Equation 9.5. The available power is the summation of power required and the power left. With the ROC, it was calculated how long it will take for the aircraft to climb using Equation 9.6, where t_{climb} is the climb time is s, and h is the segment of climb, for computation selected in 1000 meters segments. However, the climb time outcome may not be suitable, as the UAV needs continuous solar irradiance to perform the climb. Therefore, the model calculated how much extra power the propulsion system shall have in order to fulfil the time limitation. As such, the propulsion system was designed for the required power for cruise plus the extra power required for climb. A general overview of the power analysis model is visualised in Figure 9.2.

$$D = W \cdot \frac{C_D}{C_L} \tag{9.3}$$

$$P_{req} = D \cdot v_{TAS} \tag{9.4}$$

$$ROC = \frac{P_{available} - P_{req}}{W} \tag{9.5}$$

$$t_{climb} = \frac{h}{ROC} \tag{9.6}$$

Figure 9.1: *Power Required over Altitude*

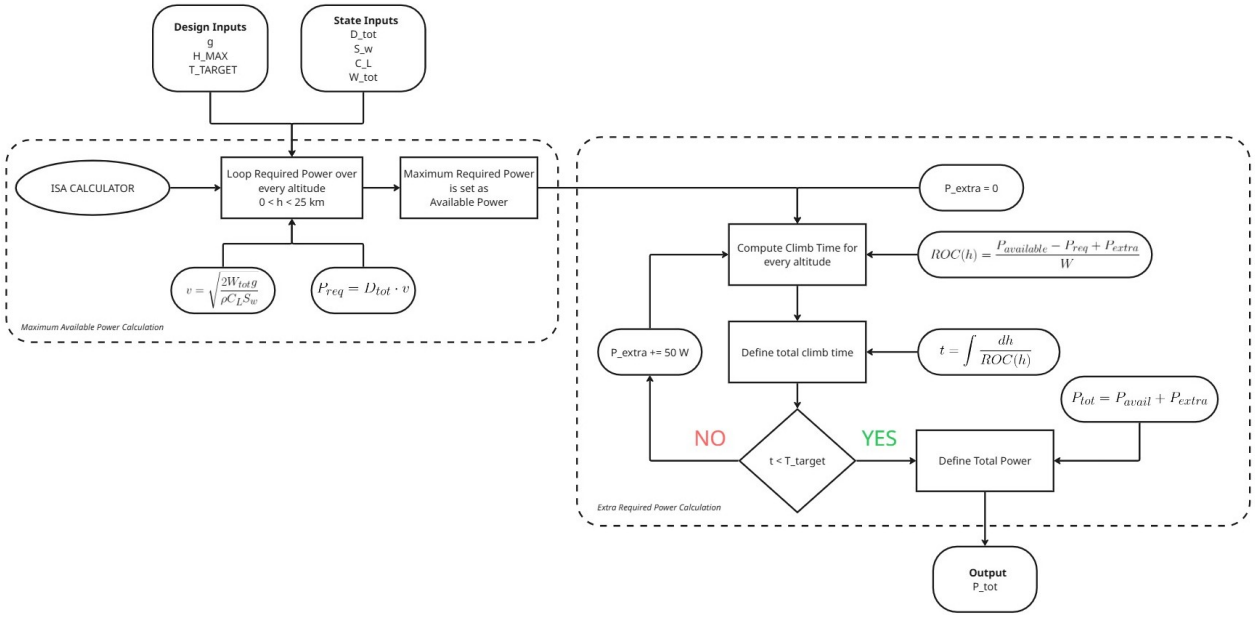

Figure 9.2: *Power Analysis Flowchart*

9.3.3. Blade Element Theory Propeller Sizing

To determine the optimal number of propellers, a different model was developed, focusing on minimizing the combined mass of the blades and electric motors. Several combinations involving the blade radius and motor RPM were made. For each combination it was calculated how many propellers were required to reach the required power. As a first constraint for each combination, it was set that the tip velocity of the blade could not exceed 0.75 Mach, since this will cause shock waves on the blades, decreasing their efficiency [81]. To impose this requirement, it was first necessary to calculate the speed of sound at 25 km. This was done by using Equation 9.7. In this equation γ is the heat capacity ratio, R is the universal gas constant, and T is the temperature at 25 km, from the ISA. The tip velocity of the blade is calculated using Equation 9.8. In this equation, RPM are the rotations per minute of the blade and R is the radius of the blade. A radius–RPM combination only continued in the model if $v_{tip} < 0.75 \cdot a_{25km}$. This constraint was set only for the highest operating altitude since this was found to be the most critical, as the speed of sound decreases with altitude [83]. An additional sanity check was included, limiting the radii of the propellers to such that they do not exceed the 36 m wingspan.

$$a_{25km} = \sqrt{\gamma \cdot R \cdot T_{25km}} \tag{9.7}$$

$$v_{tip} = \frac{2\pi \cdot RPM}{60} \cdot R \tag{9.8}$$

The relative velocity was calculated for every radius and RPM option to eventually determine the amount of thrust generated on the blade. The blade was divided into elements with equal length dR starting at a radius of 0.05 m to account for the blade-motor attachment. First, the tangential velocity was calculated using Equation 9.9. Then the relative velocity to the blade was calculated with Equation 9.10. Also the flow angle ϕ was determined in Equation 9.11, to calculate the forces on the blade. As described in Subsection 9.2.3, twist was applied to the blade in order to obtain a constant angle of attack along the blade. The twist along the blade was calculated using Equation 9.12. A visualisation of the angles on the blade is shown in Figure 9.3. The lift coefficient along the blade was calculated using Equation 9.13. Lastly, the drag coefficient C_D of the propeller was assumed to be 0.010 for an electric driven propeller from literature [55].

$$dv_{tangential} = \frac{2\pi \cdot RPM}{60} \cdot dR \tag{9.9}$$

$$dv_{relative} = \sqrt{v_{cruise}^2 + dv_{tangential}^2} \tag{9.10}$$

$$\phi = \arctan \frac{v_{cruise}}{dv_{tangential}} \tag{9.11}$$

$$\beta = \phi + \alpha_{local} \tag{9.12}$$

$$C_L = C_{L_\alpha}(\alpha - \alpha_0) \tag{9.13}$$

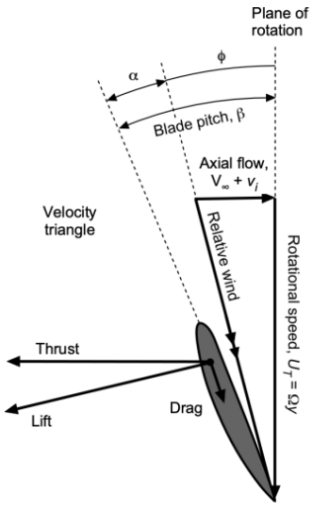

Figure 9.3: *Blade Angles and Forces*[1]

The lift and drag per section of the blade were calculated using Equation 9.14 and 9.15. For the lift equation, F is the Prandtl tip loss factor that was calculated using Equation 9.16 and 9.17 [84]. With the calculated angles and forces on the blade, the total thrust and torque of the blade were calculated using Equation 9.18 and 9.19. The amount of useful power that one propeller generated is than calculated using Equation 9.20. Consequently, it was calculated how many propellers were required to overcome the total power required that was calculated in Subsection 9.3.2 using Equation 9.21.

[1] URL: https://eaglepubs.erau.edu/introductiontoaerospaceflightvehicles/chapter/propellers/ [cited 09/06/2026]

$$dL = \frac{1}{2} \cdot \rho \cdot dv_{relative}^2 \cdot dR \cdot c \cdot C_L \cdot F \quad (9.14)$$

$$dD = \frac{1}{2} \cdot \rho \cdot dv_{relative}^2 \cdot dR \cdot c \cdot C_D \quad (9.15)$$

$$F = \frac{2}{\pi} \arccos e^{-f} \quad (9.16)$$

$$f = \frac{B(R-r)}{2r \sin\phi} \quad (9.17)$$

$$dT = dL\cos\phi - dD\sin\phi \quad (9.18)$$

$$dQ = r \cdot (dL\sin\phi + dD\cos\phi) \quad (9.19)$$

$$P_{single-prop} = T_{single-prop} \cdot v \quad (9.20)$$

$$n_{propellers} = roundup(\frac{P_{total}}{P_{single-prop}}) \quad (9.21)$$

Once the number of propellers were known for each radius and RPM combination, the mass for each of these combinations was determined. The mass of a single blade was calculated with Equation 9.22. In this formula, $\frac{t}{c}$ is the thickness to chord ratio, k is the shape factor of the blade assumed to be 0.65, c is the chord length, R is the blade radius, and ρ is the selected CFRP material density, assumed to be 1550 kg/m^3 [82]. In addition to the mass of the blades, the mass of the electric motor was computed using Equation 9.23 [75]. The total mass for each combination was calculated by multiplying the mass of the blade and motor with how many were needed for that combination. The combination with the lightest total mass was selected, while adhering to the minium four propeller requirement previously set. A general overview of the propeller sizing flowchart can be seen in Figure 9.4.

$$m_{blade} = \frac{t}{c} \cdot k \cdot c^2 \cdot R \cdot \rho \quad (9.22)$$

$$m_{motor} = 0.2669 + 9.845 \cdot 10^{-4} P_{motor} - 1.22 \cdot 10^{-10} P_{motor}^2 \quad (9.23)$$

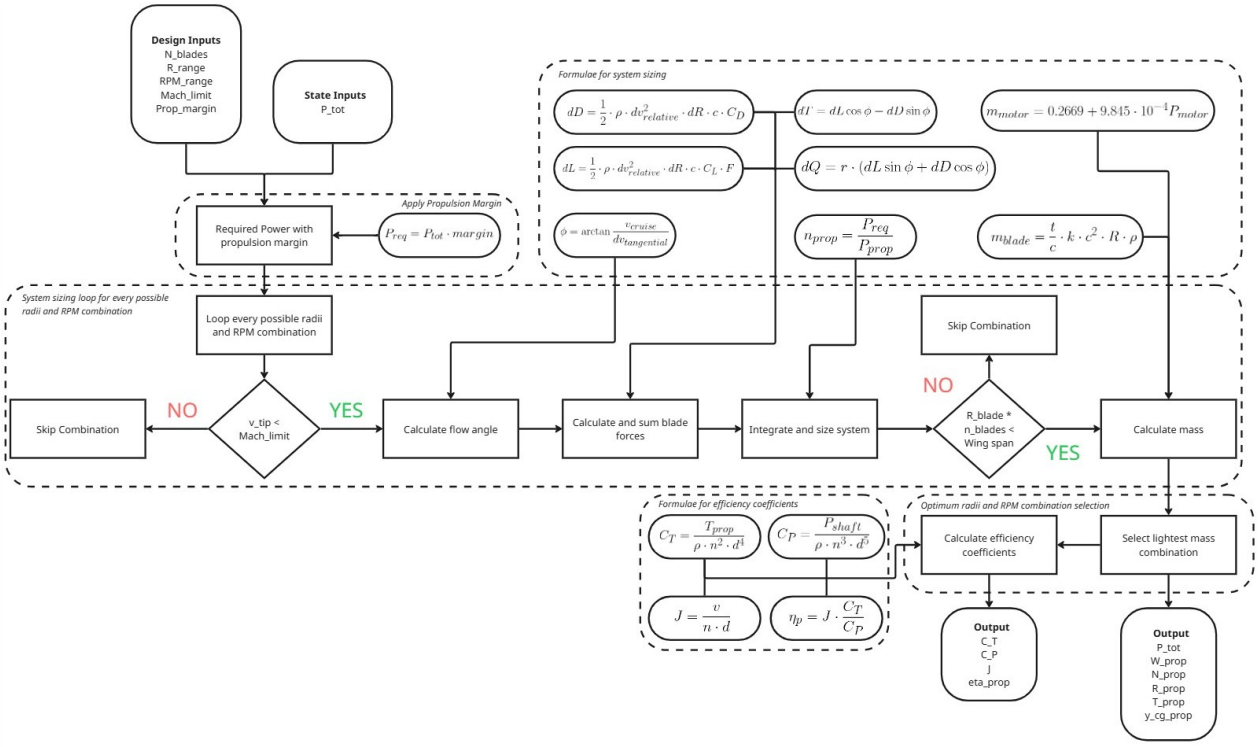

Figure 9.4: *Propeller Sizing Flowchart*

9.3.4. Outputs

The model produced multiple outputs, not only for the sizing of the propulsion system, but also those necessary to size other systems. An overview of the outputs of the model is visualised in Table 9.2. The final design of the propulsion system with sizing numbers is presented in Section 9.5.

Table 9.2: *Data Flow Propulsion Module*

Target Subsystem	Output Variables
Propulsion (Self)	Number of propellers, Radius of propeller, RPM
Power	Power (Cruise), Power (Climb), Power (Night)
Aerodynamics	Number of propellers, Radius of propeller
Wing	Thrust per propeller, y_{cg} of propeller, Weight of one propeller

9.4. Verification and Validation

As the model to size the propulsion system was set up, it also required to be verified and validated. The code of the model was verified using `pytest`. Validation consisted of comparing model output, namely different efficiency coefficients to similar propulsion systems.

9.4.1. Model Verification

`Pytest` was used to verify if the functions within the code work as expected. Mock inputs were set up and used to hand calculate the expected function's outcomes. Within the test environment, tests were set up to run the used functions with the mock inputs. The tests' results were compared with the expected result, and if those were the same, the test had passed. Additionally, an end-to-end test was performed in order to test if the different modules communicated correctly to each other.

From the testing module, several tests failed. Firstly, the calculated efficiency had an impossible value of more than 100%. The issue was caused by calculating the efficiency of the overall system and not at an individual propeller. Since the amount of propellers was always rounded up, the propulsion system was always overdesigned, resulting in an unrealistic efficiency value. Additionally, the propellers did not yet account for torque drag, resulting in a too optimistic efficiency. The efficiency formula was adjusted and the torque drag was implemented in the calculations, causing the propulsion efficiency to take realistic numbers. Secondly, the test showed that there was a fault in communication between the modules. One module was run twice, resulting in longer computation times and overwriting issues for the model. The model was adjusted and tested again, resulting in the same outputs with a reduced computational time. Lastly, a division by zero error was found from Equation 9.6, requiring a logic patch to prevent it. An overview of the final status of the performed tests is shown in Table 9.3.

Table 9.3: *Propulsion Model Verification and Unit Test Summary*

Test Suite / Component	**Tests Executed**	**Passed**	**Status**
TestAtmosphericConditions	3	3	PASSED
TestBladeCl	2	2	PASSED
TestBladeTwist	3	3	PASSED
TestTipLossFactor	3	3	PASSED
TestTaperedChord	4	4	PASSED
TestComputeMass	4	4	PASSED
TestEfficiencyCoefficients	3	3	PASSED
TestFindBestAndOutput	4	4	PASSED
TestClimbPowerRequired	4	4	PASSED
TestPropulsionMainIntegration	3	3	PASSED
Total	**33**	**33**	**100%**

9.4.2. Efficiency Coefficients Validation

In order to validate the model, efficiency coefficients were computed such that they could be compared with already existing propulsion systems for similar missions. The efficiency coefficients were only calculated for the maximum cruise altitude of 25 km. Firstly, the thrust and power coefficients were calculated using Equation 9.24 and 9.25. In this formula, T_{prop} is the thrust per propeller in N, P_{shaft} is the shaft power per propeller in W, ρ is the air density in $\frac{kg}{m^3}$, n are the rotations per second of the electric motor, and d is the diameter of the propeller. The advance ratio J was calculated using Equation 9.26, where v_{cruise} is the cruise speed in $\frac{m}{s}$. Consequently, the propeller efficiency was calculated using Equation 9.27.

$$C_T = \frac{T_{prop}}{\rho \cdot n^2 \cdot d^4} \tag{9.24}$$

$$C_P = \frac{P_{shaft}}{\rho \cdot n^3 \cdot d^5} \tag{9.25}$$

$$J = \frac{v_{cruise}}{n \cdot d} \tag{9.26}$$

$$\eta_p = J \cdot \frac{C_T}{C_P} \tag{9.27}$$

From the formula, and the output of the propulsion system sizing model, it was calculated that the thrust coefficient C_T of the propeller is 0.135. This is a reasonable number, since common C_T values range between 0.05 and 0.18 [85]. The power coefficient was calculated to be 0.099, also fitting in the realistic range of 0.02 and 0.22 [85]. The resulting advance ratio is 0.571, which is valid when comparing to other HALE UAVs that range between 0.4 and 0.6

[80]. Eventually, these coefficients resulted in a propulsion efficiency of 77.67%. This efficiency was also considered valid, since typical efficiencies range around 75% for the given advance ratio [80, 85]. A graph with the efficiency coefficients is visualised in Figure 9.5. As can be seen in the graph, the propeller does not yet operate at the highest efficiency possible. Therefore, increasing the advance ration to 0.8 should be considered. This is possible by either increasing v_{cruise} or decreasing the RPM and radius of the propeller.

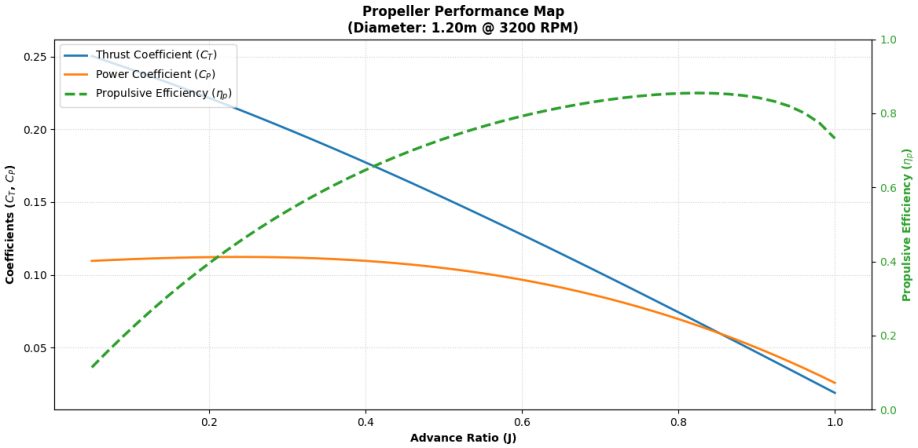

Figure 9.5: *Influence of J on C_T, C_P, and η_p*

9.5. Final Configuration

After the model was run, the final configuration of the propulsion system was determined. The model determined that four propellers with two blades each was the best option in terms of weight. The final design of the propulsion system are summarised in Table 9.4.

Table 9.4: *Propulsion System Configuration Summary*

Parameter	**Value**
Number of Propellers	4 [-]
Blades per Propeller	2 [-]
Blade Radius	0.6 [m]
Rotational Speed	3200 [RPM]
Thrust per Propeller	31.4 [N]
Total Power Availability	5915 [W]
Mass per Propeller	4.0 [kg]
Total Propulsion Mass	16.0 [kg]

10

Power Systems

This chapter presents the design and sizing of the aircraft's power system. Section 10.1 visually represents the flow and logic of the calculations in this chapter. It is followed by the design of the main power-system components. The solar-panel selection and mass estimation are discussed in Section 10.2, while the battery selection, configuration, charge and discharge properties, and thermal-control approach are presented in Section 10.3. The remaining electrical components, including the DC–DC converter, ESC, BMS, and MPPT, are described in Section 10.4. Their overall configuration and power flow are then summarised graphically in the electrical block diagram in Section 10.5. The removable battery concept is introduced in Section 10.6, with emphasis on maintainability, sustainability, and future upgrade potential. The power-system sizing method is then verified and validated in Section 10.7. Finally, the chapter concludes with the results summary in Section 10.8, where the main power-system outputs are presented together.

10.1. Power Flowchart

The logic flow of the calculation for power is summarised in Figure 10.1. This logic was integrated in an iterative design loop, which is detailed in Section 3.3.

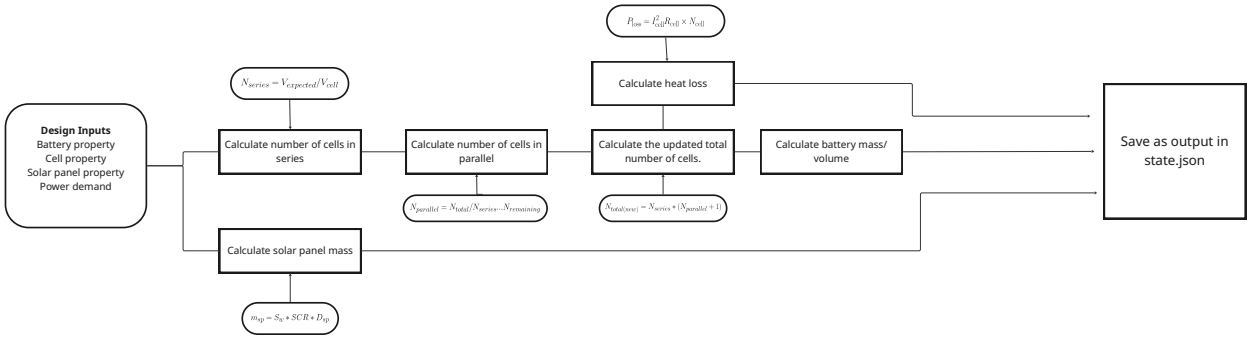

Figure 10.1: *Power Calculation Flow Chart*

10.2. Solar Panels

The estimation of the solar-panel efficiency and mass is discussed in Subsection 10.2.1 and Subsection 10.2.2, respectively.

10.2.1. Solar Panels Efficiency Estimation

The previously selected SHARP triple-junction solar module [1] was eliminated because its efficiency was insufficient to meet the mission's power requirements. The updated selection is a triple-junction solar cell based on thick quantum-well superlattices. This cell was experimentally demonstrated in 2022 under laboratory conditions, achieving efficiencies of 39.5% under the global terrestrial spectrum and 34.2% under the AM0 space spectrum [86]. To ensure a conservative estimate, the lower reported efficiency of 34.2% is selected as the baseline reference. This value was measured at room temperature, approximately 25°C, while the expected ambient temperature at an altitude of 15 km to 25 km is approximately −50°C. Since no temperature coefficient was available for the selected thick quantum-well triple-junction cell, an temperature coefficient of −0.09%/°C (the efficiency would increase an absolute value of 0.09% when the temperature drops by 1°C), reported by Aho et al. [87], for a similar solar cell is used as a first-order approximation. The temperature-corrected efficiency is thus estimated to be 40.95%. To account for uncertainties and the preliminary nature of this analysis, a derating factor of 0.9 is applied. Therefore, the final design solar-cell efficiency is taken as 36.9%.

10.2.2. Solar Panels Mass Estimation

The first reference module has a specific mass of 500 g/m^2 at an efficiency of 29.6% [88]. The second has a specific mass of 280 g/m^2 at 25.6% efficiency.[1] The estimated specific mass is obtained by averaging the specific mass per

[1] URL: https://global.sharp/solar/en/high-efficiency/pdf/datasheet_atmospheric-solar-module.pdf [cited 08/06/2026]

percentage point of efficiency across the two references and then scaling to η_{sp}:

$$m_{sp,est} = \left[\frac{1}{2}\left(\frac{m_{sp,ref,1}}{\eta_{ref,1}} + \frac{m_{sp,ref,2}}{\eta_{ref,2}}\right)\right]\eta_{sp} \tag{10.1}$$

Substituting the reference values gives an estimated specific mass of approximately $m_{sp,est} = 513\ \mathrm{g/m^2}$, which is used for the preliminary solar-panel mass estimation.

The solar cells are assumed to cover 90% of the wing area, which has an area of $S_w = 58.9\ \mathrm{m^2}$. Therefore, the total solar-panel mass is estimated as following:

$$m_{sp} = 0.9\, S_w\, m_{sp,est} \tag{10.2}$$

where S_w is the wing area and $m_{sp,est}$ is the estimated specific mass of the solar panel. Using this method, the total solar-panel mass is estimated to be 27.2 kg.

10.3. Battery

This section presents the battery-system design. Subsection 10.3.1 explains the selection process of the battery, followed by the determination of the bus voltage and the power-distribution architecture in Subsection 10.3.2 and Subsection 10.3.3, respectively. The battery cell configuration is then defined in Subsection 10.3.4. The discharge and charge properties are discussed in Subsection 10.3.5. Finally, the battery thermal-control approach is presented in Subsection 10.3.6.

10.3.1. Battery Selection

The Amprius SiCore 450 Wh/kg cell was selected as the onboard energy storage solution owing to its exceptional gravimetric energy density and demonstrated suitability for High-Altitude Platform Station applications.[2] High energy density is a critical requirement for this mission: the aircraft must accumulate sufficient energy reserves during daylight hours to sustain operation throughout the night, while minimising the mass penalty associated with the battery pack.

10.3.2. Bus Voltage

The power distribution bus uses a 270 VDC (Volts Direct Current) architecture, as 270 VDC is commonly used in aircraft electrical systems to reduce current, cable mass, and power losses in high-power applications.[3] This voltage level is suitable for the propeller system, which is the main power load driver onboard the aircraft. All lower-power electrical components are supplied through a 28 VDC bus. This 28 VDC bus is generated from the 270 VDC main bus using a DC–DC converter.

10.3.3. Power Distribution

The battery pack supplies the main 270 VDC bus, which distributes power to the high-power propulsion system. The propeller system is supplied through an electronic speed controller (ESC), which converts the DC input into a controlled three-phase output for the electric motor.

For avionics, payload systems, sensors, control electronics, and other low-power components, the voltage is stepped down from 270 VDC to 28 VDC using a DC–DC converter. This separation between the high-voltage propulsion bus and the lower-voltage equipment bus improves the overall power distribution efficiency while keeping the voltage level suitable for different subsystems.

10.3.4. Battery Cell Configuration

The required battery mass follows from the mission energy demand and is determined to be 52.0 kg. The total number of cells is first estimated by dividing the required battery mass by the mass of a single cell. For the selected cell, a cell mass of 33.2 g is used.[4]

The pack is arranged in a series-parallel configuration. The number of series-connected cells, N_s, is chosen to satisfy the target pack voltage. The number of parallel strings, N_p, is then determined from the total cell count required to meet the energy capacity. These values are computed as

[2] URL: https://amprius.com/amprius-launches-sicore-450-wh-kg-high-energy-cell-with-near-term-mass-production-capability-to-scale/ [cited 08/06/2026]

[3] URL:https://tt-ms.com/wp-content/uploads/sites/4/2020/12/270vDC-in-Avionics.pdf [cited 08/06/2026]

[4] URL:https://vepimg.b8cdn.com/uploads/vjfnew//content/files/17467219557-ionelstefan-pdf1746721955.pdf [cited 08/06/2026]

$$N_s = \text{round}\left(\frac{V_{\text{pack,target}}}{V_{\text{cell,nom}}}\right), \tag{10.3}$$

$$N_{\text{cells,raw}} = \left\lfloor \frac{m_{\text{bat,initial}}}{m_{\text{cell}}} \right\rfloor, \tag{10.4}$$

$$N_p = \left\lceil \frac{N_{\text{cells,raw}}}{N_s} \right\rceil. \tag{10.5}$$

The initial cell count $N_{\text{cells,raw}}$ is not necessarily an exact multiple of N_s. Therefore, N_p is rounded up to ensure that the final battery pack consists only of complete parallel strings. The final number of cells is then

$$N_{\text{cells}} = N_s N_p \tag{10.6}$$

The resulting pack mass is calculated as

$$m_{\text{bat}} = N_{\text{cells}} m_{\text{cell}} \tag{10.7}$$

Using a cell energy of 14.9 Wh, the total pack energy is

$$E_{\text{bat}} = N_{\text{cells}} E_{\text{cell}} \tag{10.8}$$

Based on a volumetric energy density of 1150 Wh/L, the battery pack

volume is estimated as

$$V_{\text{bat}} = \frac{E_{\text{bat}}}{\rho_{E,\text{vol}}} \tag{10.9}$$

Therefore, the final battery configuration is 123S13P, corresponding to 1599 cells, a pack mass of 53.1 kg, a total energy capacity of 23.8 kWh, and an estimated pack volume of 20.7 L.

10.3.5. Discharge and Charge Properties

The total nominal night-time system power demand is estimated as

$$P_{\text{system}} = 1.2\left(P_{\text{payload,heat}} + P_{\text{other,night}} + P_{\text{prop,night}} + P_{\text{bat,heat,night}}\right) \tag{10.10}$$

where the factor of 1.2 accounts for system-level inefficiencies and margins. This demand defines the required discharge and charge operating points derived below.

Discharge Given P_{system} and the pack discharge voltage $V_{\text{pack,dis}}$, the pack discharge current required to sustain night-time operation is

$$I_{\text{pack,dis}} = \frac{P_{\text{system}}}{V_{\text{pack,dis}}\,\eta_{\text{dis}}} \tag{10.11}$$

where η_{dis} accounts for discharge-path losses. Since the N_p parallel strings share the current equally, the per-cell discharge current is

$$I_{\text{cell,dis}} = \frac{I_{\text{pack,dis}}}{N_p} \tag{10.12}$$

For the cell to operate within its rated limits, this current must satisfy

$$I_{\text{cell,dis}} \leq I_{\text{dis,max}} \tag{10.13}$$

Substituting the selected configuration ($N_s = 123$, $N_p = 13$) yields a pack discharge voltage of $V_{\text{pack,dis}} = 270.6$ V. With $\eta_{\text{dis}} = 0.95$, the night-time system power demand (Eq. 10.10) evaluates to $P_{\text{system}} = 5401$ W, from which the required pack discharge current (Eq. 10.11) is $I_{\text{pack,dis}} = 21$ A. Dividing by $N_p = 13$ gives a per-cell discharge current of $I_{\text{cell,dis}} = 1.62$ A, which is well below the rated maximum of $I_{\text{dis,max}} = 4.39$ A, confirming that the constraint in Eq. 10.13 is satisfied.

Charging For charging, a typical cell current of $I_{\text{cell,ch}} = 0.439$ A scales to a pack charge current of $I_{\text{pack,ch}} = 5.71$ A. The charging C-rate is defined at the cell level as the ratio between the charging current and the cell capacity [5]:

$$C_{\text{rate,ch}} = \frac{I_{\text{cell,ch}}}{C_{\text{cell}}} \tag{10.14}$$

[5] URL: https://www.ossila.com/pages/what-is-battery-c-rate [cited 11/06/2026]

Therefore, the charging C-rate is independent of the pack topology. Series connection changes the pack voltage, while parallel connection scales both the pack charging current and the pack capacity by the same factor. For the nominal charging current $I_{ch,typ}$, the corresponding charging C-rate is $C_{rate,ch} = 0.1\,C$, which gives a nominal charge time of $t_{ch,nom} = 10.00$ h. If the available solar charging window is shorter, charging at the maximum rated current increases the C-rate to $0.5\,C$ and reduces the minimum charge time to $t_{ch,min} = 2.00$ h.

Resistive Heat Generation The cell internal resistance is taken as $R_{cell} = 67$ mΩ $= 0.067$ Ω. When current flows through this internal resistance, Joule heating is generated. The heat dissipation per cell during discharge and charge is calculated as

$$P_{cell,dis} = I_{cell,dis}^2 R_{cell}, \qquad P_{cell,ch} = I_{cell,ch}^2 R_{cell}. \tag{10.15}$$

The corresponding total heat dissipation at pack level is

$$P_{pack,dis} = N_{cells} P_{cell,dis}, \qquad P_{pack,ch} = N_{cells} P_{cell,ch}, \tag{10.16}$$

The pack-level resistive heat dissipation varies during discharge because the cell current changes with the instantaneous power demand. Therefore, the discharge heat dissipation is evaluated over the discharge phase and the nominal discharge situation is used for subsequent calculations. For the nominal discharge condition as suggested in Subsection 10.3.5, the pack-level resistive heat dissipation is $P_{pack,dis} = 281$ W. During nominal charging, the pack-level resistive heat dissipation is calculated to be $P_{pack,ch} = 20.6$ W. The discharge and charging heat dissipation values are used as inputs for the battery thermal control analysis in Section 10.3.6.

10.3.6. Battery Thermal Control

The safe operating temperature range for the cells spans from −10 °C to 50 °C; however, charging is strictly restricted to a narrower window of 0 °C to 50 °C. At cruise altitude, the ambient temperature can drop to approximately −50 °C, necessitating active thermal management to maintain the battery pack within these operational limits.

The internal heat generated by the cells during operation (defined by Eq. 10.16) partially offsets the external thermal load. Consequently, the supplemental heating power required from the active thermal control system is formulated as:

$$P_{bat,heat} = \max\left(0,\, P_{heat,required} - P_{pack}\right), \tag{10.17}$$

where $P_{heat,required}$ is the total thermal power required to maintain the battery at its target operating temperature, and P_{pack} represents the internal heat dissipation, substituted as either $P_{pack,dis}$ or $P_{pack,ch}$ depending on the respective discharging or charging phase. The calculation for heat power required then follows a similar process as done for the payload compartment (see Section 6.8), and this process was integrated in the global aircraft iteration loop as well.

10.4. Other Components

This section presents the remaining electrical components required for the power-system architecture.

DC–DC Converter The 270 VDC bus directly supplies the propeller system, while a DC–DC converter is used to step the voltage down to 28 VDC for the remaining components, such as sensors, heating devices, and other low-voltage subsystems. This voltage conversion is required because these components are not designed to operate at 270 VDC, and direct connection to the high-voltage bus could result in electrical damage.

ESC The propeller system is supplied through electronic speed controllers (ESCs), which convert the DC input from the 270 VDC bus into a controlled three-phase output for the electric motors. The ESCs regulate motor speed by adjusting the power delivered to the motors, thereby controlling the propeller thrust.[6]

BMS The battery pack is controlled by a battery management system (BMS). A BMS is an electronic control system used to monitor and manage a battery pack, which consists of multiple cells connected in series and parallel to provide the required voltage and current. Its main purpose is to ensure safe and reliable battery operation by monitoring cell voltage, current, and temperature during both charge and discharge.[7]

[6] URL: https://www.tytorobotics.com/blogs/articles/what-is-an-esc-how-does-an-esc-work [cited 08/06/2026]
[7] URL: https://www.synopsys.com/glossary/what-is-a-battery-management-system.html [cited 08/06/2026]

MPPT An MPPT (Maximum Power Point Tracking) is a device that continuously controls the voltage and current of solar panels so that they operate at their maximum power point, even when solar irradiance and temperature change. This can increase the real-world energy yield by approximately 10–30%[8]. The implementation of MPPT allows the solar panels to operate closer to their maximum power point during the mission. This is important because solar irradiance and temperature change during flight, which can otherwise reduce the power output. The MPPT unit is therefore placed between the solar array and the DC bus or battery charging system to improve the amount of usable solar energy[9].

PDU The Power Distribution Unit (PDU) ensures the distribution and availability of electrical power throughout the system. It manages power delivery between essential and non-essential loads and provides protection for the connected electrical circuits. In addition, the PDU can monitor wiring and isolate faults to prevent a failure in one subsystem from affecting the rest of the electrical system.

10.5. Electrical Block Diagram

Figure 10.2 shows the electrical block diagram of the aircraft power system. The solar panels supply unregulated power to the MPPT unit, which regulates the solar output for use by the aircraft electrical system. During daytime operation, the MPPT supplies power to the 270 V PDU and also charges the battery through the BMS. The BMS monitors and protects the battery during charging and discharging. During night-time operation, the battery supplies power through the BMS to the 270 V PDU.

The 270 V PDU distributes high-voltage power to the propulsion system through the ESCs and to the DC–DC converter. The DC–DC converter steps the voltage down from 270 V to 28 V. The 28 V PDU then distributes low-voltage power to the avionics devices, payload, communication system, and other low-power electrical loads.

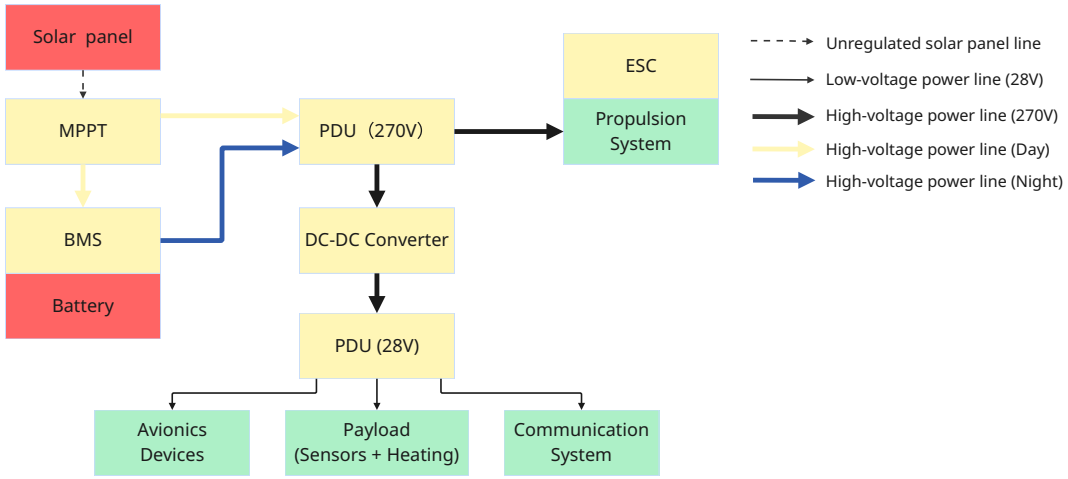

Figure 10.2: *Electrical Block Diagram*

10.6. Removable Battery

This section presents the removable battery concept for the aircraft power system. The motivation for using a removable battery is first discussed in Subsection 10.6.1 by discussing its advantages. Following, the design considerations for integrating the removable battery into the aircraft are then presented in Subsection 10.6.2.

10.6.1. Motivation for Removable Battery

A removable battery approach is considered to improve the operational flexibility and long-term sustainability of the aircraft power system. Since the battery pack is one of the most mass-intensive and degradation-sensitive components in the system, its replacement strategy has a strong influence on the overall lifetime, maintenance effort, and environmental impact.

Battery degradation is mainly driven by charge and discharge cycling, temperature variation, and depth of discharge. For the selected cell, operation at approximately $0.2C/-0.2C$ can provide around 200 cycles before the battery reaches 80% state of health (SOH). [10] Although this cycle life is acceptable for early-stage operation, it also indicates

[8] URL: https://www.anern.com/mppt-inverter.html [cited 08/06/2026]
[9] URL: https://www.safran-group.com/products-services/primary-power-distribution-system [cited 16/6/2026]
[10] URL:https://vepimg.b8cdn.com/uploads/vjfnew//content/files/17467219557-ionelstefan-pdf1746721955.pdf [cited 08/06/2026]

that the battery pack may become a limiting component over the lifetime of the aircraft. Once the battery reaches 80% SOH, after 200 cycles, its capacity might no longer be suitable for the mission.

A removable battery system allows the degraded battery pack to be replaced without redesigning or discarding the rest of the aircraft. This improves sustainability because only the battery module needs to be serviced, refurbished, or recycled, while the airframe, propulsion system, solar array, and avionics can remain in use. In addition, removable batteries make it possible to inspect battery health more easily and to replace individual packs when their performance drops below the required mission threshold.

Another advantage of the removable battery approach is that it leaves room for future technological improvement. As battery technology continues to develop, cells with higher specific energy, longer cycle life, or improved thermal performance could be integrated into the same aircraft architecture. Cao et al. showed that several next-generation conversion-reaction battery systems can theoretically achieve energy densities above 1000 $\mathrm{Wh\,kg^{-1}}$ [89]. Therefore, designing the battery as a removable module provides flexibility for future upgrades and reduces the risk of locking the aircraft design to one specific battery technology.

10.6.2. Design Considerations for Removable Battery Integration

Based on the removable battery approach, the battery pack is divided into smaller units, with the cells connected in series inside each unit as described in Subsection 10.3.4. The removable design also affects operations and logistics. A damaged or degraded battery module can be replaced individually instead of replacing the complete battery system. This improves maintainability and supports sustainability, since modules that reach their end of life can be removed for inspection, repair, recycling, or second-life use.

Each module would be installed inside a dedicated battery bay and connected to the aircraft structure through a defined mechanical interface. This interface should include guide rails or locating pins to ensure correct positioning during installation, as well as locking mechanisms to prevent movement during flight. The attachment points must be able to carry the expected aerodynamic loads, manoeuvre loads, vibration loads, and landing impact loads. Access panels[11] are recommended so that maintenance personnel can remove and replace a module without disassembling major surrounding aircraft structures.

The mechanical design must also ensure that the battery module remains securely fixed during long-endurance operation. Since the aircraft is intended to operate for extended periods, small relative movements between the battery module and the airframe could lead to wear, connector damage, or fatigue at the mounting points. Therefore, the module should be supported by a rigid tray or frame, with vibration-isolating features where needed. Clear handling points are also included so that the module can be lifted or slid out safely during ground maintenance.

The electrical interface must allow safe connection and disconnection of the high-voltage battery pack. Since the battery pack operates on a high-voltage DC bus, the removable connector must be rated for the maximum pack voltage and current. The connector should include mechanical keying to prevent incorrect installation and should be protected against accidental contact during maintenance. Before the main high-voltage contactors close, a pre-charge circuit should be used to limit inrush current to the power electronics and DC-link capacitors. Additional protection should include fuses, insulation monitoring, short-circuit protection, and interlock circuits that ensure the battery cannot be energized when the module is not fully locked in place.

10.7. Verification and Validation

The section on verification and validation ensures the correctness and physical reasonableness of the calculations in this section. Subsection 10.7.1 checks that there are no mistakes in the calculation logic implemented in the Python code, while Subsection 10.7.2 ensures that the calculated results are representative of reality.

10.7.1. Verification

Verification was performed to check that the battery and power-system calculations were implemented correctly. The verification process focused on the main functions used in the sizing code, including Joule heat generation, battery-pack geometry, total system power demand, charge and discharge calculations, battery volume, solar-panel mass, and the saving of output results. The tests were carried out using the `pytest` package.

The complete test suite passed successfully, as shown in Table 10.1. This indicates that the implemented functions give the expected outputs for the tested cases.

[11] URL:https://palcouk.com/blog/informative/what-is-an-access-panel [cited 08/06/2026]

Table 10.1: *Battery and Power-System Verification Test Results.*

Test	Result
`test_joule_heat_w`	Passed
`test_pack_geometry`	Passed
`test_system_power`	Passed
`test_discharge_calculation`	Passed
`test_charge_calculation`	Passed
`test_battery_volume`	Passed
`test_solar_panel_mass`	Passed
`test_save_results`	Passed
`test_run_returns_saved_results`	Passed

Since all nine tests passed, the current battery sizing code is considered verified for the implemented calculation logic. The results show that the main equations have been correctly translated into code and that the calculated outputs are saved.

10.7.2. Validation

As a validation check, the simulated battery heat generation is compared with the expected energy loss during discharge, approximately 5% of the battery output power is expected to be dissipated as losses:

$$\frac{P_{\text{heat}}}{P_{\text{bat}}} \approx 5.2\%. \tag{10.18}$$

Literature reports round-trip energy efficiencies for lithium-ion batteries ranging from approximately 85.5% to 96% depending on operating conditions [90], corresponding to losses of 4%–14.5%. The 5.2% loss obtained here falls within this range, supporting the order-of-magnitude validity of the 5% loss estimate.

10.8. Results Summary

The results of the power-system sizing are summarised in Table 10.2.

Table 10.2: *Summary of Power-System Sizing Results.*

Parameter	Symbol	Value
Battery mass	m_{bat}	53.1 [kg]
Battery volume	V_{bat}	20.7 [L]
Solar-panel mass	m_{sp}	27.2 [kg]
Battery heat generation during charging (nominal)	$P_{\text{pack,ch}}$	20.6 [W]
Battery heat generation during discharging (nominal)	$P_{\text{pack,dis}}$	281.0 [W]
Number of series cells	N_s	123 [-]
Number of parallel strings	N_p	13 [-]
Total number of cells	N_{cells}	1599[-]

11

Communication and Data Handling

This chapter explores the design of the communication system. First, Section 11.1 compiles the key requirements governing the communication subsystem. Next, Section 11.2 provides an overview of the communication architecture. The subsequent sections present the major design decisions: Section 11.3 discusses the data rates associated with both payload and non-payload data; Section 11.4 describes the primary communication link; Section 11.5 presents the redundant communication system; and Section 11.6 discusses the remaining elements of the communication subsystem. In addition, Section 11.7 explains the verification and validation activities performed for the communication system. Finally, Section 11.8 concludes the chapter with a summary of the final communication system design, including the mass, power, and cost budgets.

11.1. Communication Requirements

The communication system is a critical aircraft subsystem, enabling both mission execution and operational safety. It provides the connection between the aircraft and the ground segment for command, control, telemetry and scientific data transmission.

Stakeholder requirement **REQ-STK02** specifies that the aircraft shall support both data storage and data transmission. Consequently, the communication system must fulfil three primary functions: (1) real-time transmission of telemetry and payload data to the ground station, (2) reception of command and control (C2) signals from the ground station, and (3) onboard storage of measurement data that cannot be transmitted in real time. Together, these functions ensure reliable mission operations while safeguarding the quality of the recorded data.

11.2. Communication Architecture Overview

The communication subsystem is designed to ensure robust data routing, reliable command and control, and high-capacity payload storage. The architecture consists of a Ku-band Starlink Mini terminal[1] as the primary high-bandwidth link, an L-band Iridium terminal providing redundant command and control capability, an onboard NVIDIA[2] processing unit for data handling and compression, a 2 TB SSD for high-resolution payload storage, and a quartz fibre radome with PMI foam insulation and a controllable thermal vent to protect the primary terminal under extreme atmospheric conditions. An overview of the communication architecture is given in the data handling block diagram and can be seen in Figure 11.1.

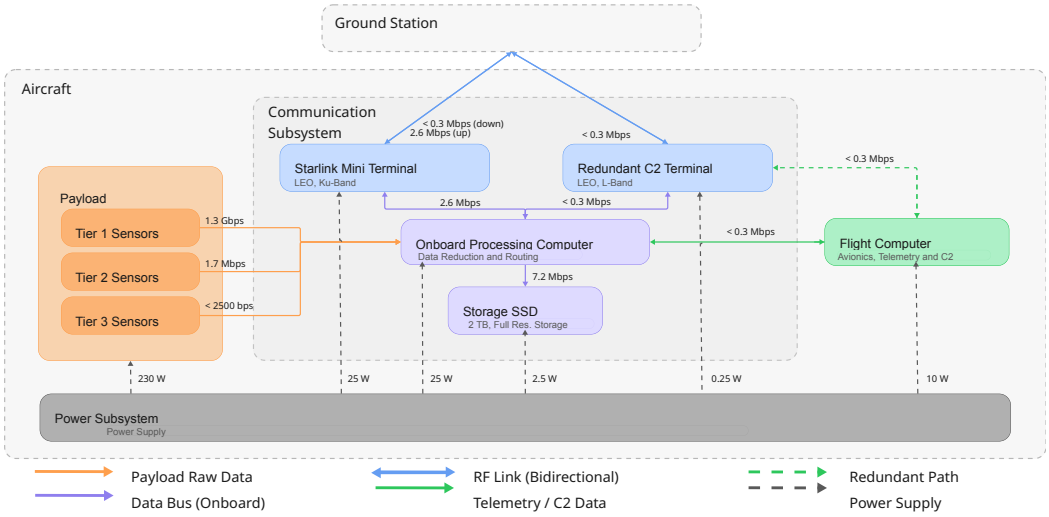

Figure 11.1: *Data Handling Block Diagram*

[1] URL: https://starlink.com/lc/business/aviation [cited 22/05/2026]
[2] URL: https://www.nvidia.com/en-us/autonomous-machines/embedded-systems/jetson-orin/ [cited 05/06/2026]

11.3. Data Rates

Driving the preliminary communication design is the expected data rate to be transmitted. The data rate is split into two components: the scientific data rate originating from the payload sensors, and the data rate necessary for control, command, and telemetry of the aircraft.

Payload Payload data is considered the limiting factor in the communication system design. Providing continuous high-resolution data transmission or complete onboard storage of the payload data at full resolution is not feasible, a hybrid solution is selected.

The payload is divided into three tiers, with Tier 1 being the most limiting factor, followed by Tier 2. Tier 3 is not considered limiting due to its relatively low data rate. To reduce storage and transmission requirements, data compression strategies are applied only to Tier 1 and Tier 2 sensors. For Tier 1, reductions are implemented in spatial resolution, bit depth, and sampling frequency. For transmission, the across-track spatial sampling is reduced from 640 to 320 pixels for the SWIR imager and from 1500 to 750 pixels for the UV imager, with bit depth reduced from 16 to 8 bits. For onboard storage, the full spatial resolution is retained while bit depth is reduced to 12 bits. In both cases, the sampling frequency is reduced to 1 Hz, corresponding to a spatial resolution of approximately 36.6 m at a cruise speed of 36.6 m/s, consistent with comparable airborne science missions [3] [91]. For Tier 2 sensors, only bit depth is reduced from 16 to 8 bits for transmission and to 12 bits for storage. An overview of original, stored and transmitted data rates can be found in Table 11.1.

Non-payload communication Non-payload communication includes telemetry, command, and control (C2). The aircraft should provide continuous telemetry and C2 communication throughout the mission. Literature indicates that the data-rate requirements for non-payload communication are significantly less demanding than those for payload data transmission. Reported maximum data rates for high altitude platforms are on the order of approximately 300 kbps [92]. In the following analysis, this conservative upper bound is adopted for system sizing.

Table 11.1: *Original, Stored, and Transmitted Payload Data Rate*

Category	Data Size	DR Original [bps]	DR Stored [bps]	DR Transmitted [bps]	Source
Tier 1 Dominant Drivers					
Ocean Insight QEPRO	59392 [pixels] × 16 bit × 1 [Hz]	133 038 000	712 700	475 100	[4]
Resonon Pika SWIR	640 × 245 × 16 bit × 120 [fps]	301 056 000	1 881 600	627 200	[5]
Resonon Pika UV	1500 × 255 × 16 bit × 142 [fps]	869 040 000	4 590 000	1 530 000	[6]
Tier 2 Moderate Drivers					
MiniMPL	3000 bins × 16 bit × 1 [Hz]	48 000	36 000	8 000	[7]
NIRQuest	512 pixels × 16 bit × 1 [Hz]	1 638 400	6 100	4 100	[8]
Tier 3 Low Data Rate					
SMP22x	Scalar data	400	400	400	[9]
SGR4	Scalar data	400	400	400	[10][11]
Radiosonde DFM17	Scalar data	1 250	1 250	1 250	[12]
	Total Bit Rate	**1 304 822 450**	**7 228 450**	**2 646 450**	

11.4. Primary Communication Link

The primary communication link should be able to transmit both the reduced payload data, as the non-payload telemetry and C2 data. Subsection 11.4.1 discusses the design elements taken into consideration for selecting the primary communication link. Additionally, the chosen primary communication system is presented. After which, in Subsection 11.4.2 the integration of the primary communication link is discussed.

[3] URL: https://airbornescience.nasa.gov/program/airborne_missions?page=1 [cited 19/05/2026]
[2] URL: https://spegroup.ru/upload/wikifiles/1589842.pdf [cited 22/05/2026]
[3] URL: https://resonon.com/content/files/Resonon---Camera-Data-Sheets-Pika-SWIR.pdf [cited 17/05/2026]
[4] URL: https://resonon.com/content/files/Resonon---Camera-Data-Sheets-Pika-UV.pdf [cited 22/05/2026]
[5] URL: https://www.dropletmeasurement.com/product/mini-mpl/ [cited 22/05/2026]
[6] URL: https://www.ill.eu/documents/1328/SpectroOO.pdf [cited 17/05/2026]
[7] URL: https://cdn.hach.com/1XMCM0ZF/at/rhvp966mh48jtqtc5c8s37q/KippZonen_Data_sheet_SMPx_2025_online.pdf [cited 22/05/2026]
[8] URL: https://www.kippzonen.com/products/sgr4-pyrgeometer [cited 22/05/2026]
[9] URL: https://manuals.plus/m/ffce9e900a60bf52fdaa59136b249ebfe439f37f339704e6cb892c36ef7762ed.pdf [cited 22/05/2026]
[10] URL: https://www.weather.gov/media/upperair/Documents/DB-DFM-17-EN_V01.06.pdf [cited 22/05/2026]

11.4.1. Design Considerations

Several communication architectures were evaluated for the primary communication link. A direct aircraft-to-ground link was initially considered. However, such a configuration required continuous line-of-sight coverage between the aircraft and a ground station. Given the global mission profile and extended operations over oceanic and remote regions, maintaining uninterrupted line-of-sight communication would require a dense worldwide ground station network, making this approach impractical.

An aircraft-to-satellite-to-ground link was therefore selected. Both Geostationary Earth Orbit (GEO) and Low Earth Orbit (LEO) satellite constellations were assessed. GEO satellites operate at an altitude of approximately 35,800 km, resulting in significant free-space path losses and consequently higher transmission power requirements. In contrast, LEO constellations typically operate at altitudes between 500 and 1500 km, substantially reducing the required power for transmission. [92]

Since the aircraft is strongly constrained by the available onboard power, minimising communication power consumption is a key design driver. Consequently, a LEO-based communication architecture was selected. To satisfy the requirement for near-global coverage, preference was given to systems employing large satellite constellations.

The Starlink Mini terminal was selected as a representative communication system due to its suitability for airborne applications[13]. It supports data rates up to approximately 25 Mbps [14], while requiring a typical power consumption of 25 - 40 W during operation and 15 W in idle mode [15]. Because the required operational transmission data rate for this mission is nearly an order of magnitude lower than the terminal's peak throughput capacity, the active power draw is conservatively assumed to scale down toward the lower boundary of its operational range and is budgeted at 25 W.

11.4.2. Starlink Integration

Once the primary link is selected, the integration of the Starlink terminal with the aircraft must be considered. The Starlink Mini terminal has an operational temperature range of $-30°C$ to $50°C$ [15], the minimum temperature experienced by the aircraft is $-80°C$. Therefore, the Starlink terminal must be integrated in a manner that protects it from these conditions, and other atmospheric effects.

A promising solution is to house the Starlink terminal within a blister-shaped radome mounted on top of the fuselage. This configuration protects the communication terminal from the external environment while also providing an aerodynamically streamlined enclosure, thereby minimising the impact of the communication system on the overall aircraft drag [93]. The radome is positioned forward of the wings, near the payload bay section of the fuselage. This location is selected due to geometric constraints, as the aft fuselage section does not provide sufficient volume to accommodate the required radome structure.

An important factor in the material selection of the radome is the dielectric properties of the material. A widely used material for radomes operating in the 10-20 GHz frequency, the range relevant for the Starlink Mini system, is quartz fibre. Quartz fibre is commonly selected due to its low dielectric constant and low loss tangent, which help minimise signal attenuation through the radome wall [94] [16]. Another study identifies Kevlar as a potential radome material due to its low insertion loss performance [95]. However, further investigation shows that Kevlar exhibits a relatively high moisture absorption rate. At high altitudes, this moisture uptake can lead to microstructural degradation due to freeze-thaw cycling in low-temperature environments [96]. Although quartz fibre exhibits comparable insertion losses (below 1 dB), it does not suffer from the same moisture-related degradation. Therefore, quartz fibre is selected as the preferred radome material.

To determine whether an additional insulation layer is required, a thermal analysis was performed. The internal temperature was estimated with Equation 11.1, where T_{skin} is the external skin temperature, assumed to be $-80°C$ in accordance with Chapter 5. Q is the dissipated power of the Starlink terminal, assumed to be 25 W. L is the radome thickness, assumed to be 2.5 mm [95], and k is the thermal conductivity of quartz fibre, assumed to be 0.1 W/mK [97]. A is the total radome area. The Starlink terminal has an area of 0.078 m^2. However, a conservative radome area of 0.15 m^2 was used to account for installation margins.

$$T_{int} = T_{skin} + \frac{QL}{kA} \tag{11.1}$$

The resulting internal temperature was calculated to be $-76°C$. Based on this result, additional insulation is required.

[13] URL: https://starlink.com/lc/business/aviation [cited 22/05/2026]
[14] URL: https://starlink.com/lc/support/article/6137b121-dcfb-2f70-af62-90d2d379e05a [cited 19/05/2026]
[15] URL: https://starlink.com/public-files/specification_sheet_mini.pdf [cited 19/05/2026]
[16] URL: https://www.advanced-ceramic-composites.saint-gobain.com/news/using-quartz-fiber-aerospace-radomes [cited 05/06/2026]

A PMI foam layer was therefore selected as additional insulation material, as it is commonly used in radomes and offers a low dielectric constant and low loss tangent [17]. For the thermal analysis, T_{skin} was again taken as $-80°C$, with $Q = 25W$ and a thermal conductivity of $k = 0.05W/mK$ for PMI foam [98]. To achieve an internal temperature of $-25°C$ under these conditions, an insulation thickness of approximately 15 mm is required.

It was also verified that the maximum operational temperature is not exceeded within the radome. The Starlink terminal upper operating limit of 50°C would be exceeded if the external temperature rises above approximately $-5°C$. While this condition is unlikely during cruise at high altitude, it may occur during take-off and landing phases. Therefore, a controllable ventilation system will be integrated into the radome to regulate internal temperatures during ground and low-altitude operations [18].

11.5. Redundant Communication System

Command and control (C2) data integrity is a critical design driver for the communication architecture. In Subsection 11.5.1 the measurements taken to ensure a safe C2 link are explained. After which in Subsection 11.5.2 the fault management of the communication system is discussed.

11.5.1. Command and Control Integrity

In order to ensure a safe, continuous C2 link, two measures have been taken:

Firstly, a dedicated bandwidth of 300 kbps is reserved on the Starlink terminal at all times for non-payload data. In the event of link degradation, this ensures that non-payload data is prioritised over payload data, preserving aircraft controllability and system awareness.

Secondly, a secondary communication system is included to provide redundancy in the event of Starlink failure. A key requirement for this system is that it must not interfere with the primary Starlink terminal, which operates in the Ku-band. Therefore, an Iridium terminal operating in the L-band is selected and integrated as a patch antenna on the fuselage, minimising the aerodynamic impact. The Iridium system is capable of supporting data rates up to 700 kbps, sufficient for the non-payload communication requirements [19]. It is widely used as a redundant satellite communication system in aerospace applications [20] and has also been employed in comparable environmental UAV missions [21].

11.5.2. Communication Fault Management and Flow Diagram

To ensure smooth communication, three modes have been predetermined. To ensure robust and fail-safe communication, a state-based fault management architecture is implemented. The system defines three operational modes governing communication behaviour under nominal, degraded, and failure conditions.

State 1 - Nominal Operation The Starlink terminal is active (25 W), while the Iridium terminal remains in idle mode (0.25 W). Both payload and non-payload data can be transmitted continuously.

State 2 - Degraded Starlink This mode is triggered when the Starlink link margin drops below 3 dB. The Iridium terminal is activated automatically, and C2 together with minimal telemetry are routed via the Iridium link. The Starlink terminal continues operation where possible, while payload transmission is reduced if necessary.

State 3 - Safe Mode This mode is triggered after complete Starlink loss persisting for 15 seconds. The Iridium system becomes the primary communication link and transmits only C2 and essential telemetry. All payload transmission is suspended until Starlink connectivity is restored.

An overview of the fault management is given in the communication flow diagram and can be seen in Figure 11.2.

11.6. Onboard Data Storage and Processing

In addition to the transmission units, the communication system requires supporting elements for data storage and onboard processing.

For data storage, the required capacity was estimated based on an assumed operational duty cycle of 7 hours per day over the full mission duration (Chapter 5), corresponding to approximately $1.51 \cdot 10^6$ seconds. Using the data rates defined in Table 11.1, this results in a total storage requirement of approximately 1.36 TB. To provide sufficient

[17] URL: https://www.generalplastics.com/wp-content/uploads/2016/12/White-Paper-PU-Foam-Dielectric-Materials-for-Use-in-Radomes-and-Other_Applications.pdf [cited 05/06/2026]
[18] URL: https://patents.justia.com/patent/12431606 [cited 05/06/2026]
[19] URL: https://ifp.iridium.com/service-type/broadband/ [cited 05/06/2026]
[20] URL: https://htt.io/learning-center/iridium-satellite-and-scada-system-communication [cited 05/06/2026]
[21] URL: https://www.iridium.com/case-studies/record-breaking-nasa-uav-mission-made-possible-satcom [cited 05/06/2026]

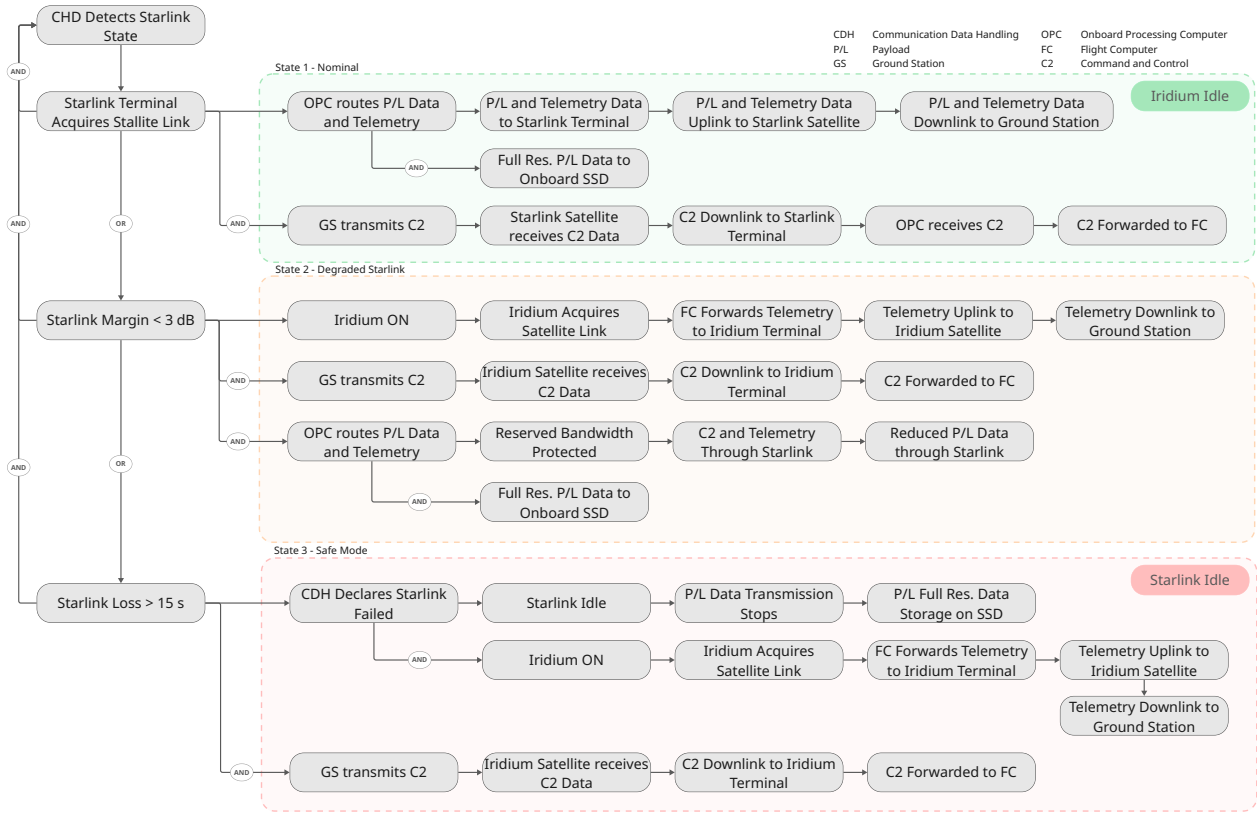

Figure 11.2: *Communication Flow Diagram*

design margin, a 2 TB commercial solid-state drive (SSD) was selected. The chosen unit has a mass of approximately 0.05 kg and a power consumption of approximately 2.5 W [22].

An onboard data processing unit is also required to manage the data between the payload sensors and the communication system. The unit serves two primary functions: data reduction and data routing. For data reduction, the processing unit applies the compression and downsampling described in Section 11.3. For data routing, it directs the processed data streams to the appropriate output channels: compressed low-resolution data is transmitted in real time via the Starlink terminal, while high-resolution data is stored locally on the onboard SSD. A suitable candidate is an NVIDIA computing platform commonly used in UAV applications[23]. Such systems typically have a power consumption in the range of 15 - 40 W and a mass of approximately 0.3 - 0.5 kg [24].

11.7. Verification and Validation

For the verification and validation of the communication subsystem design, the high-level communication requirements are used as the primary reference framework: (1) real-time transmission of telemetry and payload data to the ground station, (2) reception of command and control (C2) signals from the ground station, and (3) onboard storage of measurement data that cannot be transmitted in real time.

In addition to the requirement-based verification, all numerical parameters and equations adopted from literature sources have been cross-validated using at least two independent references where possible, in order to reduce dependency on single-source assumptions.

Real-Time Telemetry and Payload Transmission A link budget analysis was performed to verify the feasibility of both the uplink and downlink communication links between the aircraft-mounted Starlink terminal and the satellite constellation. The resulting link budgets are presented in Table 11.2 and Table 11.3. Both demonstrate positive link margins, indicating successful link closure under the assumed operating conditions. Values used in the link budget were either derived using Equation 11.2 to Equation 11.5, or obtained directly from manufacturer data and literature sources, as indicated in the tables.

[22] URL:https://download.semiconductor.samsung.com/resources/data-sheet/Samsung_SSD_870_EVO_Data_Sheet_Rev1.1_230509_10129505074839.pdf [cited 22/05/2026]
[23] URL: https://www.roboticsandautomationmagazine.co.uk/news/drones/27010.html [cited 05/06/2026]
[24] URL: https://www.nvidia.com/en-us/autonomous-machines/embedded-systems/jetson-orin/ [cited 05/06/2026]

Table 11.2: *Downlink Budget - Satellite to Aircraft*

Parameter	Value	Unit	Source
Downlink Data rate	0.3	Mbps	
Distance	600	km	[26]
Downlink Frequency	11450	MHz	[99] [100]
FSPL	-169.2	dB	
EIRP	37.3	dB	[27] [28]
Gain Rx	31.9	dBi	[27] [28]
T_{sys}	200.0	K	[29]
G/T	8.9	dB/K	[101] [29]
k	-228.6	dB	[101]
$L_{attenuation}$	-7.3	dB	[101]
L_{radome}	-1	dB	[95]
C/N_0	97.3	dB	
E_b/N_0	43.5	dB	
Margin	3.0	dB	[102]
Excess	**39.5**	dB	
Link budget closed			

Table 11.3: *Uplink Budget - Aircraft to Satellite*

Parameter	Value	Unit	Source
Uplink Data rate	2.9	Mbps	
Distance	600	km	[26]
Uplink Frequency	14250	MHz	[99]
FSPL	-171.1	dB	
EIRP	38.2	dB	[27] [28]
Gain Rx	–	dBi	
T_{sys}	–	K	
G/T	9.3	dB/K	[29]
k	-228.6	dB	[101]
$L_{attenuation}$	-10.3	dB	[101]
L_{radome}	-1	dB	[95]
C/N_0	104.0	dB	
E_b/N_0	39.3	dB	
Margin	3.0	dB	[102]
Excess	**36.3**	dB	
Link budget closed			

The free-space path loss (FSPL) is calculated using Equation 11.2[25], where d is the distance from the aircraft to the satellite in km, and f the link frequency in MHz.

$$\text{FSPL} = 20\log_{10}(d) + 20\log_{10}(f) + 32.45 \tag{11.2}$$

The antenna gain-to-noise-temperature ratio (G/T) is given by Equation 11.3 [101], where G_{rx} is the receiver antenna gain in dBi and T_{sys} is the system noise temperature in K.

$$\frac{G}{T} = G_{\text{rx}} - 10\log_{10}(T_{\text{sys}}) \tag{11.3}$$

The noise power spectral density is given by Equation 11.4 [101], where k is Boltzmann's constant expressed in dB, and L_{other} represents additional losses in dB.

$$\frac{C}{N_0} = \text{EIRP} + \frac{G}{T} - k - \text{FSPL} - \text{other losses} \tag{11.4}$$

The energy per bit to noise power spectral density ratio (E_b/N_0) is given by Equation 11.5 [101][30], where DR is the data rate in bps.

$$\frac{E_b}{N_0} = \frac{C}{N_0} - 10\log_{10}(\text{DR}) \tag{11.5}$$

A link margin of 3 dB is used as a design rule of thumb [102]. Both uplink and downlink budgets exceed this minimum requirement, confirming adequate performance margin.

Link budget analysis was limited to the aircraft-to-satellite segment, as this represents the portion of the system directly influenced by the aircraft design. The satellite-to-ground communication segment is part of the Starlink network infrastructure and is therefore outside the scope of the present report. It is assumed that the communication beyond the satellite is maintained by the service provider.

[25] URL: https://ib-lenhardt.com/kb/glossary/fspl [cited on 04/06/2026]
[26] URL: https://starlink.com/public-files/Gen2StarlinkSatellites.pdf?srsltid=AfmBOordFbWd2krYkhk2h_mDSYsYdOXAqLY17HL0CEZr2l6Xm7Gw7AQh [cited 04/06/2026]
[27] URL: https://apps.fcc.gov/els/GetAtt.html?id=259301 [cited 04/06/2026]
[28] URL: https://www.ofcom.org.uk/siteassets/resources/documents/consultations/category-3-4-weeks/281181-kepler-communications-inc-application/associated-documents/starlink-annex.pdf?v=393905 [cited 04/06/2026]
[29] URL: https://starlink.com/public-files/12GHzInterferenceStudy_062022.pdf?srsltid=AfmBOoqwC_l82pgEgU5shdU1XaY227MTPjzxMiCRIxe1eqo86s-g351r [cited 04/06/2026]
[30] URL: https://satellitegroundstation.com/resources/satellite-link-budget-basics-step-by-step-plain-english/ [cited 04/06/2026]

As previously mentioned, the numerical assumptions used in this analysis have been cross-checked against multiple literature sources. In addition the resulting link budgets are consistent with representative LEO satellite link budgets presented in standard references [103].

Continuous command and control Continuous command and control (C2) reception is verified through functional tracing of the fault management states defined in Section 11.5. In the nominal case, C2 is routed via the Starlink terminal with a reserved bandwidth allocation of 300 kbps. During link degradation, continuous C2 transmission is maintained while the system transitions towards the redundant communication link, ensuring that control authority is preserved throughout the degradation process. In the event of complete Starlink failure, the Iridium system becomes the primary communication link and continues to provide C2 functionality. Across all operational states, the C2 data path remains continuously available, ensuring uninterrupted command and control of the aircraft.

The 15-second failure criterion is further supported by literature describing Starlink's LEO orbit handover behaviour. Starlink satellites perform frequent handovers with intervals of 15 seconds, with individual handover events lasting between 139 ms and 384 ms. The loss of link margin persisting beyond a full handover cycle cannot be attributed to routine constellation switching and is instead treated as genuine link failure condition [104].

Onboard Storage The total storage requirement is derived from a payload data rate of 7.2 Mbps and an assumed operational duty cycle of 7 hours per day over a 60-day mission, resulting in approximately 1.36 TB of required storage. The selected 2 TB SSD therefore provides a storage margin of approximately 47%. This margin ensures sufficient capacity even under more conservative operating scenarios, such as an extended payload operation of 10 hours a day, while remaining within onboard storage limits throughout the mission.

11.8. Final Communication Configuration

The communication system is designed to satisfy three primary functions: real-time transmission of telemetry and payload data, continuous command and control reception, and onboard storage of high-resolution measurement data. These functions are fulfilled through a hybrid architecture combining a Starlink Mini terminal as the primary high-bandwidth link, an Iridium terminal providing redundant command and control capability, a 2 TB SSD for onboard data storage, and an NVIDIA processing unit for data reduction and routing. The Starlink terminal is housed within a quartz-fibre radome with 15 mm PMI foam insulation and a controllable thermal vent, ensuring operation within the terminal's specified temperature limits across all flight phases. Link budget analysis confirms that both uplink and downlink close with margins exceeding 36 dB, above the 3 dB minimum threshold. The three-state fault management architecture ensures that C2 connectivity is maintained under nominal, degraded, and failure conditions at all times. The total subsystem mass is 5.06 kg, power consumption is 58 W, and estimated cost is 3630 Euro, including a safety margin. The communication subsystem mass, power, and cost breakdown can be seen in Table 11.4.

Table 11.4: *Communication Subsystem Mass, Power, and Cost Breakdown*

Component	Power [W]	Mass [kg]	Cost [€]
Starlink Mini Terminal	25	3.00	400
Iridium Terminal	0.25	0.31	700
Storage SSD	2.5	0.05	1000
NVIDIA	25	0.40	1000
RF cabling and connectors	0	0.10	< 100
Mounting hardware	0	0.65	< 100
Safety factor	1.1	1.1	1.1
Total	**58**	**5.06**	**3630**

12

Stability and Control

This chapter presents the stability and control design of the aircraft. First, the sizing philosophy is introduced in Section 12.1, after which the aileron and V-tail sizing procedures are described in Section 12.2 and Section 12.3 respectively. Special attention is given to the coupled pitch and yaw control introduced by the V-tail ruddervators. The chapter then presents the flight control instrumentation in Section 12.4, aerodynamic derivative analysis in Section 12.5, tail force calculation method in Section 12.6, and the verification and validation approach in Section 12.7.

12.1. Design Philosophy

Since the aircraft is intended to perform high-altitude long-endurance operations, the design must prioritize energy storage and management. In this regard, control surface sizing is crucial, as it influences the remaining area available for the solar panels on the aircraft. Therefore, the design philosophy for control surface sizing was established as providing sufficient manoeuvrability with minimum surface area, while also minimizing tail volume to reduce weight and drag. Since both climb and descent are expected to be conducted within segregated airspace, the manoeuvrability requirements associated with traffic avoidance were not treated as primary drivers in the control surface sizing process.

12.2. Aileron Sizing

From the maximum load factor $n_{max} = 2.5$, a value of $n_{roll} = 2.4$ was considered to get a maximum bank angle of 65.38° using Equation 12.1 to have a safe limit.

$$cos(\phi_{max}) = \frac{1}{n_{roll}} \tag{12.1}$$

It was decided that in most demanding conditions, the aircraft should have a maximum steady roll rate that will allow to reach the maximum bank angle between 2 to 3 seconds, which was chosen as $T_{roll} = 2.6\,\text{s}$. This value led to a maximum roll rate of 25 °/s from Equation 12.2. A maximum aileron deflection of 20° was considered as a design limit to avoid flow separation [105].

$$p_{max} = \frac{\phi_{max}}{T_{roll}} \tag{12.2}$$

A steady-state roll can be described with Equation 12.3 in a non-dimensionalized form.

$$c_{l_{\delta a}} \delta a + c_{l_p} \frac{pb}{2V} = 0 \tag{12.3}$$

Given the cruise speed ($V_{cruise} = 36.55\,\frac{\text{m}}{\text{s}}$) and stall speed ($V_{stall} = 32.47\,\frac{\text{m}}{\text{s}}$), Equation 12.4 indicated an 12.5% increase in the maneouvrability requirement under landing conditions. This increase was considered negligible, and therefore the cruise speed was adopted as the sizing condition. Since higher flight speeds provide greater aerodynamic effectiveness, this choise yields a smaller required aileron surface area, which was found more beneficial for the aircraft design over a better manoeuvrability.

To size the ailerons, it was decided that with a maximum aileron deflection $\delta a_{max} = 20°$, the aircraft should reach a maximum steady-state roll rate $p_{max} = 25\,°/\text{s}$ at cruise speed (V_{cr}). Assuming that the roll damping derivative (c_{l_p}) does not vary significantly with the aileron design when compared to the roll authority derivative ($c_{l_{\delta a}}$), the criteria in Equation 12.4 was established.

$$|c_{l_{\delta a}}| = |\frac{c_{l_p} \cdot p_{max} \cdot b}{\delta a_{max} \cdot 2 \cdot V_{cr}}| \tag{12.4}$$

Following the criteria in Equation 12.4, the following design sequence was used to size the ailerons. The sequence is also visualized in Figure 12.1. For the equality conditions, tolerance of 10^{-3} was used.

1. For a given wing area (S_w), root chord length (C_{r_w}), and taper ratio (λ_w), the initial aileron width is assumed to be 10% of the chord length in the corresponding spanwise location.
2. Based on engineering judgement, it is assumed that the maximum tip position of an aileron can be 90% of the half-span of the wing, measuring from the root chord, along with an initial aileron length assumption of 10 m.
3. The initial aileron design is put into the AVL Software, and an aileron input of 5° is implemented (Left Trailing-Edge up, Right Trailing-Edge down), and the obtained $c_{l_{\delta a}}$ is compared with the required value obtained from Equation 12.4, also using c_{l_p} obtained from the software.
4. If $c_{l_{\delta a}}$ is higher than the required value, **Size Reduction Loop** is executed: Keeping the tip aileron location constant, initially-assumed aileron length is reduced in increments proportional to the offset from the required value such that the minimum aileron size is achieved, saving space for the solar panels.
5. If $c_{l_{\delta a}}$ is lower than the required value, **Span Extension Loop** is executed: Keeping the tip aileron location constant, initially-assumed aileron length is increased in increments proportional to the offset from the required value until the minimum aileron size is achieved. The loop can proceed until the root aileron location becomes 5% half-span away from the wing root.
6. In **Span Extension Loop**, if aileron root location becomes 5% half-span away from the wing root and the obtained $c_{l_{\delta a}}$ is still insufficient, **Chord Extension Loop** is executed: the aileron chord length is increased in increments until the minimum aileron size is achieved. The loop can proceed until the aileron hinge location becomes 5% wing Mean Aerodynamic Chord length away from the wing spar location.
7. In **Chord Extension Loop**, if aileron hinge chord location becomes 5% wing Mean Aerodynamic Chord length behind the wing spar and the obtained $c_{l_{\delta a}}$ is still insufficient, the wing design must be re-evaluated such that sufficient roll authority can be achieved.
8. If the required roll authority is achieved with the aileron design loops mentioned in the previous steps, the remaining wing area and the loads encountered by the aileron must be considered. If both are feasible, then the design is complete. Otherwise, the wing design must be re-evaluated.

Using the Aileron Sizing Logic, the final aileron dimensions in Table 12.1 were obtained following the design iterations.

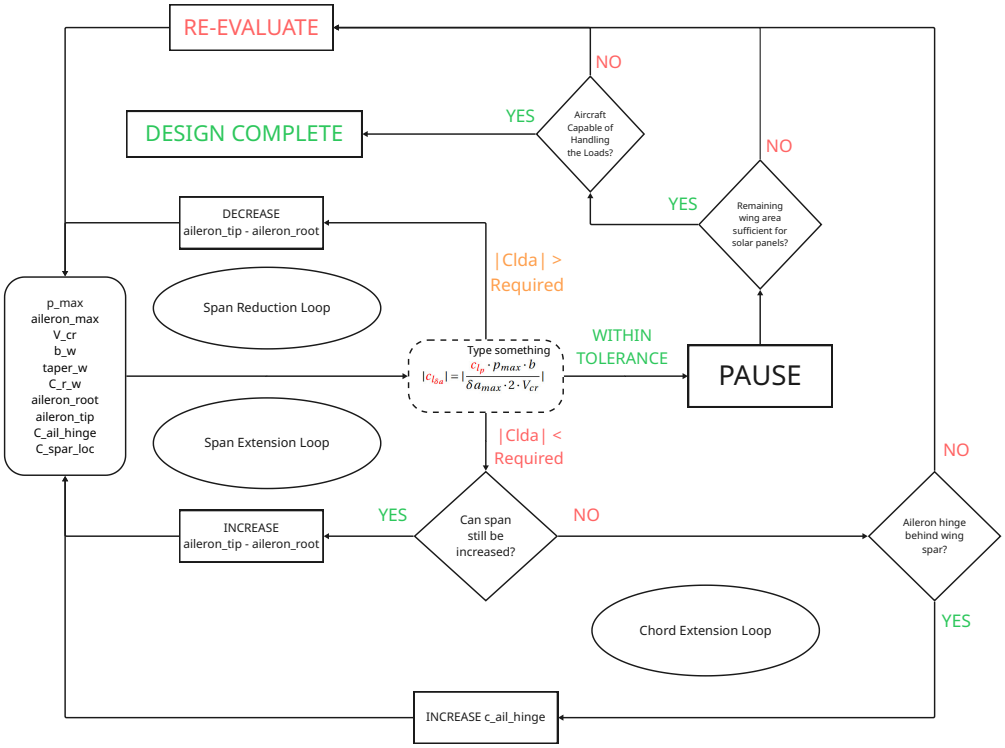

Figure 12.1: *Aileron Sizing Logic Flowchart*

Table 12.1: *Aileron Dimensions*

Aileron Root Location	49% half-span
Aileron Tip Location	90% half-span
Aileron Hinge Location	79% chord (from LE)
Aileron Surface Area (Total)	6.7 m^2

12.3. Tail Sizing

Following the trade-off process, V-Tail configuration was chosen for the tail design. While a V-Tail was found advantageous in terms of hosting only two tail surfaces and thereby reducing the drag due to fuselage-tail interference, it introduces a challenge in controllability due to the coupled control of yaw and pitch: There are no separate elevator and rudder surfaces but a ruddervator on each side of the V-tail, and the ruddervators should be able to execute simultaneous pitch and yaw commands at once. It was decided to account for control coupling through the use of programmable flight control computers and fly-by-wire system.

To assess the yaw and pitch capabilities of the tail separately, two different deflection modes were defined as **Elevator** (δe) and **Rudder** (δr). Elevator deflection angle, which is to be used for pitch control, has been defined positive for both ruddervators trailing-edge down. Rudder deflection angle, which is to be used for yaw control, has been defined positive for left ruddervator trailing-edge down and right ruddervator trailing-edge up. These ruddervator deflection modes are visualized in Figure 12.2.

(a) *Elevator Deflection Mode (δ_e)* **(b)** *Rudder Deflection Mode (δ_r)*

Figure 12.2: *Deflection Modes of the Ruddervator.*

Tail design procedure was initiated by obtaining a tail arm that ensures positive static stability, following Equation 12.5 from the aircraft equations of motion.

$$c_{m_\alpha} = c_{L_{w_\alpha}} \frac{x_{cg} - x_{ac}}{MAC_w} - c_{L_{h_\alpha}} (1 - \frac{d\epsilon}{d\alpha})(\frac{V_h}{V})^2 (\frac{S_h}{S})(\frac{l_h}{MAC_w}) < 0 \tag{12.5}$$

To provide a stabilizing tail arm, the aircraft should therefore satisfy the minimum criteria established in Equation 12.6.

$$l_h > \frac{c_{L_{w_\alpha}}}{c_{L_{h_\alpha}}} \frac{(x_{cg} - x_{ac})}{(\frac{V_h}{V})^2 (\frac{S_h}{S})(1 - \frac{d\epsilon}{d\alpha})} \tag{12.6}$$

In order to guarantee stability while keeping a minimum tail arm, it was decided to make the tail arm 5% larger than the threshold value for stability, which resulted in Equation 12.7 as the sizing criteria.

$$l_h = 1.05 \frac{c_{L_{w_\alpha}}}{c_{L_{h_\alpha}}} \frac{(x_{cg} - x_{ac})}{(\frac{V_h}{V})^2 (\frac{S_h}{S})(1 - \frac{d\epsilon}{d\alpha})} \tag{12.7}$$

After ensuring a stable design, controllability was taken into consideration, under which the V-tail and ruddervator sizing were made.

To facilitate the automation of the sizing process, certain geometric assumptions were made, such that the code could size the tail for a specified geometry. These assumptions involved the values for $\frac{S_h}{S}, \Gamma_{tail}, AR_{tail}, \lambda_{tail}$, based on engineering judgement.

Table 12.2: *Initial Assumptions used for Tail Sizing.*

Variable	Description	Value
$\frac{S_h}{S}$	Horizontal tail area (projection) to wing area ratio	0.1
Γ_{tail}	V-tail dihedral angle	100°
AR_{tail}	Tail aspect ratio	5
λ_{tail}	Tail taper ratio	1

Using these assumptions, Equation 12.8, Equation 12.9, and Equation 12.10 were used respectively to determine the dimensions of the tail.

$$S_{tail} = \frac{S_h}{S} \cdot \frac{S_w}{cos(\Gamma_{tail})} \tag{12.8}$$

$$b_{tail} = \sqrt{AR_{tail} \cdot S_{tail}} \tag{12.9}$$

$$C_{r_{tail}} = \frac{S_{tail}}{0.5 \cdot b_{tail}(1+\lambda_{tail})} \tag{12.10}$$

After setting the procedure to determine the fundamental tail dimensions, ruddervator sizing was considered. To ensure sufficient controllability, three criteria were established.

Criteria 1: For a multi-propeller configuration that has more than two propellers, the yawing moment due to One Engine Inoperative (OEI) condition of one of the aft-most propeller should be compensated by the ruddervators with a deflection $\delta r_{max} = 5°$, resulting in a yaw authority $c_{n_{\delta r}}$ specified in Equation 12.11.

$$|c_{n_{\delta r}}| = |\frac{T \cdot \max(y_{cg_{prop}})}{\delta r_{max} \cdot q_{cruise} \cdot S \cdot b}| \tag{12.11}$$

Criteria 2: Due to the dihedral of the V-tail, a yaw command will also result in a roll moment, which should be compensated by ailerons using 80% of the maximum deflection capacity at highest. This results in a criteria for the roll derivative $c_{l_{\delta r}}$, specified in Equation 12.12.

$$|c_{l_{\delta r}}| \leq 0.8 \cdot |\frac{\delta a_{max}}{\delta r_{max}} c_{l_{\delta a}}| \tag{12.12}$$

Criteria 3: The tail should be able to compensate for the longitudinal moments on the aircraft with 95% of $\delta e_{max} = 22°$. This results in a requirement for the pitch authority $c_{m_{\delta e}}$, specified in Equation 12.13, assuming the tail angle-of-attack remains independent of the ruddervator deflection.

$$|c_{m_{\delta e}}| = 1.05 \cdot |\frac{c_{m_{ac}} + c_{L_{W\alpha}} \alpha_{land} \frac{x_{cg}-x_w}{MAC_w} - c_{L_{h\alpha}} \alpha_{land}(1-\frac{d\epsilon}{d\alpha})(\frac{V_h}{V})^2(\frac{S_h}{S})(\frac{l_h}{MAC_w})}{\delta e_{max}}| \tag{12.13}$$

After the criteria were set, the Tail Sizing Logic was created to iterate and obtain the optimum tail design. The sequence is also visualized in Figure 12.3. For the equality conditions, a tolerance of 10^{-3} was used.

1. Using the assumed values of $\frac{S_h}{S}, \Gamma_{tail}, AR_{tail}, \lambda_{tail}$; initial values of tail dimensions $S_{tail}, b_{tail}, C_{r_{tail}}$ are obtained.
2. Using the initial tail dimensions, the pitch behavior of aircraft is simulated in AVL Software with a 5° elevator deflection mode (Left and Right Ruddervators Trailing-Edge Down) to generate a nose-down pitching moment, and the $c_{m_{\delta e}}$ value is checked with the criteria established in Equation 12.13.
3. Using the initial tail dimensions, the yaw behavior of aircraft is simulated in AVL Software with a $-5°$ rudder deflection mode (Left Ruddervator Trailing-Edge Down, Right Ruddervator Trailing-Edge Up) to generate a nose-right yaw moment, and the $c_{n_{\delta r}}$ value is checked with the criteria established in Equation 12.11.
4. If $c_{m_{\delta e}}$ and $c_{n_{\delta r}}$ are both above the required value, then the **Size Reduction Loop** is executed: the ruddervator root location is increased, and the tip location is decreased along the tail span in increments such that the minimum control surface area satisfying the control authority requirements is obtained.
5. If $c_{m_{\delta e}}$ or/and $c_{n_{\delta r}}$ is/are below the required value, then the **Chord Extension Loop** is executed: the ruddervator hinge location is increased in increments such that the minimum control surface area satisfying the control authority requirements is obtained.

6. If the ruddervator hinge location reaches 35% tail Mean Aerodynamic Chord and thereby gets close to the spar while still lacking sufficient control authority, **Surface Extension Loop** is executed: The tail surface area is increased in increments such that the minimum control surface area satisfying the control authority requirements is obtained.
7. If the ruddervator-induced roll moment ($c_{l_{\delta r}}$) is above the limit established in Equation 12.12, then the tail design must be re-evaluated, and a change in tail dihedral angle must be considered.
8. If the required control authority is achieved with the tail sizing loops mentioned in the previous steps, the loads encountered by the tail must be considered. If feasible, then the design is complete. Otherwise, the tail design must be re-evaluated.

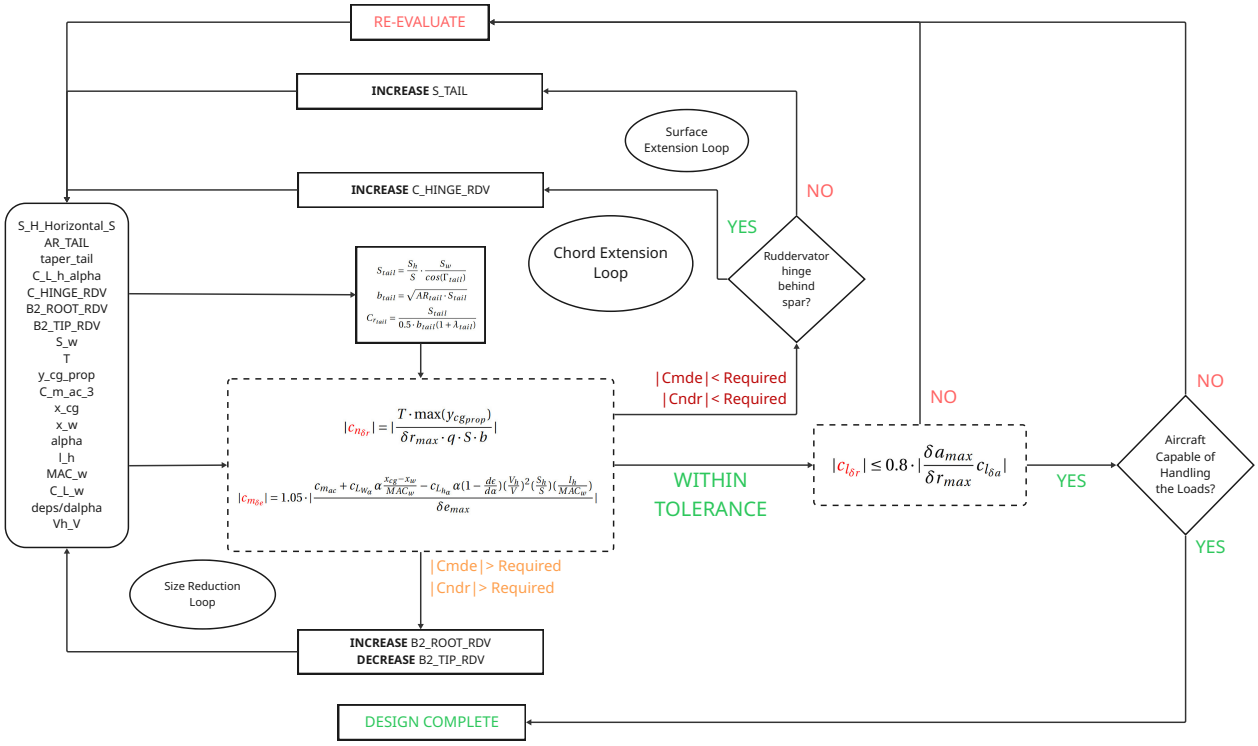

Figure 12.3: *Tail Sizing Logic Flowchart*

Using the Tail Sizing Logic, the final tail dimensions in Table 12.3 were obtained following the design iterations.

Table 12.3: *Tail Dimensions*

Tail Arm	8.18 m
V-Tail Angle	100°
Tail Area	7.69 m^2
Tail Chord Length	1.24 m
V-Tail Span (per side)	3.1 m
Ruddervator Root Location	10% Tail Half-span
Ruddervator Tip Location	90% Tail Half-span
Ruddervator Hinge Location	42% Tail Chord

12.4. Flight Control System

Taking into account the unmanned flight requirement, a fly-by-wire system was adopted for the aircraft, which incorporates a flight control computer between the operator and the actuators on flight control surfaces. The operator commands the flight control computer using satellite communication, and the computer commands the actuators using electronic wires.

The **Pegasus PA-RR-340-7-IH** actuator was selected for the ailerons and ruddervators, as its performance characteristics are well suited to the mission profile of the aircraft [1]. While the use of a single actuator has been considered per control surface at once, it has been decided to accommodate two actuators per control surface for redundancy, which resulted with 8 actuators onboard the aircraft.

As flight control computer, **Veronte Autopilot 1x** has been selected due to its autonomous flight capability, GNSS-based navigation, and compatibility with satellite communication systems. The system can also be integrated with ADS-B, ensuring traffic awareness during operation [2]. It has been decided to accommodate two flight control computers onboard the aircraft for redundancy, while using only one at once.

The contribution of the flight control system to the mass and power budgets was considered as the contributions of flight control computers, actuators, and cabling. Since the exact cable length and cable density of the flight control system were uncertain at this design stage, a conservative estimate of 900 m of fly-by-wire cable with a linear density of 4 $\frac{\text{kg}}{\text{km}}$ was assumed. This resulted in a total flight control cable mass of 3.58 kg [3]. This conservative estimate was also assumed to account for possible currently unpredicted additions to the flight control system, and a power consumption margin of 7.6 W was added.

For the actuators, the average power consumption was calculated by using an average current $I_{avg} = 1.9\,\text{A}$ and an average voltage $V_{avg} = 24\,\text{V}$ [4]. Considering 4 actuators operate at once, the power consumption (P_{act}) was calculated as 182.4 W from Equation 12.14. The mass per actuator was specified as 0.75 kg, which resulted in an actuator mass of 6 kg as there are 8 of them onboard.

$$P_{act} = 4 \cdot P_{avg} \cdot I_{avg} \tag{12.14}$$

For the flight control computers, the average power consumption was specified as 10 W, and the mass per actuator was given as 0.21 kg [2]. Power calculations were made based on the number of simultaneously operational components, while the mass calculations were made based on the number of equipment onboard. These values resulted in the power and mass estimates provided in Table 12.4.

Table 12.4: *Flight Control System Mass and Power Budget.*

Equipment	Number Onboard	Number Operational Simultaneously	Power [W]	Mass Onboard [kg]
Flight control computer	2	1	10 W	0.42 kg
Actuators	8	4	182.4 W	6 kg
Fly-by-wire cabling	[-]	[-]	7.6 W	3.58 kg
Total	[-]	[-]	200 W	10 kg

12.5. Aerodynamic Derivatives

The aerodynamic derivatives obtained from the AVL Software for the final aircraft design are provided in Table 12.5. For longitudinal behaviour, the derivatives C_{m_α}, C_{m_q}, and $C_{m_{\delta e}}$ were found to be negative, indicating that the aircraft is longitudinally statically stable and the elevator command functions as desired.

For roll behaviour, derivatives C_{l_p}, $C_{l_{\delta a}}$, and C_{l_β} were obtained as negative, indicating that the ailerons function as desired and the aircraft has static roll stability. Regarding the yaw behaviour, $C_{n_{\delta r}}$, C_{n_β},C_{n_r}, and C_{Y_β} were obtained as negative, while $C_{Y_{\delta r}}$ was obtained as positive. The signs indicate that the aircraft has static yaw stability and the rudder command functions as desired.

The non-zero $C_{l_{\delta r}}$ confirmed the expected yaw-roll coupling of the V-tail. However, its magnitude was found to be smaller than the aileron roll authority, so the coupling can likely be compensated by the flight control system, as needed by the sizing criteria in Equation 12.12.

Among damping derivatives, pitch damping (C_{m_q}) was found to be the strongest, while yaw damping (C_{n_r}) was found to be the weakest in terms of magnitude. The relatively strong pitch damping was found beneficial for suppressing short-period oscillations, whereas the weaker yaw damping suggested that the Dutch roll behaviour should be further assessed through eigenvalue analysis.

[1] URL:https://www.pegasus-actuators.com/knowledge/cases/hale-uavs.html [cited 10/06/2026]
[2] URL:https://pdf.aeroexpo.online/viewerCatalog/embention/veronte-autopilot-1x-eng-datasheet-hr-print/181390-26799-_2.html[cited 10/06/2026]
[3] URL:https://www.juddwire.com/wp-content/uploads/2017/03/2017_JuddWire_Aero.pdf[cited 10/06/2026]
[4] URL:https://www.pegasus-actuators.com/fileadmin/user_upload/products/docs/PA-R-340-7_specifications.pdf[cited 10/06/2026]

Table 12.5: *Stability and Control Derivatives*

Derivative	Description	AVL Value	Criteria
Longitudinal Derivatives (Symmetric Motion)			
C_{m_α}	Pitch (Longitudinal) Stability	$-2.837\,\text{rad}^{-1}$	< 0 (Stable)
C_{m_q}	Pitch Damping	-22.797	< 0 (Stable)
$C_{m_{\delta_e}}$	Longitudinal Control Authority	$-1.658\,\text{rad}^{-1}$	< 0 (Control Power)
Lateral Derivatives (Asymmetric Motion)			
C_{Y_β}	Side-force due to Sideslip	$-0.132\,\text{rad}^{-1}$	< 0 (Restoring)
C_{n_β}	Yaw Stability	$0.032\,\text{rad}^{-1}$	> 0 (Stable)
C_{l_β}	Dihedral Effect	$-0.005\,\text{rad}^{-1}$	< 0 (Stable)
$C_{Y_{\delta_r}}$	Side-force due to Yaw Command	$0.162\,\text{rad}^{-1}$	> 0 (Control Power)
$C_{n_{\delta_r}}$	Yaw Control Authority	$-0.041\,\text{rad}^{-1}$	< 0 (Control Power)
$C_{l_{\delta_r}}$	Roll due to Rudder (V-Tail effect)	$0.011\,\text{rad}^{-1}$	$\neq 0$ (Cross-Coupling)
Yaw Rate Derivatives			
C_{n_r}	Yaw Damping	-0.022	< 0 (Stable)
C_{l_r}	Roll due to Yaw Rate	0.234	$\neq 0$ (Cross-Coupling)
Roll Rate & Aileron Derivatives			
C_{n_p}	Yaw due to Roll Rate	$-0.082\,\text{rad}^{-1}$	< 0 (Cross-Coupling)
C_{l_p}	Roll Damping	-0.748	< 0 (Stable)
$C_{l_{\delta_a}}$	Aileron Roll Authority	$-0.574\,\text{rad}^{-1}$	< 0 (Control Power)

For spiral stability, the criterion established in Equation 12.15 was checked.

$$\frac{C_{l_\beta} C_{n_r}}{C_{l_r} C_{n_\beta}} = 0.014 < 1 \tag{12.15}$$

The value of the fraction being lower than 1 indicated that the final design has spiral instability. However, considering the cruise speed and the autonomous flight control system, the predicted spiral instability has been expected to be manageable through closed-loop lateral-directional stabilization.

The derivative-based assessment indicated that the final aircraft design has acceptable static stability and controllability, surfaces producing the intended moment responses. The main limitations identified were the predicted spiral stability and the relatively weak yaw damping. A dynamic stability analysis has been found necessary to further assess the aircraft behaviour, and to verify that the flight control system can provide sufficient closed-loop stabilization.

12.6. Tail Forces

Using the aerodynamic derivatives obtained from AVL Simulation Software in Table 12.5, the maximum tail force was calculated for structural sizing.

To obtain the maximum tail load, the maximum possible ruddervator deflection was considered as in Equation 12.16 and Equation 12.17.

$$C_{L_{h,\max}} = C_{L_{h_{\delta e}}} \delta_{e_{max}} \tag{12.16}$$

$$F_{\text{tail}} = C_{L_{h,\max}} q_{land} \left(\frac{V_h}{V}\right)^2 S_{\text{tail}} \tag{12.17}$$

To obtain the lift gradient with respect to the ruddervator deflection ($C_{L_{h_{\delta e}}}$), the pitch control authority was used as in Equation 12.18.

$$C_{L_{h_{\delta e}}} = \frac{-C_{m_{\delta e}}}{\left(\frac{l_h}{\bar{c}}\right)\left(\frac{V_h}{V}\right)^2 \left(\frac{S_h}{S}\right)} \tag{12.18}$$

Following the determination of $C_{L_{h_{\delta e}}}$, the maximum tail force was separated into its vertical and lateral components by accounting for the V-Tail dihedral angle, as in Equation 12.19 and Equation 12.20.

$$F_{\text{tail,vert}} = -F_{\text{tail}} \cos(\Gamma_{tail}) \tag{12.19}$$

$$F_{\text{tail,lat}} = F_{\text{tail}} \sin(\Gamma_{tail}) \tag{12.20}$$

12.7. Verification and Validation

The verification and validation of the controls subsystem focused on confirming that the implemented sizing logic and force calculations behaved as initially intended. Both individual calculation checks and checks with the shared project input files were performed.

First, the logic of the algorithm was verified by checking convergence behaviour, loop termination, and boundary cases. The code was tested with mock input sets to ensure that all variables were correctly implemented. Boundary cases were also inspected to ensure that the routines did not return non-physical results.

Second, the implemented equations were checked with hand-calculations. The geometry and force equations were inspected to confirm that the calculated control authority increased when the control surface area, allowable deflection, dynamic pressure, or moment arm increased. Similarly, zero-deflection cases were checked to ensure that no artificial control force or moment was generated. These checks verified that the code followed the expected physical behaviour.

Third, the interaction with external tools and other subsystem files was verified. The AVL-derived stability and control derivatives were checked for correct import, sign convention, and order of magnitude before being used in the control surface sizing calculations. The controls outputs were then checked for compatibility with the aircraft-level design state, ensuring that the resulting surface dimensions, actuator requirements, and mass and power estimates could be used by the other subsystems without format or unit inconsistencies.

The validation of the controls subsystem remained preliminary, as no wind-tunnel or flight-test data were available at this design stage. However, the results were considered physically reasonable because the calculated behaviour followed the expected trends and the selected control surfaces produced the intended motions within the assumptions of the conceptual design model. Future validation should include higher-fidelity aerodynamic simulations, dynamic eigenvalue analysis, actuator response testing, and ultimately flight testing to confirm the stability and controllability of the aircraft.

13

Performance Analysis

The performance of the aircraft can be evaluated through several lenses. As such, beyond what has already been analysed in previous chapters, Section 13.1 analyses the performance of the payload instruments and how this fits into the overall climate research field, and Section 13.2 showcases the aircraft's operational flight ceiling.

13.1. Payload Instruments Performance

The design of the payload system is described in Chapter 6. Following the payload system design, the aircraft is equipped with a set of instruments that enable to collect information on all required parameters from the project objective; including trace gas concentrations, background atmospheric properties such as pressure, temperature and humidity, and contrail properties such as their thickness, altitude, and impact on radiation balance.

As mentioned in Chapter 6, spatial resolutions of the instruments range from up to 10m for the imagers and LiDAR; 35-70m for the in-situ temperature, pressure, humidity, aerosols and short-wave radiation measurements; around 650m for the long-wave radiation sensor, and around 1.5km for the point spectrometers used for vertical profiling of the atmosphere.

Looking into currently existing climate models, a paper [106] investigating several Global Climate Models, which are tools used to study "Earth system responses to natural climate variability and anthropogenically driven increases in greenhouse gas emissions and radiative forcing", notes that most GCMs achieve at most a horizontal resolution grid of 0.5° latitude-longitude, which depending on the location on Earth translates to a horizontal grid a few dozen kilometres wide. The paper also emphasizes that this resolution is too coarse to determine specific climate policy needs on regional and local scales with sufficient reliability, which leads to the need for downscaling, a technique that applies conditions extrapolated from GCMs to finer resolution Regional Climate Models (RCMs) [107].

As such, the very fine resolution performance achieved by the instruments in SORA's payload can be used not only to improve GCMs, but also to validate current downscaling techniques and aid in the development of future GCMs with higher resolution. Furthermore, the live-data transmission capability of the aircraft allows for real-time monitoring of smaller spatial and time scale phenomena, like contrail evolution, or aircraft pollution over a certain area on a given day.

Other considerations for the operational performance of some instruments include their surrounding environment temperature and pressure ranges, but for the instruments where this is a concern, an adequate housing compartment is sized in Chapter 6. Another constraint is that measurement instruments will be turned off during the night, in order to conserve power as required by the operational strategy delineated in Chapter 5.

13.2. Aircraft Flight Ceiling

Considering the propulsion system design carried out in Chapter 9, the results obtained can be used to plot the aircraft flight ceiling as a function of true airspeed. For this, firstly the power required and power available are plotted as a function of true airspeed for each velocity (see Figure 13.1 for an example of this).

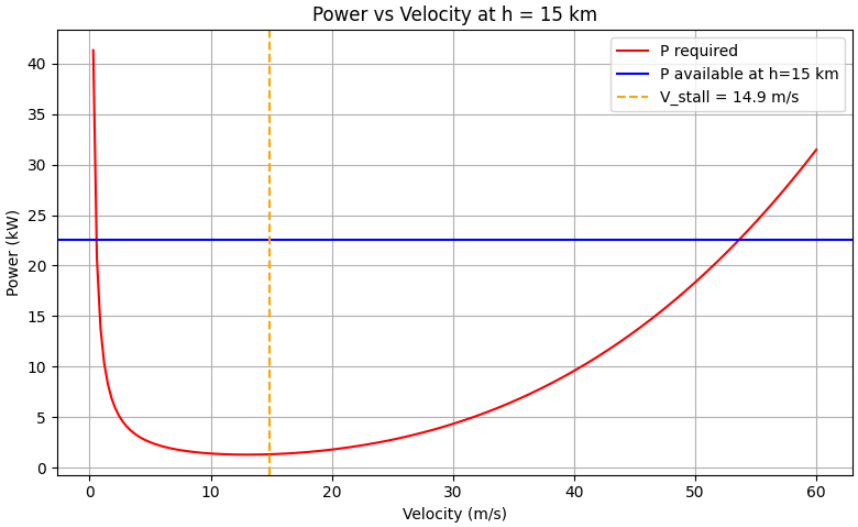

Figure 13.1: $P_{required}$ *vs.* $P_{available}$ *at 15 km Altitude*

Then, at each altitude, the maximum airspeed that the aircraft can fly at is determined by the rightmost intersection between the power available and power required curve. As for the minimum airspeed, this is either determined by the stall speed of the aircraft, or by the leftmost intersection between the power available and power required curve, whichever value is higher. Doing this for all altitudes eventually returns an altitude past which the aircraft is not able to climb, since there is not enough power available to do so, and this is known as the aircraft's theoretical ceiling (26.9 km). The aircraft's flight ceiling can then be seen in Figure 13.2.

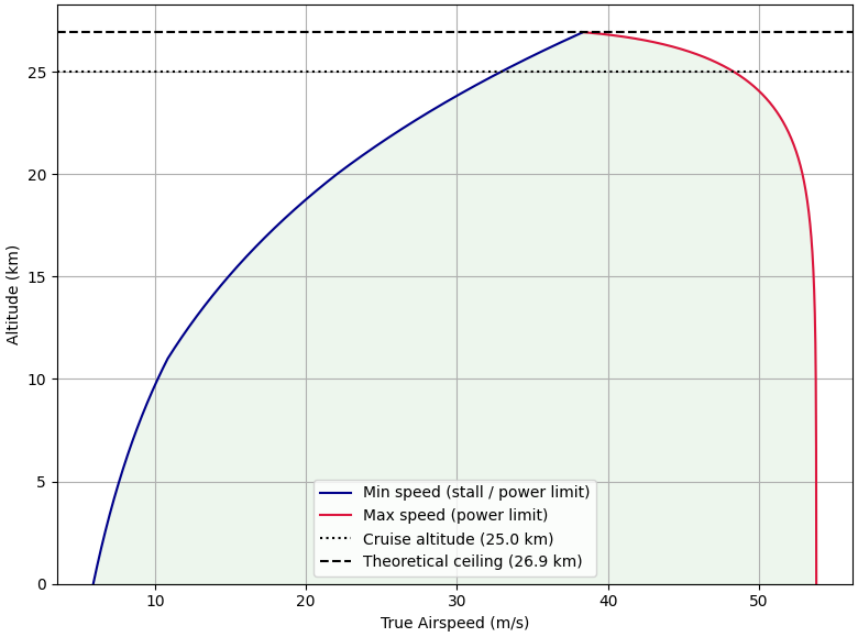

Figure 13.2: *SORA's Flight Ceiling*

Concluding this chapter, it is expected that the SORA aircraft will be able to perform its mission in a satisfactory manner, collecting scientific measurements as required by the project objective, and ensuring flexible operability across its design range.

14

Production Plan

The manufacturing, assembly, and integration plan for SORA describes the physical production of the aircraft from the material supply to the global integration. Section 14.1 shows an overview of the production plan. After which, in Section 14.2 all tools needed for the manufacturing and assembly phases are listed. In Section 14.3 the manufacturing process of Galvorn is explained. Section 14.4 discusses the attachment strategies used. Finally, Section 14.5 explains the final assembly and integration of SORA.

14.1. Production Plan Overview

An overview of the production plan can be seen in Figure 14.1. The subsystems will be manufactured and assembled using either raw materials or off-the-shelf components. Subsequently, the subsystems will be integrated in either the fuselage or wing sections, which are combined together to form the final aircraft.

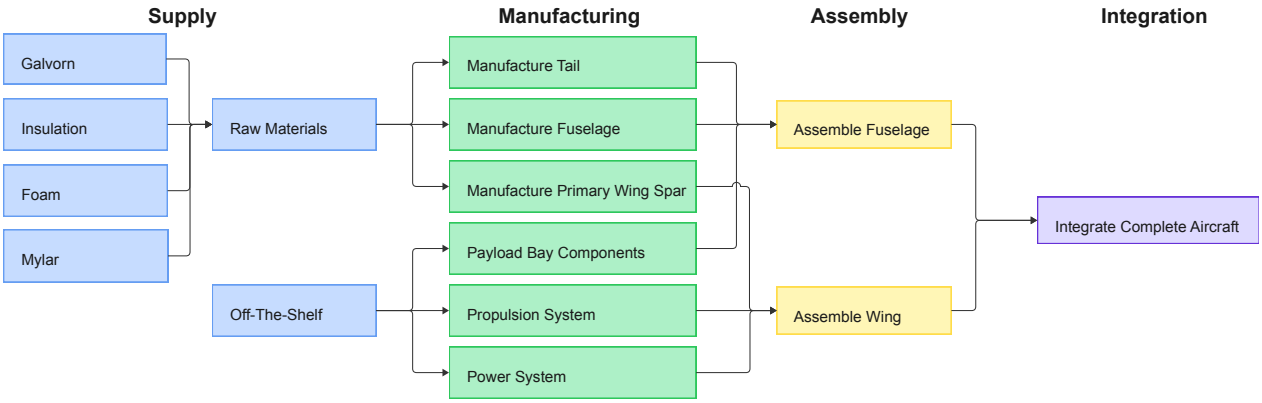

Figure 14.1: *Production Plan SORA*

14.2. Tools

All the necessary tools and materials needed for the manufacturing and assembly phases are listed in Table 14.1.

Table 14.1: *Required Resources for Manufacturing and Assembly*

Manufacturing Phase	**Assembly Phase**
Materials/Components	**Materials/Components**
• Galvorn, Resins, Adhesives, Sealants, and Realease Agent Ultra-High Molecular Weight Polyethylene (UHMWPE) • Suprasil 300, Silica Aerogel • Foam and Mylar • Paint and Coatings	• Fasteners, Adhesives, and Sealants • Electrical Wire and Connectors
Tools/Resources	**Tools/Resources**
• CNC (Computer Numerical Control) Mills, Lathes, and Water-jet/Laser Cutters • Presses, Brakes, Rollers, Heat Gun, and Squeegee • Autoclaves, AFP (Automated Fibre Placement) Machines, Angle Grinder, and Dremel • Vacuum Bags, Freezer Space, and Moulds • Manufacturing Facilities, and Skilled Personnel • Personal Protection (Gloves, Dust Mask, Safety Glasses)	• Optical Alignment Tools (Laser), Lifting Equipment • Basic Hand/Power Tools • Assembly Halls, and Clean Rooms • Skilled Assemblers, and Mechanics

14.3. Composite Manufacturing (Galvorn)

The aircraft will be primarily made of Galvorn, a newly developed composite made from packed and aligned Carbon Nantotube Fibres (CNF), as explained in Chapter 8. This composite needs to be moulted into the required shapes. A process which will be performed on a part-by-part basis, since the alignment of the fibres depend on the loads each part must carry.

Firstly, the carbon nanotubes must be dissolved and aligned to create CNF. Then, the CNF will undergo fibre wet spinning to create a fibre mesh [1]. The mesh is then pre-impregnated with partially cured resin, which can be stored in a cold environment until they are used [108].

Next, a similar layup method as used for standard composites, i.e. Carbon Fibre Reinforced Polymers (CFRP), can be used for composites with Carbon Nanotube Fibres. For these Carbon Nanotube Reinvorced Polymers (CNTRP), a unique mould is created for each part. Before the production can begin, these moulds must be properly cleaned, degreased, and checked for irregularities. Additionally, a release agent should be applied to ensure easy removal of the part from the mould.

The pre-impragnated sheets are cut to size and layered in the mould. Each layer is applied with a predetermined orientation to ensure the necessary calculated strength properties (i.e. in the direction of the loads). Each ply should be rolled to remove air and help with bonding. Once all the layers have been added the part should be sealed in a vacuum bag to remove any access air, which is important for pressurization [109].

Finally, the panel must be cured under specific environmental conditions provided by an autoclave until the panel is completely rigid. When the part is fully cured and cooled, it can be separated from the mould. Then, the part can undergo any finishing procedures, such as sanding and drilling [109].

14.4. Adhesives

When all parts have been manufactured or obtained, they must be attached to one another. The most efficient technique, in terms of aerodynamic properties and mass, is using several specialized adhesive agents. In general, epoxy adhesives are ideal for bonding CNTRP. For improved bonding carbon nanotubes (CNT), modified epoxy could be used [110]. Since the adhesive and the parts have similar structures, thermal expansion mismatches will be negligible.

To attach the solar film to the Mylar wing skin connection, 3M VHB Tapes are preferred. 3M VHB Tapes maintain their strength at high temperatures and flexibility at low temperatures, are UV-resistant, are not sensitive to pressurization risk, and add minimal weight [2]

Lastly, epoxy adhesions are relatively easy to remove, using heat and/or chemical solvents. Therefore, it will not impact the recyclability of the aircraft. However, it may damage surrounding material, and as such it is disadvantageous when considering maintainability.

14.5. Assembly and Integration

All subsystems can be manufactured independently and simultaneously, to decrease manufacturing time. Then, they can be integrated together. Figure 14.2 shows the assembly plan, in which sequential tasks are connected by arrows and simultaneous tasks are parallel to one another. In the following paragraphs, the fuselage, tail, wing, propulsion, and power assembly are further explained.

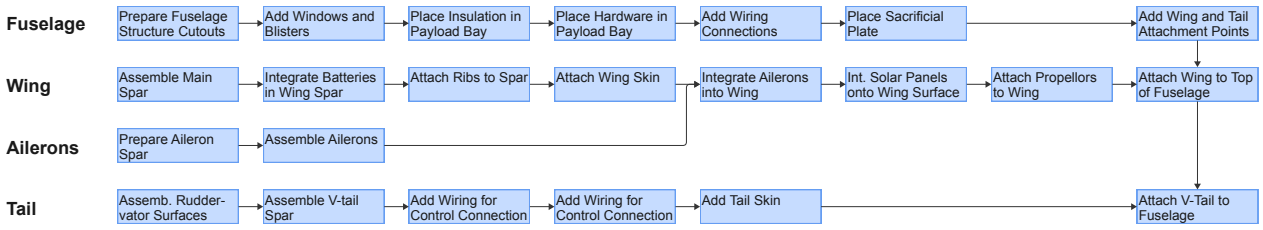

Figure 14.2: *Assembly Plan*

Fuselage and Tail Assembly

The fuselage will be split into two segments with different thicknesses; the payload bay and the tapered tail segment. These will each be split into top and bottom halves, in which needed cut-outs and windows are made. Later, they

[1] URL: https://www.designworldonline.com/galvorn-redefines-design-for-aerospace/ [cited 11/06/2026]
[2] https://www.3m.com/3M/en_US/p/d/b40071700/ [cited 11/06/2026]

are joined with structural adhesive. The sacrificial landing plate will be secured to the belly of the aircraft with an adhesive. The tail will then be attached via an internal spar joiner inside the fuselage packed with a structural adhesive. This method ensures that minimal bending loads will be transferred through the fuselage skin. The connection points are visualized in Figure 14.3.

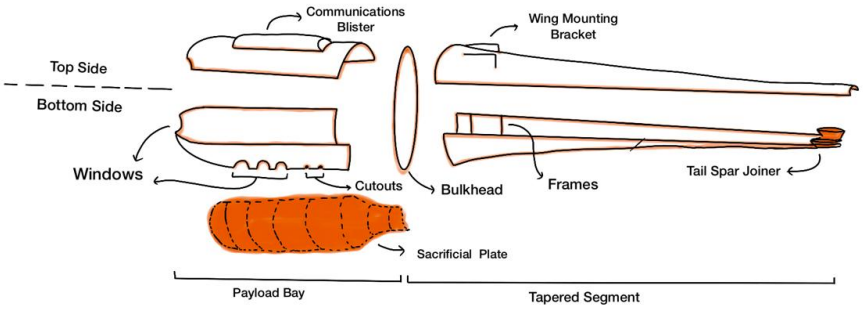

Figure 14.3: *Fuselage Production*

Wing, Propulsion and Power Assembly

The wing must house the power and propulsion subsystem. The connection points are shown in Figure 14.4. The batteries will be placed next to one another and then placed inside a sleeve in the wing spar, where they are easily removable. A small hole in the roof of the fuselage and spar will permit wiring to pass, which ensures a connection between the batteries and other subsystems such as the payload, communication system, and solar panels. The ribs will be attached to the spar with only adhesive, since they are not load carrying members. The skin will be wrapped tightly around the internal wing structure and will be attached to the ribs via an adhesive. Similarly, the solar panels will be bonded through adhesive tape onto the wing skin. The propulsion system will be mounted to the main spar via a boom which punctures the wing skin and encircles the spar. Lastly, the main wing spar will be attached to the fuselage body using a small external mount, to ensure the appropriate wing angle. This mount is expected to take the form of a small bracket connected to the internal fuselage frames.

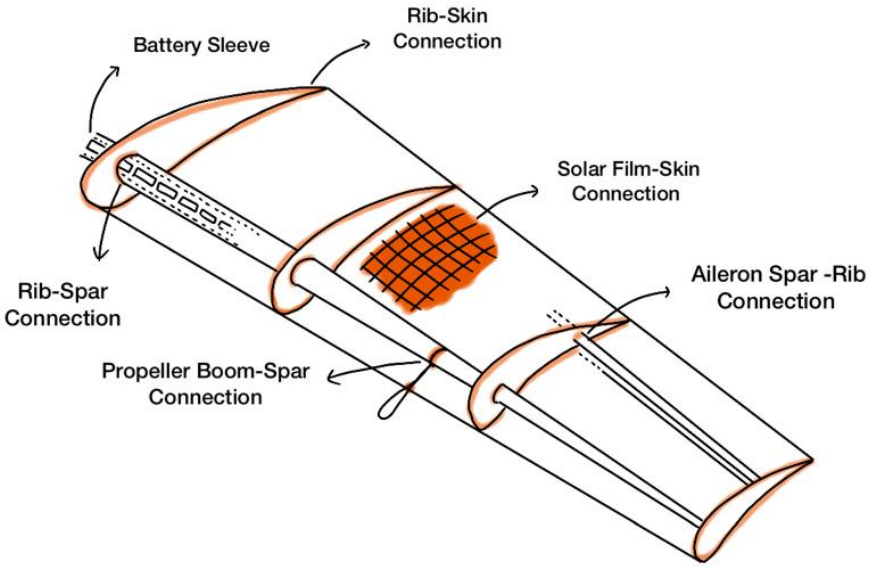

Figure 14.4: *Wing Production*

15

Budgets

Budget were set and maintained from the baseline phase onwards to constrain each subsystems use of finite or expensive resources. The procedure for setting up these budgets, their evolution and the final values are documented in this chapter. The mass budget is treated in Section 15.1, the power budget in Section 15.2 and finally the cost budget in Section 15.3.

15.1. Mass

The mass budget has gone through a couple iterations during the design process. The mass budget was initially set at baseline [111] using a conceptual solar HALE design by DLR [112]. This mass budget used theoretical mass fractions to set budgets for subsystems. This budget was used up to midterm, where using knowledge from literature, class I analyses and preliminary component selections an updated mass budget was set. For the final budget a target of 250 kg was set, based on assumed mass reductions and performance improvements fed into the class I analyses. The payload, avionics and communication subsystems were instead budgeted at their confirmed component masses, as these were fixed by component selection at midterm. The remaining budget was distributed across structures, power and propulsion in proportion to their midterm mass fractions, as these scale with the aircraft mass rather than having a fixed mass. Final masses are the converged outputs from the iterative aircraft sizing tools developed in a Python environment.

Table 15.1: *Evolution of the Subsystem Mass Budget.*

Subsystem	**Baseline**	**Midterm**			**Final**		
	Target [kg]	**Target** [kg]	**Actual** [kg]	Δ [kg] (%)	**Target** [kg]	**Actual** [kg]	Δ [kg] (%)
Structure	112.5	178.9	166.7	−12.2 (−7%)	103.8	80.6	−23.2 (−22%)
Power	176.3	162.6	185.5	+22.9 (+14%)	94.4	80.9	−13.5 (−14%)
Propulsion	22.5	20.3	17.3	−3.0 (−15%)	11.8	16.1	+4.3 (+36%)
Avionics & control	48.8*	12.2	10.0	−2.2 (−18%)	10.0	10.0	0.0 (0%)
Communication	—	8.1	6.1	−2.0 (−25%)	5.0	5.1	+0.1 (+2%)
Payload	15.0	24.4	21.0	−3.4 (−14%)	25.0	26.0	+1.0 (+4%)
Total	**375.0**	**406.5**	**406.6**	**+0.1** (0%)	**250.0**	**218.5**	−31.5 (−13%)

*Baseline (DLR-HEIKE) lumped avionics, control and communication into a single 13% allocation.

It can be seen that the converged mass falls below the target, with the aircraft mass driven subsystems coming in well under their allocations and the fixed subsystems landing on their confirmed masses. In general for the design of SORA, mass convergence was not an issue, rather the aircraft's power consumption was driving. The power budget is treated next.

15.2. Power

The power budget was first established at baseline using reference values from the DLR HAP concept [112], yielding a single lumped figure split only into propulsive and non-propulsive consumers. Once the subsystems were defined this was decomposed per consumer and reevaluated using engineering judgement. The resulting midterm power budget breakdown is shown in Table 15.2. Thereafter, for the final power budget, the midterm allocation of 7795 W was retained as the target, with the per-subsystem split refined according to the selected components. The payload budget now accounts for heating power, which is continuously required. Avionics and control remain unchanged from midterm, as the selected components were carried over without modification. The power subsystem now includes the battery heating power required for thermal management at altitude, which was not anticipated in the midterm allocation.

It can be seen in Table 15.2 that the power subsystem ended up greatly overshooting its targeted power consumption. This was due to the heating power required to keep the batteries in their operational range turning out to be greater than expected. Moreover, having obtained a lower converged aircraft mass, as well as drag reduction, resulted in the

Table 15.2: *Evolution of the Power Budget.*

Subsystem	Midterm			Final		
	Target [W]	Actual [W]	Δ [W] (%)	Target [W]	Actual [W]	Δ [W] (%)
Propulsion	7400	10571	+3171 (+43%)	7260	5915	−1345 (−19%)
Payload	285	230	−55 (−19%)	230	205	−25 (−11%)
Avionics & control*	10	200	+190 (+1900%)	200	200	0 (0%)
Communication	50	55	+5 (+10%)	55	58	+3 (+5%)
Power†	50	50	0 (0%)	50	264	+214 (+428%)
Total	**7795**	**11106**	**+3311** (+42%)	**7795**	**6642**	−1153 (−15%)

*Midterm avionics target was an early placeholder set before the consumption was known. †Battery-heating target was a preliminary estimate set before the thermal model matured.

propulsion system undershooting its allocated budget. Payload power consumption decreased through the use of a better insulation material, requiring less heating power and leveraging the heat produced by operating the payload instruments to self-heat the payload compartment.

15.3. Cost

15.3.1. Cost Breakdown Method

The cost breakdown is based on four different estimation methods, depending on the availability and reliability of the cost data. These methods are listed below.

- **Supplier Price:** When an official supplier price or quotation is available, this value is used directly in the cost breakdown.
- **Similar Product:** If no direct supplier price is available, the cost is estimated based on similar products available on the market. To account for uncertainty, shipping, integration, and price variation, a margin factor of 0.25 is applied to the estimated market price.
- **Parametric Estimate:** For components where no direct supplier price or similar market product is available, the cost is estimated using known reference information and scaled accordingly.

15.3.2. Cost Breakdown Summary

The estimated system cost is broken down by subsystem and by the individual components within each subsystem. The cost of each component is estimated using the methods described in Subsection 15.3.1. The results are summarized in Table 15.3 [1] [2] [3] [4] [5] [6] [7] [8] [9] [10] [11]. The sum of the the total cost will apply a margin of 1.2 in order to compensate the uncertainty in the cost estimation.

Table 15.3: *Cost Breakdown*

Subsystem	Component	Quantity	Unit Cost [€]	Method
Payload				
Payload	Known payload costs only	1	**327,000**	From Table 6.4
Power System				

[1] URL: https://eu.mouser.com/c/power/dc-dc-converters/ [cited 09/06/2026].
[2] URL: https://evcraft.en.made-in-china.com/product/pflUZOFdrnkH/China-400V-160A-High-Voltage-High-Current-Motor-Speed-Controller-ESC-for-BLDC-Motor-Heavy-Lift-Drone-and-Big-Drone.html [cited 09/06/2026].
[3] URL: https://shop.canev.com/products/battery-management-system-orion-2 [cited 09/06/2026].
[4] URL: https://energetechsolar.com/solar-charge-controller-mppt-96v-120v-192v-216v-384v [cited 09/06/2026].
[5] URL: https://guntherportfolio.com/2016/12/alta-devices-is-flying-high-with-uavs/ [cited 09/06/2026].
[6] URL: https://discussion.fool.com/t/new-company-amprius-ampx/105277 [cited 09/06/2026].
[7] URL: https://www.embention.com/veronte-ecosystem/autopilots/1x-sensor-redundancy/ [cited 09/06/2026].
[8] URL: https://baspartsales.com/control/actuators/ [cited 09/06/2026].
[9] URL: https://www.ligpower.com/?srsltid=AfmBOorqaa3XFbrGVulkJZ1-NaNNegGe9K9TkwQVWhJSyXOWL1hHhNl6 [cited 09/06/2026].
[10] URL: https://dexmat.com/store/galvorn-fabric/ [cited 09/06/2026].
[11] URL:https://it-market.com/en/security/ups-systems-power-distribution/aruba/af538a/887825-620088?srsltid=AfmBOoro9UjExdCgEQa8BQRXDYShGZAVk4-9XHfSgJtrLqnNxLDhexCOEqM [cited 16/06/2026]

Subsystem	Component	Quantity	Unit Cost [€]	Method
Power system	Battery system	24.03 kWh	≈ 11200 per kWh	Parametric estimate
Power system	Solar panel	≈ 12000 W	≈ 110 per W	Similar product
Power system	MPPT unit	1	2200	Supplier price
Power system	BMS	1	864	Supplier price
Power system	DC–DC converter	1	356	Supplier price
Power system	PDU	2	3629	Supplier price
Power-system subtotal	Battery, solar panel, and fixed power-system costs		**1,599,815**	
Propulsion System				
Propulsion	Electric motor	4	≈ 800	Similar product
Propulsion	Propeller	4	≈ 100	Similar product
Propulsion	ESC	4	≈ 3000	Similar product
Propulsion subtotal	Known propulsion costs only		**15,600**	
Communication System				
Communication subtotal	Known communication costs only	1	**3630**	From Table 11.4
Structure and Material				
SM subtotal	Known structure costs only	1	**1,507,360**	Parametric estimate
Avionics and Control				
Avionics	Flight computer	2	6450	Supplier price
Avionics	Actuator	8	4000	Supplier price
Avionics subtotal	Known avionics and control costs only		**44,900**	
Total				
Total known cost	Sum of listed known and estimated items		**3,498,305**	
Total cost with margin			**4,197,966**	

Development Cost

The development process is summarized by Phases 1–6 in Figure 3.4, which include design review, manufacturing, assembly and integration, testing, and certification. Based on these activities, the development cost is divided into three main groups: human cost, component and production cost, and external testing and certification cost as can be seen in Equation 15.1.

$$C_{\text{dev,total}} = C_{\text{dev,human}} + C_{\text{dev,comp}} + C_{\text{dev,test}} \tag{15.1}$$

In this equation, $C_{\text{dev,human}}$ is the labour-related development cost, $C_{\text{dev,comp}}$ is the cost of hardware, components, prototypes, and production activities during development, and $C_{\text{dev,test}}$ is the cost of external testing, certification, and specialist validation activities.

Human Cost

During development, the team size is assumed to start at 50 people and gradually increase as the project moves from detailed design to manufacturing and testing.[12] For this preliminary estimate, an average team size of 75 people is assumed over the full development period.

[12] Sceye representative, unpublished interview, May 2026.

Since the company is assumed to be registered in the Netherlands, the labour cost is based on an average aerospace engineering salary of approximately 43,599 €/year. This value is consistent with current salary estimates for aerospace engineers in the Netherlands.[13] To account for employer-side costs, including taxes, insurance, pension contributions, overhead, and software tool licences, a cost factor of 1.3 is applied. Therefore, the effective annual labour cost per employee is then:

$$S_{\text{eff}} = 1.3 \cdot 43{,}599 = 56{,}679 \text{ €/year} \tag{15.2}$$

The development period is assumed to last seven years until deployment. The development human cost is therefore estimated using Equation 15.3.

$$C_{\text{dev,human}} = N_{\text{avg}} \cdot S_{\text{eff}} \cdot t_{\text{dev}} \tag{15.3}$$

where N_{avg} is the average number of employees during development, S_{eff} is the effective annual labour cost per employee, and t_{dev} is the development time. Substituting $N_{\text{avg}} = 75$, $S_{\text{eff}} = 56678$ €/year, and $t_{\text{dev}} = 7$ years, gives:

$$C_{\text{dev,human}} = 75 \cdot 56678 \cdot 7 = 29{,}756{,}317 \text{ €} \tag{15.4}$$

Thus, the estimated development human cost is approximately 29.8 M€.

Component and Production Cost
The component and production cost includes all physical parts, materials, subsystems, tooling, prototype hardware, and assembly-related costs required during development. This cost is based on the flight vehicle component cost previously summarized in Table 15.3. To account for interface issues, integration challenges, design iterations, damaged components, and additional prototype modifications during development, an additional margin factor of 1.2 is applied. This results in a total component and production cost of:

$$C_{\text{comp,prod}} = 4{,}197{,}966 \times 1.2 = 5{,}037{,}559 \text{ €} \tag{15.5}$$

External Testing and Certification Cost
The external testing and certification cost accounts for development activities that cannot be fully performed internally. These activities may include wind-tunnel testing, environmental testing, structural testing, battery safety testing, flight-test support, certification documentation, external consultancy, and regulatory assessment. Since these costs depend strongly on the final certification route, the number of test campaigns, and the required level of external support, they are estimated separately from the internal labour and component development costs.

For this preliminary estimate, the external testing and certification cost is expressed as a fraction of the total development cost as seen in Equation 15.6.

$$C_{\text{dev,test}} = f_{\text{test}} \left(C_{\text{dev,human}} + C_{\text{dev,comp}+C_{\text{dev,test}}} \right) \tag{15.6}$$

where f_{test} is the external testing and certification cost factor. RAND reports that contractor and government test and evaluation costs account for approximately 21% of total development costs for fixed-wing aircraft [113]. However, this value is used only as a reference, since the present aircraft is at a preliminary design stage and the final certification route is not yet defined. In addition, external testing costs may increase due to battery safety qualification, environmental testing, flight-test support, and possible regulatory assessment requirements. Therefore, a conservative value of:

$$f_{\text{test}} = 0.30 \tag{15.7}$$

is selected for this estimate.

Since the human cost and the component and production cost have already been estimated, the testing and certification cost can be calculated using Equation 15.6. The total development cost is then obtained from Equation 15.10. The resulting costs are calculated using Equation 15.8.

$$C_{\text{dev,test}} = \frac{f_{\text{test}}}{1 - f_{\text{test}}} \left(C_{\text{dev,human}} + C_{\text{dev,comp}} \right) \tag{15.8}$$

[13] URL:https://www.payscale.com/research/NL/Job=Aerospace_Engineer/Salary [cited 10/06/2026].

Substituting $f_{\text{test}} = 0.30$, $C_{\text{dev,human}} = 29{,}756{,}317$ €, and $C_{\text{dev,comp}} = 5{,}037{,}559$ €, gives

$$C_{\text{dev,test}} = \frac{0.30}{1-0.30}\,(29{,}756{,}317 + 5{,}037{,}559) = 14{,}911{,}661 \text{ €} \tag{15.9}$$

The total development cost is therefore

$$C_{\text{dev,total}} = 29{,}756{,}317 + 5{,}037{,}559 + 14{,}911{,}661 = 49{,}705{,}539 \text{ €} \tag{15.10}$$

Thus, the external testing and certification cost is estimated to be approximately 14.9 M€, resulting in a total development cost of approximately 49.7 M€.

Operational Cost

The operational cost of the aircraft must also be considered. For this preliminary estimate, the operational cost is estimated on a yearly basis, assuming that four missions are carried out per year. The main recurring cost drivers considered in this estimate are personnel cost, maintenance cost, and other operational expenses.

Personnel Cost

According to a Sceye representative, an operation similar to MALEO4CRE would require four personnel members.[14] The average annual salary of a drone operator in the Netherlands is estimated to be 52,607 €/year.[15] Therefore, the annual operational personnel cost can be estimated using Equation 15.11.

$$C_{\text{op,personnel}} = N_{\text{op}} \cdot S_{\text{op}} \tag{15.11}$$

where N_{op} is the number of personnel required for operation and S_{op} is the annual salary per operator. Substituting the assumed values gives:

$$C_{\text{op,personnel}} = 4 \cdot 52{,}607 = 210{,}428 \text{ €/year} \tag{15.12}$$

Maintenance Cost

In addition to personnel cost, recurring maintenance activities are required to keep the aircraft operational over repeated missions. These activities may include inspection, repair, replacement of worn components, maintenance of ground support equipment, and general servicing after each mission.

For this preliminary estimate, the annual maintenance cost is assumed to be a fixed fraction of the total aircraft cost. Since a detailed maintenance schedule is not available at this design stage, a maintenance cost factor of $f_{\text{maint}} = 0.2$ is applied based on engineering judgement. This factor accounts for recurring technical support and maintenance-related activities during operation.

The annual maintenance cost is therefore estimated using Equation 15.13.

$$C_{\text{op,maint}} = f_{\text{maint}} \cdot C_{\text{aircraft}} \tag{15.13}$$

where f_{maint} is the maintenance cost factor and C_{aircraft} is the total aircraft cost. Substituting the assumed values gives the annual maintenance cost is estimated to be approximately 839,600 €/year.

Other Operational Cost

Other recurring operational costs may include communication, data handling, logistics, launch and recovery support, software licences, insurance, transport, and general mission preparation. Since these costs are difficult to estimate accurately at this preliminary stage, they are included using an additional margin factor.

For this estimate, other operational costs and uncertainties are represented by an operational margin factor of $f_{\text{op,margin}} = 0.1$, applied to the sum of the personnel and maintenance costs. The total annual operational cost is therefore calculated with Equation 15.14.

$$C_{\text{op,total}} = \left(1 + f_{\text{op,margin}}\right)\left(C_{\text{op,personnel}} + C_{\text{op,maint}}\right) \tag{15.14}$$

Substituting the assumed values gives the total annual operational cost, estimated to be approximately 1.16 M€/year.

[14] Sceye representative, unpublished interview, May 2026.

[15] URL: https://www.salaryexpert.com/salary/job/drone-operator/netherlands [cited 11/06/2026].

Disposal Cost

The end-of-life cost of the aircraft should not be neglected in the life-cycle cost assessment. Literature indicates that aircraft disposal cost can be estimated as approximately 10% of the aircraft purchase price [114]. Since the actual purchase price is not available at this design stage, it is approximated using the cost per aircraft from Table 15.3. A factor of 1.3 is then applied based on engineering judgement. Therefore, the disposal cost can be estimated:

$$C_{\text{disp}} = 0.10 C_{\text{purchase}} \tag{15.15}$$

$$C_{\text{purchase}} = 1.3 C_{\text{aircraft}} \tag{15.16}$$

where C_{aircraft} is the estimated cost per aircraft obtained from the component and production cost breakdown. Thus, the estimated disposal cost is approximately 545,700 €.

15.4. Return on Investment

The aircraft is mainly designed for climate research, rather than for direct commercial profit. Therefore, the conventional return on investment (ROI), which is usually based on revenue, market share, and profit margin, is not very suitable for this project. In this case, the return should be considered as scientific, environmental, and societal value.

The main value of the aircraft is that it can provide persistent high-altitude atmospheric measurements. This data can be used for climate modelling, environmental monitoring, and improving the understanding of atmospheric processes. Although these benefits cannot be easily converted into direct financial income, they can still provide long-term value by supporting climate research and better decision-making.

Therefore, the return on investment of this aircraft is considered to be non-monetary. The project can be justified if the scientific data obtained during the missions is valuable enough compared with the development, production, and operational cost. For this reason, the ROI assessment mainly focuses on mission effectiveness and research value instead of profitability.

16

Technical Risk Assessment

This chapter identifies, assesses, and controls the main technical risks associated with the development and operation of MALEO4CRE. The risk identification and assessment are based on the more detailed design information available at this stage, as presented in Section 16.1. The corresponding mitigation measures are then discussed in Section 16.2. For the final report, additional risks are mainly added to address future development, testing, and operational uncertainties.

16.1. Technical Risk Identification & Assessment

To ensure a consistent and traceable assessment, both likelihood and consequence are evaluated using the five-level scale defined in Table 16.1. The risks are identified and assessed across the main life-cycle phases of the system. Each phase is abbreviated as follows: Design (DE), Manufacturing (MAN), Assembly, Integration, and Testing (AIT), Operations (OP), Maintenance (MAIN), and End-of-Life (EOL). For each phase, specific responsible person(s) are assigned to monitor and manage the associated risks. It is acknowledged by the group that the Design phase is the most critical to the project. The Manufacturing, Assembly, Integration, and Testing, Maintenance, and End of Life are included for completeness.

Table 16.1: *Quantified Definition of Likelihood and Severity Levels used in the Product Risk Assessment.*

Level	Likelihood	Severity
1	Rare: probability of occurrence is below 5% during the project or aircraft life-cycle phase considered.	Negligible: No safety impact, no mission impact, and no effect on compliance with key requirements.
2	Unlikely: probability of occurrence is 5% - 20%. Possible, but not expected under normal	Minor: The aircraft remains compliant with major requirements, only minor design changes, checks, or operational adjustments are needed.
3	Moderate: probability of occurrence is 20% - 50%. realistic possibility of occurring in at least one life-cycle phase.	Moderate: Mission effectiveness is reduced, but feasible. Mitigation, redesign, or additional testing is required.
4	Likely: probability of occurrence is 50% - 80%. Occurs at least once if no preventive measures are implemented.	Major: Mission capability, safety margin, or regulatory compliance is significantly affected. Substantial redesign, additional testing, or operational restrictions are required.
5	Almost certain: probability of occurrence is above 80%. Occurs repeatedly or under most relevant project or operational conditions.	Critical: The aircraft may fail to meet essential mission requirements, safety objectives, regulatory constraints, or operational feasibility.

Phase: Design (Davide)

The identified technical risks during the design phase are summarized in Table 16.2. These risks mainly relate to requirement definition, design assumptions, stakeholder interpretation, and the convergence of the design process.

Table 16.2: *Technical Risks during the Design Phase.*

Identifier	Description	L	S
TR-DES-01	Design solution iterations don't converge within project time.	4	4
TR-DES-02	System requirements defined unrealistically with the available technology, budget, or project resources.	3	4
TR-DES-03	Design assumptions are oversimplified, leading to inaccurate performance estimates and over-/under-designed concept.	3	4

Identifier	Description	L	S
TR-DES-04	Essential design steps, analyses, or verification activities are omitted during the planning or design process.	3	4
TR-DES-05	Stakeholder needs are incorrectly interpreted, resulting in design requirements that do not reflect the actual mission objectives.	2	4
TR-DES-06	Interfaces between subsystems are poorly defined, causing integration problems in later design phases.	3	4
TR-DES-07	Regulations restrict feasible design options, resulting in suboptimal design.	3	4
TR-DES-08	Stakeholder requirements change during the design phase.	4	3

Phase: Manufacturing (Sam)

The identified technical risks during the manufacturing phase are summarized in Table 16.3. These risks mainly relate to production delays, quality control, supplier communication, cost control, and worker safety.

Table 16.3: *Technical Risks during the Manufacturing Phase.*

Identifier	Description	L	S
TR-MAN-01	Manufacturing delays occur due to delays from suppliers.	3	3
TR-MAN-02	Errors in CAD models, drawings, or technical documentation are sent to suppliers, resulting in incorrect or unusable manufactured parts.	2	4
TR-MAN-03	Manufacturing costs exceed the planned budget.	2	3
TR-MAN-04	Manufacturing cannot continue due to supplier production failure.	1	5
TR-MAN-05	Stakeholder requirements change during the manufacturing phase.	2	5
TR-MAN-06	Electrical components may be installed incorrectly, causing a possible short circuit or electrical failure.	2	4

Phase: Assembly, Integration, & Testing (Diogo)

The identified technical risks during the assembly, integration, and testing phase are summarized in Table 16.4. These risks mainly relate to subsystem compatibility, functional verification, validation, certification, cost control, and possible redesign needs.

Table 16.4: *Technical Risks during the Assembly, Integration, and Testing Phase.*

Identifier	Description	L	S
TR-AIT-01	Assembly, integration, and testing take longer than expected.	4	4
TR-AIT-02	Subsystem interfaces are incompatible, resulting in integration difficulties, additional modifications, or delayed system-level testing.	3	5
TR-AIT-03	The system or subsystem fails functional tests, indicating that one or more components do not perform according to the design requirements, requiring a redesign.	3	4
TR-AIT-04	The system fails validation because its measured performance does not satisfy the mission needs or stakeholder requirements.	2	5
TR-AIT-05	Required certification or approval cannot be obtained within the planned timeframe.	2	4
TR-AIT-06	Testing costs exceed the planned budget.	3	3
TR-AIT-07	Stakeholder requirements change during the assembly, integration, or testing.	1	5

Phase: Operations (Isabel & Eve)

The identified technical risks during the operations phase are summarized in Table 16.5. These risks mainly relate to flight safety, system reliability, communication, navigation, environmental conditions, cybersecurity, and operational support.

Table 16.5: *Technical Risks during the Operations Phase.*

Identifier	Description	L	S
TR-OPS-01	Operational costs exceed expectations.	3	4
TR-OPS-02	Scientific payload malfunction after launch, leading to incomplete, inaccurate, or unusable mission data.	3	5
TR-OPS-03	Collected or transmitted data becomes corrupted.	3	3
TR-OPS-04	An onboard fire occurs due to an electrical fault.	2	5
TR-OPS-05	The aircraft encounters adverse weather conditions, such as strong winds, turbulence, icing, thunderstorms, or heavy precipitation, reducing flight safety or mission performance.	4	5
TR-OPS-06	A partial or complete control system failure occurs, reducing the ability to maintain stable and controlled flight.	2	5
TR-OPS-07	Structural failure due to excessive loads, fatigue or manufacturing defects.	2	5
TR-OPS-08	The aircraft has insufficient power during operation due to degradation or damage of the power system.	3	4
TR-OPS-09	GPS data is inaccurate, resulting in incorrect positioning and increased risk of entering restricted airspace.	3	3
TR-OPS-10	The UAV communication link is hacked, jammed, or otherwise compromised, potentially causing loss of command and stolen data.	2	5
TR-OPS-11	Communication with the aircraft is temporarily lost due to antenna failure or ground-station malfunction.	3	4
TR-OPS-12	A mid-air collision with an aircraft, UAV, bird, or airborne object.	2	5
TR-OPS-13	Radiation damages components resulting in failure.	3	4
TR-OPS-14	Components overheat during operation.	3	4
TR-OPS-15	Structural degradation occurs during operation due to fatigue, vibration, environmental exposure.	3	4
TR-OPS-16	Metal components oxidize or corrode during operation, compromising structural integrity.	4	3
TR-OPS-17	Operating software updates during operation resulting in unexpected behaviour or compatibility issues.	2	4
TR-OPS-18	Flight parameters sensors malfunction resulting in incorrect state estimation or inability to control the aircraft.	2	5
TR-OPS-19	Power generation of solar panel is lower than required due to internal and external factors	4	5
TR-OPS-20	Propeller damage or failure reduces the available thrust and affects aircraft controllability.	3	5
TR-OPS-21	Wing damage reduces lift efficiency, structural integrity, and flight stability.	2	5
TR-OPS-22	Battery overheating reduces battery performance and may lead to battery failure or thermal runaway.	3	5
TR-OPS-23	Tail damage reduces aircraft stability and control capability.	2	5
TR-OPS-24	A short circuit interrupts the power supply to critical components, such as the propulsion or flight-control system.	3	5
TR-OPS-25	Heating-device malfunction causes the payload compartment or battery system to fall outside its required operating temperature range.	3	4
TR-OPS-26	Battery degradation reduces usable battery capacity over the mission, resulting in insufficient night-time endurance.	3	5

Phase: Maintenance (Walter)

The identified technical risks during the maintenance phase are summarized in Table 16.6. These risks mainly relate to maintenance cost, spare-part availability, personnel availability, maintenance quality, software compatibility, and insufficient maintenance planning.

Table 16.6: *Technical Risks during the Maintenance Phase.*

Identifier	Description	L	S
TR-MAI-01	Maintenance costs exceed expectations.	3	4
TR-MAI-02	Required replacement components are unavailable or have long lead times, delaying maintenance and reducing aircraft availability.	3	3
TR-MAI-03	Qualified mechanics or maintenance personnel are unavailable when needed, delaying inspection, repair, or replacement activities.	3	3
TR-MAI-04	Human error during maintenance may lead to improper repair or overlooked faults.	3	4
TR-MAI-05	Replacement parts do not meet the required quality, tolerance, or reliability standards, causing reduced performance or premature failure.	2	5
TR-MAI-06	Hardware becomes incompatible with software updates, requiring different hardware for the UAV than used during design.	2	4
TR-MAI-07	Required maintenance is not performed often enough, increasing the likelihood of failure or otherwise unsafe operation.	2	3
TR-MAI-08	Required maintenance schedule limits aircraft availability and limits the scope of the mission.	1	4
TR-MAI-09	Required location limits aircraft availability and limits the scope of the mission.	1	4
TR-MAI-10	Unsafe handling during battery replacement may result in electric shock or injury.	2	4

Phase: End of Life (Yue)

The identified technical risks during the end-of-life phase are summarized in Table 16.7. These risks mainly relate to safe disposal, data removal, hazardous components, operator compliance, and the availability of local disposal or recycling infrastructure.

Table 16.7: *Technical Risks during the End-of-Life Phase.*

Identifier	Description	L	S
TR-EOL-01	Electrical components are improperly disposed of, leading to increased lifecycle emissions.	3	4
TR-EOL-02	Stored operational data is not removed before disposal, causing data leakage or security issues.	2	4
TR-EOL-03	Hazardous components are improperly handled or disposed of, resulting in safety, environmental, or legal risks.	3	4
TR-EOL-04	Local infrastructure is insufficient to execute the end-of-life plan, leading to incorrect disposal or limited recycling options.	3	4

16.2. Technical Risk Control

Based on the risks identified and assessed in Section 16.1, this section presents the risk control measures for each project phase. The objective of these measures is to reduce the likelihood and/or severity of the identified risks before they occur, while also defining appropriate actions in case the risks materialise. The corresponding mitigation (M) plans for each phase are presented in Table 16.8.

The identified risks are visually summarised in Figure 16.1a, while the residual risks after applying the mitigation procedures are summarised in Figure 16.1b. By comparing these two risk maps, the effectiveness of the risk control measures can be evaluated.

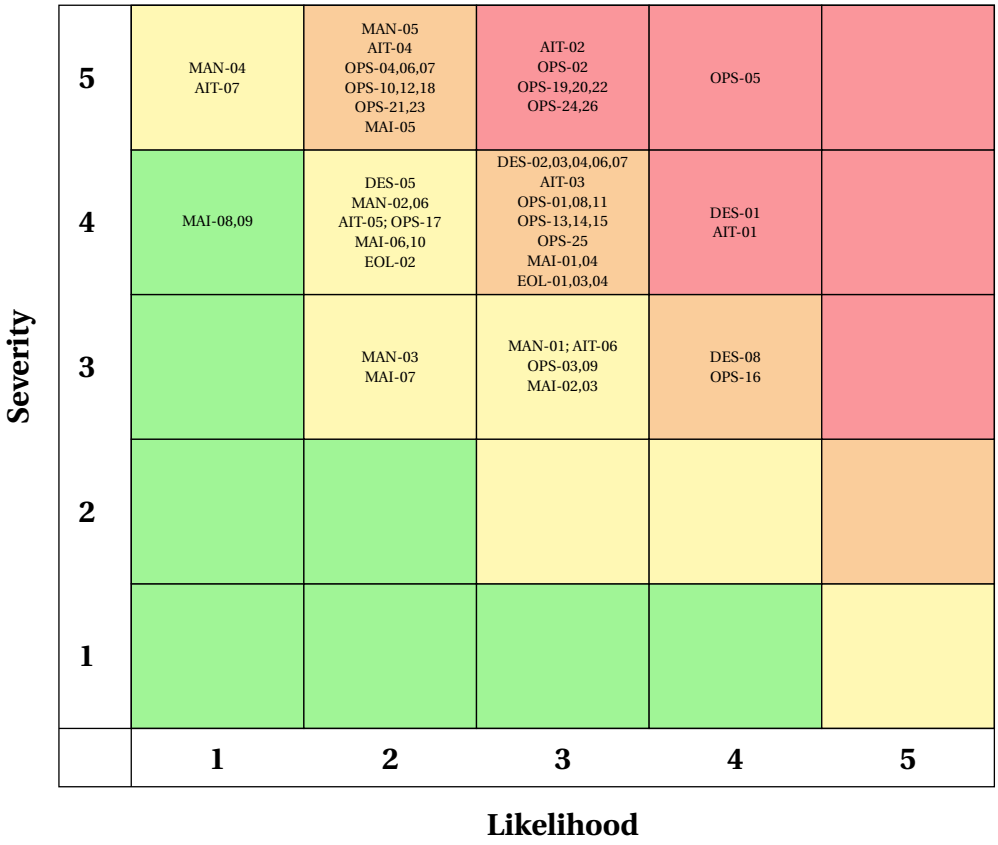

(a) *Pre-mitigation risk map.*

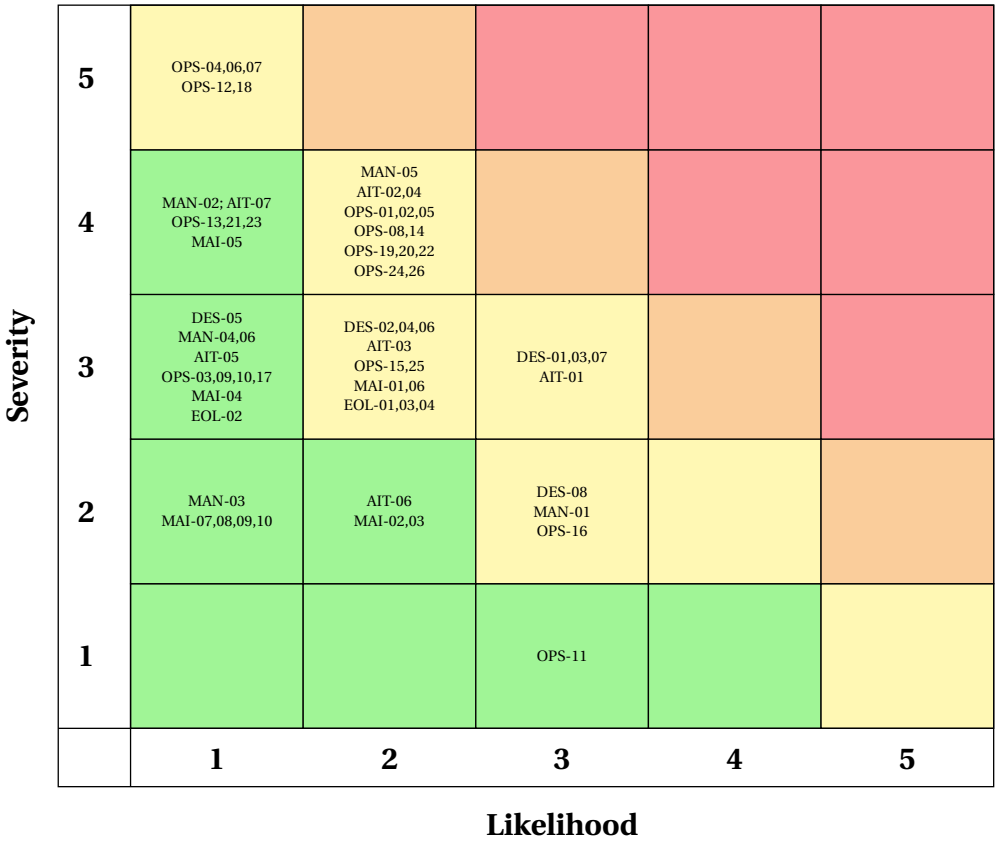

(b) *Post-mitigation risk map.*

Figure 16.1: *Pre- and Post-Mitigation Technical Risk Maps.*

Table 16.8: *Risk Mitigation Measures for the Design Phase.*

Risk ID	Pre-M		Post-M		Mitigation strategy	Contingency plan
	L	S	L	S		
TR-DES-01	4	4	3	3	Clear convergence criteria are defined early, including requirement priorities, performance margins, and iteration limits.	If the design does not converge in time, the most feasible baseline concept is chosen and limitations are documented.
TR-DES-02	3	4	2	3	Uncertain requirement values are marked as *TBD*, documented, and clarified before finalisation.	If a requirement is unrealistic, it is revised where justified, and the reason and design impact are documented.
TR-DES-03	3	4	3	3	Key assumptions are verified by reasoning, references, or calculations, the effect is quantified where possible.	If results deviate significantly, the assumptions are reviewed, updated, and the affected analyses are repeated.
TR-DES-04	3	4	2	3	A design checklist is used to track required design steps, analyses, and verification activities.	If an essential step is missing, its impact is assessed and the task is prioritised or simplified if time is limited.
TR-DES-05	2	4	1	3	Stakeholder needs are checked against mission objectives and reviewed by a team member not directly involved in defining them.	If a stakeholder need is misinterpreted, the requirement is revised and its design impact is documented.
TR-DES-06	3	4	2	3	Interface margins are included for key parameters, and interface requirements are documented and reviewed between subsystems.	If an interface issue is found, affected subsystems are identified, corrective actions are agreed, and the design is updated.
TR-DES-07	3	4	3	3	Relevant regulations and operational constraints are identified early and checked during trade-off analysis.	If the preferred option is restricted, the next-best feasible alternative is selected and the reason is documented.
TR-DES-08	3	3	3	2	Project planned for flexibility and potential extra time needed. Close communication with the main stakeholders means any changes can be implemented quickly.	The scope of likely changes is assessed first and project planning is updated and followed.
TR-MAN-01	3	3	3	2	Alternative suppliers are found before the manufacturing stage. Time margin is added to the delivery times.	An explanation is asked from the supplier and the customer is informed about the delay.
TR-MAN-02	2	4	1	4	Quality control is performed, approval from all contributing designers needed before sending documents to a third party.	N/A
TR-MAN-03	2	4	1	2	Manufacturing costs should be estimated early, including a sufficient cost margin for supplier price changes, material waste, rework, and unexpected manufacturing difficulties.	If manufacturing costs exceed the budget, review the design for possible simplifications, compare alternative suppliers or manufacturing methods, and prioritise essential components.
TR-MAN-04	1	5	1	3	Alternative suppliers are identified during design and strict contract rules are established with the supplier.	The suppliers are changed to those identified in the risk mitigation plan.
TR-MAN-05	2	5	2	4	Project planned for flexibility and potential extra time needed. Close communication with the main stakeholders means any changes can be implemented quickly.	Project planning is updated, the schedule and budget are negotiated with the customer and, if necessary, manufacturing is outsourced.
TR-MAN-06	2	4	1	3	Electrical continuity and functional tests shall be performed to verify correct installation.	If a fault is detected, the affected electrical component shall be disconnected, inspected, and reinstalled or replaced before further integration.
TR-AIT-01	4	4	3	3	An AIT schedule with time margins is created, progress is reviewed regularly.	If delays occur, critical tests are prioritised and non-essential activities are reduced where justified.

Continued on next page

Risk ID	Pre-M		Post-M		Mitigation strategy	Contingency plan
	L	S	L	S		
TR-AIT-02	3	5	2	4	Subsystem interfaces are defined, reviewed, and updated before integration.	If interfaces are incompatible, affected subsystems are identified, corrected, and retested.
TR-AIT-03	3	4	2	3	Test procedures are based on design requirements, and subsystem-level tests are performed before integration.	If functional testing fails, the cause is identified, corrected, and the affected test is repeated.
TR-AIT-04	2	5	2	4	Validation criteria are linked to mission needs and stakeholder requirements.	If validation fails, the unsatisfied requirements are identified, the design is updated/limitation is documented.
TR-AIT-05	2	4	1	3	Sufficient schedule margin is included for the certification and approval process.	If approval is delayed, missing evidence or non-compliance issues are identified and corrected.
TR-AIT-06	3	3	2	2	Testing costs are estimated early, including margins for repeated tests and equipment use.	If costs exceed the budget, critical tests are prioritised and lower-cost test methods are considered.
TR-AIT-07	1	5	1	4	Testing costs are estimated early, including margins for repeated tests and equipment use.	Schedule, budget, and strategy are discussed with the customer to capitalize on possible mission options or, make a new design in an efficient manner.
TR-OPS-01	3	4	2	4	Do a cost analysis and the end of a design iteration and compare operational costs with competitors.	N/A
TR-OPS-02	3	5	2	4	Scientific payload, its power and data connection tested before flight. Redundancy implemented where possible. Replacement parts available for scientific payload.	Drone returns to base prematurely to replace malfunctioning components, a new launch date is scheduled as soon as possible. Cause of failure is identified and avoided in the future.
TR-OPS-03	3	3	1	3	The data storage system is stress tested.	Data sent to external experts/manufactures for data recovery.
TR-OPS-04	2	5	1	5	A fire safety analysis is performed.	The UAV is commanded to dive in an attempt to put out the fire.
TR-OPS-05	4	5	2	4	Gusts loads are considered during design, weather conditions are continuously monitored during operations.	The UAV is commanded to climb above the weather, steered away from the weather or divert.
TR-OPS-06	2	5	1	5	Control redundancies are installed for pitch and roll control.	The impact on controllability is assessed and if necessary, the UAV is commanded to divert.
TR-OPS-07	2	5	1	5	Extreme load tests, fatigue tests and acceptance tests are performed for all structural components, and the structural assembly.	N/A
TR-OPS-08	3	4	2	4	Margin is added in the power budget.	The impact on mission duration is assessed, the mission duration is shortened.
TR-OPS-09	3	3	1	3	Sufficient GPS coverage is checked beforehand in mission area.	Local authorities are informed.
TR-OPS-10	2	5	1	3	Use end-to-end encryption of data.	UAV is commanded to ignore all instructions and autonomously return to base.
TR-OPS-11	3	4	3	1	A secondary ground station is on standby to take over communication.	Secondary ground station takes over.
TR-OPS-12	2	5	1	5	UAV is equipped with a transponder and/or TCAS system.	TCAS takes over UAV command in case of a TCAS-RA event.
TR-OPS-13	3	4	1	4	Identify radiation sensitive components during design and implement protective measures.	Run diagnostics and return to base.

Continued on next page

Risk ID	Pre-M		Post-M		Mitigation strategy	Contingency plan
	L	S	L	S		
TR-OPS-14	3	4	2	4	Perform thermal analysis during design.	Turn off overheated components if possible.
TR-OPS-15	3	4	2	3	Assess materials critically during material selection, using fatigue resistance, vibration resistance, environmental exposure, and other relevant factors as trade-off criteria.	N/A
TR-OPS-16	4	3	3	2	Critically assess the materials and (possibility) use of coating	N/A
TR-OPS-17	2	4	1	3	Define blocked periods during flight in which software updates are not allowed.	If an update is accidentally initiated during flight, warn the operator immediately and pause or roll back the update where possible.
TR-OPS-18	2	5	1	5	The critical sensors and systems are designed with redundancy and emergency procedures are implemented. Systems are extensively tested pre-flight.	N/A
TR-OPS-19	3	5	2	4	Regular inspection and maintenance are applied before flight. A power margin is included in the solar-array sizing, and panel degradation is included in the energy budget.	Non-critical power consumption is switched off and stored battery energy is used to maintain safe operation or perform a controlled landing, if necessary, request the ground to interrupt the mission.
TR-OPS-20	3	5	2	4	The propeller system is inspected before flight and designed with sufficient safety margin. Redundancy is included where possible so that one failed propeller does not immediately lead to loss of the aircraft.	The failure is reported to the ground station, the aircraft switches to an emergency mode, and the remaining propellers are used to return to a safe recovery location.
TR-OPS-21	2	5	1	4	The wing is designed with suitable structural safety factors and inspected before operation. Critical structural areas are checked for damage, fatigue, and manufacturing defects.	The damage is reported to the ground station, manoeuvring loads are reduced, and a controlled return or landing is performed if safe operation cannot be maintained.
TR-OPS-22	3	5	2	4	Battery temperature monitoring, thermal protection, and a battery management system are used during charging and discharging. The battery is operated within safe temperature and depth-of-discharge limits.	The overheated battery module is isolated if possible. Non-critical loads are reduced, temperature control is activated, and the aircraft enters a safe operating mode.
TR-OPS-23	2	5	1	4	The tail structure and control surfaces are designed with sufficient structural safety margin and inspected before operation. Control-surface hinges and linkages are checked for damage or excessive play.	The damage is reported to the ground station, manoeuvres are limited, and a controlled return or landing is performed if stable flight cannot be maintained.
TR-OPS-24	3	5	2	4	Proper electrical insulation, circuit protection devices, and redundant power cables are used for critical components. Electrical interfaces are checked during integration and testing.	The faulty circuit is isolated, the backup power line is used, and the aircraft enters an emergency mode until the power supply is recovered.
TR-OPS-25	3	4	2	3	Redundant heating devices and temperature sensors are included for critical compartments. The heating power is included in the power budget with margin.	The aircraft descends to a warmer altitude if possible, non-critical payload operation is interrupted, or the mission is terminated if the temperature cannot be recovered.
TR-OPS-26	3	5	2	4	The battery is designed to be replaceable and its usable capacity is checked before flight. Battery ageing, cycle degradation, temperature effects, and depth-of-discharge limits are included in the sizing.	The aircraft enters a low-power mode, reduces unnecessary component capacity, if necessary, request the ground to interrupt the mission.
TR-MAI-01	3	4	2	3	Maintenance cost margins are included in the budget estimation, especially for critical components and high-risk activities.	If costs exceed expectations, safety-critical tasks are prioritised and lower-cost options are reviewed without reducing safety or reliability.

Continued on next page

Risk ID	Pre-M		Post-M		Mitigation strategy	Contingency plan
	L	S	L	S		
TR-MAI-02	3	3	2	2	Critical replacement components are identified early, and their availability, lead times, and supplier reliability are checked.	If parts are unavailable, approved alternative suppliers or substitute parts are used; otherwise, operation is delayed until safe replacement is possible.
TR-MAI-03	3	3	2	2	Qualified maintenance personnel are identified before operation, and procedures are clearly documented.	If personnel are unavailable, non-critical maintenance or operation is postponed, or external qualified support is requested.
TR-MAI-04	3	4	1	3	Clear maintenance procedures, checklists, and training are provided, with critical actions checked by a second qualified person where possible.	If improper repair is found, operation is stopped, the system is inspected, and the repair is corrected before returning to service.
TR-MAI-05	2	5	1	4	Quality, tolerance, and reliability requirements are defined, and replacement parts are inspected or tested before installation.	If a part does not meet the required standards, it is rejected or replaced before further operation.
TR-MAI-06	2	4	2	3	Hardware and software compatibility is checked before updates, and updates are tested on representative hardware.	If incompatibility occurs, the previous verified software version is restored or required hardware changes are assessed.
TR-MAI-07	2	3	1	2	A clear maintenance schedule is defined based on reliability, operational hours, and safety-critical inspection needs.	If maintenance is overdue, operation is suspended until required inspections and maintenance tasks are completed.
TR-MAI-08	1	4	1	2	The aircraft maintenance aspects are taken into account when designing the aircraft.	Mission planning is reconsidered.
TR-MAI-09	1	4	1	2	Aircraft is designed in such a way that broadly-available maintenance technologies are sufficient for its maintenance.	Acquiring the necessary technology, licences and personnel is considered.
TR-MAI-10	2	4	1	2	Personnel shall receive sufficient training and pass a qualification test before performing battery replacement.	Appropriate protective clothing and electrical safety equipment shall be worn during the procedure.
TR-EOL-01	3	4	2	3	Clearly define a disposal plan for electrical components and separate them according to applicable environmental guidelines.	If disposal cannot be completed as planned, store the components safely until an approved recycling or disposal option is available.
TR-EOL-02	2	4	1	3	Clearly define and verify a data removal procedure before disposal of any storage device.	If data removal is incomplete or uncertain, suspend disposal until the device has been inspected, wiped, or destroyed if necessary.
TR-EOL-03	3	4	2	3	Identify hazardous components early and provide safe handling, storage, disposal procedures, and adequate training.	If hazardous components are found to be mishandled, stop the disposal process, assess the impact, and contact an approved disposal service if required.
TR-EOL-04	3	4	2	3	Check local disposal, recycling, and hazardous-waste facilities before selecting the end-of-life strategy.	If local infrastructure is insufficient, use an approved facility elsewhere or store components safely until disposal is possible.

17

Mission Verification and Validation

This chapter covers the planned and performed mission verification and validation (V&V) of the aircraft. Verification and validation are essential steps in product design to ensure the product satisfies both the requirements set by the design team and the intended mission of the customers. Procedures for verifying the aircraft are covered in Section 17.1, while validation procedures are explained in Section 17.2

17.1. Verification

Verification of the mission entails ensuring SORA meets all requirements. These requirements were established in the Baseline Report [111]. A mission V&V plan was presented in the Midterm Report [15], which proposed three verification methods, outlined in Table 17.1.

Table 17.1: *Verification Methods used in the MALEO4CRE V&V Plan.*

Method	Description
Inspection	Inspect the design documentation or the product to show compliance with the requirement.
Analysis	Establish by mathematical or other analysis techniques that the product complies with the requirement.
Test	Test a representative model of the product under representative conditions to show compliance with the requirement.

The verification methods can be subdivided into the following categories:

- **Flight tests:** Includes short- and medium-duration flight tests (hours to days) and endurance tests to validate the 60-day endurance requirement. Flight tests are classified as medium cost due to personnel, planning, and external coordination requirements, while endurance tests are classified as high cost.
- **Ground tests:** Includes physical tests performed on the ground, such as thermal, structural load, wind tunnel, chamber, crash, and electrical grounding tests. Wind tunnel and chamber tests require specialised facilities and are classified as high cost. Thermal, structural, and instrument tests are classified as medium cost. Ground taxi tests are classified as low cost as they require minimal personnel.
- **Analysis and simulation:** Used when physical testing is impractical or to support and de-risk subsequent flight testing. Covers navigation, endurance, cost, and performance assessments. Classified as low cost, requiring only personnel time and computational resources.
- **Inspection:** This is done when a requirement can be sufficiently considered as verified by inspecting the design document, component specifications or compliance with regulations that do not require physical testing.

In this report, the final verification status for each requirement is shown in the compliance matrix in Section 17.3. The status is shown as a "Yes" for verified requirements, "Prelim. yes" for requirements that are considered likely to be met based on engineering judgement, "TBD" for unverified requirements, and "No" for definitively unmet requirements. The status in the compliance matrix is supported where possible. Finally, a cost estimation is given per verification activity.

17.2. Validation

Mission validation was conducted to assess whether the proposed aircraft design fulfils the intended mission and addresses customer needs. These needs have been identified through customer requirements, market analysis, and regular meetings with the client. The Mission Need Statement (MNS) defines the mission as performing long-duration measurements of atmospheric parameters at medium- to high-altitude in order to increase the available data for the validation of climate models. Mission validation therefore focuses on determining whether the proposed design satisfies these needs and provides an appropriate solution for the intended mission.

17.2.1. Validation approach

The validation approach assessed whether, and to what extent, the aircraft fulfils the four identified mission needs, covering both completed and planned validation activities. Throughout development, the design was continuously validated with respect to the customer needs through weekly meetings, which guided design decisions and resulted in formal approval of the payload selection and the derived system requirements. Furthermore, the most critical needs for the mission were identified. These include gathering adequate data for climate models, having a global mission profile, enabling long endurance for persistent local measurements, and cruising stratospheric altitudes.

17.2.2. Validation against critical needs

Validation was performed for all critical mission needs found in Subsection 17.2.1. The methods used are detailed for each need below.

Adequate Data for Climate Models: A literature study was performed, covering studies that use climate models and measurement campaigns run by established climate research institutions such as NASA and DLR. The payload selection, detailed in Chapter 6, was based on the instruments used during these campaigns and on the papers describing the climate models. The selected payload was then analysed to ensure it could operate in the stratosphere. This partially validated the aircraft's ability to capture the data required to support the development and accuracy of climate models. Future validation efforts include operating the payload during a test flight.

Global Mission Profile: A fully global mission profile was deemed unrealistic. The presence of jet streams, number of daylight hours and turbulent areas limit the operational areas for a solar-powered aircraft. The aircraft batteries were therefore sized to enable, in any month, a daily mission profile cruising up to 25 km over a latitude range of at least 45° under ISA conditions, with the most limiting cases occurring during spring and autumn in both hemispheres due to reduced daylight hours. Moreover, SORA is not limited to line-of-sight (LOS) operations, since the communication system uses SpaceX Starlink infrastructure that includes both land and ocean coverage. Future validation efforts include test flights to demonstrate the performance across the months of the year and to validate the solar and atmospheric models used. In addition, more accurate atmospheric models for turbulence and winds-aloft data are required to further refine the operational area of the aircraft.

Long-Endurance: The long-endurance need was addressed by the use of solar power to regenerate the energy consumed over a 24-hour cycle. Python-based analysis indicated that with improved solar panel efficiency, a closed energy balance is achievable in the near future (Chapter 10), and the concept is supported by existing solar-powered aircraft. Future validation will incorporate more advanced solar irradiance models, taking wing deflection and cruise orientation into account, and multi-day endurance flight testing.

High-Altitude: The high altitude requirement was partially validated through aerodynamic and propulsion nalyses, which indicated that the aircraft can generate enough thrust using specially optimized propellers for HALE applications. It was also indicated that the aircraft can generate sufficient lift through the use of MH114 airfoil, which is purpose-designed for the extremely low Reynolds numbers encountered in the stratosphere. Future validation efforts include 3D CFD simulations of the complete aircraft, wind tunnel tests, and test flights.

17.2.3. Validation Conclusion and Outlook

It was determined that the aircraft satisfies its mission needs. It carries validated atmospheric instruments capable of providing data for climate model validation. In any month, the aircraft can fly over a latitude range of 45° in a theoretical ISA. This therefore partially validates global coverage, although fully refining the operational area requires more advanced models that account for turbulence and winds aloft. Long endurance is also partially validated. A simplified solar irradiance model showed that, using solar panels with near-future efficiencies, the 24-hour energy balance can be closed. Future validation includes a more advanced solar irradiance model, taking wing deflection and cruise orientation into account. After the aircraft is complete, the team plans to execute a full 60-day flight test as an initial mission, to confirm that the aircraft operates within the specified mission profile for the specified duration, and can provide the necessary climate data with its payload. This data will be inspected by the clients to confirm that the final product is suitable for their needs. Overall, the aircraft is preliminarily validated against all four critical mission needs, with full validation to be achieved through future testing.

17.3. Compliance Matrix

The compliance matrix in Table 17.2 lists every requirement together with the method used to verify it, the corresponding verification activity, the estimated cost, and its current verification status. The verification methods are abbreviated as I (Inspection), A (Analysis) and T (Test), as defined in Section 17.1. The cost estimation is given as L (low), M (medium) or H (high). The verification status is one of: "Yes" for verified requirements, "Prelim. yes" for requirements considered likely to be met based on engineering judgement, "TBD" for requirements that are not yet verified and will be dealt with post-DSE and finally "No" for requirements that are definitively not met. The timeline

of the future verification activities is shown in Section 3.4 and visualised in Figure 3.4.

The performed and future verification activities can be broadly subdivided into the following categories:

- Flight tests: This covers both short and medium length flight tests (lasting from a couple hours to a couple days) and endurance flight tests, which aim to validate the 60 day endurance requirement from the customer. This can only be done once a working flight-ready prototype has been constructed. Flight tests involve many personnel, planning, working together with external parties, and are thus classified as medium cost. Endurance tests, which demonstrate the aircraft's ability to meet the 60 day endurance requirement, are classified as high cost due to the additional man-hours needed.
- Ground tests: This covers a variety of physical tests performed on the ground. These include thermal tests, structural load tests, ground taxi tests, instrument ground tests, wind tunnel tests, chamber tests, crash tests, and electrical grounding tests. The cost varies depending on the type of test: wind tunnel and chamber tests require specialised facilities and are classified as high cost, while thermal, structural, and instrument tests are classified as medium cost due to the less complex equipment involved. Ground taxi tests are classified as low cost as they require minimal personnel and are not complex. These tests can be done before a flight prototype is completed, but require the detailed design to be finished before.
- Analysis and simulation: This is preferred when testing is impractical or as precursor to a flight test, which then validates the results. This covers navigation, mission endurance, cost, and performance. These are classified as low cost as they require only personnel time and computational resources, with no testing needed. This was already applied to verify some requirements, although often a physical test is still required to fully verify the requirement.
- Inspection: This is done when a requirement can be sufficiently considered verified by inspection design documentation, component specifications or compliance with regulations that do not require physical testing. For this it is still needed to obtain the applicable regulations and to verify that the design documentation satisfies them. Thereafter, it needs to be presented to the regulator as proof of compliance. This is classified as low cost, as it only requires personnel time and communication with relevant authorities instead of physical testing. This process can be started after the detailed design phase is completed.

Table 17.2: *Compliance Matrix*

Req. ID	Requirement (abbreviated)	Method	Description of verification activity	Cost	Status	Status explanation
Functional Requirements (F)						
REQ-STK01-MIS01-SYS01	Stable flight in range 15–25 km	A+T	Perform stability analysis and validate with test flight	M	Prelim. yes	Correct stability derivatives calculated analytically, test flight pending
REQ-STK01-MIS01-SYS02	Recover from disturbance	T	Perform test flight with simulated disturbance inputs	M	TBD	Test flight pending
REQ-STK01-MIS02-SYS07	Manoeuvrable per regulations	T+I	Perform test flight and inspect results against relevant regulations	M	TBD	Test flight pending
REQ-STK01-MIS02-SYS08	Manoeuvrable per mission profile	T+A	Perform mission simulations for possible mission profiles and validate with multiple test flights	M	Prelim. yes	Mission profiles simulated, test flights pending
REQ-STK02-MIS01-SYS01	Transmit live data > 2.7 Mbits/s	T+I	Inspect transmitter data-rate specification and validate with a test flight using ground-based communication equipment	M	Prelim. yes	Specifications inspected, test flight pending
REQ-STK02-MIS01-SYS02	Transmit images at TBD resolution	T+I	Inspect optical instrument specifications and communication architecture, perform test flight while transmitting images to a ground receiving station	M	Prelim. yes	Optical instrument inspected, communication architecture inspected, test flight pending
REQ-STK03-MIS01-SYS01	Store data for 60 days	I+T	Inspect storage-system specification and validate with test flight	M	Prelim. yes	Storage system selected and inspected, test flight pending
REQ-STK04-MIS01-SYS01	Fully autonomous during cruise	T	Perform test flight	M	TBD	Current regulations do not allow fully autonomous operations, feasibility TBD post-DSE.
REQ-STK04-MIS01-SYS02	Autonomously avoid no-fly zones	T	Perform test flight directed towards a no-fly zone in a simulated airspace environment	M	TBD	Autopilot logic yet to be developed, test flight pending
REQ-STK04-MIS03-SYS01	Receive commands from 1200 km distance	T+I	Inspect communication architecture documentation, Perform test flight at 1200 km distance from the nearest ground station	M	Prelim. yes	Communication architecture inspected, test flight pending
REQ-STK06-MIS03-SYS01	Autonomous return-to-launch within TBD s after communication failure	T	Perform test flight with deliberate communication cut-off	M	TBD	Autopilot logic yet to be developed, test flight pending
REQ-STK06-MIS03-SYS02	Cut power to non-critical systems	T	Perform test flight with deliberate cut to non-critical systems	M	TBD	Flight computer logic yet to be developed, test flight pending
REQ-STK06-MIS03-SYS03	Redundant control system	I	Inspect design documentation for redundant control architecture	L	Yes	Redundant control architecture exists
REQ-STK06-MIS04-SYS01	Measure critical component temperatures	T	Perform ground thermal test of component temperature sensors in a thermal chamber	M	Prelim. yes	Temperature sensors installed in payload bay and battery compartments, thermal test pending
REQ-STK06-MIS04-SYS02	Activate protection on out-of-range component temperature	T	Perform ground thermal test and verify protection activation at threshold temperatures in a controlled thermal chamber setup	M	TBD	Flight computer logic to deal with out of range temperatures not yet developed, thermal test pending
REQ-STK07-MIS01-SYS01	Power supply to all systems	I+T	Inspect power budget and verify correct operation of the power supply during a test flight	M	TBD	Power supply details not yet designed, test flight pending
REQ-STK07-MIS01-SYS02	Critical power backup	T	Perform flight test with deliberate cut to part of the battery supply	M	TBD	Flight computer logic yet to be developed, test flight pending
REQ-STK07-MIS02-SYS01	Minimum energy storage capacity of 20.2 kWh	I+T	Inspect battery specifications and validate energy capacity with test flight	M	Prelim. yes	Battery specifications inspected, test flight pending
REQ-STK12-MIS02-SYS01	Wingspan < 36 m	I	Inspect design documentation for compliance	L	Yes	Design documentation inspected
REQ-STK12-MIS02-SYS02	Take-off distance < 2200 m	A+T	Perform take-off performance analysis and validate with test flight	M	TBD	Take-off analysis and test flight pending

Continued on next page

Req. ID	Requirement (abbreviated)	Method	Description of verification activity	Cost	Status	Status explanation
REQ-STK13-MIS01-SYS01	Determine altitude of neighbouring aircraft in real time	T	Perform test flight in an area with known air traffic and validate against transponder altitude data	M	TBD	Air traffic detection logic yet to be developed, test flight pending
REQ-STK13-MIS01-SYS02	Autonomous altitude changes to maintain safety buffers	T	Perform test flight with simulated conflicting traffic and verify autonomous altitude response	M	TBD	Air traffic conflict resolution logic yet to be developed, test flight pending
REQ-STK13-MIS02-SYS01	Determine geographic location of neighbouring aircraft in real time	T	Perform test flight with neighbouring aircraft at known positions	M	TBD	Air traffic detection logic yet to be developed, test flight pending
REQ-STK13-MIS02-SYS02	Autonomous course changes to maintain safety buffers	T	Perform test flight with simulated conflicting traffic and verify autonomous course response	M	TBD	Air traffic conflict resolution logic yet to be developed, test flight pending
Operational Requirements (O)						
REQ-STK06-MIS03-SYS04	Autonomous health monitoring and fault management for 60-day mission	A+T	Perform mission simulation and validate health monitoring and fault responses with test flight	M	TBD	Flight computer logic yet to be developed, test flight pending
REQ-STK08-MIS01-SYS01	Measure ambient airflow temperature	T	Test sensor in wind tunnel and validate with test flight	H	Prelim. yes	Temperature probe included in design, wind tunnel test and test flight pending
REQ-STK08-MIS01-SYS02	Measure ambient airflow pressure	T	Test sensor in wind tunnel and validate with test flight	H	Prelim. yes	Pressure probe included in design, wind tunnel test and test flight pending
REQ-STK08-MIS01-SYS03	Measure ambient airflow humidity	T	Test sensor in wind tunnel and validate with test flight	H	Prelim. yes	Humidity probe included in design, wind tunnel test and test flight pending
REQ-STK08-MIS01-SYS04	Measure ambient radiation	T	Perform instrument ground test and validate with test flight	M	TBD	Ground test and test flight pending
REQ-STK08-MIS02-SYS01	Measure aerosol particle number concentration	T	Perform instrument ground test and validate with test flight	M	TBD	Ground test and test flight pending
REQ-STK08-MIS02-SYS02	Measure aerosol particle size distribution	T	Perform instrument ground test and validate with test flight	M	TBD	Ground test and test flight pending
REQ-STK08-MIS02-SYS05	Measure greenhouse and aircraft emissions trace gas concentration	T	Perform instrument ground test and validate with test flight	M	TBD	Ground test and test flight pending
REQ-STK08-MIS03-SYS01	Measure ice crystal number concentration in contrails	T	Perform test flight above a region with contrails	M	TBD	Test flight pending
REQ-STK08-MIS03-SYS02	Measure ice crystal size in contrails	T	Perform test flight above a region with contrails	M	TBD	Test flight pending
REQ-STK08-MIS03-SYS03	Measure geometric visual properties of plume	T	Perform test flight above a region with contrails	M	TBD	Test flight pending
REQ-STK08-MIS03-SYS04	Measure plume thickness	T	Perform test flight above a region with contrails	M	TBD	Test flight pending
REQ-STK09-MIS01-SYS01	Payload temperature environment within most restrictive paylaod operational limits across altitude range	T	Perform chamber test and validate with test flight	M	TBD	Chamber test and flight pending
REQ-STK09-MIS01-SYS02	Payload pressure environment within operational pressure limits across altitude range	T	Perform chamber test and validate with test flight	M	TBD	Chamber test and flight pending
REQ-STK09-MIS02-SYS01	Onboard systems functional at 195 K at 25 km altitude	T	Perform test flight at 25 km altitude	M	TBD	Test flight pending
REQ-STK09-MIS02-SYS02	Onboard systems functional at 2385 Pa at 25 km altitude	T	Perform test flight at 25 km altitude	M	TBD	Test flight peding

Continued on next page

Req. ID	Requirement (abbreviated)	Method	Description of verification activity	Cost	Status	Status explanation
REQ-STK10-MIS01-SYS01	Autonomous execution of all flight functions	T	Perform autonomous test flight and verify proper autonomous decision making	M	TBD	Flight computer and autopilot logic not yet developed
REQ-STK10-MIS01-SYS02	Autonomous decision-making for nominal scenarios	T	Perform test flight covering all nominal scenarios	M	TBD	Flight computer logic not yet developed
REQ-STK10-MIS02-SYS01	Autonomous navigation and guidance throughout mission	A+T	Perform navigation and guidance simulation and validate with test flight	M	TBD	Simulation and test flight pending
REQ-STK10-MIS02-SYS02	Autonomous control of flight parameters in all mission phases	T	Perform test flight across all mission phases	M	TBD	Flight computer logic not yet developed
REQ-STK10-MIS02-SYS03	Autonomous handling of predefined off-nominal conditions	T	Perform test flight with deliberate triggering of predefined off-nominal conditions	M	TBD	Flight computer logic not yet developed
REQ-STK10-MIS03-SYS01	Real-time monitoring link to operator	T	Perform test flight with active operator monitoring link	M	TBD	Ground infrastructure not yet developed, test flight pending
REQ-STK10-MIS03-SYS02	Operator intervention via command inputs	T	Perform test flight with operator command inputs	M	TBD	Ground infrastructure not yet developed, test flight pending
REQ-STK10-MIS04-SYS01	Increased operator control during take-off	T	Perform test flight and verify increased operator control during take-off	M	TBD	Ground infrastructure not yet developed, test flight pending
REQ-STK10-MIS04-SYS02	Increased operator control during landing	T	Perform test flight and verify increased operator control during landing	M	TBD	Ground infrastructure not yet developed, test flight pending
REQ-STK11-MIS05-SYS01	Continuous flight for 60 days without landing	A+T	Perform 60-day mission simulation and validate with endurance test flight	H	TBD	Multiday mission simulation yet to be performed, endurance flight test pending
REQ-STK11-MIS05-SYS02	60-day availability to measurement instrumentation	T	Perform endurance test flight and verify instrumentation availability throughout	H	TBD	Endurance test flight pending
REQ-STK11-MIS05-SYS03	Autonomous operation for 60 days	T	Perform long-endurance autonomous test flight	H	TBD	Flight computer logic yet to be developed, test flight pending.
Constraint Requirements (C)						
REQ-STK17-MIS01-SYS01	Production cost ≤ TBD budget	A	Perform production cost analysis against budget	L	Yes	Production cost analysis done
REQ-STK17-MIS01-SYS03	Minimized maintenance cost	A	Perform analysis of maintenance cost drivers	L	TBD	Maintenance cost driver analysis yet to be completed
REQ-STK17-MIS02-SYS01	Design cost plan exists	I	Inspect design process documentation for existence of cost plan	L	Yes	Cost plan exists
REQ-STK17-MIS02-SYS02	System costs monitored	I	Inspect project records to verify assignment of cost monitoring responsibility	L	Yes	Team member was assigned to monitor costs
REQ-STK20-MIS01-SYS01	Detect manned aircraft on ground within TBD range	T	Perform test flight with manned aircraft at known ground position	M	TBD	Ground traffic detection logic yet to be developed, ground test pending
REQ-STK20-MIS01-SYS02	Safe stop capability during ground operations	T	Perform ground taxi test and verify safe stop capability	L	TBD	Safe stop logic yet to be developed, ground test pending
REQ-STK20-MIS02-SYS01	Identify and avoid surface hazards while taxiing	T	Perform ground taxi test with surface hazards present	L	TBD	Surface hazard detection logic yet to be developed, ground test pending
REQ-STK20-MIS02-SYS02	Recognize aerodrome markings and signage	T	Perform ground taxi test at operational aerodrome	L	TBD	Logic for sensing environment yet to be developed, taxi test pending
REQ-STK21-MIS02-SYS01	Execute ATC instructions within required response time	A+T	Simulate ATC instructions during mission simulation and validate response time with test flight	M	TBD	Flight computer logic not yet developed, mission simulation and test flight pending

Continued on next page

Req. ID	Requirement (abbreviated)	Method	Description of verification activity	Cost	Status	Status explanation
REQ-STK21-MIS02-SYS02	Link performance meets RCP and PBN requirements	A+T	Perform link performance analysis and validate RCP and PBN compliance during test flight	M	TBD	Link performance analysis and test flight pending
REQ-STK23-MIS01-SYS01	Camera shall not capture identifiable individuals	T	Perform test flight and verify that images contain no identifiable individuals	M	TBD	Test flight pending
REQ-STK23-MIS01-SYS02	Instruments adhere to data protection codes	I	Inspect instrument specifications against applicable data protection regulations	L	TBD	Inspection of instrument specification pending
REQ-STK23-MIS02-SYS01	Record keeping covers entire data lifecycle	I	Inspect data storage specifications for full lifecycle coverage	L	TBD	Inspection of data storage specification pending
REQ-STK24-MIS01-SYS01	Flight Data Recorder or equivalent logging system	I	Inspect design documentation for FDR or equivalent logging system	L	Yes	Flight data logging though telemetry downlink present in design documentation.
REQ-STK24-MIS01-SYS02	Data stored in crash-protected medium	T	Perform crash test on data storage	L	No	Requirement scrapped, replaced by live transmission of data
REQ-STK24-MIS01-SYS03	Continuous data recording from pre-flight to post-flight	T	Perform test flight and verify completeness of recorded data	M	TBD	Test flight pending
REQ-STK24-MIS03-SYS01	Aircraft equipped with DAA capabilities	T+I	Inspect design documentation for DAA capabilities and validate during test flight	M	TBD	DAA logic yet to be developed, test flight pending
REQ-STK24-MIS03-SYS02	DAA interoperable with other collision avoidance systems	I+T	Inspect design documentation for interoperability and verify compatibility during test flight	M	TBD	DAA logic yet to be developed, test flight pending
REQ-STK24-MIS03-SYS03	DAA certified by competent authorities	I	Inspect design documentation for DAA certification evidence	L	TBD	DAA logic yet to be developed and certified.
REQ-STK24-MIS05-SYS01	Autonomous functions overridable by remote pilot	T	Perform test flight and verify remote-pilot override of autonomous functions	M	TBD	Override logic yet to be developed, test flight pending
REQ-STK24-MIS06-SYS01	Electrical pathway grounded	I+T	Inspect electrical design for grounding and validate with ground test	L	TBD	Detailed electrical design not yet developed, ground test pending
REQ-STK24-MIS06-SYS02	Materials not easily ignited	I	Inspect flammability properties of selected materials in design documentation	L	Yes	Flammability properties of selected materials inspected
REQ-STK24-MIS06-SYS03	Fire zone classification made	I	Inspect design documentation for fire zone classification	L	TBD	Fire zone classification pending
REQ-STK24-MIS07-SYS01	Anti-collision lights in low visibility	I	Inspect design documentation for anti-collision lighting compliance	L	Yes	Anti-collision lights present in design documentation
REQ-STK24-MIS07-SYS02	Structural extremity lights in low visibility	I	Inspect design documentation for structural extremity lighting compliance	L	Yes	Structural extremity lights present in design documentation
REQ-STK24-MIS07-SYS03	Navigation lights in low visibility	I	Inspect design documentation for navigation-lighting compliance	L	Yes	Navigation lights present in design documentation
REQ-STK24-MIS08-SYS01	Transponder per ICAO Annex 10	I	Inspect design documentation for ICAO Annex 10 transponder compliance	L	Yes	ADS-B present in design documentation
REQ-STK25-MIS01-SYS01	Sound power level ≤ ICAO Annex 16 limit	T	Perform test flight and measure sound power level against ICAO Annex 16 limit	M	TBD	Test flight pending
REQ-STK25-MIS01-SYS02	Noise monitoring instrumentation fitted	I	Inspect design documentation for noise monitoring instrumentation	L	No	Requirement scrapped, replaced by ground equipment
REQ-STK26-MIS01-SYS01	≥50 % recyclable mass at EOL	A	Perform analysis of material recyclability at end-of-life	L	Yes	Material recyclability analysis present in design documentation
REQ-STK26-MIS01-SYS03	Recyclable material fraction simulated before design finalization	I	Inspect design process records for recyclability simulation	L	TBD	Recyclability simulation pending

Continued on next page

Req. ID	Requirement (abbreviated)	Method	Description of verification activity	Cost	Status	Status explanation
REQ-STK26-MIS02-SYS01	No LTO emissions	I	Track LTO emissions during flight test	M	Yes	LTO emmissions considered zero due to electric propulsion system
REQ-STK26-MIS02-SYS02	LTO emissions analysis performed	I	Inspect documentation for LTO analysis	L	No	LTO emmissions considered neglegible due to electric propulsion system, requirement scrapped
REQ-STK26-MIS03-SYS01	Zero emissions during cruise	I	Inspect propulsion system design for zero-emission cruise compliance	L	Yes	Cruise emmissions considered neglegible due to electric propulsion system
REQ-STK26-MIS03-SYS02	Zero-emission power sources used during cruise	I	Inspect power subsystem design for zero-emission sources during cruise	L	Yes	Electric power subsystem does not produce emissions
REQ-STK27-MIS02-SYS01	Standardized components used where possible	I	Inspect design documentation for use of standardized components	L	TBD	Detailed component design not yet developed
REQ-STK27-MIS02-SYS02	Critical structural components accessible for inspection	I	Inspect design for accessibility of critical structural components	L	TBD	Current design not easily inspectable, iterations pending
REQ-STK27-MIS02-SYS03	Critical structural components undergo NDT	T	Perform non-destructive testing on critical structural components	M	TBD	Critical structural component identification and NDT pending
REQ-STK27-MIS03-SYS01	Assembly tasks documented in SOPs	I	Inspect SOPs for inclusion of assembly tasks	L	TBD	SOPs not yet developed
REQ-STK27-MIS03-SYS02	Complex assembly documentation includes visual aids	I	Inspect complex assembly documentation for visual aids	L	TBD	Assembly documentation visual aids not yet developed
REQ-STK27-MIS03-SYS03	Components tracked by serial number, batch number, manufacturer, and expiry	I	Inspect component tracking records for serial number, batch number, manufacturer, and expiry data	L	TBD	Component tracking records guidelines not yet developed
REQ-STK27-MIS05-SYS01	Materials tested under operating temperatures	T	Perform ground thermal test of materials at operating temperature limits	M	TBD	Ground thermal test pending
REQ-STK27-MIS05-SYS02	Materials tested under operating loads	T	Perform ground structural test of materials under operating load conditions	M	TBD	Ground structural test pending

18

Quality Assurance

This chapter covers the quality assurance process for the achieved design. Section 18.1 assesses the the analysis of the aircraft's Reliability, Availability, Maintanability and Safety. Section 18.2 investigates how the global iteration scripts led to the final design and Section 18.3 showcases the sensitivity analysis process for these scripts.

18.1. RAMS

Including considerations on Reliability, Availability, Maintainability and Safety (RAMS) during the design process is essential to reach a complete and well rounded solution. RAMS is an engineering technique involving a wide range of methodologies, from Fault Tree Analysis (FTA) to Probability Risk Assessment (PRA) [1].

18.1.1. Reliability

Reliability is defined as a system ability to perform its intended function continuously [115]. This is implemented in the design with both a fail safe and a safe life philosophies.

Fail Safe

The UAV design includes multiple aspects from the fail safe design methodology, by allocating redundancy to critical systems. This aspect was taken into account during the entire design process, driving some important decisions during the design. Firstly, the propulsion system, described in Chapter 9, had to be properly sized with multiple engines to ensure a controlled descent in case of an engine failure. This limited the design from having only one engine, and incentivized four engines. Secondly, the communication system was designed with ample margins and secondary communication paths. The main communication system was chosen as it was a proven and reliable solution, ensuring low failure rates. Furthermore, a secondary telemetry communication link was developed, to ensure critical information such as location, speed, and battery state could be communicated to the ground station in case of an unlikely failure of the prime communication system.

Safe Life

Furthermore, the UAV includes aspects also from a safe life philosophy. This is more relevant on parts where a redundant system is not feasible, like the aircraft fuselage and materials. Due to the corrosion effects of ozone and intense solar radiation, the fuselage and wing materials may develop damage during the mission. The chosen materials have low reactivity with ozone [116]. This low reactivity, together with the use of safety factors in the design, render the fuselage able to safely endure the 60 day mission without failure.

18.1.2. Availability

Availability is defined as the readiness for a correct service [115], translating into what percentage of the year the system can be used. Due to the uniqueness of the design, being solar powered, the main availability constraint is the sun solar irradiance and the night duration. The UAV was designed to be able to operate in every part of the world, given the correct time of the year. A graph showing the available latitudes at the corresponding months is shown in Figure 18.1

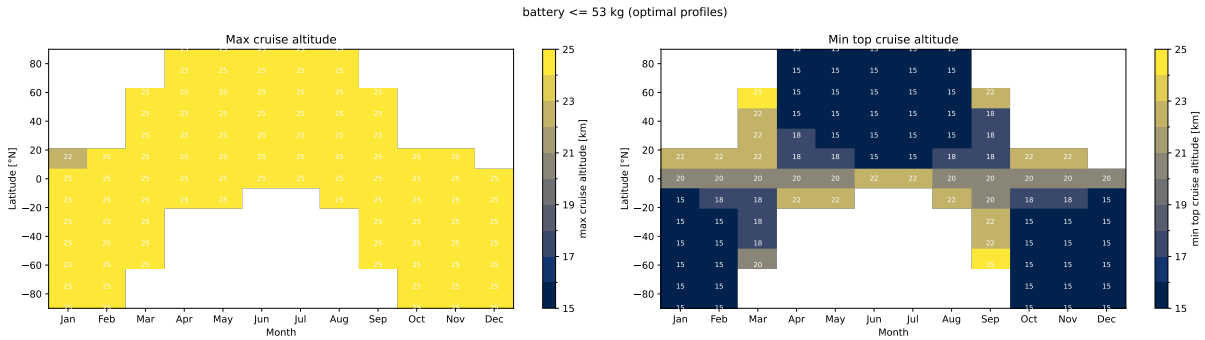

Figure 18.1: *Operational Ranges per Month for a Design Battery Mass of 53 kg*

[1] URL: https://www.protect.airbus.com/blog/safety-101-understanding-operational-reliability-terminology/ [cited 11/06/2026]

18.1.3. Maintainability

Maintainability is an essential factor to consider while designing. It consists in how quickly damages or other issues can be fixed to return the system to fully operational status and is usually measured in Maintenance Man Hours per Flight Hours (MMH/FH) and Mean Time Between Maintenance (MTBM) [117]. Maintenance tasks can be split into planned and unplanned, the first consisting of battery replacement, pre and post flight inspection, propeller and engine checks. To help reduce the MMH/FH, batteries will be easily removable, while engines will continuously send diagnostics to the ground station. To further reduce MMH/FH adaptive maintenance based on collected data can be implemented.

18.1.4. Safety

The design of any flying object has to take safety into consideration, to protect the UAV itself, humans, and the surrounding environment. To ensure this, multiple factors have been taken into account during the design phase. Firstly, the aircraft has a redundant telemetry system to ensure controllability of the UAV even in case of a primary communication system failure. Secondly, self diagnostic checks and resolution will be autonomously performed by the UAV, focusing on batteries and flight computers. Furthermore, the flight profile will be customized to each mission, focusing on minimizing turbulence on the climb phase, to impose the lowest stresses on the airframe and avoid a mid flight failure. Finally, an ADS-B transponder is placed into the aircraft, informing TAC of its position and helping to avoid any possible mid air collisions. Even with all the autonomous safety systems in place, human monitoring and override will be available in case of other unaccounted for failures.

18.2. Global Iteration Loop Analysis

Analysing the convergence of the global iteration loop of the aircraft design, explained in Chapter 3, is important to understand if this loop is working correctly. In the global iteration script, iterations were run from initial guesses of the total mass from 100kg to 1000kg, in steps of 50kg. For initial guesses up to 750kg, the iterations converged to about the same value of final mass, around 215kg, as seen in Figure 18.2

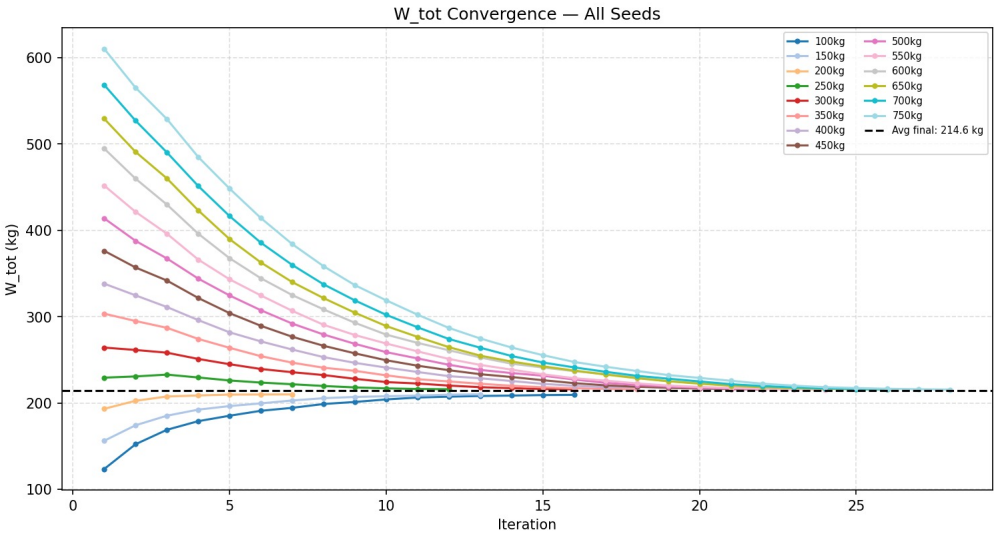

Figure 18.2: *Convergence of Global Iterations*

A final mass of ≈215kg seems to be the global minimum for the design space of the aircraft. The iterations arising from an initial guess of the aircraft converge to 218.5kg, and this value is taken for the design of SORA, since during the midterm phase of this project a mass of 406.6kg had been achieved for the conceptual design (see Chapter 15). Iterations with initial guesses higher than 750kg failed since aircraft this heavy would require more energy than what is possible to obtain with solar panels while satisfying the operational goal of being able to climb to 25km and guaranteeing a geographical operational range of at least 45° of latitude every month of the year. For the initial mass guesses that converged to the final value, the distribution of masses between the different aircraft subsystems can be seen in Figure 18.3.

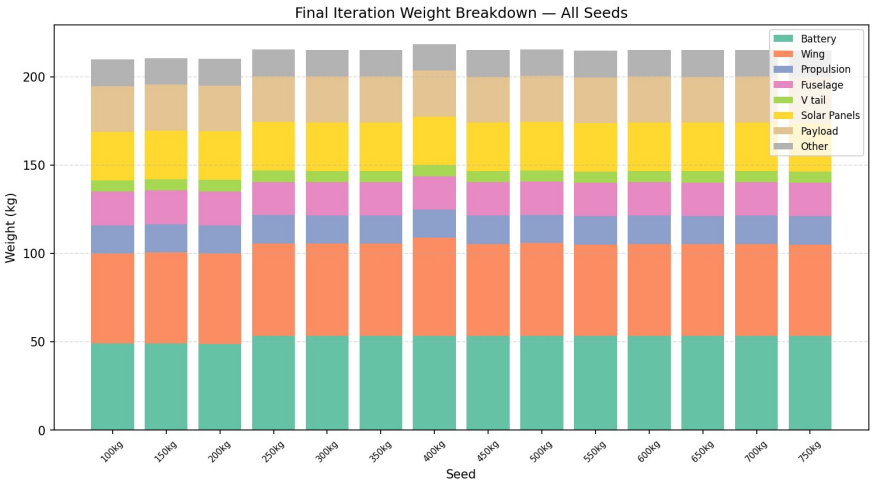

Figure 18.3: *Weight Breakdown of Converged Design*

As seen, all subsystems converge to about the same mass fraction in the aircraft across the different initial guesses, which grants further confidence that the iteration loop works correctly and indeed converges to the global minimum. Note that the "Other" section in the figure includes the mass of the communications system, actuators, flight computers and cabling.

18.3. Sensitivity Analysis

The design model for sizing the aircraft consists of multiple predefined key design inputs. However, it is possible that these design inputs variate due to their uncertainties. Therefore, a sensitivity analysis is performed to evaluate the robustness of the final aircraft design for these design parameter variations. The analysis was performed on each different parameter individually, discussed in Subsection 18.3.1. Additionally, a system level analysis was performed using Monte Carlo, that is discussed in Subsection 18.3.2. The parameters that were analysed for this sensitivity analysis were payload mass, aspect ratio, taper ratio, and wing placement location.

18.3.1. One-At-a-Time Analysis

This analysis varied only one parameter at at time for ±5% and ±10% to analyse what the influence of each parameter is on the design and to analyse how sensitive each parameter is. Each of these parameters were then analysed on what their influence is on the total weight and power of the aircraft. Changing the payload weight, aspect ratio, taper ratio and wing position parameters showed convergence, and the results are presented in Figure 18.4.

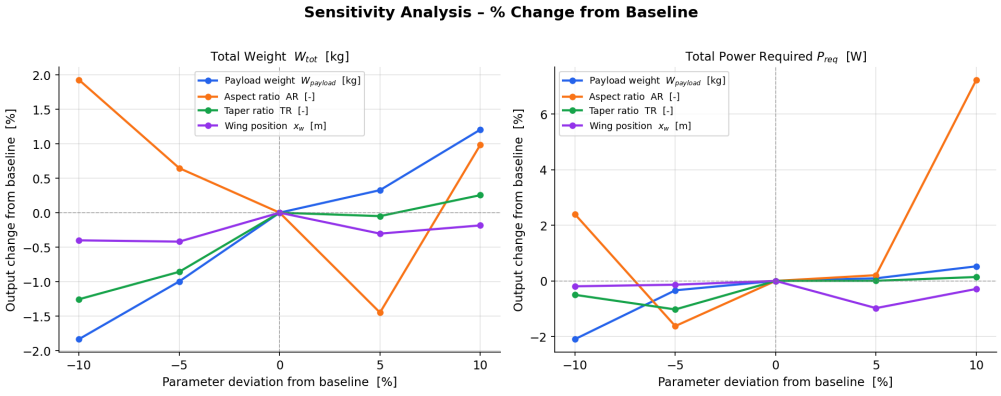

Figure 18.4: *Effect of Changing Parameter on Baseline Design*

It can be seen that the aspect ratio is most sensitive to the design, since it has the highest change in percentage. However, it is important to note that the aspect ratio does not show linear behaviour. Therefore, the aspect ratio shall be considered as a critical design constraint that cannot be varied. The payload weight has the most predictable sensitivity: this parameter shows linear behaviour, indicating that an increase in the payload weight will increase the total weight, which is as expected beforehand. Therefore, the design is robust for the uncertainties of the payload weight. Both the taper ratio and wing position show little linear behaviour. However, comparing the influence on of these parameters on the design with the influence of the payload mass, the sensitivity of these parameters is much lower. Due to their low influence, these parameters can be optimised in favour of the different subsystems, as

changing the parameters has only little effect on the final design.

Concluding, the aspect ratio dominates the parameters, but does show non-linear behaviour, giving uncertainty in the validity of the outcome. Payload weight drives the design with linear behaviour, whereas both taper ratio and wing position are parameters that are not very sensitive.

18.3.2. Monte Carlo Analysis

A Monte Carlo sensitivity analysis was performed on system level. Several input parameters from the iterative sizing model were all randomly varied within predefined uncertainties, ranging in ±10%. A total of 99 runs were performed with all random variation for the parameters. Due to lack of time, it was not possible to perform more runs. These parameters were all uniformly randomly varied within selected ranges, where the iterative design process is repeated until convergence.

As can be seen in Figure 18.5, both the median and mean are below the nominal value of the design. This indicates that the current design parameters were conservative. Additionally, it can be concluded that the design will not exceed 220.1 kg with 95% confidence. The histogram also shows that the total mass of the aircraft is spread to the left, indicating that it is more likely that the design will result more in a lighter than a heavier design. Therefore, it can be concluded that the current design is conservative, and if parameters change in the future, there is high confidence that this will not come with an increase in mass. Also, the possibility of varying some parameters to find their optimum values shall be considered in the future, as the histogram shows that there are parameter combinations that result in a lighter total mass.

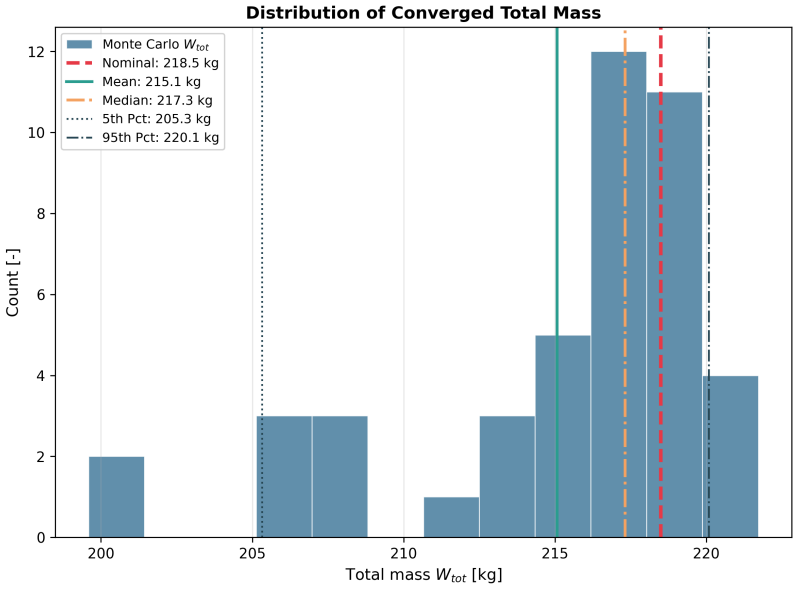

Figure 18.5: *Monte Carlo Histogram*

18.3.3. Design Implications

The results from the One-At-a-Time (OAT) and Monte Carlo sensitivity analyses result in recommendations for the design implications. The aspect ratio shall be frozen as a critical constraint, because it shows highly sensitive, non-linear behaviour, making it a design risk.

The Monte Carlo simulation confirmed that the nominal design mass (W_{tot} = 218.5 kg) is conservative, as it is above both the mean (215.07 kg) and median (217.31 kg). Because there is a 95% confidence that the mass will not exceed 220.1 kg, a design margin of around 1.75 kg shall be set to consider unforeseen increase in weight.

Since the taper ratio and wing position show low sensitivity on both the total weight and power, these parameters can be optimised for local subsystems. For example, the wing placement can be placed to get the correct centre of gravity, without having a big influence on the total weight and power. Additionally, the taper ratio can be modified to optimise the aerodynamics or wing structure. Lastly, the Monte Carlo histogram indicated that some of the converged combinations resulted in a total mass of approximately 200-210 kg. Therefore, it shall be considered to find the optimum combination of parameters to achieve the most optimum design configuration.

19

Conclusion

This report presented the design of the SORA (Stratospheric Observatory Research Aircraft), an unmanned high-altitude autonomous drone which will perform long-endurance missions (up to 60 days), taking measurements of the atmospheric composition, aircraft cruise emissions and radiation, to further climate research. The final design consists of a 36 m wingspan aircraft, with a total fuselage length of 12 m and a weight of 218.5 kg, and can be seen in Figure 19.1.

In order to achieve this design, it was first necessary to identify the market gap that SORA will aim to fill, and for this, a thorough market analysis was conducted. This was followed by an analysis of the different stakeholders that can impact or be impacted by this project, which was then used to derive an extensive requirements list.

Considering the requirements related with the scientific mission of the aircraft, it will feature a range of different measurement instruments, including radiation sensors to study the impact of contrails on Earth's radiation balance, spectrometers covering the Short Wave Infrared and Ultraviolet/Visual band for detection of trace gases, a LiDAR for measuring contrail properties like thickness, altitude and ice particle concentration, an in-situ aerosol sensor for measuring stratospheric aerosols, a whole air sampler to collect samples which can later be analysed in laboratory for detection of substances too rare for the other instruments to capture, and lastly a sensor to measure ambient temperature, pressure and humidity, which allows to understand how these variables influence the behaviour of all the other measured parameters.

Then, the different subsystems of the aircraft were designed. On the aerodynamics side, the airfoil chosen was the MH114. Then, the 3D wing was analysed for lift distribution and drag estimation, which was followed by drag estimation of the fuselage, tail and propellers as well. The aircraft will have 4 propellers, with 2 blades each, with the blades using the FX63-137 airfoil. The propulsion system was sized to minimize drag and weight, while ensuring it provides the required thrust for the aircraft to perform its mission. All subsystems of the aircraft need to be supplied with power, which, considering the need for the aircraft to remain in the air for 60 days, will be produced on-board, using solar panels installed on top of the wing. To support night operations, the aircraft will feature a set of Amprius SiCore 450 Wh/kg battery cells, chosen for their high energy density and demonstrated suitability for high altitude drone systems. The aircraft will also have to maintain communication with the ground station(s), enabling live transmission of measurement data and commands. For this, it will feature two satellite-based communication systems, which allow beyond-line-of-sight communication: a Starlink Mini system, for measurement data and commands transmission, and an Iridium terminal, for redundancy regarding ground-station commands. All of these subsystems need to be supported by the body of the aircraft; as such, the fuselage and the wing were sized considering the different applied loads that the aircraft will be subjected to during its life. The main material used for the fuselage and for the wing spars will be Galvorn, while the wing will also feature CFRP Honeycomb ribs and Mylar film skin. Finally, to ensure stability and controllability of the aircraft, its V-tail, ailerons and ruddervators were sized accordingly.

Some additional considerations were taken into account considering the future life of the aircraft. A production plan was developed, a comprehensive technical risk analysis spanning the different life phases of the product was conducted, and a plan for mission verification and validation of the final product was also written.

There are several reflections that the team has regarding this project, the progress so far and what could have been done better. Firstly, regarding what could have been done in a different way, there are several reflections: the team decided to use Excel for the early conceptual design and iterations, up until about halfway during this project, but this tool proved to be too limiting for the complex interactions between the different aircraft subsystems, and the team believes it was one of the reasons why up to the midterm the design did not converge to a design satisfying mass and power constraints; once the team moved to the use of Python instead, it was possible to better organize and integrate work from different members, in the end achieving a design which satisfies the mission objective. Then, when trying to bring all subsystems together in Python to perform the final global iterations, the team ran into some problems regarding the interaction between scripts sizing different subsystems and difficulty in making the global loop converge. While in the end these problems were solved, a lot of time was wasted on this, which could have been avoided if the code was developed in a modular way, with each department first developing a simplified sizing script for their respective subsystem which could be integrated early into a global iteration loop, to start gaining insights early about how to best make this loop converge.

When it comes to things where the team improved all throughout the project, there are also some reflections. Up

until halfway through the project, the team worked purely as a group of smaller teams together at the same table, with little interaction between different departments. This ended up harming the team's ability to reach a converged conceptual design at the midterm point of this project. Afterwards, a strategy was delineated to solve this issue, whereby communication between different members and departments started being a major point of focus in the team's daily work, as well as frequent daily meetings where each of the team members brought the rest up-to-date with their progress, serving as clear points throughout the day where working strategy could be adjusted.

Finally, the team would like to address its path on stepping out of the "student mindset", and into a more proactive mentality as the project went on. In past projects, team members were used to having very clear guidance on the steps that should be taken in order to achieve the solution to a certain problem, but with this project being so broad in terms of the possible paths to achieve success, it took time to get adjusted to this reality. Now, the team feels much more capable of charting its own path and making its own decisions, using external help purely as a tool of support and validation of our decisions, and not as source of all decisions that should be made throughout the project.

Figure 19.1: *SORA's Final Design*

20

Recommendations

The preliminary design of SORA leaves several aspects open for further investigation and refinement. This chapter compiles the recommendations that follow from the design process. Chapter 20 presents recommendations at the system and subsystem level, providing a basis for future development of SORA and guidance for other HALE design teams. Chapter 20 looks outwards, offering recommendations to the climate research and aviation sectors to help to create an environment in which SORA and similar platforms can thrive and contribute to society.

System Recommendations

This section contains the global system level recommendations that were put together for the MALEO4CRE mission, as well as subsystem level recommendations. These recommendations were compiled after the completion of the preliminary design phase and exist to identify foreseen and unforeseen shortcomings of the design. Moreover, the recommendations give a basis for future design efforts to further develop SORA or serve as guidelines for other design teams to follow in their efforts to develop a HALE platform.

Firstly, it is recommended to verify the capabilities of of-the-shelf (OTS) components. For SORA these include the instruments of the scientific payload, batteries, actuators and (external) sensors. All OTS components have been inspected for their specified capabilities, however, testing them is essential to ensure that the performance of the product is as expected. This is especially important given the extreme nature of the stratospheric environment, where SORA is set to operate in.

Secondly, it is recommended to inspect the design for maintainability and manufacturability. Currently, little attention has been paid to these domains. The feasibility of the manufacturing process is presently based on assumptions and limited knowledge of manufacturing processes. It is thus required to either acquire more knowledge in this domain or employ external experts for this subject. Possibly, a redesign of (a part of) the aircraft will be required to make the design manufacturable. Moreover, little attention has been paid to the maintainability of the aircraft. This is an important aspect of design that enables safe operations by for instance identifying weaknesses in the structure and replacing damaged or broken parts. Thus, it is crucial to investigate which areas of the aircraft shall need to be inspected and maintained during the lifecycle of the product and to consider a redesign if needed to improve maintainability.

Thirdly, it is recommended to employ higher fidelity models to reduce the uncertainty in model predictions and including physical phenomena that lower fidelity or analytical models cannot represent. For instance, CFD models 3D separation, interference drag, laminar to turbulent transitions and low-Re behaviour that XFLR5, the model currently used, only approximates. FEM models a real stress field, local buckling and the effect of cutouts that the current analytical beam and cylinder models for the wing and fuselage structures cannot replicate. The result is a tighter margin and a more trustworthy number rather than an estimate wrapped in a conservative margin. Regarding atmospheric models, there are improvements needed, as currently, the theoretical ISA model was used for modelling all atmospheric properties except temperature. Aligning with industry standards, and as confirmed by a meeting with a representative of Sceye[1], it is recommended to develop or purchase a high resolution weather model, used to ensure a safe climb to cruise altitude during launch day. Moreover, during the cruise phase a high fidelity model that is specifically well validated for stratospheric altitudes is required. Furthermore, a higher fidelity solar model is required, as currently, a simplified model is adopted where the panels are assumed to be completely flat and angled parallel to the Earth's surface. The deformation of the wing is significant, thus future solar power models need to include the real deformation of the aircraft's wings, incorporating real aircraft geometry and orientation, and accounting for self-shadowing.

Lastly, there are improvements to be made to the mission simulation. Currently, only a 24 hour window is modelled to confirm energy balance closure, which is then evaluated across discrete latitudes and months of the year to size the battery. To properly ensure the viability of a 60 day mission, full mission simulations are required, incorporating change in solar declination and all charging cycles the batteries will undergo. Furthermore, non-nominal scenarios should be incorporated, such as station-keeping against wind, varying payload duty cycles and adverse weather during the climb to cruise altitude. The accuracy of this simulation is directly coupled to the solar power model discussed in the previous recommendation, as a reliable worst-case analysis requires the correct panel geometry as an input.

[1] Sceye representative, unpublished interview, May 2026

In the following subsections, specific recommendations are given per subsystem. Since each recommendation is specific to its discipline, this was split from this system level recommendation overview.

Operations
Three recommendations are given for developing the operational aspect of SORA. Firstly, it is recommended to investigate possible gain from developing strategic flight patterns, such that the panel area exposed to the sun is maximal and the average angle of incidence is minimised. Next, it has been shown that formation flying can lead to efficiency gains[118]. Thus, it is recommended to investigate the possible benefits of splitting the payload across two or more, possibly lighter, SORA aircraft and to investigate the feasibility of formation flight to increase efficiency. Lastly, little attention has been paid to possible launch sites. To have a better idea of the operational area of SORA, it is recommended to develop a method to assess whether an airport is suitable for SORA's launch, and apply this to airports worldwide.

Aerodynamics
The design of the wing was done by choosing an airfoil, aspect ratio and taper ratio. It is recommended to investigate other methods of optimising the wing geometry such that the aerodynamic efficiency is increased. Options identified but not analysed within the project timeframe include geometric twist and winglets. Furthermore, it is recommended to expand the scope of the aerodynamic analyses performed to the entire flight envelope, with emphasis on extreme cases; currently, only a level cruise condition was analysed.

Structures & Materials
Firstly, it is recommended that both the fuselage and wing design methods get updated to account for cutouts on the structure. Inspection ports, maintenance access point and battery replacement have to be designed and the structure design should reflect those changes. Furthermore, the internal aircraft geometry needs to be designed to a higher level of detail, including components mounts, stringers and reinforcements. Also, more information on CNT layup (number of layers, angles etc.) should be investigated for specific parts.

Propulsion
In the design of the propulsion subsystem, empirical formulas were used to estimate the mass of the electric motor providing the required power. It is recommend to perform a market research and find an existing motor, focusing on its performance at high altitudes and degradation over extended continuous usage. Furthermore, it is necessary to account for the low cooling characteristics of the atmosphere at such altitudes, and ensure the selected motor can endure all flight conditions.

Power
Three recommendations are made for the power subsystem further design. Firstly, it is recommended to model the aircraft performance under different solar cell efficiencies and densities, as well as battery energy densities. This will allow a more in depth understanding of the limiting factors, accounting for the increased mission possibilities with newer technology. The best solar panel to battery combination can be selected, allowing for further optimization of the design. Next, as SORA moves towards a more in-depth design, battery and solar cell degradation over a single mission needs to be properly modelled and planned. This could require changing the flight profile for later stages of a mission, or increasing seasonal constraints at different latitudes. Finally, it is recommended to proceed with a more detailed design of the power subsystem, including power losses in cables and other electronics, mass due to extra components and optimizing the energy path to allow for the least resistance.

Communication
The communication design focused on implementing off the shelf components into the final assembly, allowing for proven reliability and power consumption. The primary communication link has been handled by the Starlink constellation, but more options should be considered, for example the OneWeb and Amazon Kuiper LEO constellations. Factors like global coverage, future expansion plans, data rates and costs should be considered for a more detailed design.

Stability & Control
Multiple recommendations can be made for the stability and control design. Firstly, a dynamic stability analysis should be performed, exploring the aircraft eigenmotions. This requires a more accurate mass model of the aircraft, including mass moment of inertias about the three major axis. Such analysis would allow for better control surface sizing as well as a more efficient flight control system. Secondly, a more optimized tail geometry is required for a more detailed design. In the current design a S_h/S ratio of 0.1 was initially set, and a stability and controllability

analysis followed. This reaches a stable and controllable aircraft, but does not optimize for minimum mass or minimum power. A better iterative approach is suggested, sweeping different tail ratios to find the one with the minimum overall power requirement. Lastly, it is recommended to explore the automated flight control logic, as in the current design stage it has not been explored. The UAV requires an automated flight control system, able to manoeuvrer the aircraft in normal flight regime as well as in emergencies. A complete control logic should be set up, including the inputs received, autopilot thresholds and human override.

Payload

For any aerospace mission the payload plays an essential factor, and even more in a solar powered HALE, where the entire aircraft is designed around the payload requirements. For a more detailed design it is recommended to directly contact manufacturers to optimize the design of the instrumentation, focusing on eliminating non needed parts, such as power supply or external shell, to strive for weight reduction. Furthermore, with a direct link to manufactures, instruments could benefit from a redesign taking the harsh high altitude conditions into account, for example focusing on low temperature resistance.

Industry Recommendations

With multiple aspects of the design being optimized and explored more in detail, some recommendations to the climate research industry and aviation industry are given to ensure a beneficial environment for SORA and similar HALE projects.

With the advent of solar powered HALE platforms that can perform missions longer than a few days, the possibilities of better data for climate research emerges. Currently, most Global Climate Models (GCMs) operate with a cubic resolution of about 100 km per side, rendering sub kilometre resolution data less useful. Furthermore, global standards on data type and format are missing, requiring significant post processing to access the newly sampled data. The GCMs industry should move towards standardization of datasets, making better use of the newly available data collection platforms, and increase model resolution as well as utilize this data for better dynamical downsampling. Finally, real time data can be fully utilized only if calibration standards are set in advance.

Solar powered aviation is and will always be limited by solar panel efficiency and battery energy density. Advanced performance solar panels and batteries have been tested, reaching better efficiency and weight to energy ratio, but further testing is needed to utilize them in real world usage. Research institutes should work closely together with manufacturers to refine production techniques and lower the product cost, as well as perform in-situ testing rather than in a laboratory environment.

Finally, a push for standardized HALE platforms regulations across the world needs to be made to utilize them at their fullest potential. Different regulations from country to country hurt performance and global coverage, as the flight plan needs to be adjusted to comply with airspace rules. Set climb and descent sectors should be implemented over certain airports, as well as standardizing ATC communication for a UAV.

A

AI Usage

In this appendix, a comprehensive explanation of Artificial Intelligence (AI) use throughout this project can be found. For all points mentioned, the following holds: All responses have been checked and have never been directly pasted into the report. It is widely known that AI tools make mistakes, therefore all contents given by these models have been critically assessed, as can be read in the following paragraphs.

Search Machine: Throughout the project, mainly during the literature research phase, AI tools were used as search machines, comparable to the way one would use Google Scholar. It was used as a way of finding accurate and usable scientific articles and reports. AI models can provide faulty sources, i.e. sources that do not exist, non-credible sources, or sources that do not contain the information asked for. To make sure no faulty sources were used within the report, all sources given by AI tools were checked at least twice. Firstly, during the writing of the literature research, a source given by an AI would be accessed, checked if it existed, checked if the source was deemed trustable, and thoroughly read to ensure the right information was available. Additionally, during the proofreading phase, all sources in the bibliography were checked again on the same criteria. This ensured only existing and credible sources were used.

Coding: AI tools were used in coding in the following instances;

- Planning the code structure.
- Generation of code upon providing the AI a pseudo code prompt.
- Debugging the code.
- Generation of verification tests.
- Printing the outputs in the correct format.
- Generating plots.

In all these instances, the AI generated code was checked for mistakes before being implemented on the main branch. Furthermore, AI was used to implement verification tests, but the actual comparison was done with hand-calculated numbers.

Proofreading: AI tools were used to proofread written texts in the report, in order to ensure a professional, and technical report without spelling mistakes and unreadable sentences. Texts prompted by an AI tool were never directly pasted into the report, but adjusted by the team. Additionally, all texts generated by AI were always critically assessed and checked on content correctness.

Latex Formatting: AI tools were used with Latex formatting. This was especially used in the generation of long tables, in order to ensure a professional and consistent looking layout of the entire document. The texts written in the tables were never generated by AI, but written by the team. Additionally, AI tools were asked how to create minipages, how to shorten the table of contents, how to put multiple equations in one line, etc. Please note that all these things do not have a direct influence on the contents of the report, only on formatting style and layout.

Image Enhancer/Upscaler: In some cases, AI tools were used to upscale the resolution of images or to convert rough sketches made by group members into vectorized images.

Bibliography

[1] Minobe, S., Behrens, E., Findell, K., Loeb, N., Meyssignac, B., and Sutton, R., "Global and regional drivers for exceptional climate extremes in 2023–2024: beyond the new normal," 2023. doi:10.1038/s41612-025-00996-z.

[2] Lee, D., Fahey, D., Skowron, A., Allen, M., Burkhardt, U., Chen, Q., Doherty, S., Freeman, S., Forster, P., Fuglestvedt, J., Gettelman, A., Léon, R. D., Lim, L., Lund, M. T., Millar, R., Owen, B., Penner, J., Pitari, G., Prather, M., Sausen, R., and Wilcox, L. J., "The contribution of global aviation to anthropogenic climate forcing for 2000 to 2018," *Atmospheric Environment*, , No. 21, 2021. doi:10.1016/j.atmosenv.2020.117834.

[3] Lee, D. S., Fahey, D. W., Skowron, A., Allen, M. R., Burkhardt, U., Chen, Q., Doherty, S. J., Freeman, S., Forster, P. M., Fuglestvedt, J., Gettelman, A., de León, R. R., Lim, L. L., Lund, M. T., Millar, R. J., Owen, B., Penner, J. E., Pitari, G., Prather, M. J., Sausen, R., and Wilcox, L. J., "The contribution of global aviation to anthropogenic climate forcing for 2000 to 2018," *Atmospheric Environment*, Vol. 244, 2021, p. 117834. doi:10.1016/j.atmosenv.2020.117834.

[4] Beadling, R., Swaminathan, R., Beucher, R., Blockley, E., Brands, S., Hassler, B., Hegedűs, D., Hoffman, F., Lee, J., Lewis, J., Lu, J., Malinina, E., Medeiros, B., Scoccimarro, E., Tjiputra, J., Turner, B., and Watson-Parris, D., "Observational Data for Next-Generation Climate Model Evaluation: Requirements, Considerations, and Best Practices," *Earth System Science Data Discussions*, 2026. doi:10.1175/BAMS-D-25-0079.1.

[5] Teoh, R., Engberg, Z., Schumann, U., Voigt, C., Shapiro, M., Rohs, S., and Stettler, M. E. J., "Global aviation contrail climate effects from 2019 to 2021," *Atmospheric Chemistry and Physics*, Vol. 24, 2024, pp. 6071–6089. doi:10.5194/acp-24-6071-2024.

[6] National Academies of Sciences, Engineering, and Medicine, "Chapter 5: Contrail Forecast and Verification," *Developing a Research Agenda on Contrails and Their Climate Impacts*, The National Academies Press, 2025. doi:10.17226/29073.

[7] Wilmot, T. Y., Mallia, D. V., Hallar, A. G., and Lin, J. C., "Wildfire plumes in the Western US are reaching greater heights and injecting more aerosols aloft as wildfire activity intensifies," 2022. doi:10.1038/s41598-022-16607-3.

[8] Vaezi, R. B., Martin, M. R., and Hosseinpour, F., "Impacts of wildfire smoke aerosols on radiation, clouds, precipitation, climate, and air quality," *Atmospheric Environment: X*, 2024. doi:10.1016/j.aeaoa.2025.100322.

[9] Bärfuss, K. B., Schmithüsen, H., and Lampert, A., "Drone-based meteorological observations up to the tropopause – a concept study," *Atmospheric Measurement Techniques*, Vol. 16, 2023, pp. 3739–3765. doi:10.5194/amt-16-3739-2023.

[10] Cadiou, P., Plougonven, R., Podglajen, A., Hertzog, A., and Mac Farlane, A., "Strateole 2 balloons reveal persistent errors in reanalyzed winds and trajectory calculations in the tropical lower stratosphere," *Atmospheric Chemistry and Physics*, Vol. 26, 2026, pp. 1665–1684. doi:10.5194/acp-26-1665-2026.

[11] Lieder, D., Bien, M., Seume, E., Lück, S., Ferraro, F., Friedrichs, J., and Goeing, J., "Performance and Emission Analysis of Aircraft Engines under Realistic Conditions," *16th European Conference on Turbomachinery Fluid Dynamics and Thermodynamics, ETC 2025*, European Conference on Turbomachinery (ETC), 2025. doi:10.3390/ijtpp11010002.

[12] Murphy, F., Devlin, G., and McDonnell, K., "Miscanthus production and processing in Ireland: An analysis of energy requirements and environmental impacts," , 2013. doi:10.1016/j.rser.2013.01.058.

[13] Mrozik, W., Rajaeifar, M. A., Heidrich, O., and Christensen, P., "Environmental impacts, pollution sources and pathways of spent lithium-ion batteries," *Energy & Environmental Science*, Vol. 14, 2021, pp. 6099–6121. doi:10.1039/D1EE00691F.

[14] Siqueira, I. R., Durán-Chaves, M., Dewey, O. S., Williams, S. M., Ginestra, C. J., De La Garza, J., Song, Y., Wehmeyer, G., and Pasquali, M., "Fully recyclable carbon nanotube fibers," *Carbon*, 2025.

[15] Group 19, "Midterm Report: Medium Altitude Long Endurance Observatory Aircraft for Climate Research," , 2026. AE3200 Design Synthesis Exercise.

[16] Hersbach, H., Bell, B., Berrisford, P., Biavati, G., Horányi, A., Muñoz Sabater, J., Nicolas, J., Peubey, C., Radu, R., Rozum, I., Schepers, D., Simmons, A., Soci, C., Dee, D., and Thépaut, J.-N., "ERA5 Monthly Averaged Data on Pressure Levels from 1940 to Present," , 2023.

[17] Ko, H.-C., Chun, H.-Y., Geller, M. A., and Ingleby, B., "Global Distributions of Atmospheric Turbulence Estimated Using Operational High Vertical-Resolution Radiosonde Data," *Bulletin of the American Meteorological Society*, Vol. 105, No. 12, 2024, pp. E2551 – E2566. doi:10.1175/BAMS-D-23-0193.1.

[18] Palmén, E., and Newton, C. W., "The Lower Stratosphere," *Atmospheric Circulation Systems: Their Structure and Physical Interpretation*, International Geophysics, Vol. 9, Academic Press, 1966, pp. 57–128. doi:10.1016/S0074-6142(08)60314-9.

[19] Seidel, D. J., Free, M., and Wang, J., "Diurnal cycle of upper-air temperature estimated from radiosondes," *Journal of Geophysical Research: Atmospheres*, Vol. 110, No. D9, 2005. doi:https://doi.org/10.1029/2004JD005526.

[20] Lilie Weaver, "Between Air and Space - Zephyr and the Future of High Altitude Pseudo-Satellites within Defence," Tech. rep., 2018.

[21] Shulman, H., and Ginell, W. S., "Nuclear and Space Radiation Effects on Materials," NASA Space Vehicle Design Criteria (Structures) NASA SP-8053, National Aeronautics and Space Administration, Jun. 1970.

[22] Sanchez, V. M., Barbosa, R., Cruz, J. C., Chan, F., and Hernandez, J., "Optimal Sizing of a Photovoltaic-Hydrogen Power System for HALE Aircraft by means of Particle Swarm Optimization," *Mathematical Problems in Engineering*, Vol. 2015, No. 1, 2015, p. 183701. doi:https://doi.org/10.1155/2015/183701.

[23] Arvesen, J. C., Griffin, R. N., and Pearson, B. D., "Determination of Extraterrestrial Solar Spectral Irradiance from a Research Aircraft," *Appl. Opt.*, Vol. 8, No. 11, 1969, pp. 2215–2232.

[24] European Union Aviation Safety Agency (EASA), "Proposal for a Roadmap on Higher Airspace Operations," Tech. rep., European Union Aviation Safety Agency, March 2023.

[25] Reuber, E., and Boyero Perez, M., "EUROCONTROL Guidelines for High Altitude Long Endurance (HALE) RPAS in European Airspace," Tech. Rep. EUROCONTROL-GUID-201, EUROCONTROL, September 2025. ISBN 978-2-87497-134-1.

[26] HAPS Alliance, "Cooperative, Seamless, and Global Digital Skies for Higher Airspace," Tech. rep., HAPS Alliance, May 2025.

[27] Gettelman, A., Hoor, L., Pan, L., Randel, W., Hegglin, M. I., and Birner, T., "The Extratropical Upper Troposphere and Lower Stratosphere," *Reviews of Geophysics*, Vol. 49, 2011, p. RG3003. doi:10.1029/2011RG000355.

[28] Peter, P., Matthes, S., Frömming, C., Jöckel, P., Bugliaro, L., Giez, A., Krämer, M., and Grewe, V., "Influence of temperature and humidity on contrail formation regions in the general circulation model EMAC: a spring case study," *Atmospheric Chemistry and Physics*, Vol. 25, 2025, pp. 5911–5934. doi:10.5194/acp-25-5911-2025.

[29] Dupont, J.-C., Haeffelin, M., Badosa, J., Clain, G., Raux, C., and Vignelles, D., "Characterization and Corrections of Relative Humidity Measurement from Meteomodem M10 Radiosondes at Midlatitude Stations," *Journal of Atmospheric and Oceanic Technology*, Vol. 37, No. 5, 2020, pp. 857–871. doi:10.1175/JTECH-D-18-0205.1.

[30] Seelig, T., Wolf, K., Bellouin, N., and Tesche, M., "Quantification of the radiative forcing of contrails embedded in cirrus clouds," *Nature Communications*, Vol. 16, 2025, p. 10703. doi:10.1038/s41467-025-66231-8.

[31] United States Environmental Protection Agency, "Inventory of U.S. Greenhouse Gas Emissions and Sinks 1990-2022," Tech. Rep. EPA 430-R-24-004, United States Environmental Protection Agency, 2024.

[32] Chipperfield, M. P., Bekki, S., Dhomse, S., Harris, N. R. P., Hassler, B., Hossaini, R., Steinbrechta, W., Thiéblemont, R., and Weber, M., "Detecting recovery of the stratospheric ozone layer," *Springer Nature*, Vol. 549, No. 218, 2017. doi:10.1038/nature23681.

[33] Brasseur, G., Cox, R., Hauglustaine, D., Isaksen, I., Lelieveld, J., Lister, D., Sausen, R., Schumann, U., Wahner, A., and Wiesen, P., "Contrails and Climate Change: Understanding Formation, Impact, and Mitigation Strategies for Aviation-Induced Clouds," *Elsevier Science*, Vol. 6, No. 8, 1998, pp. 100–120. doi:10.37502/IJSMR.2023.6808.

[34] Wetzel, G., Fischer, H., and Oelhaf, H., "Remote sensing of trace gases in the midinfrared spectral region from a nadir view," *Applied Optics*, Vol. 34, No. 3, 1995, pp. 467–479.

[35] Roscoe, H., and Hill, J., "Vertical resolution of oversampled limb-sounding measurements from satellites and aircraft," *Journal of Quantitative Spectroscopy Radiative Transfer*, Vol. 72, 2001, pp. 237–248.

[36] Dudhia, A., "Infrared Limb Sounding — MIPAS and HIRDLS," Tech. rep., Atmospheric, Oceanic and Planetary Physics, Oxford University, Oxford, UK, 2003.

[37] D. Crisp, "Measuring Atmospheric Carbon Dioxide from Space with the Orbiting Carbon Observatory-2 (OCO-2)," , 2015.

[38] Lorente, A., Borsdorff, T., Butz, A., Hasekamp, O., aan de Brugh, J., Schneider, A., Wu, L., Hase, F., Kivi, R., Wunch, D., Pollard, D. F., Shiomi, K., Deutscher, N. M., Velazco, V. A., Roehl, C. M., Wennberg, P. O., Warneke, T., and Landgraf, J., "Methane retrieved from TROPOMI: improvement of the data product and validation of the first 2 years of measurements," *Atmospheric Measurement Techniques*, Vol. 14, 2021, pp. 665–684. doi:10.5194/amt-14-665-2021.

[39] Riaz, A., Sun, K., Baker, B. D., Buma, B., Cady-Pereira, K. E., Miller, C. C., Eddy, W. C., Farris, B. M., Kampe, T. U., Kort, E. A., Leisso, N. P., Spurr, R., Stuchiner, E. R., and Yang, W. H., "Towards a Remote Sensing Solution to Quantify Nitrous Oxide Emissions by Integrating Shortwave and Thermal Infrared Bands," 2026, pp. 199–208.

[40] Xu, J., Zhang, Z., Rao, L., Wang, Y., Letu, H., Shi, C., Tana, G., Wang, W., Zhu, S., Liu, S., Shi, E., Wang, Y., Chen, L., Dong, X., and Shi, J., "Remote Sensing of Tropospheric Ozone from Space: Progress and Challenges," *Journal Of Remote Sensing*, 2024, pp. 1–20. doi:10.34133/remotesensing.0178.

[41] Carslaw, D., and Rhys-Tyler, G., "Remote Sensing of NO2 Exhaust Emissions from Road Vehicles," , 2013.

[42] Schad, T., and Penn, M., "IR Spectroscopy of COmosphere Dynamics with the CO First Overtone Band," *Astronomische Nachrichten*, 2010.

[43] Tamburello, A., McGonigle, A. J. S., Kantzas, E. P., and Aiuppa, A., "Recent advances in ground-based ultraviolet remote sensing of volcanic SO2 fluxes," *Annals of Geophysics*, Vol. 54, No. 2, 2011, pp. 199–208. doi:10.4401/ag -5179.

[44] Wei, P. S., Chiu, H.-H., Hsieh, Y.-C., Yen, D.-L., Lee, C., Tsai, Y.-C., and Ting, T.-C., "Absorption coefficient of water vapor across atmospheric troposphere layer," *Heliyon*, Vol. 5, 2019.

[45] Kremser, S., Thomason, L. W., von Hobe, M., Hermann, M., Deshler, T., Timmreck, C., Toohey, M., Stenke, A., Schwarz, J. P., Weigel, R., Fueglistaler, S., Prata, F. J., Vernier, J.-P., Schlager, H., Barnes, J. E., Antuña-Marrero, J.-C., Fairlie, D., Palm, M., Mahieu, E., Notholt, J., Rex, M., Bingen, C., Vanhellemont, F., Bourassa, A., Plane, J. M. C., Klocke, D., Carn, S. A., Clarisse, L., Trickl, T., Neely, R., James, A. D., Rieger, L., Wilson, J. C., and Meland, B., "Stratospheric aerosol - Observations, processes, and impact on climate," *Reviews of Geophysics*, Vol. 54, No. 2, 2016, pp. 278–335. doi:10.1002/2015RG000511.

[46] Petzold, A., Gysel, M., Vancassel, X., Hitzenberger, R., Puxbaum, H., Vrochticky, S., Weingartner, E., Baltensperger, U., and Mirabel, P., "On the effects of organic matter and sulphur-containing compounds on the CCN activation of combustion particles," Vol. 5, No. 12, 2005, pp. 3187–3203. doi:10.5194/acp-5-3187-2005.

[47] Schumann, U., "On Conditions for Contrail Formation from Aircraft Exhausts," *Meteorologische Zeitschrift*, Vol. 5, No. 1, 1996, pp. 4–23. N.F. 5.

[48] Teoh, R., Engberg, Z., Schumann, U., Voigt, C., Shapiro, M., Rohs, S., and Stettler, M. E. J., "Global Aviation Contrail Climate Effects from 2019 to 2021," *Atmospheric Chemistry and Physics*, Vol. 24, No. 10, 2024, pp. 6071–6093. doi:10.5194/acp-24-6071-2024.

[49] Jarry, G., Dalmau, R., Very, P., Ballerini, F., and Bocu, S.-D., "GVCCS: A Dataset for Contrail Identification and Tracking on Visible Whole Sky Camera Sequences," *Earth System Science Data*, Vol. 18, No. 1, 2026, pp. 1037–1059. doi:10.5194/essd-18-1037-2026.

[50] Goldstein, N., Tannian, B., M.Stark, McCann, J., Wiggins, R., Santman, J., Nasca, M., Woodman, P., Saleh, M., and Nakanishi, K., "Fabrication and Testing of a UAS-Based Visible to Extended-SWIR Hyperspectral Sensor," *2019 10th Workshop on Hyperspectral Imaging and Signal Processing: Evolution in Remote Sensing (WHISPERS)*, 2019. doi:10.1109/WHISPERS.2019.8921001.

[51] National Aeronautics and Space Administration, "Supplementary Material Spreadsheet," , 2021. NTRS 20210017083.

[52] Gilmore, D. G., Stuckey, W. K., and Fong, M., "Thermal Surface Finishes," *Spacecraft Thermal Control Handbook*, edited by D. G. Gilmore, The Aerospace Press, El Segundo, CA, 2002, Chap. 4, 2nd ed., pp. 139–159.

[53] Glenair, Inc., "Hermetic Leak Rate Testing Limits and Qualification for Connectors Used in Military and Aerospace Applications," Tech. rep., Glenair, Inc., 1211 Air Way, Glendale, California 91201, 2025.

[54] Munson, B. R., Young, D. F., Okiishi, T. H., and Huebsch, W. W., *Fundamentals of Fluid Mechanics*, 6th ed., John Wiley & Sons, Inc., 2009.

[55] Serrano, J. R., García-Cuevas, L. M., Bares, P., and Varela, P., "Propeller Position Effects over the Pressure and Friction Coefficients over the Wing of an UAV with Distributed Electric Propulsion: A Proper Orthogonal Decomposition Analysis," *Drones*, Vol. 6, No. 2, 2022, p. 38. doi:10.3390/drones6020038.

[56] Raymer, D. P., *Aircraft Design: A Conceptual Approach*, 2nd ed., AIAA Education Series, 1992.

[57] Kapoulas, I. K., C. Statharas, J., Hatziefremidis, A., and Baldoukas, A. K., "Fast Airfoil Selection Methodology for Small Unmanned Aerial Vehicles," *Applied Sciences*, Vol. 12, No. 18, 2022. doi:10.3390/app12189328.

[58] Selig, M. S., "Low Reynolds Number Airfoil Design," , November 2003.

[59] Rajagopal, S., and Ganguli, R., "Multidisciplinary Design Optimization of Long Endurance Unmanned Aerial Vehicle Wing," *Computer Modeling in Engineering & Sciences*, Vol. 86, No. 4, 2012, pp. 283–316. doi:10.3970/cmes.2012.086.283.

[60] Niță, M., and Scholz, D., "Estimating the Oswald Factor from Basic Aircraft Geometrical Parameters," *Deutscher Luft- und Raumfahrtkongress 2012*, Deutsche Gesellschaft für Luft- und Raumfahrt (DGLR), Bonn, Germany, 2012. Document ID: 281424.

[61] Kamal, N. N. M., Basri, A. A., Basri, E. I., Basri, I. S., and Abas, M. F., "Comparison Study Between Schrenk's Approximation Method and Computational Fluid Dynamics of Aerodynamic Loading on UAV NACA 4415 Wing," *Journal of Advanced Research in Fluid Mechanics and Thermal Sciences*, Vol. 64, No. 2, 2019, pp. 283–292.

[62] Prieto, M., Escartí-Guillem, M. S., and Hoyas, S., "Aerodynamic Optimization of a VTOL Drone Using Winglets," Vol. 17, 2023, p. 100855. doi:10.1016/j.rineng.2023.100855.

[63] Oettershagen, P., "Solar-Powered Unmanned Aerial Vehicles: Design and Environment-Aware Navigation for Robust Low-Altitude Multi-Day Continuous Flight," , 2018. Diss. ETH No. 24947.

[64] Morgado, J., Vizinho, R., Silvestre, M., and Páscoa, J., "XFOIL vs CFD performance predictions for high lift low Reynolds number airfoils," *Aerospace Science and Technology*, Vol. 52, 2016, pp. 207–214.

[65] Beresnev, S. A., Gryazin, V. I., and Gribanov, K. G., "Analysis of Wind Vertical Component Characteristics in the Stratosphere," *Russian Meteorology and Hydrology*, Vol. 34, No. 11, 2009, pp. 724–731. doi:10.3103/S1068373909110041.

[66] Salih, R., Zhou, F., Abbas, N., and Mastoi, A. K., "Experimental Investigation of Reinforced Concrete Beam with Openings Strengthened Using FRP Sheets under Cyclic Load," 2020. Accessed via ResearchGate.

[67] Kim, D. W., Jin, C. K., Lee, M. S., Kang, C. G., and Seo, H. Y., "Investigation of Optimal Lamination Condition of CFRTP by Compression Molding Method and a Comparison of Mechanical Properties with CFRTS," *Advances in Mechanical Engineering*, Vol. 12, No. 12, 2020, pp. 1–11. doi:10.1177/1687814020986252.

[68] Zu, M., Lu, W., Li, Q.-W., Zhu, Y., Wang, G., and Chou, T.-W., "Characterization of Carbon Nanotube Fiber Compressive Properties Using Tensile Recoil Measurement," *ACS Nano*, Vol. 6, No. 5, 2012, pp. 4288–4297. doi:10.1021/nn300857d.

[69] Dikin, D. A., Stankovich, S., Zimney, E. J., Piner, R. D., Dommett, G. H. B., Evmenenko, G., Nguyen, S. T., and Ruoff, R. S., "Strong, Light, Multifunctional, and Processable Graphene Composite Papers," *ACS Nano*, Vol. 4, No. 8, 2010, pp. 4806–4814. doi:10.1021/nn102925a.

[70] Frulla, G., and Cestino, E., "Design, manufacturing and testing of a HALE-UAV structural demonstrator," *Composite Structures*, Vol. 83, No. 2, 2008, pp. 143–153. doi:10.1016/j.compstruct.2007.04.008.

[71] Zahm, A. F., "Relation of Rib Spacing to Stress in Wing Planes," Technical Note 5, National Advisory Committee for Aeronautics, Washington, D.C., May 1920.

[72] Hilburger, M. W., "Buckling of Thin-Walled Circular Cylinders," Tech. Rep. NASA/SP-8007-2020/REV 2, National Aeronautics and Space Administration, Langley Research Center, Hampton, Virginia, December 2020. Second revision of NASA SP-8007, originally published September 1965, first revised August 1968.

[73] Sun, J., Zhou, Y., Zhou, Z., and Wang, Z., "Analysis of Structural Characteristics of the HALE Joined-Wing Configuration UAV," *International Journal of Aerospace Engineering*, , No. 1, 2025, pp. 1121–1135. doi:10.1155/ijae/9931529.

[74] Yi, Z., and Heping, W., "A Study of Structure Weight Estimating for High Altitude Long Endurence (HALE) Unmanned Aerial Vehicle (UAV)," *Proceedings of the 25th International Congress of the Aeronautical Sciences (ICAS)*, International Council of the Aeronautical Sciences (ICAS), Hamburg, Germany, 2006.

[75] Riccio, E., Alifano, F., Baraniello, V. R., and Coiro, D., "A Comprehensive Review of Propeller Design and Propulsion Systems for High-Altitude Pseudo-Satellites," *Applied Sciences*, Vol. 15, No. 14, 2025, p. 8013. doi:10.3390/app15148013.

[76] Aref, P., Ghoreyshi, M., Jirasek, A., Satchell, M. J., and Bergeron, K., "Computational Study of Propeller Wing Aerodynamic Interaction," *2018 AIAA Aerospace Sciences Meeting*, American Institute of Aeronautics and Astronautics, Kissimmee, Florida, 2018, p. 0778. doi:10.2514/6.2018-0778.

[77] García-Gutiérrez, A., Gonzalo, J., Domínguez, D., López, D., and Escapa, A., "Aerodynamic Optimization of Propellers for High Altitude Pseudo-Satellites," *Aerospace Science and Technology*, Vol. 96, 2020, p. 105562. doi:10.1016/j.ast.2019.105562.

[78] You, K., Zhao, X., Zhao, S.-Z., and Faisal, M., "Design and Optimization of a High-altitude Long Endurance UAV Propeller," *IOP Conference Series: Materials Science and Engineering*, Vol. 926, No. 1, 2020, p. 012018. doi:10.1088/1757-899X/926/1/012018.

[79] Fulton, D., Gallagher, P., Grannan, W., Martin, J., Mastej, N., and Wujek, B., "The Bunny: A Simulated Commercial Air Transportation Study," Final Design Proposal NASA-CR-195537, Department of Aerospace and Mechanical Engineering, University of Notre Dame, Notre Dame, IN, April 1993. NASA/USRA University Advanced Design Program 1992-1993.

[80] Moelyadi, M. A., Amalia, E., Putranto, A. B., Diasta, I. N., Witjaksono, M. L., Tsaqif, F. M., and Ginting, S. A., "Design optimization of HALE propeller by using SLSQP method," *Discover Applied Sciences*, Vol. 8, No. 208, 2026. doi:10.1007/s42452-026-08298-6.

[81] Colozza, A., "High Altitude Propeller Design and Analysis Overview," Overview report, Federal Data Systems, Cleveland, Ohio, March 1998. Prepared for NASA Lewis Research Center / ERAST Program.

[82] Mastali, M., Dalvand, A., and Sattarifard, A., "The impact resistance and mechanical properties of the reinforced self-compacting concrete incorporating recycled CFRP fiber with different lengths and dosages," *Composites Part B: Engineering*, Vol. 112, 2017, pp. 74–92. doi:10.1016/j.compositesb.2016.12.029.

[83] Kirtskhalia, V. G., "Speed of Sound in Atmosphere of the Earth," *Open Journal of Acoustics*, Vol. 2, No. 2, 2012, pp. 80–85. doi:10.4236/oja.2012.22009.

[84] Wood, D. H., Okulov, V. L., and Bhattacharjee, D., "Direct calculation of wind turbine tip loss," *Renewable Energy*, Vol. 95, 2016, pp. 269–276. doi:10.1016/j.renene.2016.04.017.

[85] McCormick, B. W., *Aerodynamics, Aeronautics, and Flight Mechanics*, John Wiley & Sons, The Pennsylvania State University, 1979.

[86] France, R. M., Geisz, J. F., Song, T., Olavarria, W., Young, M., Kibbler, A., and Steiner, M. A., "Triple-junction solar cells with 39.5% terrestrial and 34.2% space efficiency enabled by thick quantum well superlattices," *Joule*, Vol. 6, No. 5, 2022, pp. 1121–1135. doi:10.1016/j.joule.2022.04.024.

[87] Aho, A., Isoaho, R., Tukiainen, A., Polojärvi, V., Aho, T., Raappana, M., and Guina, M., "Temperature Coefficients for GaInP/GaAs/GaInNAsSb Solar Cells," *AIP Conference Proceedings*, Vol. 1679, AIP Publishing, 2015, p. 050001. doi:10.1063/1.4931522.

[88] Yang, J. K., Jiao, X. Y., Yang, Y., Chen, Z. C., et al., "High-Efficiency Flexible GaAs Solar Modules Used for Unmanned Aerial Vehicles and Stratospheric Airships," *Lecture Notes in Electrical Engineering*, Springer, 2020. doi:10.1007/978-981-15-3947-3_29.

[89] Cao, W., Zhang, J., and Li, H., "Batteries with high theoretical energy densities," *Energy Storage Materials*, Vol. 26, 2020, pp. 46–55. doi:10.1016/j.ensm.2019.12.024.

[90] Beckers, C. J. J., Hoedemakers, E. R. G., Dağkılıç, A., and Bergveld, H. J., "Round-Trip Energy Efficiency and Energy-Efficiency Fade Estimation for Battery Passport," *2023 IEEE Vehicle Power and Propulsion Conference (VPPC)*, 2024. doi:10.1109/VPPC60535.2023.10403325.

[91] Judd, L. M., Al-Saadi, J. A., Janz, S. J., Kowalewski, M. G., Pierce, R. B., Szykman, J. J., Valin, L. C., Swap, R., Cede, A., Mueller, M., Tiefengraber, M., Abuhassan, N., and Williams, D., "Evaluating the impact of spatial resolution on tropospheric NO_2 column comparisons within urban areas using high-resolution airborne data," *Atmospheric Measurement Techniques*, Vol. 12, 2019, pp. 6091–6111. doi:10.5194/amt-12-6091-2019.

[92] Hosseini, N., Jamal, H., Matolak, D. W., Haque, J., and Magesacher, T., "UAV Command and Control, Navigation and Surveillance: A Review of Potential 5G and Satellite Systems," *IEEE Aerospace Conference*, 2019. doi:10.1109/AERO.2019.8741719.

[93] Davis, D., Mathew, F., Jamaludheen, K., Seenivasaraja, N., and Karthikeyan, A., "Design and Analysis of Different Types of Aircraft Radome," *International Journal of Engineering Research and Technology*, 2018.

[94] Wang, Y., "Application of Quartz Fiber Reinforced Composite Material in High Frequency Radome," *Proceedings of the Eighth Asia International Symposium on Mechatronics*, Lecture Notes in Electrical Engineering, Springer, 2022, pp. 214–221. doi:10.1007/978-981-19-1309-9_22.

[95] Khichi, S., Bhutto, A., Maitlo, I., and Chandio, A., "Processing and Characterization of Aerospace Composites for Advanced Radome Applications," *ACS Omega*, Vol. 10, No. 32, 2025, pp. 36421–36431. doi:10.1021/acsomega.5c04792.

[96] Jung, S., Roustaei, M., Harvey, J., Taieb, H., Bhat, S., Froese, D., Piche, N., and Maghoul, P., "Freeze-thaw-induced microstructural damage in polyester fiber-reinforced cementitious composites revealed by X-ray microtomography," *Construction and Building Materials*, 2026. doi:10.1016/j.matdes.2025.115256.

[97] Xu, K., Wu, C., Chen, Z., Liu, H., Li, M., Yang, L., Ai, S., and Cui, S., "Anti-ablation and insulation integrated gradient quartz fiber needle felt reinforced SiO2 ceramic/aerogel composite for thermal protection," *Ceramics International*, 2025. doi:10.1016/j.ceramint.2024.11.186.

[98] Lai, F., Xu, L., Zhang, J., Qian, J., and Chen, Q., "Topological Constraint-Enabled High-Temperature Creep Resistance and Mechanical Robustness in Organic-Inorganic IPN-Like PMI Aerogels," *Chemical Engineering Journal*, 2026. doi:10.1016/j.cej.2026.176303.

[99] De Pree, C., Rau, U., Selina, R., Svoboda, B., and Beasley, T., "Coordinated Starlink User Terminal Testing Near the VLA," Tech. rep., National Radio Astronomy Observatory (NRAO), 2023.

[100] Humphreys, T., Iannucci, P., Komodromos, Z., and Graff, A., "Signal Structure of the Starlink Ku-Band Downlink," Tech. rep., Radionavigation Laboratory, The University of Texas at Austin, 2023. doi:10.1109/TAES.2023.3268610.

[101] Aral, G., Bousquet, M., and Sun, Z., *Satellite Communications Systems: Systems, Techniques and Technology*, Wiley, 2020. doi:10.1002/9781119673811.

[102] Cheung, K., "The Role of Margin in Link Design and Optimization," *2015 IEEE Aerospace Conference*, IEEE, 2015. doi:10.1109/AERO.2015.7119220.

[103] Wertz, J. R., and Larson, W. J., *Space Mission Engineering: The New SMAD*, Microcosm Press, 2011.

[104] Ohmori, M., Ogawa, K., and Kashiwazaki, H., "A Discussion on Periodic Communication Disruption in LEO Satellite Constellations," *Proceedings of the International Conference on Communication Technology (ICCT-Pacific)*, 2025. doi:10.1109/ICCT-Pacific63901.2025.11012871.

[105] Sadraey, M. H., *Aircraft Design: A Systems Engineering Approach*, John Wiley & Sons, Chichester, United Kingdom, 2012. doi:10.1002/9781118352700.

[106] Ashfaq, M., Rastogi, D., Kitson, J., Abid, M. A., and Kao, S.-C., "Evaluation of CMIP6 GCMs Over the CONUS for Downscaling Studies," *Journal of Geophysical Research: Atmospheres*, , No. 21, 2022. doi:10.1029/2022JD036659.

[107] Tapiador, F. J., Navarro, A., Moreno, R., Sánchez, J. L., and García-Ortega, E., "Regional climate models: 30 years of dynamical downscaling," *Atmospheric Research*, , No. 21, 2020. doi:10.1016/j.atmosres.2019.104785.

[108] Sharma, A., Thakur, N., Hashem, A., Dawoud, T. M., and Abd_Allah, E. F., "Insecticidal potential of Bacillus thuringiensis, Beauveria bassiana and Metarhizium anisopliae individually and their synergistic effect with barazide against Spodoptera litura," *Heliyon*, Vol. 10, No. 17, 2024, p. e37175. doi:10.1016/j.heliyon.2024.e37175.

[109] Campbell, F. C., Jr., "Chapter 12 - Assembly," *Manufacturing Processes for Advanced Composites*, Elsevier, 2004, pp. 439–470. doi:10.1016/B978-1-85617-415-2.50012-5.

[110] Bakis, G., Wendel, J.-F., Zeiler, R., Aksit, A., Häublein, M., Demleitner, M., Benra, J., Forero, S., Schütz, W., and Altstädt, V., "Mechanical Properties of the Carbon Nanotube Modified Epoxy–Carbon Fiber Unidirectional Prepreg Laminates," *Polymers*, Vol. 13, No. 5, 2021, p. 770. doi:10.3390/polym13050770.

[111] Group 19, "Baseline Report: Medium Altitude Long Endurance Observatory Aircraft for Climate Research," , 2026. AE3200 Design Synthesis Exercise.

[112] Hasan, Y. J., Roeser, M. S., Hepperle, M., Niemann, S., Voß, A., Handojo, V., and Weiser, C., "Flight mechanical analysis of a solar-powered high-altitude platform," *CEAS Aeronautical Journal*, Vol. 14, No. 1, 2023, pp. 201–223. doi:10.1007/s13272-022-00621-2.

[113] Younossi, O., Arena, M. V., Moore, R. M., Lorell, M. A., Mason, J., and Graser, J. C., "Test and Evaluation Trends and Costs for Aircraft and Guided Weapons," Tech. Rep. MG-109-AF, RAND Corporation, 2004.

[114] Zhao, X., Verhagen, W. J. C., and Curran, R., "Disposal and Recycle Economic Assessment for Aircraft and Engine End of Life Solution Evaluation," *Applied Sciences*, Vol. 10, No. 2, 2020, p. 522. doi:10.3390/app10020522.

[115] Jiménez Pérez, A., and Alonso López, M., "The Importance of RAMS Analysis for Unmanned Systems," , Oct. 2021.

[116] Middleton, J., Burks, B., Wells, T., Setters, A., Jasiuk, I., Predecki, P., Hoffman, J., and Kumosa, M., "The effect of ozone on polymer degradation in Polymer Core Composite Conductors," *Polymer Degradation and Stability*, Vol. 98, No. 1, 2013, pp. 436–445.

[117] Department of Defense, "Military Handbook: Designing and Developing Maintainable Products and Systems," , Aug. 1997.

[118] Voskuijl, M., "Cruise Range in Formation Flight," *Journal of Aircraft*, Vol. 54, No. 6, 2017, pp. 2184–2191. doi:10.2514/1.C034246.